INTEGRATED LOW-COST READING DEVICE TARGETING THE ACCESSIBILITY TO QUALITY EDUCATION FOR THE VISUALLY IMPAIRED.

Submitted by: Ms. Ingrid Retha Botha (BScEng, UKZN) – 215024569

Supervisor:

Prof. Glen Bright

Co-supervisor:

Mr. James Edward Thomas Collins

January 2021

Submitted in the fulfilment of the academic requirements for the degree of Master of Science in Engineering at the School of Mechanical Engineering, University of KwaZulu-Natal

DECLARATION 1: SUBMISSION

As the candidate's supervisor, I agree to the submission of this dissertation.

Supervisor: [redacted] Date: 25/1/21

Prof Glen Bright

As the candidate's co-supervisor, I agree to the submission of this dissertation.

Co-supervisor: [redacted] Date: 25/1/21

Mr James Collins

COLLEGE OF AGRICULTURE, ENGINEERING AND SCIENCE

DECLARATION 2: PLAGIARISM

I, Ingrid Retha Botha, declare that

1. The research reported in this thesis, except where otherwise indicated, is my original research.

2. This thesis has not been submitted for any degree or examination at any other university.

3. This thesis does not contain other persons' data, pictures, graphs or other information, unless specifically acknowledged as being sourced from other persons.

4. This thesis does not contain other persons' writing, unless specifically acknowledged as being sourced from other researchers. Where other written sources have been quoted, then:
   a. Their words have been re-written but the general information attributed to them has been referenced
   b. Where their exact words have been used, then their writing has been placed in italics and inside quotation marks, and referenced.

5. This thesis does not contain text, graphics or tables copied and pasted from the Internet, unless specifically acknowledged, and the source being detailed in the thesis and in the References sections.

Signed: [redacted] Date: 25/1/21

Ms. I. Botha

COLLEGE OF AGRICULTURE, ENGINEERING AND SCIENCE

COLLEGE OF AGRICULTURE, ENGINEERING AND SCIENCE DECLARATION 3: PUBLICATIONS

DETAILS OF CONTRIBUTION TO PUBLICATIONS that form part and/or include research presented in this thesis (include publications in preparation, submitted, *in press* and published and give details of the contributions of each author to the experimental work and writing of each publication)

Publication 1: 12th Robotics and Mechatronics Conference of South Africa, 2020 (Published)

Botha I.R., Bright G., Collins J.E.T, *Evaluation of Dielectric Elastomers in Applications as Low Cost, Small-Scale Actuators,* in proceedings of 12th Robotics and Mechatronics Conference of South Africa (SAUPEC/ROBMECH/PRASA), 2020, pp 196-201

Ingrid Botha was the lead author of this paper and conducted all research under the supervision of Prof. Bright and Mr. Collins

Publication 2: IEEE 1st Malaysian International Biomedical Engineering Conference, 2020 (Accepted)

Botha I.R., Bright G., Collins J.E.T, *Impact of Electrode Application and Geometry on Performance of Diaphragm-Shaped Dielectric Elastomer Actuator,* Kuala Lumpur, Malaysia, IEEE 1st Malaysian International Biomedical Engineering Conference, 2020

Ingrid Botha was the lead author of this paper and conducted all research under the supervision of Prof. Bright and Mr. Collins

Signed: [redacted]

Ms. I. Botha

Date: 25/1/21

ACKNOWLEDGMENTS

This work is based on the research supported in part by the National Research Foundation of South Africa (Scarce Skills Masters Block Grant).

I would like to take this opportunity to thank my mother, father and sisters for their love and endless encouragement over the course of this research project.

Special gratitude goes to my supervisor, Prof. G. Bright for not only the academic guidance, support, and time that he has invested in the success of this research project, but also in his unwavering belief in me as a student and young academic. I also thank my co-supervisor Mr. J.E.T Collins for his assistance, inspiration, and support – your kind words and open mind made this project a reality.

Thank you to Quiverful for shaping me into the person I am today, I will see you again.

ABSTRACT

The movement of society into the Fourth Industrial Revolution introduces a fundamental shift in how Mechatronic devices are implemented in daily life and the workplace. Terms such as ‘efficiency’ and ‘competitive advantage’ bolster the drive to develop technology that sets one company, business or manufacturer apart from the rest. However, is there a possibility that the same technology can be used to unify society by providing equal opportunity within the workplace, academia, and everyday life? This research addresses the position of the South African visually impaired community within Industry 4.0 and how Mechatronic technology can be used to improve current employment statistics and quality of life.

The purpose of the research project was to assess the financial and operational viability of a portable text to braille transcription device with focus on the implementation of novel small-scale Dielectric Elastomer Actuators (DEAs). The device was required to transcribe printed characters into braille in real-time. This allowed visually impaired individuals access to books, journals and newspapers without assistance or the need to wait for the production of a braille-embossed printed copy. In addition, the research included an assessment of the current employment and educational circumstances of the blind and visually impaired community of South Africa as well as an investigation of the ideal approach to address multiple key factors using a single device.

The design of the selected device was comprised of three major subsystems; the optical character recognition hardware, the software and electronics required to transcribe the characters into a series of voltage outputs and the actuation system of the tactile display. The synthesis and operating conditions of the dielectric elastomer actuators were experimentally assessed. The tactile display was required to be low cost, small-scale, portable, and robust to present a sustainable solution to the challenges presented by the lack of accessible reading material and high cost of commercially available options. Scaled models of the DEA were synthesised. The subsequent experiments included the comparison of elastomer materials, electrode materials, the effect of pre-strain on DEA performance, the effect of different application methods of carbon electrodes and the performance of inflated DEA membranes. The electronic subsystem was simulated to investigate the reaction time of the device. Design challenges included the requirement of a high voltage power supply to actuate the DEA, the insulation of the synthesised membranes, electrical protection of the micro-controller and the incorporation of optical character recognition programmes. This research aimed to assist in the development of actuators with greater portability and scope for miniaturisation than commercially available pneumatic or piezoelectric alternatives while addressing the challenges faced by the visually impaired community of South Africa.

TABLE OF CONTENTS

LIST OF ACRONYMS

3D:	Three-Dimensional
AC:	Alternating Current
ASCII:	American Standard Code for Information Interchange
CAPTCHA:	Completely Automated Turing Test to tell Computers and Humans Apart
CNT:	Carbon Nanotube
CSI:	Camera Serial Interface
DC:	Direct Current
DE:	Dielectric Elastomer
DEA:	Dielectric Elastomer Actuator
EAP:	Electroactive Polymer
GPIO:	General-Purpose Input/Output Pins
HV:	High Voltage
JAWS:	Job Access with Speech
LED:	Light Emitting Diode
LSTM:	Long-Short Term Memory
MOSFET:	Metal-Oxide-Semiconductor Field Effect Transistor
OCR:	Optical Character Recognition
OEM:	OCR Engine Modes
OpenCV:	Open Source Computer Vision
OS:	Operating System
PC:	Personal Computer
PDMS:	Polydimethylsiloxane
PIL:	Pillow Library
PLA:	Polylactic Acid
PSM:	Page Segmentation Modes
RAM:	Random Access Memory
SVHN:	Street View House Number
USB:	Universal Serial Bus

NOMENCLATURE

A	Area
C	Constant
ε_r	Relative Electric Permittivity
ε_0	Electric Permittivity of Free Space
E	Applied Electric Field
V	Voltage
t	Unit Thickness
Y	Elastic Modulus
s_t	Elastic Compressive Strain
a	Unactuated Length
δ	Induced Strain in Lateral/Radial
r	Radius of Curvature
θ	Angle of Curvature
h	Convex Height

TABLE OF FIGURES

TABLE OF TABLES

1. INTRODUCTION

1.1 Introduction

The following dissertation presents the systematic study of a Mechatronic approach to improving accessibility of the blind and visually impaired in the workplace and educational environment. The design of the mechatronic device aimed to bridge the gap between the lack of literary resources and media available for the visually impaired in South Africa, particularly to school-age children. The appropriate function and requirements of such a device were first investigated through a literature review before the ideal solution was defined. The final device was required to transcribe printed text into braille in real-time using novel Dielectric Elastomer Actuators (DEAs). The device consisted of three sub-systems: the optical character recognition scanner, text to braille transcription software and supporting hardware, and the haptic feedback output. The haptic feedback output actuated the refreshable braille display. The literature review accounted for selecting the appropriate haptic feedback actuation system, of which DEAs were the final choice. A proof-of-concept design of the DEA was then manufactured and tested against specifications compiled in the literature review. The following motivation and background provide a detailed account of such a device's validity in the search for equal access to information for the blind and visually impaired in South Africa.

1.2 Motivation and background

The initial aim of the research project was to develop a solution to incorporate a larger percentage of the disabled members of the South African population in industry and manufacturing. This intended to carve out a position for the disabled community in South Africa’s movement into the fourth industrial revolution. The project's focus was narrowed down to individuals affected by visual impairments and blindness to restrict the specifications of the project while reaching as large a percentage of the population as possible. Vision impairment was identified as the highest percentage of all disabilities, comprising 32% of the disabled population in South Africa [1]. In order to develop an understanding of the ideal mechatronic solution to improve accessibility to the blind and visually impaired in the modern workplace, a study was conducted on the current global and national statistics relating to the visually impaired.

The number of blind or visually impaired individuals in the world was identified as approximately 253 million by the Orbis Annual Report [2]. The report further defined that 89% of effected individuals live in low/middle income countries and that 75% suffered from preventable or treatable conditions. Both statements prove true for a country such as South Africa where majority of the visually impaired population reside in remote areas and fall within the low-income bracket [1]. This economic position results in a limited access to treatment and a greater risk of developing

malnutrition based visual impairments. To expand upon this statement, Figure 1-1 illustrates the leading causes of blindness worldwide [3]. The top three causes of blindness are identified as cataracts, uncorrected refractive errors, and glaucoma. Of these three, both cataracts and uncorrected refractive errors are considered preventable or treatable conditions. However, the inequality of healthcare in South Africa results in many not being treated. Evidence of this is presented by Twsanya [4] who asserts that the recommended cataract surgery rate is 2000 per million population per year, with South Africa having a rate of 729 per million population per year. The third major cause, glaucoma, is often associated with individuals suffering from diabetes. Diabetes also cause individuals to be twice as likely to develop cataracts at an earlier age. Diabetes is a major issue in South Africa due to the prevalence of malnutrition in the low-income demographic of South Africa [5].

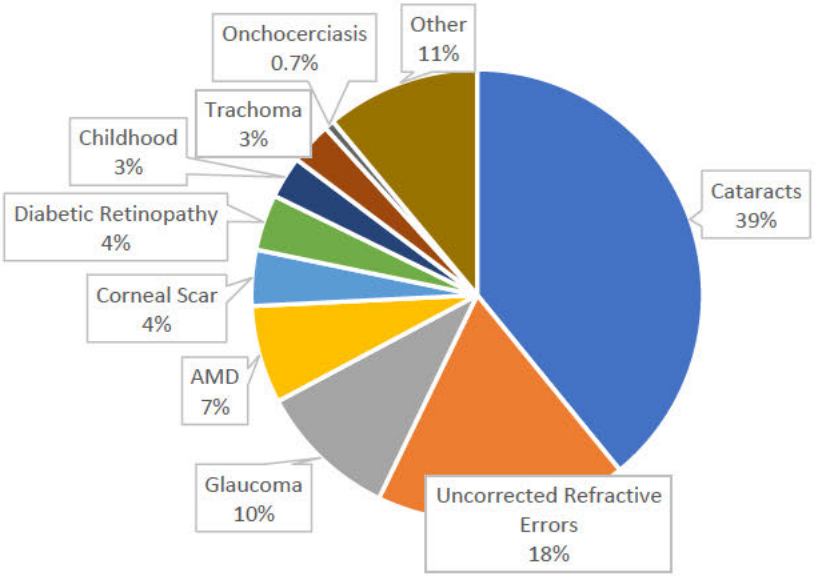

Figure 1-1 Global causes of blindness [3]

Through the abovementioned research, the conclusion was drawn that the cost of corrective eye surgery and balanced nutrition was outside the income range of the majority of effected individuals. Therefore, a high priority design objective was identified as presenting a solution at minimum production cost to make it accessible to the largest population of blind and visually impaired individuals. This assertion is specific to South Africa.

The next point to be considered is why 97% of the blind and visually impaired population of South Africa is unemployed [1]. Is it a question of lack of accessibility in the workplace or a more profound societal concern? Life Healthcare states that the high unemployment rate is affected by the perception that the visually impaired cannot carry out daily tasks [1]. This stigma is undoubtedly an issue in today's society; however, it also serves as a blanket statement to detract from a larger problem that highlights the education system's role in the precipitation of this stigma.

When investigating possible job opportunities and careers for the blind, the following statement from the American Printing House for the Blind [6] is considered, “People who are blind or visually impaired are employed in as many diverse jobs as those who are sighted in the workforce. Individuals with vision loss can perform jobs across all industries, including marketing, human services, business management and administration, health science, law, agriculture, and more.” To assess the viability of this statement and understand the scope of accessibility, five professionals from diverse career paths were researched. These individuals and their respective careers are briefly described below.

Nathaneal Wales is an advocate for the National Centre for Blind Youth in Science in America and the president of the California Association for Blind Students. He completed his bachelor’s degree in Civil and Environmental Engineering in 2001. Wales credited his ability to complete his degree in four and a half years to a strong basis in braille literacy and attendance of an adjustment to blindness training course he attended before commencing college [7]. Wales made all class notes using a slate and stylus, his braille typewriter, and Braille Lite, which was particularly useful to record matrices and differential equations. He employed readers to assist in reading his textbooks since not all course material was available on tape or in braille. Further, he employed lab partners to read gauges and make visual observations during practicals. Wales attributed his successful university experience to the assistance of the Disabled Student Services to provide funding, the guidance of blind mentors in the National Federation of the Blind, as well as his determination to be independent and reach the high expectations that he set for himself [8].

John Furniss is a woodworker based in Washougal, Washington. Furniss was diagnosed as legally blind after an accident when he was 16 years old. He attended a vocational rehabilitation school in Utah where he learnt braille and woodworking using accessible tools; he went on to graduate from the Emil Fries School of Piano Technology for the Blind [9]. Furniss uses the lathe in his workshop without assistance and uses a rotomatic to measure components. The rotomatic is a threaded tool designed to allow blind artisans to measure using a notched rectangular nut and hexagonal locking nut which runs on the threaded rod. Through counting the number of turns of the rectangular nut between notches on the threaded rod, exact measurements in multiples of one-sixteenth of an inch can be determined [10].

Justice Zakeria Yacoob served as a constitutional judge in South Africa and has served as the Chairperson of the South African National Council of the Blind. Justice Yacoob was diagnosed as blind at 16 months and completed his education at the Arthur Blaxall School for the Blind. He completed a BA majoring in English and Law and an LLB at the University of Durban-Westville [11]. Justice Yacoob is well known for his role as an anti-apartheid activist and advocate of social justice in South Africa. During his time as a judge on the South African constitutional court,

Justice Yacoob utilised the JAWS computer reader software, a braille printer, a Braille-Note braille note-taker and the assistance of a legally trained personal assistant to perform his duties. His response to an interviewer posing the question on what he believes to be the ideal balance between braille, assistive technology and sighted assistance for a blind lawyer was as follows “, I think each blind person would require a different balance. I use braille for anything that needs to be carefully studied and other assistive technology for the rest.” [12]

Michael Forzano started his career as a programmer at Amazon at the age of 26 in 2013 after graduating from Birmingham University. Forzano was born blind due to a genetic condition. Forzano uses a standard laptop with a screen reader program to read each line while writing code [13].

Molly Burke is a Canadian social media personality and motivational speaker. Burke became legally blind at age 14 after suffering from a degenerative eye disease since adolescence [14]. The slow onset of her condition allowed her to learn braille, the use of a Perkins braille typewriter and typing classes on a keyboard while sighted. This was provided to her by the educational board of the school that she was attending and included finger sensitisation, sensory books and the braille system. She further states that, even with the assistance of modern technology, braille is blind individuals’ access to a proper education. Braille is the only solution to learning correct English spelling and grammar. Burke used a Perkins braille typewriter and braille display during her schooling. She now uses a range of Apple products in her career as a social media personality. Apple products are accessible for the blind with built-in voice-over technology. Similarly, Android products have also adopted voice over technology. As with Forzano, Burke uses a standard Apple laptop with voice-over software and navigates using key commands instead of the tracker pad [15] .

The information above is not an exhaustive account of the variety of professions performed by the blind and visually impaired but does succeed in providing an indication of what can be achieved as well as the technology and resources available to achieve it. The importance of braille as a means of communication has further been highlighted. What can also be concluded from this research is that, although all noted individuals are now successful in their own right, the funding provided by foreign education systems, such as America and Canada, or employers was imperative in the accessibility to equipment and information. Therefore, the expectations and budget of the education system in South Africa must be considered when analysing the suitability of the abovementioned equipment and technology in schools. This statement, in combination with the overview of professionals provided, gives a clear indication that accessibility within the workplace is within reach, however, it must be supported by a stable foundation provided by the education system.

Therefore, the question of the high unemployment statistic must now be analysed in the scope of the education provided to blind and visually impaired students in South Africa. The primary challenges faced by the government in providing an equality-based educational system for the visually disabled can be summarised as follows: [11]

1. Staff provisioning
2. Adequate training of teachers
3. Access to learner teacher support material in braille
4. Access to assistive learning devices

Are these challenges being met? Khumalo et al. [11] asserts that a lack of an equitable budget dedicated to inclusive education at both a provincial and national level is a major opposition to overcoming these challenges. The lack of appropriate budget designation is revealed to have a long-term impact on all the challenges listed above, most often not for lack of effort from the leaders and educators of these schools. These systemic issues further separate the goals of American and other first world schools dedicated to the visually impaired from their South African counterparts through introducing complex socio-economic issues such as having to choose between access to electricity or appropriate learning material. Therefore, even though it may not be the result of the decisions of individual schools, problem areas must be identified to build an understanding of what is required in these institutions.

Statistically, of the 22 schools dedicated to the blind and visually impaired in South Africa, 17 do not have access to braille textbooks of the CAPS syllabus [11]. Further, the absence of sufficient Perkins braille typewriters result in students having to share during class, making note-taking difficult. This leaves many students at a disadvantage when studying for tests and exams. The lack of funds to even repair damaged Perkins typewriters rules out the option for majority of the 22 schools to provide computers with JAWS screen-reader software. This results in students leaving school with no computer literacy skills, drastically impacting their chances of being able to attend tertiary education or work without assistance [11].

Beyond the lack of technological and academic resources, the absence of professionals trained to educate the visually impaired and blind impact the students' academic success. The absence of an education qualification dedicated to the visually impaired results in many teachers starting their career at these specialised schools with no knowledge of braille or the unique requirements of teaching blind students [11]. Wolffe [16] states, "There is an almost universal misunderstanding about differences between people with vision loss and those who are fully sighted exists and is demonstrated when sighted people speak to others with vision accompanying blind individuals rather than to them or automatically assume that someone without sight must also have a hearing or cognitive impairment." Of course, this is entirely untrue. However, in the

case of instructors and teachers who do not have experience living or working with the blind and visually impaired, the consequence of this bias is severe. It can be argued that career education is equally as important as the content and subjects taught to attain access to that career path. If the student's goals and aspirations are not taken seriously, an idea of futility is cultivated within their mind, thus eroding the pressure and drive to continue their studies and practice their braille reading skills.

The ideal solution would be the employment of education professionals who are trained to work with specific disabilities such as the blind and visually impaired. However, in an already financially strained system, the ideal solution may not be possible. Alternatively, caring adults in the student's lives must be provided with the tools to convey their high expectations of the child and develop the child's disability-specific skills [16]. A possible example of this is shared reading time, where the sighted parent can read along with the child in order to provide feedback on their performance and assist them in developing their skills outside the school environment. This scenario could be enabled through the use of a portable text to braille transcription device, which will allow the child to read using the braille interface while the parent follows by reading the printed text. This introduces the requirement that the device be easy to operate and maintain without training in order to allow parents to assist the child when using it at home.

Upon analysis of the information above, it can be concluded that the device to be designed must meet the following requirements. The device must be low cost to account for the socio-economic challenges of distribution in South Africa. The device must fulfil the needs of school-age children in order to assist with their education, as this is the area faced with the largest challenges. The device must be able to convey written information in a medium accessible to blind students. This is due to the noticeable lack of computers or funding for digital equipment. Therefore, the device must be able to deal with the most common and inexpensive existing material, thus textbooks and printed subject matter provided by the Department of Education and public libraries. It must be capable of transcribing printed text into a medium accessible to the blind and visually impaired in real-time.

1.3 Challenges

The above information highlighted an area of deficiency in the education of blind or visually impaired individuals, specifically the absence of appropriate braille printed learning material. The challenges of developing the design included the use of low-cost materials and synthesis procedures to make the device as accessible as possible to the visually impaired community. The design was required to be robust to be handled by both children and adults on a daily basis without failure or the need for short term maintenance. As a reading apparatus, the device needed to be capable of miniaturisation and weight reduction to be portable. The miniaturisation of the haptic

feedback system posed the greatest challenge since both actuators and auxiliary mechanics were required to be scaled to fit on a single, handheld device.

1.4 Research question

Can a Mechatronic design approach to portable text transcription provide a low-cost solution to the job accessibility crisis affecting the blind and visually impaired in South Africa?

1.5 Research objectives and dissertation structure

The aim of the research project was to investigate, design and analyse the viability of a portable, low-cost text transcription device as a solution to the lack of accessible information available to the visually impaired. The following research objectives facilitated the achievement of this aim:

1. Analysed the ideal approach to making information and printed media accessible to the blind and visually impaired.
2. Identified an appropriate medium to which the printed or written test is to be transcribed, most notably audio or braille.
3. Identified a haptic feedback system that would facilitate real time text to braille transcription while meeting the requirements of the research question.
4. Identified appropriate software and programming to control the device and enable optical character recognition.
5. Designed the electrical, mechanical and software subsystems of the device with emphasis on miniaturisation and a low-cost design.
6. Tested and analysed a proof of concept of the haptic feedback subsystem against the requirements of the design.

The dissertation served as a record of the above-mentioned objectives and through the completion of the objectives, answered the research question.

The dissertation was structured as follows: Chapter 2 presented a literature review in which the transcription medium, transcription technology and optical character recognition software were researched and identified. Chapter 2 also identified the requirements and specifications of the design through analysing braille mechanics and similar commercially available devices.

The research collected in Chapter 2 was applied in Chapter 3 which detailed the proposed mechanical and electronic design of the device. The first subsection of Chapter 3 summarised the specifications and requirements and was followed by a series of conceptual designs. Thereafter, the final mechanical design and final electronic design was discussed.

The analysis of system performance was divided into three chapters. Each chapter included a methodology, description of the testing, results and an analysis of the results.

Chapter 4 included the installation and configuration of the experimental Optical Character Recognition (OCR) program and further discussed the results of the tests conducted to test the accuracy and processing speed of the subsystem. The OCR software comprised the control subsystem of the device.

The second subsystem which included the DEA output was tested in two stages, each stage was recorded in Chapters 5 and 6 respectively. Chapter 5 was comprised of the initial set of experimental results and analysis of the ideal materials to be used in the synthesis of the Dielectric Elastomer Actuators. The data collected in the chapter was then utilised in Chapter 6 to synthesise and test a proof of concept of the dielectric elastomer diaphragm-type actuators to analyse the response against product specifications.

Chapter 7 detailed a comprehensive discussion of the applicability of the entire system with consideration toward the aims and objectives of the dissertation. Further, the results of the system performance chapters were summarised and compared to design specifications, and potential areas of further study were explored.

Chapter 8 served as the conclusion of the dissertation and explored the key insights of the dissertation, the limitations of the research and recommendations for future work in the field of study.

1.6 Chapter Summary

This chapter introduced the reader to the research topic and highlighted the challenges faced by the blind and visually impaired in South Africa. The welfare, financial and educational situations of the visually impaired community were explored from both an international and local perspective. This allowed a background of the topic to be constructed and provided a focussed portrait of the motivation behind the research topic and aims of the project. The challenges of the research and proposed Mechatronic device were identified and a succinct research question was presented. An action plan was established through a set of objectives and the resultant structure of the dissertation was presented. The following chapter presents the literature review exploring the dynamics of braille and voice-over technology as a possible solution to the research question. Thereafter, the requirements of the selected system are refined through the analysis of commercially available technology.

2. LITERATURE REVIEW

2.1 Introduction

The literature review serves to identify key requirements and specifications of the design while fulfilling the first four objectives of the project as set out in Chapter 1.5. The first area of interest being the analysis of the ideal approach to making information and printed media accessible to the blind and visually impaired. Thereafter, an appropriate transcription medium is explored followed by a Mechatronic-specific analysis of the technology required to produce the transcription medium.

2.2 Braille versus voice-over

Once the target market has been narrowed down the student body of South African schools dedicated to the blind and visually impaired the following question must be posed: will a design based on braille or text-to-speech technology be most successful in improving the education and employment statistics of this group? A survey conducted by the National Federation of the Blind Jernigan Institute [17] provided evidence of education and employment levels being directly dependent on the ability to read braille. However, in a society that is becoming progressively more dependent on technology and favours efficiency above all, it is challenging to believe that a braille system will continue to exceed the performance of audio-based technology. Of course, the use of braille and text-to-speech technology in conjunction would be ideal; this discussion deals with a scenario in which the economic situation of the majority of learners calls for a single device in which to interpret printed reading material. The discussion below analyses the advantages and disadvantages of each.

Examples of accessible audio technology include text-to-speech synthesisers, audiobooks, tapes and voice-over software on laptops and mobiles. The primary advantage of this approach is that the technology involved is progressing much faster than braille counterparts. This is partially since this technology is not only limited for use by the visually impaired. Sighted individuals who favour efficiency and multi-tasking are now listening to audiobooks during their daily commute. Typing is steadily being replaced by voice input on mobile devices. Therefore, the target market and resulting motivation for companies to produce voice-over technology are increasing. It can further be argued that voice-over technology is more accessible than braille typing and reading equipment since most iOS and Android smartphones now possess voice-over functions. Free text to audio scanning applications such as KNFB reader is also available to be downloaded to smartphones [18]. Voice-over software such as NVDA are also free to download on laptops and computers [19]. However, this will only apply to a small group of students who are in the financial position to afford personal smartphones and laptops.

A significant appeal of voice-over software or text-to-speech synthesisers is the lack of requirement to learn a new method of interpretation such as the grades of braille. It is easy to use and requires minimal effort from the user [20]. This concept is further influenced by the spiral of misunderstanding connected to braille literacy. This misunderstanding is influenced by three factors, the difficulty to learn braille, the limitations on reading speed when using braille and the stigmatization of learners who use braille by peers who read print. These points are particularly true for learners who are integrated into mainstream schools. The lack of learning material and teachers who are braille literate further build on the façade of inaccessibility of braille [17]. The long lead time to order and produce books in braille using braille embossing printers is both a national and global problem that has influenced the opinion of braille. Braille printed books are also much larger than their printed counterparts, an example of this is the popular Harry Potter series which is printed in 56 volumes [21].

Braille literacy is a right advocated for by many, the reasons for which will be discussed below. Studies have proven that the information retained through purely listening memory is considerably less than reading memory due to the focus of the attention of the reader [22]. Learning through purely audio sources also places limitations on the student's understanding of spelling, grammar, and mathematics-based courses. The ability of sighted individuals to read mathematic symbols and music notes and form their own interpretations is an uncontested necessity in the mainstream education system. Similarly, visually impaired students should be afforded the same opportunity, an opportunity made possible by the diversity of the braille system. The braille system is used to represent all 26 letters of the Latin alphabet in upper and lower case, punctuation symbols, numbers, mathematical operators and can be used to write musical compositions [23]. The braille alphabet can also represent dialects such as Urdu and Japanese.

Braille literacy introduces the opportunity for silent reading. Studies indicate that silent reading results in increased neural plasticity and activation of deeper areas of the brain, such as the thalamus and brain stem [24]. The processing of spoken language can also experience increased speed and accuracy through the improvement of an individual's literacy skills [25]. Literacy does not only have a cognitive and developmental impact but also presents a social and cultural effect on the individual. The concept of literacy generates a sense of belonging within human psychology since it forms a method of communication with others of an identifiable group [26]. Beyond this sense of social union, braille literacy specifically has attributed to the self-esteem of children and facilitated the acceptance of their disability. Further, it allows braille literate individuals a greater sense of independence later in life through allowing them to search for alternate sources of information, decreasing their dependence on a single source or caregiver [27].

The long-term impacts of the cognitive advantages and independence granted by braille literacy result in higher employment rates. A study conducted by Ryles [28] in 1996 analysed the employment achieved by 74 working-age adults who have been blind since birth. It was recorded that 56% of individuals who were taught braille were employed while non-braille users only had an employment rate of 23%. A larger study consisting of 1000 blind adults was conducted by Bell in 2013 confirmed this hypothesis and went on to note that the level of earnings and quality of employment also improved the more proficient the individual was at communicating using braille [29].

It must also be noted that, even though the spiral of misunderstanding surrounding braille exists and is a valid challenge when tasked with adjusting the attitude of newly blind individuals, children and sighted parents of affected individuals, it is based on incorrect facts. Under the tutelage of a well-educated teacher, braille is not more challenging to learn than traditional reading; however, the stigma is caused by the limited supply of teachers and learning material [30]. There is currently no formal qualification for teachers to work with the visually disabled; therefore, many teachers arrive at the special schools without the appropriate knowledge of braille [11]. A further misconception is the idea that braille readers are slower than traditional readers, the National Federation of the Blind Jernigan Institute recorded readings speeds of 200 words per minute in children who learnt braille at an early age [17].

It is doubtful whether an equal level of creativity and self-expression can be attained through purely audio input or with the assistance of a sighted person. The presence of a condition such as blindness does not over-ride the individual personality of the person affected. As with many introverted children within the mainstream education system who function at their best when left to work through academic assessments alone and with the freedom to dedicate a self-determined period of time to the question, this trait is also true for individuals of the blind community [31]. Beyond academics, many perceive the reading experience as an opportunity for introspection and self-reflection. To be limited to linear tapes, audio recordings, or the reliance on a reader will afford little chance for an opportunity that the sighted are given since the early stages of their education.

Upon consideration of the opposing ideas of the research presented above, it can be concluded that a device dedicated to the transcription of text to braille would be both a novel concept as well as more suitable to cover a larger number of challenges faced by the blind community. Lack of appropriate reading material, the cognitive benefits as well as the improved employment statistics all support the decision for a braille-based system. It can further be concluded that the text to speech medium satisfies an immediate problem. However, the impact of text to braille not only serves as a means of communication but has more prominent long-term effects through advocating for higher braille literacy statistics.

2.3 Existing braille technology

Commercially available braille technology can be divided into three categories:

- Embossers and braillers: These devices “print” braille onto embossing paper by pressing indentations into the paper to form the braille cells.
- Refreshable Braille-display: A device connected to a PC, tablet or Smartphone device that transcribes the output into braille and allows the user to input information using the Perkins-style keyboard.
- Note-takers: Personal digital assistants which includes a Perkins-style input and voice synthesizer, touch screen and refreshable braille outputs

Notable examples and supporting technology of each category are discussed below.

2.3.1 Embossers and braillers

- Embossing printers

Embossing printers are manufactured in a variety of sizes. Industrial or large-volume printers range from R160 000 to R1 350 000 and can print textbooks and magazines. Personal or small-volume printers’ cost between R30 000 and R84 000 [32]. Some printers such as the Braille Express 150 are portable and can emboss braille at a speed of 150 characters per second. The Braillo 400SR is a high speed, large volume printer and is advertised to print 1200 pages per hour [33].

- Perkins brailler typewriter

The Perkins Brailler is perhaps the most well known and most common piece of technology utilised by the visually impaired. It is a braille typewriter with six keys that correspond with the six braille dots that make up a braille cell. The embossing paper is fed into the machine in a manner similar to a traditional typewriter as illustrated in Figure 2-1. It is the primary method of braille communication used in South African schools dedicated to the visually impaired [34]. However, many schools do not utilise their total number of Perkins typewriters due to poor budgeting for maintenance and repairs. Therefore, due to the high cost of replacement parts and specialised technicians, students are required to share typewriters during class and assessments [11]. This is a concerning observation, particularly when designing a secondary mechatronic device to be used in schools. It can be concluded that the designed device must be robust and prioritise low-cost maintenance and replaceable parts that are cheap and easily sourced.

- Slate and stylus

The slate and stylus represent the traditional pen and paper within the world of braille technology. The slate is manufactured from plastic or metal and is designed with a hinge to allow for the embossing paper to be slipped between the front and back plates. The common pocket slate measures 29,7cm x 4,4cm x 0,27 cm [35]. The stylus comes in variety of shapes depending on the requirement of the user and has a metal tip used to punch dots into the embossing paper. It remains the cheapest method of taking notes in braille and is priced at R207 on Amazon for a stylus and plastic slate [36].

Figure 2-1 Perkins brailler [34]

Figure 2-2 Slate and stylus

2.3.2 Refreshable braille display

- Focus 14/40/80 Braille Displays

Refreshable braille displays such as the Focus line are utilised in conjunction with the JAWS screen reading software to transcribe digital text into a braille output. The braille-display can be connected to computers, smartphones and tablets using a Universal Serial Bus (USB) or Bluetooth connection. The model number of the Focus line indicates the number of refreshable braille cells per device. The Focus 80 depicted in Figure 2-3 contains 80 refreshable braille cells and the aluminium and steel frame result in a total device weight of 1.02 kg. [37] The cost of the Focus braille displays range from R 20 187,17 for the Focus 14 to R 124 630,46 for the Focus 80 [38].

Figure 2-3 Focus 80 braille display [39]

Commercially available refreshable braille displays utilize piezo-bimorph actuators to control the displacement of the dots in the braille cells. The height of the Focus models is 19 mm, which provide an indication of the level of miniaturisation which the piezo-bimorph actuators are capable of [38]. The piezo-bimorph actuators are further discussed in Section 2.4.

2.3.3 Note-takers

Note-takers such as the Braille Sense, Actilino and Braillenote take the refreshable braille displays a step further by combining a refreshable braille display with an internet connection and word processor software [40]. Therefore, it is possible to complete tasks without the requirement of an additional PC, tablet, or smartphone connection. The Actilino is a compact device that functions as both a refreshable braille display and note-taker. It consists of a braille keyboard and 16 concave braille cells, indicated in Figure 2-4. It can connect to four smartphones/PCs at a time via Bluetooth and USB. The device has a 30-hour battery life and measures 16,6cm x 10,9cm with a height of 2,9cm. The current price is listed as R47 287,35 [40]. The Braillenote Touch pictured in Figure 2-5 includes a touchscreen that uses voice-over to indicate the readers finger position on the screen. The average touching force of the Braillenote refreshable braille dots are between 0.05 N and 0.39 N [41]. The Braillenote Touch is priced at R 88 776,79 [42].

Figure 2-4 Actilino Note-taker [40]

Figure 2-5 Braillenote Touch [42]

2.4 Applicable actuation technology

In order to assess the ideal actuation technology ideal for the application as a portable braille reading device, the scale and requirements of a typical refreshable braille cell were first reviewed. Thereafter, applicable actuation technology was explored.

2.4.1 Summary of mechanics behind braille

The standard dimensions of a braille cell are indicated in Figure 2-6. The average dimensions of the dot base diameter and height are 1,44 mm and 0,48 mm respectively [43]. The tactile braille display will be mounted on the forefinger of the reader's hand to simulate the natural position when reading braille. The braille cell must conform to the finger and be as thin as possible as to not interfere with the proprioception of the reader [17]. Proprioception is defined as the perception or awareness of the position and movement of the body [44]. In the case of reading braille, proprioception is centred around the pad of the index finger. A line of braille is read by running the pad of the index finger from left to right over the embossed line of braille. A light pressure is encouraged when reading in order to increase the quality of perception to the braille symbols. Wu et al [45] states that a minimum contact force of 50 mN at a minimum displacement of 0,25 mm is required to stimulate the shallowest mechanoreceptor. The average reading rate of braille is approximately 120 words per minute [46].

As with experienced sighted readers, readers experienced in braille can predict the complete word before all letters of the word are read. This pattern recognition is considered a result of proprioception by Foulke et al. in studies that compared the recognition of braille characters under static and dynamic test conditions [47]. Foulke hypothesised that there was a high correlation between the movement of the finger and the recognition time. Heller goes on to divide this movement into two categories: active and passive [48]. The non-movement or static condition involved keeping the finger stationary while the pins of the refreshable braille display pressed into the pad of the finger. Active movement was identified as the finger moving over the braille display. The passive movement involved the finger remaining stationary relative to the braille

display but both finger and display were free to move horizontally. The method that generated the best performance was active movement of the finger across the braille display. This result is supported by the work of Darden et al which investigates the effect of friction induced by the sliding motion over embossed braille characters on fingertip sensitivity [49]. Heller's work was reviewed by Russommanno et al. in 2015 and it was hypothesised that the passive movement resulted in better performance statistics than the static tests due to the ability to mimic the proprioceptive feedback in the hand while moving from left to right [46].

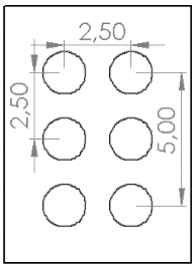

Figure 2-6 Braille cell dimensions

2.4.2 Comparison of actuation technology

With an understanding of the requirements of the method of actuation established, possible actuation systems can now be explored. Piezo-bimorph actuators remain the only type of actuation utilised in commercialised refreshable braille displays, however, the rapid miniaturisation of technology in recent years has led to many alternative actuation techniques being analysed [46]. Possible actuator technologies explored in literature pertaining to braille displays include:

- Electric motors
- Solenoids
- Piezoelectric
- Electrothermal
- Shape Memory Alloys
- Pneumatic
- Electroactive Polymers (Dielectric Elastomers)

Electric motors were not included in the discussion below due to the prioritisation of miniaturisation and portability of the design. Piezoelectric actuators have dominated the market of refreshable braille displays due to their response time and variable force output. The piezo-bimorph actuators utilised in braille displays can be divided into two mechanisms: the bimorph bender and relay-lever mechanism, Figure 2-7. The piezoelectric bimorph bender relies on vibrations initiated by the presence of an electric field to displace the pin while the relay-lever system actuates the pin upward when a voltage is supplied to the relay [50]. The drawback of these mechanisms is the module being comprised of additional components attached to the pin,

therefore limiting the minimum dimensions of the device, and increasing the risk of mechanical failure. The aforementioned auxiliary mechanics are depicted in Figure 2-8, which illustrates the typical configuration of a piezo-bimorph braille cell. Beyond placing limitations on miniaturisation, these drawbacks also result in piezoelectric based braille displays being exorbitantly expensive, as illustrated by the commercially available products discussed under the previous heading [46].

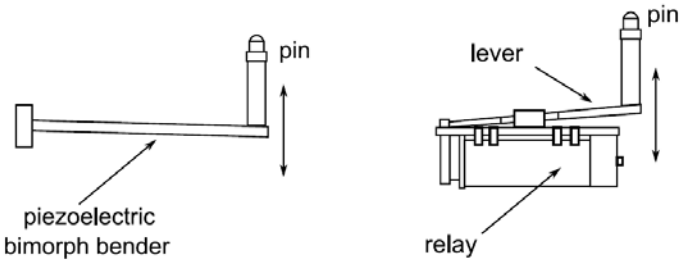

Figure 2-7 Examples of existing Braille mechanisms: (a) piezoelectric bimorph bender and (b) relay-lever system. [50]

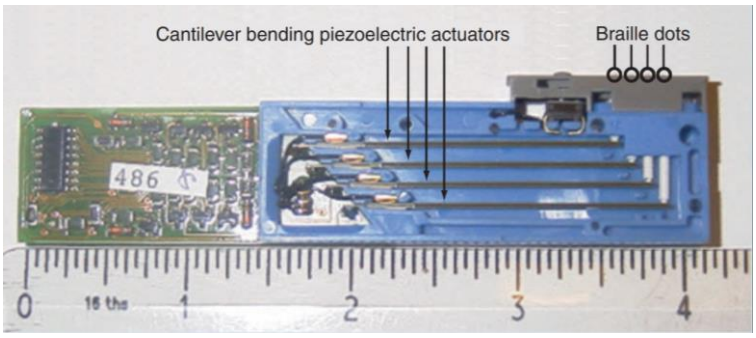

Figure 2-8 Configuration of piezo-bimorph braille cell [51]

The attraction of researching alternative actuation technology was primarily motivated by the reduction of these high costs as well as further miniaturisation of the design. The ideal actuator to be implemented in portable tactile displays were required to encompass the following properties: light weight design, low power, mass manufacturable and robust. Maximum pressure, strain and relative response speed of possible actuator materials are compared in Table 2-1, adapted from the work of Pei et al [52].

Table 2-1 Comparison of Actuators Materials

Type	**Maximum Pressure (MPa)**	**Maximum Strain (%)**	**Response Speed**	**References**
Piezoelectric Ceramic (PZT)	110	0,2	Fast	[53]
Piezoelectric Polymer (PVDF)	4,8	0,1	Fast	[53]
Shape Memory Alloy (TiNi)	>200	>5	Slow	[53]
Solenoid	0,1	50	Fast	[53]
Pneumatic	0,1	56	Fast	[45]
Dielectric Elastomer (acrylic with prestrain)	3	63	Fast	[53]
Dielectric Elastomer (silicone with prestrain)	7,2	380	Fast	[53]

Other factors that were considered when selecting the actuator best suited for the application included the scalability of the mechanism and the power required. The scalability particularly effected the potential selection of piezoelectric and pneumatic actuators. Pneumatic actuators have the potential for miniaturisation while still maintaining a suitable pressure, however, the additional valves and control components limit the compactness and portability of the entire system [45] [54]. Similarly, a prototype developed by Velázquez et al [55] using shape memory alloys initially satisfied the size requirements of a portable design, but reduction of thickness was limited by the requirement for forced air convection supplied by a computer mini fan. Without the additional temperature regulation, the speed of actuation reduced dramatically. The combination of the technical data presented in Table 2-1 and the disadvantages detailed, highlighted the presence of dielectric elastomer actuators amongst the others listed. This novel approach to actuation is discussed further in Section 2.5.

2.5 Dielectric elastomers

2.5.1 Overview

The development of soft actuator technology has experienced an increase of interest in recent years as emerging materials have made it possible to synthesise the theoretical designs into applicable mechanisms [52]. Soft actuator technology is capable of providing a unique solution to the common miniature actuator problem of maintaining mechanical integrity while reducing weight, size and cost [56]. There are a variety of applications where the aforementioned properties would be required with some notable examples being: haptic feedback in touchscreen devices and gaming controllers, refreshable tactile displays and use in biomedical applications such as rehabilitation or artificial muscle synthesis [57] [56].

Common small-scale actuation technology includes electric motors, solenoids, piezoelectric actuators, shape memory alloys and pneumatic devices [56]. However, many of these devices have limitations regarding miniaturisation while maintaining low cost of fabrication, portability, and mechanical integrity, as discussed in Section 2.4. Notable problems are the expense of piezoelectrics and the portability limitations of pneumatic devices [58] [59]. This brings to attention Electroactive Polymers (EAP), colloquially known as soft actuators. EAP's is a broad category of motion generating polymers which are controlled by an applied electric field [60]. EAP's can be further divided into two categories: ionic electroactive polymers and electronic electroactive polymers. Ionic EAP's depend on the diffusion of ions to generate motion while electronic EAP's require an electric field to generate motion. Ionic EAP's are further divided into ionic polymer gels, ionic polymer metal composites, conductive polymers, and carbon nanotubes

[61]. Similarly, electronic EAP's consist of the subdivisions; piezoelectric polymers, dielectric elastomers, electrostrictive polymers and liquid crystal elastomers [61].

Of the subdivisions, dielectric elastomers were selected upon consideration of the maximum strain, maximum pressure, efficiency, and relative speed of multiple EAP actuators. A detailed comparison of material was documented in the journal paper written by Brochu and Pei [52]. The aforementioned paper documented that pre-strained DE's with an acrylic film exhibited the largest maximum strain at 380%, this is approximately 950% greater than the maximum strain that the human muscle can produce and 3 times greater than its competitor; shape memory polymer. The DE also exhibited maximum efficiencies between 60-90% with relative speeds of medium to fast depending on which film material is selected. A major drawback of DEA technology is the large voltage (1-10 kV) input required to actuate the device, however, the production and accessibility of small-scale DC voltage to DC high voltage converters has led to these actuators gaining greater interest in recent years [62].

In order to generate a conclusive decision on the application of DEAs as the actuator system in the portable braille device the working principle, mathematical modelling and present examples of its application were investigated.

2.5.2 Working principles of DEs

Dielectric elastomers can act as either a generator, sensor or actuator depending on the required applications [63]. DE's as actuators have been researched for applications such as artificial muscles, tactile displays, biomimetic robots, and loudspeakers amongst others [52] [56] [64] [65]. A Dielectric Elastomer Actuator (DEA) is primarily comprised of three active layers which produce the actuation of the structure. A polymeric material such as silicone or acrylic elastomers forms the central layer which is sandwiched between two layers of flexible electrodes. Figure 2-9 a) illustrates the dielectric elastomer composite when there is no voltage supply. There is no electric field created between the two layers of electrode material and therefore no force of attraction between oppositely charged electrodes. Figure 2-9 b) illustrates the dielectric elastomer when the switch is closed and allows a voltage to be supplied to the opposing electrode layers.

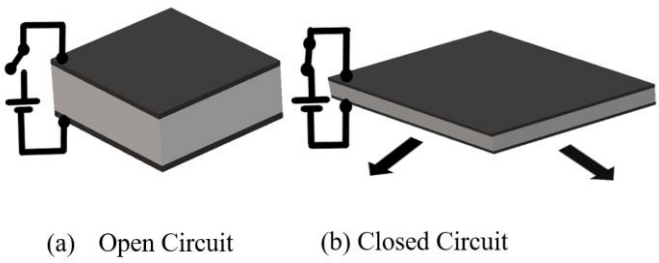

Figure 2-9 Simplified representation of DEA configuration. a) Switch open, therefore no voltage supply to opposing electrode layers. b) Reaction of DEA to voltage supply.

The top layer will generate a positive charge and the bottom layer will generate a negative charge, thus creating an electric field in which the electrodes of either layer are attracted to the opposing layer. This force of attraction forces the polymeric elastomer layer to reduce in thickness. Assuming the elastomer is composed of incompressible linearly elastic material, the reduction in thickness will result in a directly proportional increase in area. Therefore, if the DEA is not constrained about the edges of the electrode layers, the DEA will expand outwards as thickness reduces. Alternatively, if the DEA were to be constrained with rigid boundaries about its edges, the expansion of area will result in the DEA buckling upwards and mimicking the mechanical motion of a diaphragm [56]. The direction of the vertical displacement must be constrained in a specific direction. Methods of constraining the direction of the buckling include embossing the elastomer, attaching a spring mechanism to one side or creating a fluid filled recess between the active DEA layer and a passive elastomer layer [56] [66] [67].

2.5.3 Mathematical modelling of dielectric elastomers

It must be noted that the mathematical modelling of DE's currently available is limited to cases under ideal conditions and with polymer films assumed to have constant volume. Environmental conditions will impact the practical results. Polymer films, once pre-strained, also exhibit altered properties from non-pre-strained samples. Therefore, experimental results are imperative when analysing the performance of the DE, however, mathematical relationships drawn from the fundamental equations are used to form the necessary hypotheses before testing commenced.

Before expanding upon the mathematical modelling of a DEA, it must first be noted that a DEA exhibits properties of a capacitor and therefore stores charge during operation, a reason why it can also be used successfully as a sensor and generator. The circuit schematic in Figure 2-10 represents the circuit breakdown of a dielectric elastomer, reused from the journal paper by Rizzelo et al. [68] In earlier studies a DEA was originally simply modelled as a capacitor, however, the electrical dissipation of the device was not considered, the presence of the R_l resistor represents that electrical dissipation. [68] The R_e resistors represent the electrodes and R_a simply acts as the external resistance of the DEA e.g., wires.

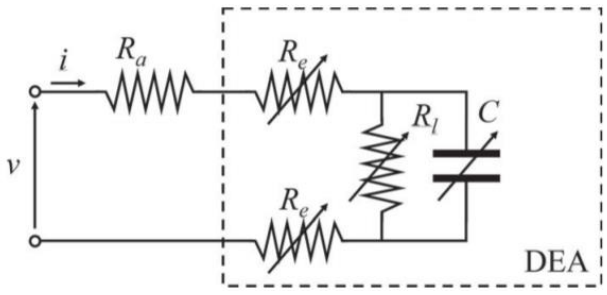

Figure 2-10 Equivalent electrical circuit of a DEA [68]

The mathematical modelling of DEAs is performed under ideal conditions and under the assumption that the elastomeric matrix is an incompressible linearly elastic material of constant volume. [52] This relationship is illustrated by Equation 2-1 where C is a constant, A represents the area of the polymer and t represents the thickness. The Maxwell stress (P), also known as the electrostatic stress, Equation 2-2 uses this assumption as well as the capacitive properties of the DEA to define the response of a DEA to an applied electric field where ε_r represents the relative electric permittivity of the material, ε_0 represents the electric permittivity of free space and E is the applied electric field. [52]

$$C = At \tag{2-1}$$

$$P = \varepsilon_r \varepsilon_0 E^2 \tag{2-2}$$

Equation 2-3 further defines the Maxwell stress where the Electric field is defined by the applied voltage (V) per unit thickness (t) of the elastomeric film. Pelrine et al. [69] indicated that if this Maxwell stress is then divided by the elastic modulus (Y), the product will represent the elastic compressive strain (st), as seen in Equation 2-4. Considering Equation 2-3, a reduction in thickness through pre-strain would result in a higher applied electric field and, therefore, a reduced elastic compressive strain. Upon return to Equation 2-1, it is concluded that a relative reduction in elastic compressive strain will result in an increased strain in plane with the elastomer.

$$P = \varepsilon_r \varepsilon_0 (\frac{V}{t})^2 \tag{2-3}$$

$$s_t = -\frac{\varepsilon_r \varepsilon_0 V^2}{Y t^2} \tag{2-4}$$

The following conclusions can be drawn from the equations presented: an elastomeric material of higher relative permittivity and possessing a small elastic modulus will produce strains in plane with the DEA and that a reduction in thickness, through either material selection or pre-tension, of the elastomer will produce larger strains.

2.5.4 Applications of DEAs

As a result of the variety of materials with which to synthesise DEAs, these actuators are capable of being applied in a diverse range of unique configurations. These configurations include, but are not limited to, unimorph, bimorph, stacked, diaphragm, rolled and stretched frame structures.

As interest in this field of actuation continues to grow, as does the variety of configurations in which it can be applied.

Unimorph and bimorph structures are comprised of flat dielectric elastomer structures which produce bending motion in the direction in which they are constrained. These structures can be applied as low force, high strain gripper attachments. Bend angles of up to 360° has been achieved using these DEA benders, outperforming the available rigid piezoelectric alternatives. Controlled strain in a predetermined direction can be achieved by coating the elastomer in non-uniform electrodes. For example, a stiffer electrode material on the side that does not require high strain, this will induce a biased deflection in the direction of the electrode of greater stiffness [70].

A similar configuration to the unimorph and bimorph structures are stretched-frame DEAs which operate as a form of artificial muscle actuated by contractions. The flexible frame buckles as a pre-strained dielectric elastomer material is applied, holding the buckled position at 0 V due to the forces of tension in the elastomer matrix [52]. Once voltage is applied and the area of the elastomer expands, and the frame will uncurl to return to its original shape. This resulting mechanism can be used for artificial muscle movement, such as in the work presented by O'Brien et al. [71].

A stacked configuration consists of multiple individual DEA films layered on top of each other. The application of voltage reduces the overall thickness of the stacked structure and therefore induces linear contractile actuation. An advantage of the stacked configuration is the reduction of driving voltages to the individual layers while still achieving the required strain results [72]. Stacked configurations have been implemented in designs such as robot legs in order to mimic mammalian leg movement [73]. This is achieved through manipulating the joints to operate as a crank slider mechanism using two stacked DEA actuators. The actuators measure 23mm in length, weigh 9,68g and are capable of supporting a load of 900g with a compression strain of 3,6% [56].

Along with the stacked configuration, rolled spring DEAs are also capable of elongation motion. An elastomer layer is wrapped around a compressed spring to fabricate this configuration. The application of voltage to the DE layer allows the spring to relax and elongate. Potential areas of application for such actuators are robotic limbs, high force grippers and as an alternative to solenoid or linear actuators [70]. Maximum strokes of 5-7% of their active length have been recorded in experimental analysis of rolled spring DEAs [52].

Diaphragm-type DEAs are circular electrodes adhered to an elastomer with edges constrained by a rigid frame. The circular DEAs are inflated or embossed to hold initial hemispherical shape and encourage strain in a specific direction, Figure 2-11. An example of an application of this configuration is the study by Hosoya [65] which investigated a small lightweight loudspeaker using a dielectric elastomer actuator vibrating in the breathing mode - a motion which mimics the

pulsating expansion and contraction of a balloon. A similar study was conducted by Boys et al [74] which analysed the performance of a single spherical tactile display when interacted with by the pad of a finger. This specimen utilised a hydrostatically coupling gel to maintain initial curvature of the actuator before voltage was applied. A maximum force of 0,7 N was generated when a voltage of 4,5 kV was applied. The tests conducted demonstrated the repeatability of the vibratory deflections of a diaphragm-type DEA. This observation lends itself to the assumption that this configuration is a robust actuating system. Other examples of miniature applications include a tactile display utilising a 10x10 array of embossed diaphragm type actuators. This application manipulated the flexibility of the elastomer matrix to wrap around the user's finger. Each actuator cell was designed to be controlled independently using two signal inputs. One signal input along the rows and the other along each column of the matrix. Only when both signals registered as high, did the actuator cell respond by deflecting upward. With this strategy, n^2 tactile cells can be easily controlled with only 2n lines, this is denoted as Dynamic Scanning Actuation [56].

Figure 2-11 Inflated diaphragm-type DEA [65]

The vertical displacement of a diaphragm-type DEA can be predicted using a combination of the calculated lateral strain and trigonometric relations of the actuator before and after an electric field is applied, as illustrated in Figure 2-12.

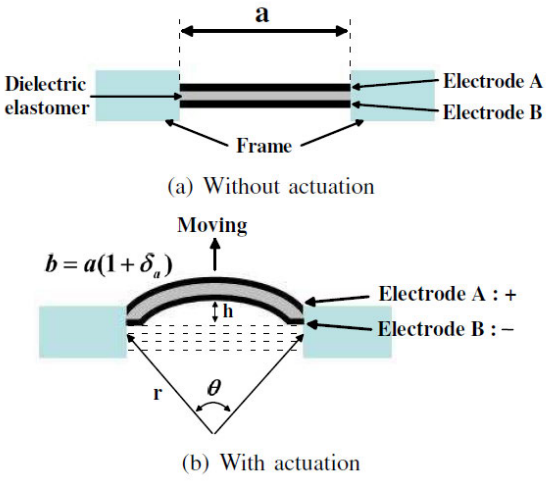

Figure 2-12 Actuation principle of tactile diaphragm type DEA [56]

Assuming no pre-strain of the elastomer material, the resultant circumference of the buckled convex induced in an elastomer sheet can be defined as b in Equation 2-4 [64]. Where a is the initial unactuated length, δ_a is the induced strain in the lateral/radial direction, r is the radius of curvature and θ is the corresponding angle.

$$b = a(1 + \delta_a) = r\theta \tag{2-4}$$

$$r \sin\left(\frac{\theta}{2}\right) = \frac{a}{2} \tag{2-5}$$

Substituting Equation 2-4 into Equation 2-5 generates the following relationship, Equation 2-6.

$$\frac{\theta}{\sin(\frac{\theta}{2})} = 2(1 + \delta_a) \tag{2-6}$$

Rearranging Equation 2-6 to make θ the subject.

$$\theta = 2(1 + \delta_a) \sin(\frac{\theta}{2}) \tag{2-7}$$

Equation 2-6 and 2-7 illustrates the application of the Taylor series expansion to $\sin(\frac{\theta}{2})$ to find an approximate value of θ using Equation 2-8. Note that the third term of the infinite expansion and all terms thereafter are assumed as negligible due to the large denominator values. Therefore, due to this assumption, the final theoretical answer will differ from the true value by 10^{-4} units.

$$\sin(\frac{\theta}{2}) \approx \frac{\theta}{2} - \frac{\left(\frac{\theta}{2}\right)^3}{3!} = \frac{\theta(24 - \theta^2)}{48} \tag{2-8}$$

$$\theta = \sqrt{\frac{24\delta_a}{(1 + \delta_a)}} \tag{2-9}$$

Therefore, substituting Equation 2-9 into Equation 2-4, the radius of curvature can be defined as a function of the induced lateral strain and initial length of the DE sheet, Equation 2-10.

$$r = \sqrt{\frac{(1 - \delta_a)^3 a^2}{24\delta_a}} \tag{2-10}$$

Utilising trigonometric relations, the convex height h can be determined, Equation 2-11. Finally, Equations 2-9 and 2-10 can be substituted into Equation 2-12 to create a definition of h using only known variables a and δ_a.

$$h = r(1 - \cos\left(\frac{\theta}{2}\right)) \tag{2-11}$$

$$h = \sqrt{\frac{(1-\delta_a)^3 a^2}{24\delta_a}}\left[1 - \cos\left(\frac{\sqrt{\frac{24\delta_a}{(1+\delta_a)}}}{2}\right)\right] \tag{2-12}$$

2.6 Synthesis of Dielectric Elastomer Actuators

This subsection discusses the synthesis and materials required to synthesise the dielectric elastomer actuators. A brief overview of possible synthesis approaches is discussed along with the concept of pre-straining the elastomer matrix and how this effects performance. Thereafter, an in-depth discussion of available elastomer and electrode materials is presented with notable examples of how these measures have been applied in previous research.

2.6.1 Synthesis

The variety of possible electrode and elastomeric film materials available to manufacture DEAs provide several synthesis options. These methods can range from simple to complex. A simple, low-cost option would be to apply graphite powder or carbon grease to an adhesive acrylic or silicone elastomer using a brush. However, there are drawbacks to such a method, e.g., inconsistent thickness of electrode layers and difficulty to ensure the correct shape of the DEA. A possible solution to this is using a stencil or masking the areas around the electrode shape to ensure a higher precision of electrode formation. Electrode patterning using an electrode solution further improves the precision of application through now being able to control the exact thickness of the electrode layers, however this increases the cost and complexity of manufacturing [56]. Most elastomeric matrices are sourced as acrylic films or adhesive strips of predetermined thickness which reduces manufacturing time of the elastomer film, however, should an elastomeric matrix such as silicone be used then further synthesis techniques such as spin coating will be required to ensure homogenous properties [56].

2.6.2 Pre-strain

Elastomer films are often pre-strained before the electrodes are applied. This improves the performance of the DEA and increases efficiency, response time and breakdown strength. Figure 2-13 illustrates the radial strain of a DEA using an elastomer film that was pre-strained to 300% of its original size [75]. It can also be used to increase actuation in one direction if stretched perpendicular to the direction in which greater percentage of strain is required. However, pre-strain does not only reduce the thickness of the film but also modifies material properties. The Maxwell stress equation in Section 2.5 is no longer valid when anticipating the reaction of the DEA to voltage input at high pre-strains [52]. Novel instabilities are also introduced in the DEA since the material no longer conforms to the constant volume relationship exhibited by most

elastomeric films. Instabilities result in pull-in failure and relaxation over time [63]. Additives such as interpenetrating polymer networks can be sprayed onto existing acrylic films to improve material instabilities and hold pre-strained films in tension when removed from the frame [76].

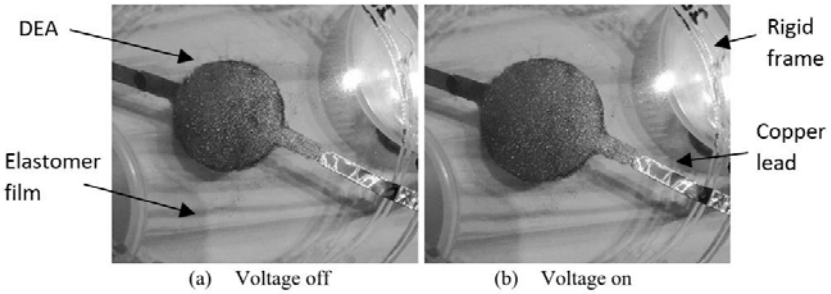

Figure 2-13 Actuation of circular DEA using pre-strained elastomer film stretched across a Perspex frame. [75]

2.6.3 Electrode Materials

The selected electrode material must have negligible stiffness, maintain good stability during cyclic loading and must be resistant to loss of conductivity under large strains [77]. Cost and accessibility are also major deciding factors. Table 2-2 catalogues common electrode materials and the advantages and disadvantages of each.

Table 2-2 Comparison of common electrode materials

Electrode Material	**Advantages**	**Disadvantages**	**References**
Thin metal films	High electrical conductivity Most efficient for large-scale production	Limited strains to ≈ 1% Patterning only possible on small-scale Requires machinery/patterning equipment to apply	[52] [77]
Carbon grease	Inexpensive Easy to apply Easily accessible Good Conductivity at high strains Low stiffness	Result in slip between layered dielectric elastomer constructs Experiences creep	[52] [77]
Graphite / Carbon Powder	Most widely used method Inexpensive Can be applied by hand using a paintbrush Easily accessible Good conductivity at high strains Better for multilayer DEA's Low stiffness Can be applied as a solution using an inkjet nozzle for complex electrode shapes	Sensitive to static charge Requires further synthesis to apply as a layer of uniform thickness (must be mixed as carbon solution and sprayed on masked elastomer)	[52] [56] [77]
Conductive Rubber	More robust than carbon grease/powder High electrical conductivity	Requires complex synthesis process Expensive More effective on thicker elastomer films	[77]
Carbon Nanotubes	Self-healing Breakdown resistant Tolerant of high strains	Prone to instabilities Requires complex synthesis process Expensive	[52] [78] [79]

Thin metal films were some of the first materials implemented as electrodes in early DE research. These films were initially selected due to their superior conductivity properties, however the rigidity of metal films limited maximum strain values. Examples of metal films include silver and gold.

Graphite or carbon powders are the most common materials used in compliant electrode synthesis in current research. Graphite or carbon powders are the cheapest electrode option and provided greater flexibility to larger strains than the metallic alternatives. Powders were originally challenging to apply to elastomer materials in early research since elastomers available on the market were limited to synthesised silicone or acrylic films. This resulted in an additional adhesive to be used between electrode and elastomer or combining the powder in an elastomeric matrix. Synthesis options using powders have since been simplified with the introduction of commercially available double-sided elastomer films which allow the powders to be brushed on and adhere to the surface. Accurate application in the form of complex shapes and patterns can be achieved by applying a stencil or mask to the adhesive film before electrode application. Laser ablation and sprayable carbon solutions also utilise a mask during application.

Although capable of much larger strains, purely powder based carbon applications also experience limitations in maximum strain values since only the surface layer of powder is adhered to the adhesive elastomer layer. The upper layers of powder are not adhered to the surface and, unless the electrode layer is sealed, will be displaced by environmental conditions or the rapid expansion of the elastomer layer. Therefore, the surface layer of carbon will experience separation as the elastomer expands, thereby increasing the resistivity experienced by the elastomer and decreasing the strength of the induced electric field. This problem area introduced the application of conductive particles suspended in a non-conductive matrix, such as carbon grease, metal paints or graphite/carbon powders mixed into a silicone matrix. Of course, particulate matrices also experience the risk of the non-conductive matrix thinning as the elastomer stretches, thereby increasing the distance between conductive particles. However, the matrix allows for greater volume of conductive particles to be applied at a time, allowing the 3-dimensional layers of particulates to interact with each other and decrease the risk of single layer conductive separation. Examples of conductive carbon grease include Chemtronics CW7200, Nyogel 756G, MG Chemicals 846, MG Chemical 847, Molykote 44 combined with Cabot Vulcan XC72 carbon black [71] [53] [80].

Recent studies have proven that single layer carbon nanotube (CNT) based electrodes maintain a conductive network under high strains at an equivalent performance to carbon powders and carbon grease electrodes [52]. Therefore, reducing the minimum electrode thickness by utilising the flexibility of the nanotubes to maintain the conductive network. Both functionalized and non-

functionalized single-walled nanotubes have been tested with performance equivalent to carbon grease while including the additional benefit of synthesising transparent electrodes. Therefore, resulting in a completely transparent DEA when combined with a silicone or acrylic elastomer matrix. A disadvantage of CNT electrodes is the susceptibility to corona discharge through the air which results in loss of electrode conductivity [78]. Non-functionalized are also at risk of continuous breakdown-clearing effects which eventually lead to mechanical failure of the DEA. Breakdown-clearing effects are unique to CNT electrodes and occur when an electrical short burns off a localised region of CNTs without damaging the elastomer layer. A single occurrence breakdown-clearing is considered an advantage since it prevents total mechanical failure which would be the case should a similar short occur in a carbon grease/powder or metal film-based electrode. However, continued occurrences result in a loss of DEA stability as more localized regions lose functionality [79]. Overall, CNT electrodes provide a promising future for DEA applications, however, the high cost of the CNTs and specialised synthesis procedures must be considered during selection for application.

It must be noted that Pelrine et al. [53] states that most electrode materials are capable of self-healing if a sufficiently thin layer is applied to the elastomer. Therefore, this property is simply more noticeable in compliant electrodes such as CNT electrodes since it is possible to apply an exceptionally thin layer without compromising the conductive matrix under large strains. Should research indicate a solution to the reduction of thickness of carbon grease electrodes without compromising conductivity, self-healing will also be possible.

Another recent addition to possible compliant electrode materials are ion implanted metal electrodes in Polydimethylsiloxane (PDMS). These are particularly attractive due to the ability to achieve a smooth, uniform thickness electrode. Conductivity is recorded to be maintained up to 175% by these electrodes [81]. Other advantages include the synthesis of semi-transparent electrodes as well as a longer lifespan under cyclical loading relative to other metal film-based electrodes. Filtered cathodic arc deposition is utilised to implant metallic (gold, palladium and titanium) particles in the PDMS matrix. The requirement of equipment to synthesise both the PDMS membrane and deposit the particles makes this a notably expensive approach to the synthesis of compliant electrodes but displays improved characteristics over alternative techniques.

Another interesting application of an electrode material was documented by Christianson et al. [82]. The work discussed the design of a submersible robotic fish which utilised the surrounding salt water as the compliant electrode. The design was comprised of three layers of VHB acrylic elastomers with two inner pockets filled with salt water. A positive charge was applied to one of the pockets of fluid which resulted in an electric field being generated by the interaction with the

external fluid, thus resulting in the actuation of the dielectric elastomer. An alternating voltage being applied to the inner pockets resulted in the robot's body oscillating in the water and creating a forward motion of 9,2 mm/s.

2.6.4 Elastomer materials

As with the compliant electrodes, the variety of possible elastomer materials continues to expand as interest in DEAs grow. The ideal materials must possess a large percentage area strain, a high dielectric constant, high energy densities and efficiencies that approach 100% [52].

According to the detailed comparison of various elastomers presented by Brochu et al. [52], the acrylic elastomer films known as VHB 4905 and VHB 4910 outperform all other potential candidates in terms of a combination of area strain, maximum pressure, efficiency and electric field generation. However, the pre-strain of the materials is essential to optimize performance. An indication of the improved characteristics is the comparison of VHB 4910 at 300% pre-strain and 0% pre-strain is as follows; the former is documented to exhibit a maximum area strain of 158% while the latter produces only 7.5% [52]. The VHB films are produced by 3M in the form of a double-sided adhesive tape with VHB 4905 and VHB 4910 having thicknesses of 0.5mm and 1.0 mm respectively. Both grades are readily available in South Africa and are low cost, particularly since no further synthesis of the film is required and the adhesive surface provides the ideal solution when applying electrodes that do not possess their own adhesive properties. Research indicated that the VHB 4910 was the preferred grade regardless of the greater thickness [63]. Ideally the abovementioned conclusion must be verified through testing both 4910 and 4905.

Alternative elastomer materials include silicone elastomers which presents faster response times than the acrylic alternative due to the lower viscoelastic property of silicones. Silicones do not achieve equivalent strain results to acrylics materials when under the same voltage input due to their requirement for higher electric fields to cater for the lower dielectric constant of the material [52]. However, new silicone materials with improved characteristics have been mentioned in research, such as the KE441 ShinEtsu silicone used by Kwangmok et al. in the actuation of an artificial annelid worm. This film was spin coated and used in a stacked configuration [64]. Spin coating silicone films also allowed finer control of the thickness of the elastomer without the need for pre-strain. Possible improvement to silicone film performance includes thinning the silicone with poly(3-hexylthiophene) (PHT), which improved actuator performance at lower applied electric fields [83].

Rubber materials such as Oppo Band Red 8012 have also been documented as possible DE membranes [80]. The Oppo Band is designed as an orthopaedic resistance band for strength training and serves to illustrate the diversity of materials that can make suitable dielectric elastomer membranes. The rubber band was coated by carbon grease electrodes and implemented

as a parallelogram-shaped dielectric elastomer generator with a maximum imposed strain value of 4,5% to generate a voltage output [80].

2.6.5 Protective films

Protective layers between the electrodes and environment must be applied in order to protect both the user from the high voltage and the electrode layers from contamination. Although the low current required by the DEA reduces the risk of contact with the active electrodes, steps must still be taken to insulate the device and ensure the safety and comfort of the user, particularly in a situation where the device is to be applied close to the skin.

Most acrylic and silicone elastomer layers mentioned in the previous subsection can be applied as a protective layer due to the insulating properties of the elastomer films. However, the maximum strain of the selected material is equal to or greater than the elastomer layers and the Young's Modulus is less than the elastomer material. This will ensure that the protective material does not impact the maximum strain of the DEA.

Protective layers mentioned in literature include spin-coating silicone layers or PDMS membranes. Igmo et al. recorded that a protective silicone membrane of half the thickness of the elastomer layer was applied to the wearable tactile display [56]. Araromi et al. discussed the application of a 10 μm PDMS encapsulation membrane to a PDMS-based DEA of equal 10 μm thickness when designing an interactive sensor-actuator combination [84]. The capacitive sensor was still capable of detecting finger proximity through the encapsulation layer, but the hand was protected from any potential arcing.

Taking the above research into consideration, it was be concluded that the best course of action was to experiment with the effect of different thicknesses and pre-strain when applying the protective layer to ensure minimal influence on the performance of the actuator during operation. Further, it was noted that it is possible to use the same material for the protective membrane as the elastomer matrix, which will reduce the cost of excess materials.

2.7 Control of High Voltage Output

The most common reason for overlooking dielectric elastomers as a valid option for actuation is the requirement of a high voltage Direct Current (DC) power supply. This caused a problem during early research of DEA's since high voltage power supplies were not easily transportable and were costly to incorporate into the design, therefore limiting dielectric elastomers to experimental and laboratory use.

This issue was addressed in 2016 when the power supply company XP EMCO signed a global distribution agreement and made their products, which include small scale DC voltage to DC high

voltage converters, easily accessible [85]. Majority of recent DEA research that required design portability utilised XP EMCO converters in their research, from submersible robotics and biomimetic lenses to tactile displays [82] [86] [56].

Average voltage requirements of dielectric elastomers range between 2kV and 5kV but are dependent on force and displacement requirements. Possible XP EMCO products that satisfy these requirements are summarised in Table 2-3.

Table 2-3 Applicable XP-EMCO DC- HV DC Converters

Product	Power Output (W)	Maximum Output Voltage (kV)	Output Current (at Max Rated Voltage Output) (mA)	Input Voltage (V)	Input Current (at Max Rated Voltage Output) (mA)	Dimensions (mm)	Reference
G Series	1,5	6	15	0,7-12	300	38,1 x38,1 x 16	[87]
Q Series	0,5	10	5	0,7 - 5/12/15/24	400	12,7x12,7,12,7	[88]
A Series	1 & 1,5	6	15	0,7- 5/12/24	550	28,69 x 6,35 x 11,43	[89]
C Series	1	8	10	11,5-16	250	53,3x28,2x12,7	[90]
E Series	3	12	30	0,7- 12/15	400	63,5x38,1x21,6	[91]

Upon analysis of the above information as well as the availability of the possible DC- HV DC converters, it was concluded that the A series XP EMCO product was ideal for the required application. Utilising previous research conducted on dielectric elastomers, an average maximum voltage of 5 kV was specified for experimental procedures [56] [52]. The details of the A series model rated at a maximum voltage output of 5 kV are summarised below.

Model Number: A50P-5

Maximum Voltage Output: 5 kV

Voltage Input Range: 0-5 V

Maximum Current Input: 500 mA

Maximum Current Output: 0,2 mA

Major Dimensions: 28,69 x 6,35 x 11,43 mm

2.8 Text to braille transcription software

Optical Character Recognition (OCR) refers to the process of extracting text data from images. OCR is comprised of a range of tasks due to the variety of image layouts from which data must be extracted. These tasks range from identifying printed text in paper format to identifying characters on signposts from random images. Other types of OCR tasks include Street View House Numbers (SVHN), Licence Plates and Completely Automated Public Turing tests to tell Computers and Humans Apart (CAPTCHAs). All require unique strategies to complete the tasks

however most strategies dealing with typed or printed text can typically be divided into three steps, illustrated in Figure 2-14 [92].

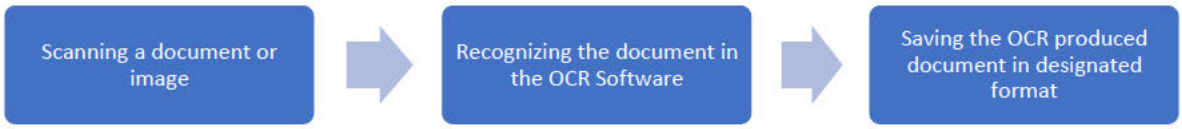

Figure 2-14 Simplified OCR Processing Method

OCR tasks that require data extraction from printed or typed text documents and images have several software packages available with popular choices being: Tesseract, ABBYY FineReader, Adobe Acrobat Pro and OpenBook, TextCloner Pro and KNFB Reader [92] [93]. Due to the commercial value of the abovementioned software, most limit the amount of customization available to the user. Of the listed packages, only Tesseract is considered one of the most accurate open-source OCR engines currently available. Supporting operating systems include Mac, Windows and Linux [94]. Therefore, in a situation where a high level of function customization is required at low cost, Tesseract is the ideal solution.

Tesseract is an OCR system that was developed by Hewlett-Packard (HP) with first versions appearing at the 1995 University of Nevada, Las Vegas (UNLV) Annual Test of OCR Accuracy. Tesseract was released for open source in 2015 [94]. Two versions of Tesseract are available for public use on Github: Tesseract 3 and 4 [95]. Tesseract 3 uses the Legacy OCR system to recognize character patterns by comparing each pattern to an existing library, this is an older version of Tesseract and is prone to errors. The more popular Tesseract 4 utilizes deep learning using the neural network; Long-Short Term Memory (LSTM) to complete more accurate character recognition [95].

Common strategies utilised by OCR software include matrix matching, fuzzy logic, feature extraction, structural analysis, and neural networks [94]. OCR Software pre-processes images to improve the ability to recognize the characters. This pre-processing consists of techniques such as [96]:

-De-skew (corrects alignment of page)
-Despeckle (smooth edges and removes positive and negative spots)
-Binarization (conversion to black and white image to lift useful data from background)
-Line removal (identifies columns, paragraphs, and sections as blocks)
-Zoning (divides words)
-Line and word detection (for multi-language documents)
-Segmentation
-Normalisation (normalize aspect ratio and scale)

As stated by Smith [94] “, Since HP had independently developed page layout analysis technology that was used in products, and therefore not released for open-source, Tesseract never needed its own page layout analysis. Tesseract therefore assumes that its input is a binary image with optional polygonal text regions defined.” Therefore, for Tesseract to complete the text recognition task and additional post-processing functions, a separate program is required to detect the text within the scanned image and feed into the Tesseract software.

Open Source Computer Vision (OpenCV) is a library utilised for OCR which detects and defines the text regions. OpenCV can be utilised to independently complete the text recognition tasks attributed to Tesseract, thus creating a standalone image capture and text recognition system without the need for Tesseract [97]. However, the development of the Tesseract software provides a concise platform for character recognition with numerous design iterations which have solved programming problems that would need to be worked through again should OpenCV be used as a standalone program. It must be emphasised that only OpenCV can be used as a standalone OCR engine, Tesseract requires a secondary program like OpenCV or Leptonica to process the image before character recognition can be completed by Tesseract [98]. An advantage of using OpenCV independently for the task of text recognition over Tesseract would be in a situation where the text-to-braille design is expanded to include a variety of linguistic scripts, such as Tamil script [97]. This is because the Tesseract engine is currently limited to Latin script recognition. Under the current circumstances where a proof of concept of the mechanical design is priority, the OpenCV-Tesseract combination is ideal to reduce the time dedicated to programming and debugging. The online support available for OpenCV-Tesseract OCR text extraction is also a motivator for selecting this system due to its popularity amongst developers of prototype systems. Step by step project tutorials such as the referenced examples provide concise instructions and resources to build rudimentary systems which can be further customised [99] [100] [101].

In order to increase the rate at which the transcription device operates, pre-processing should be limited by catering for the pre-processing techniques using the hardware of the design where possible. For example, zoning, line removal and segmentation is not required for single character OCR scanning. Light Emitting Diodes (LEDs) illuminating the scan surface will assist in improving image quality and reduce the need for despeckling. Correct hand orientation relative to the text document will reduce the need for de-skew pre-processing.

One of the potential areas for error in a single character identification design is the limited amount of post-processing that can be conducted to improve the output. Most post-processing techniques rely on a lexicon-based system. Post-processing checks lexicons against an existing library to correct possible errors and grammar [96]. In order to identify a lexicon, more than one character needs to be identified at a time. This will pose a risk in a text to braille transliteration system

which scans and produces a single character as the reader's finger progresses over the printed text.

Once the character recognition is completed by Tesseract, the digital text output must be saved in American Standard Code for Information Interchange (ASCII). A third program will then retrieve the ASCII code and output the data using the corresponding braille character. The braille character is comprised of six binary values with each corresponding to a signal output on the microprocessor. Each ASCII code is assigned to a matching dot output configuration in order to produce the required voltage output, for example the letter 'A' is represented by the braille equivalent in Figure 2-15. This will be completed for all existing ASCII characters and allow the data retrieved from Tesseract to be output as a six-dot array. An example of a full code representation of the proposed system was published by Brizio and utilised a six-solenoid array output and Arduino microcontroller [102].

Figure 2-15 Braille representation for character 'A'

A detailed breakdown of the functions of each program and hardware is illustrated in Figure 2-16. The supporting electronic design is discussed in Chapter 3.4.

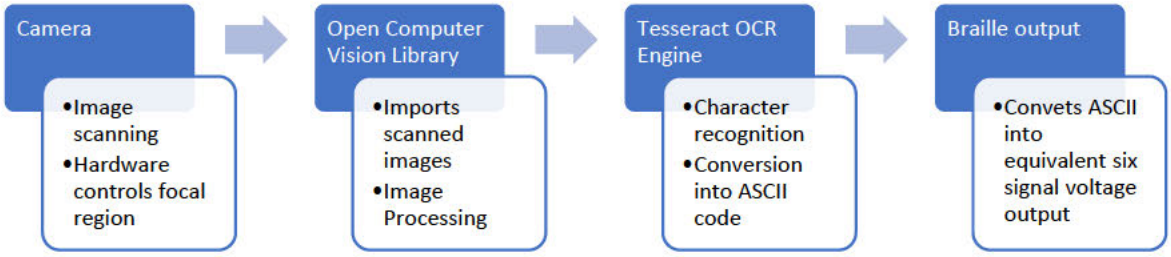

Figure 2-16 OCR system breakdown

2.9 Chapter summary

Chapter 2 detailed the literature review of the dissertation. The first area of interest was the comparison between braille and voice-over technology as the most appropriate medium to complete the transcription of printed text. Once it was determined that a braille approach would be most applicable, existing braille technology was researched to form an idea of the requirements of a refreshable braille display. Various miniature actuation systems were analysed in order to produce a final device that was capable of fitting on the end of the index finger without interfering

with the proprioception of individuals who are accustomed to reading traditional embossed braille. The actuation technology known as Dielectric Elastomer Actuators was selected and the working principles, materials and synthesis were researched. Thereafter, it was necessary to investigate high voltage control devices to ensure the DEAs were safe to use and possible to be mounted onto the user's hand. Finally, Optical Character Recognition software was studied in order to develop a plan on how all subsystems will be incorporated into a single device.

Chapter 3 summarised the specifications derived from the literature review and presents the conceptual designs of the proposed device. Once the ideal concept was selected, the final mechanical and electrical design of the text-to-braille transcription device was recorded and discussed.

3. DESIGN OF ACTUATION SYSTEM

3.1 Introduction

The following chapter details the design process of the wearable, low-cost braille display. Upon analysis of the research described in the literature review, it was concluded that the ideal mechatronic solution to improve the accessibility of the visually impaired to information was a text to braille transcription device. This device confronted economic and social challenges specific to the visually impaired demographic of South African.

The chapter is divided into specifications derived from the literature review, conceptual designs of the DEA system, the final electrical design, and the final mechanical design.

3.2 Design specifications

The information featured below, along with Table 3-1 and Table 3-2, detail the design requirements and specifications of the low-cost, wearable braille transcription device.

As per the discussion in Chapter 2.5, the device is required to scan and transcribe written text to braille in real-time. The device must fully portable, capable of being battery powered and able to be mounted on the hand in an unobtrusive manner.

The selected method of actuation upon a comparison of available miniature actuation technology is dielectric elastomer actuators due to their robust design, low power consumption, portability, and miniaturisation. Dielectric elastomer actuators require high voltage inputs at low current to operate successfully. Research dictates that the A50P-5 XP-Power DC to HV DC converters are ideal for this application. The addition of this component into the system introduces additional specifications, as listed in Table 3-2.

Table 3-1 Braille Specifications

Specification	**Measurement**	**Unit**	**Reference**
Nominal dot base diameter	1.44	mm	[43]
Nominal centre to centre distance between two dots in same cell	2.34	mm	[43]
Nominal dot height	0.48	mm	[43]
Average touching force	170	mN	[41]
Average reading speed	120	words/min	[46]

Table 3-2 Design Specifications

Specification	Measurement	Unit	Reference
Range of touching force required by commercial tactile displays*	50 - 390	mN	[41]
Reaction time to process visual information and form letter on braille display**	0,418	s	
Refreshable bandwidth of commercial piezoelectric braille displays	5	Hz	[50]
Maximum surface area of dorsum on which to mount hardware * (L x B)**	100,92 x 78,74	mm	[103] [104]
Input voltage to power A50P-5 DC to HV DC converter	5	V	[89]
Input current to power A50-P DC to HV DC converter	500	mA	[89]
Maximum output voltage of A50P-5 DC to HV DC converter	5000	V	[89]
Maximum current output of A50P-5 DC to HV DC converter	0,2	mA	[89]
Minimum cost of competitive commercially available braille display	21800,00	R	[105]
Average font size of printed text	10 – 14 3,528 – 4,939	Point mm	[106]

*The touching force of braille displays such as the Braille Note is adjustable depending on the user's preference.

** Calculated using the average reading speed and the assumption of an average of 4,79 letters per word.

***Determined using the average dimensions of female right hands. In order to ensure accessibility by largest population group, the smaller dimensions of female hands were selected. The length is measured from the crease of the palm to the first knuckle of the longest finger. The breadth is measured across the widest area where the fingers join the palm.

3.3 Conceptual designs of actuator

Four possible actuator designs were considered during the conceptual stage. Three of the conceptual designs utilised the foundation of a diaphragm-type DEA while the fourth was based on a rolled-type DEA. The advantages and disadvantages of each design were analysed before a final design was selected. The selection process consisted of a decision matrix that compared the most important aspects of the design, cost, overall actuator size, power consumption and percentage displacement.

3.3.1 Rolled-type actuator

The rolled type DEA consists of a compressed spring wrapped in pre-stretched DE. The spring is constrained to motion in only the axial direction by a solid guide tube at the centre. The DE film can be wrapped around the spring multiple times, thus increasing the induced electric field when voltage is applied. Once the circuit is closed, the DE will reduce in thickness and expand in area,

therefore allowing the spring to relax and elongate along its axis. Figure 3-1 illustrates the proposed design with arrows indicating the direction of deflection upon the application of voltage to the DE.

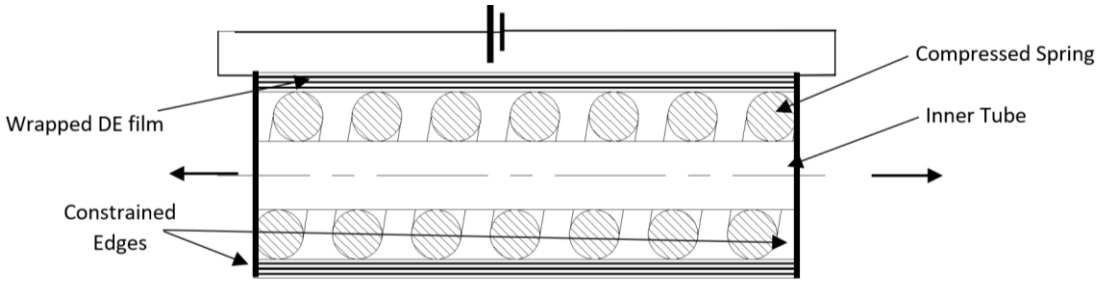

Figure 3-1 Rolled-Type DEA

The advantages of this system include the presence of the spring to apply the required actuator force while the DE plays a passive role in controlling the percentage elongation of the spring. This allows the actuator to support a greater load than the stretched frame or diaphragm type DEAs. The maximum compressive stress that the Rolled DEA developed by Zhang et al. [107] could sustain was recorded as 7.2N, notably larger than the maximum touching force of 170mN required by the braille display. The rolled DEA developed by Zhang et al. consisted of VHB 3910 acrylic electrode lined film that was wrapped 30-40 times around a spring of diameter 7mm. A voltage of 3.5 kV was applied to create a maximum displacement of 3mm.

Notable disadvantages include the relative dimensions of the component to achieve the required displacement. In the abovementioned example, the length of the device was recorded as 45mm to achieve a displacement of 3mm. Other studies indicate a similar relationship between the passive length of the component and resultant strain that introduces limitations on the miniaturisation of such a configuration [52]. Another factor to consider is the risk of premature failure and gradual film relaxation due to the continuous stress exerted by the spring on the film [52]. As relaxation occurs, the length at which the device is in passive equilibrium will change, thus impacting on the reliability of the device.

3.3.2 Diaphragm-type using air pressure

The second conceptual design consists of a single layer of acrylic film coated with compliant electrodes and pre-strained across a circular rigid frame. A chamber is created on the concave side of the DEA by adhering a thin plate to the lower rigid frame. A silicone adhesive is used between plates to allow a syringe to be inserted between the plates and inflate the DEA membrane to the required initial height. The use of a silicone adhesive is specified to utilise the self-healing properties of the matrix. Once the needle of the syringe is removed, the silicone is drawn together to reseal the needle path and create a sealed chamber on the concave side of the DEA. Therefore,

a directional bias is introduced by creating an initial curve in the membrane. Once a voltage is applied, the elastomer layer will reduce in thickness and increase in area, forcing the diaphragm upward due to the presence of rigid constraints at the edges of the expanding area. Figure 3-2 illustrates the proposed design.

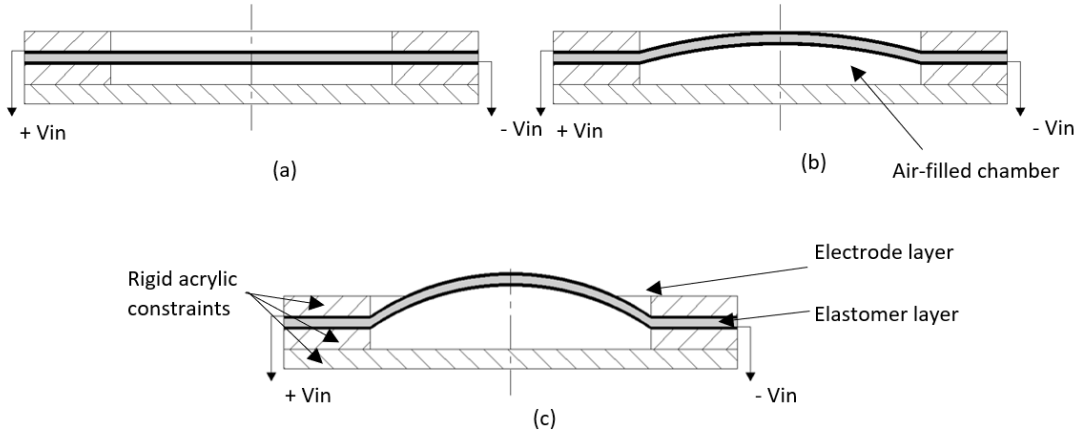

Figure 3-2 Conceptual design of inflated diaphragm-type DEA (a), DEA before inflated by a syringe inserted between acrylic surfaces (b), DEA inflated to required initial height with V=0 (c), DEA inflated with V≠0

Advantages of the abovementioned configuration include ease of manufacture and inexpensive materials and synthesis procedures. Due to the DEA being comprised of a single layer elastomer and compliant electrodes, the range of possible synthesis methods expands as compared to situations such as a stacked configuration. An adhesive acrylic film such as VHB 4910 can be used as the elastomer which negates the requirement of complex synthesis procedures of substrates, silicone films and, in turn, expensive auxiliary production equipment. Of the diaphragm type DEAs, this method is the most common approach used in related research papers, thus allowing for multiple sources of comparative data. This method also allows for the most diverse selection of compliant electrode materials, further discussed in Section 3.3.3. An example of the application of this synthesis configuration is detailed by Marette et al. [108]. Their work was based on a 4.5 diameter diaphragm DEA which produced results of 400 μm deflection at 1.05kV across the electrodes. The absence of complex synthesis allowed for a high degree of experimental repeatability.

A disadvantage of using a single layer synthesis technique is the requirement for a higher driving voltage to achieve the same displacement results as multi-layered diaphragm type arrangements. The layers of the acrylic frame must be well sealed to prevent pressure loss. The design also requires a protective layer to insulate the electrode along the convex curve and protect the user.

3.3.3 Diaphragm-type with multiple stacked layers

The third concept constitutes a similar configuration to the previous where a circular DEA is constrained by rigid acrylic layers at its edges. The difference lies in the number of elastomer and electrode layers utilised to create the DEA. Instead of a single elastomer layer sandwiched between two compliant electrodes, multiple layers are stacked using spin coating of elastomer layers. The increase in overall thickness allows for alternative methods of constraining the DEA to move in only one direction. A cavity can be created such as in Concept 2 and inflated using air or another fluid medium. Alternatively, the initial shape can be stamped or embossed in the thicker multi-layer configuration. Figure 3-3, (a) illustrates the stacked layers before being embossed and (b) represents the DEA once embossed in order to constrain direction of deflection in the upward direction.

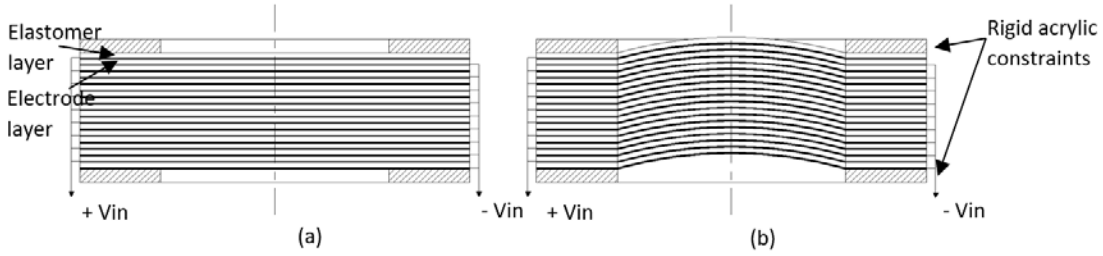

Figure 3-3 Conceptual design of multiple stacked layer diaphragm-type DEA (a), Stacked configuration before layers are constrained in single direction of deflection (b), Stacked configuration after embossing process

The stacked configuration reduces the overall driving voltage required of the DEA. Therefore, in a case where portability is essential, this will allow a smaller power source to be used. It must be noted that the reduction of voltage still results in a final driving voltage of magnitude 10^3. An example of this is the experimental results detailed by Igmo et al. [56], where 18 layers of film were stacked and embossed using a hot press to create a diaphragm-type DEA of 2mm diameter. A final displacement of 1,8mm was recorded at a voltage input of 3 kV.

The increased number of DEA layers impacts the complexity and cost of the synthesis procedure. Readily manufactured elastomer films such as VHB 4910 are challenging to use in this configuration since the stacking procedure will create a risk of bubble formation between layers. In cases where only a reduction in thickness is required in a series of stacked DEAs to produce the required actuation, simpler processes such as using VHB films can be used. However, the requirement of area expansion to raise the diaphragm into the actuated position causes the actuator performance to be more sensitive to inconsistencies in film layers than an actuator solely based on overall thickness reduction. Due to the requirement for a secondary process to emboss the completed film, pre-strain of elastomers is not ideal since relaxation may occur. Therefore, the more common materials used as the elastomer matrix in the circumstance of multi-layer diaphragms are silicones applied as a liquid and spin coated to the correct thickness. Thereafter

the electrodes are sprayed onto the surface using a masking agent. The next silicone layer will be applied, and spin coated directly to the dried electrode layer. Like the single-layer diaphragm DEA, a protective coating is required to be applied to the side of the actuator with which the user is interacting. A hot press or stamping machine is then required to emboss the final DEA and create the initial curve in the direction of actuation.

3.3.4 Diaphragm-type with fluid inflation and passive membrane

Concept 4 is considered the safest configuration since the user's finger is located furthest from the active high voltage DEA membrane. As illustrated in Figure 3-4, the DEA is comprised of an active and passive elastomer film which are inflated by a fluid inserted between the two membranes. The active layer is the elastomer with compliant electrodes on either side connected to a voltage source and the passive layer is solely an elastomer layer. Both layers are constrained by a rigid acrylic frame. Once voltage is applied, the active layer will decrease in thickness, increase in area, and buckle outwards. This will result in the passive electrode decreasing in height to maintain the pressure within the chamber.

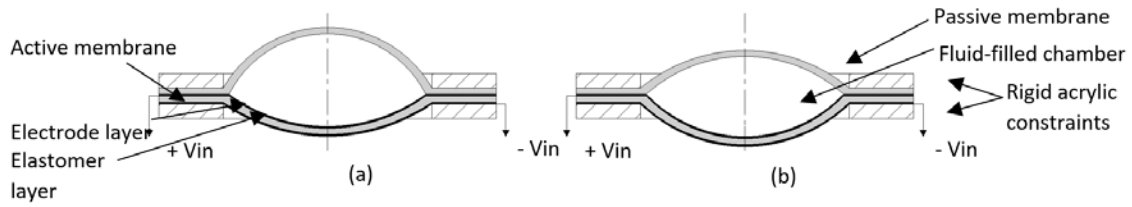

Figure 3-4 Conceptual design of diaphragm DEA with passive membrane (a), Active and passive elastomer films encompass a fluid filled recess V=0 (b), Voltage applied through active membrane V≠0

The advantage of this system is the lack of direct contact between the user and the active DEA layer. However, insulating layers will still be required along either side of the active membrane to protect the electrode from the environment and the hydrostatic fluid. A further point of consideration is the extent of miniaturisation possible for such a configuration, this was particularly noticeable in the application proposed by Boys et al as a tactile display to be mounted on a fingertip [74]. It must also be noted that this configuration responds in the inverse compared to the other diaphragm shaped DEA concepts, where increase in voltage now results in a decrease in vertical height of the curve.

3.3.5 Final concept selection

The selection matrix represented in Table 3-3 briefly compares the major requirements of each DEA concept, with a score of 4 being the highest performance and 1 being the lowest.

Table 3-3 Selection matrix of conceptual designs

Actuator Type	**% Displacement**	**Overall size**	**Power Consumption**	**Cost**	**Total**
Rolled	4	1	3	3	11
Diaphragm single layer	2	4	2	4	12
Diaphragm multiple layers	3	3	4	1	11
Diaphragm with passive membrane	1	2	1	2	6

According to the selection table, the single-layer diaphragm type is the most applicable concept according to the requirements of the design. The rolled and multi-layered diaphragm concepts achieved an almost identical total score however, each had a major drawback that impacted the final decision. Although the rolled spring DEA has been recorded to produce the greatest percentage displacement and force results, the range of miniaturisation of the device was limited by the dependence of the final displacement on the dimensions of the inner spring mechanism. It was concluded that a rolled-type DEA was not capable of the appropriate miniaturisation in order to achieve the required proprioception in the reader by minimising the distance between the pad of the finger and the medium on which the text is printed. The major drawback of the multi-layered diaphragm concept was the cost of manufacture due to the requirement for complex synthesis procedures. Although the single-layer configuration required a higher driving voltage, which was historically a major drawback from an electronics perspective, the introduction of new miniaturised high voltage converters to the market provides a modern solution while removing the need for the expensive equipment needed for multi-layer DEA production.

With a single layer diaphragm DEA configuration selected, the next point of order was to select the appropriate elastomer and electrode materials to achieve optimal displacement results. This was investigated experimentally in Chapter 5.

3.4 Final electrical design

The final electrical design consisted of a microprocessor, battery power supply, DC to high voltage DC converter and a system of relays to protect the microcontroller from the high voltage output. The electrical design was required to convert the digitized text characters into corresponding voltage outputs to be sent to each of the six braille dots. Factors that were prioritized were operator safety and protection of components from high voltage output, cost, potability and reaction speed. The block diagram below illustrates a simplified representation of the proposed system, Figure 3-5. The following sub-section discusses the selection of each component and is concluded by a complete diagrammatic representation of the sub-system. Note: the camera module selection is discussed in Section 3.5: Final mechanical design.

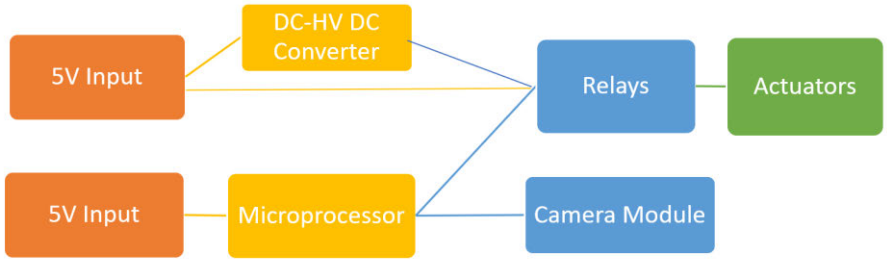

Figure 3-5 Simplified representation of electrical design

3.4.1 Microcomputer

The selected microcontroller/microcomputer was required to scan the text using the appropriate camera module, run the OCR software and convert the resultant digitised ASCII text characters into a series of six voltage outputs to correspond with the braille character. The actuator control was based on a simple binary configuration using the voltage input and a relay. The OCR software was comprised of a combination of Open CV library and Tesseract, see Chapter 2.8 for more information on the proposed OCR system.

Possible microcomputers and microcontrollers used in Open CV and Tesseract OCR applications include Arduino and Raspberry Pi. Other microcomputers such as BeagleBone Black have also been used in OCR applications, however, the relative cost and access to online support and documentation related to Arduino and Raspberry Pi result in these boards being preferred choices in prototype devices [109]. The limiting factor of the Arduino microcontroller is the available Random-Access Memory (RAM), this will limit the processing speed. Embedded computers such as Raspberry Pi are capable of processing the above-mentioned commands and programs in real-time due to their faster clock speed and greater RAM.

The ideal model of Raspberry Pi to satisfy the requirements of a portable text to braille transcription device is the Raspberry Pi Zero W. The Zero W is low-cost relative to other Raspberry Pi models and is the smallest model available with a footprint measuring at 65mm x 30mm and height of 5,4mm. The details of the board are listed below [110].

- 1GHz, single-core CPU
- 512MB RAM
- Mini-HDMI port
- Micro-USB Port
- Micro-USB power
- Composite video and reset headers
- CSI camera connector
- 802.11n wireless LAN

- Bluetooth 4.0

The Raspberry Pi embedded computers are sensitive to incorrectly applied voltage and current spikes. Therefore, to prevent damage to the board, the Pi Zero is individually powered by a LiPo battery and isolated from the high voltage relays and DC-HV DC converter.

3.4.2 DC-High voltage DC converter

Chapter 2.7 discussed the existing technology available to supply a high voltage output while maintaining a portable, low power consumption design. The XP Power A50P-5 DC – HV DC converter was selected to convert a 5 V input into 5000 V. The DEA requires a high voltage to generate a sufficient electric field to actuate the device. According to the theoretical equations in Chapter 2.6, only the voltage magnitude has an impact on the planar strain produced in the DEA, therefore the current output can be manipulated when connecting the actuator circuit. The DC – HV DC converter is the most expensive standalone component in the design, quoted at R 4 465, 44 from RS Components SA. Therefore, to avoid purchasing an individual DC-DC HV converter for each of the six actuators that comprise the braille cell display, the dots are all connected in parallel to a single DC- HV DC output. Thus, the voltage input for each actuator remains at the rated 5000 V. Figure 3-6 illustrates the DC-HV DV converter of maximum dimensions 28,69 x 6,35 x 11,43 mm [89]. Figure 3-7 indicates the expected output voltage per percentage input voltage. A set voltage of 5V is supplied by the battery in the final design.

Figure 3-6 A Series XP Power DC- HV DC Converter

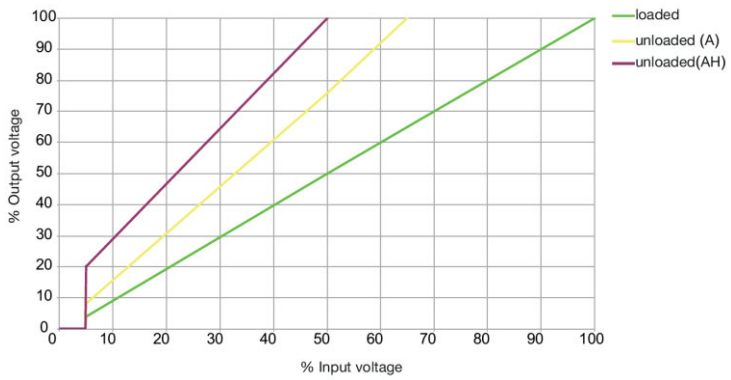

Figure 3-7 Typical Input vs Output Voltage for A Series XP Power DC-HV DC Converter [89]

3.4.3 High voltage switching circuit

The rated output of the A50P-5 DC - HV DC converter at 5V input is 1 W. The A50P-5 DC-HV DC converter is purchased with built-in input to output and short circuit protection. This reduces the complexity of additional components required for circuit protection on the input and output sides of the converter, such as reverse polarity protection. A necessary additional protection component is a bleeder resistor positioned in parallel to the output terminals of the converter. The bleeder resistor drains the high voltage charge of the DEA, which acts as a capacitor when the circuit is switched off. XP-Power recommends a resistor capable of withstanding maximum voltage output at a bleeder current of less than 10% of the converter's rated output current. The resistance calculation below was used to determine bleeder resistance. The total calculated resistance of $25\ M\Omega$ can be created by placing resistors in series in order to avoid sourcing a single high-cost resistor capable of providing the required resistance at a maximum working voltage of 5 kV. An example of an appropriate resistor combination that can be applied in a series is the HB15M0FZRE 5 MΩ Radial Fixed Resistor and HB120MFZRE 20 MΩ Radial Fixed Resistor, both manufactured by TE Connectivity and supplied by RS Components South Africa [111] [112].

$$R = \frac{V}{I}$$

$$R = \frac{5000}{0.2mA}$$

$$R = 25\ M\Omega$$

The next component to be discussed as a contributor to the circuit protection of the electrical design is the voltage control between the HV output and the Raspberry Pi. Two options exist to control the DEAs from the HV side of the circuit while protecting the Raspberry Pi: a HV transistor switch or HV relays. The variety of available devices were severely limited by the requirement to control a high voltage while meeting the scale requirements of the device. Five potential HV transistor/relay solutions are reviewed below. These components were selected for their availability, cost, and small scale.

- **Behlke HTS 50-05 High Voltage Transistor Switch** [113]

- Input voltage: 5V
- Max operating voltage: 5kV
- Rise time: 1 ms
- Maximum peak current: 50 A
- Dimensions: 80 x 38 x 25 mm
- Approximate cost: $572.41
- Encapsulated

- **LRL-102-100PCV HV Reed Relay (Toward Relays)** [114]

- Nominal coil voltage: 12V DC
- Breakdown voltage: DC 10kV
- Coil resistance: 200 Ω ±10%
- Min release voltage: 1.2V DC
- Max release voltage: 8.2V DC
- Switching voltage: 10kV DC
- Max switching current: 2.0A
- Max carry current: 3.0A
- Dimensions: 70 x 19 x 20 mm
- Approximate cost: $103.00
- Encapsulated

• **Pickering Series 67-1-A-5/2-D 10kV HV** [115]

- Nominal coil voltage: 5V
- Max switching current: 3A
- Max carry current: 3A
- Max switching voltage: 7.5 kV
- Breakdown voltage: DC 10 kV
- Operating time: 3 ms
- Release time: 12 ms
- Coil resistance: 40 Ω
- Dimensions: 14.5 x 58.4 x 12.6 mm
- Approximate cost: $32.14
- Encapsulated

• **Gigivac G41A232 HV Relay 5kV** [116]

- Nominal coil voltage: 12V DC
- Max operating voltage: 5 kV
- Max continuous current: 30A
- Operating time: 10 ms
- Release time: 10 ms
- Dimensions: 43.2 x Ø 16.6 mm
- Approximate cost: $296.00
- Not encapsulated

• **TE Connectivity K41A234 Kilovac 5kV** [117]

- Max operating voltage: 5 kV
- Nominal coil voltage: 12 V DC
- Max continuous carry current: 30A

- Operating time: 10 ms
- Release time: 10 ms
- Dimensions: 46 x Ø 16.5 mm
- Approximate cost: $334.91
- Not encapsulated

Upon analysis of the above specifications, the Pickering Relay was determined superior in both cost and overall dimensions. Although the Kilovac relay was more compact, it was disadvantaged by the requirement for a 12V DC input voltage. Similarly, the Behlke transistor option only required a 5V input but did not have as compact a design nor a competitive price when compared to the Pickering relay. Further, the Pickering relay could be purchased with pre-installed internal flyback diodes, therefore reducing the complexity of the final assembly. In conclusion, the Pickering 67-1-A-5/2-D reed relay was implemented to control each of the actuators in the six-dot configuration.

3.4.4 Power source and circuit protection

Two 3,7 V lithium polymer batteries were selected to power the prototype device. This was necessary to provide sufficient power to the set of high voltage relays, DC- HV DC converter and Raspberry Pi Zero while maintaining a small footprint to be mounted to the user's hand. One battery was dedicated to the operation of the Raspberry Pi Zero while the other powered the DC-HV DC converter and relay array.

The selected LiPo batteries were sourced from DIY Electronics, a local supplier, and consisted of the following specifications:

Table 3-4 Specifications of PIJUICE ZERO LiPo Battery (9RPIJUICEZB12M) [118]

Rated Capacity (Typical)	1200mAh
Nominal Voltage	3.7V
Voltage After Discharge	2.75V
Charging Voltage	4.2V
Standard Charge	240mA x 2 (0.2C) (Parallel Charging)
Onboard Battery Protection	4.2V Over-Charge Protection 2.9V Under-Voltage Protection
Ideal Operating Temperatures	-20° to +55°C
Ideal Storage Temperatures	0° to +45°C
Weight	±80g
Dimensions	30 x 35 x 9mm

One of the batteries was connected solely to the Raspberry Pi via a power booster and charger module. This served to protect the Pi from possible voltage surge at the input side should the relays or the DC-HV DC converter be connected along the same circuit. The connection of the relays to an external power source further prevented the chance of the voltage spike on the output side of the Pi when a relay switch was de-energized.

It is further recommended by the Raspberry Pi manufacturers that only 3.3V signal logic be utilized at the output of the General-Purpose Input/Output (GPIO) pins [119]. The Pickering relays have a listed 'must operate voltage' of 3,75 V and a recommended voltage input of 5 V. The relays are also connected in parallel and therefore act as a substantial current draw. The current draw of each relay is 125mA, resulting in a total of 750mA. An individual GPIO pin can safely draw 16 mA, according to the Raspberry developers [120]. The developers go on to state ", Should the current draw and subsequent power rating be greater, an external power source should be used." [120] Fortunately, this problem can be circumvented by the introduction of MOSFETS and transistors to the output circuit. The transistor makes it possible to carry the required current of 125 mA per GPIO for the successful operation of the relay.

An individual transistor circuit which included a diode, resistor and the transistor, was installed individually between each GPIO pin and relay. However, due to the number of relays required, it was concluded that the resultant complex schematic and circuit design could be simplified by introducing an integrated circuit such as the ULN2003. The ULN2003 is a high current high voltage Darlington transistor array that simplifies the output circuit [121]. This component will serve as a robust and compact solution between the GPIOs of the Pi and the relays, without the requirement of additional circuit components.

It must be noted that it was possible to power the relays using the 5V output pin of the Raspberry Pi, even though the developers recommend against this due to the risk of possible voltage surges that may harm the circuitry of the Pi. The 5 V output pin derives power directly from the source powering the Pi. This will therefore divide the current draw from the source between the Pi and the relays. The Pi takes up to approximately 800mA at peak operation; therefore, of the 2.5 A supplied by the power booster and charger module, 1,7 A will be remaining to be used by the relays. Note the current limitations on the GPIOs still require the ULN2003 transistor array to be used. This argument is theoretically sound, however, since another power source was already necessary to power the DC-HV DC converter, the more cautious decision was made to connect the relays to include the secondary power source and further isolate the sensitive Raspberry Pi.

An MP2636 Power Booster and charger module were connected between the LiPo and the Pi input to provide a manner of charging the LiPo using a MicroUSB and to boost the voltage from 3,7 V to 5 V at a maximum output current of 2,5 A [122]. The module also protected the battery from over-charge, over-discharge, high temperatures and over-current. Two LEDs acted as status indicators and the entire module measured 35 mm x 30 mm. To decrease the height of the component the USB output to the Pi and the PH2.0 connector to the battery will be removed and wires soldered directly to the board.

It was decided that the same MP2636 module was not necessary to be connected between the second battery and the relays and DC-HV DC converter. This decision was primarily based on the footprint of the MP2636 and it was not considered feasible to include the same module for the secondary battery, particularly since the connected devices are more electrically robust than the Pi. Therefore, a 25,91 x 17,02 x 9,91 mm LiPo charger (TP4056) developed by MakerFocus was selected along with a separate buck/boost converter developed by Pololu (S9V11F5) [123] [124]. Alternative products that combined the charger and booster into a single module was available with a smaller footprint than the MP2636, however a current output of 1,25 A was required since the relay array and DC-HV DC converter were connected in series, thus limiting the available modules. The Pololu S9V11F5 is capable of converting an input voltage of 2-16 V to a 5 V output at a maximum current of 1.5A while only measuring 7.6 × 11.4 × 3.8 mm, therefore making it ideal for the required application. The S9V11F5 also has integrated over-temperature and short-circuit protection [123].

3.4.5 Detailed electrical diagram

Figure 3-8 below illustrates a detailed schematic of the final electrical system to be implemented in the design. All components were of the appropriate size to be arranged on the dorsal size of the hand, allowing for full wrist and finger mobility. Approximate weight of all components was 160 grams. The casing design of the electrical components and circuit is discussed in Section 3.5.

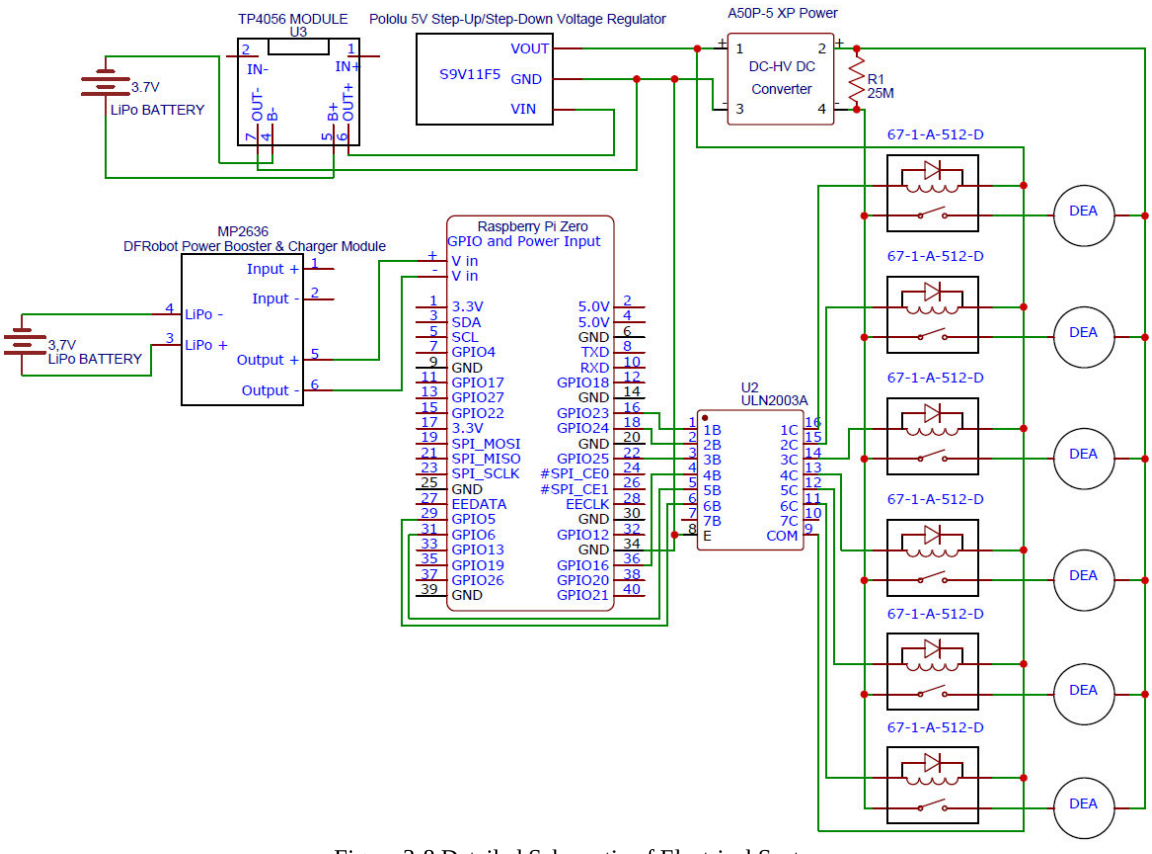

Figure 3-8 Detailed Schematic of Electrical System

3.5 Final Mechanical Design

The final design consisted of the subsystems depicted in the simplified representation, Figure 3-9. In terms of the mechanical contribution to each subsystem, this was further divided into the scanning hardware, finger mounting, the casing of electrical components and the tactile display to be mounted on the final joint of the index finger. The tactile display design relied on results of the first phase of DEA testing and is elaborated upon in Chapter 5.

Figure 3-9 Simplified Representation of Final Design

3.5.1 Scanning hardware

The Raspberry Pi Zero W includes a Camera Serial interface (CSI) port and MicroUSB data port which can be used to connect camera modules. The design-specific requirements of the camera module were primarily based on the logistics of mounting the module on the index finger in an inobtrusive manner. Braille reading technique differs between each reader and the device must therefore ensure that all common finger positions are possible to ensure a realistic effect likened to that of reading a traditionally embossed page of braille. This reduced the possible positions of the camera since some readers press their index and middle fingers together when reading, thus negating the possible camera position to the right of the index finger, Figure 3-10.

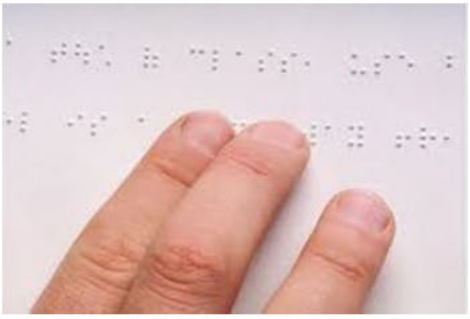

Figure 3-10 Position of right-hand indicating proximity of index and middle finger during reading [125]

More experienced braille readers adopt the butterfly technique where both forefingers follow the same line of braille until approximately two-thirds into the line the fingers separate with the right forefinger completing the line and the left forefinger moving to begin the next line of text, Figure 3-11. In this case, a camera placed to the left of the forefinger with the mounted device will intercept this natural reading position [126].

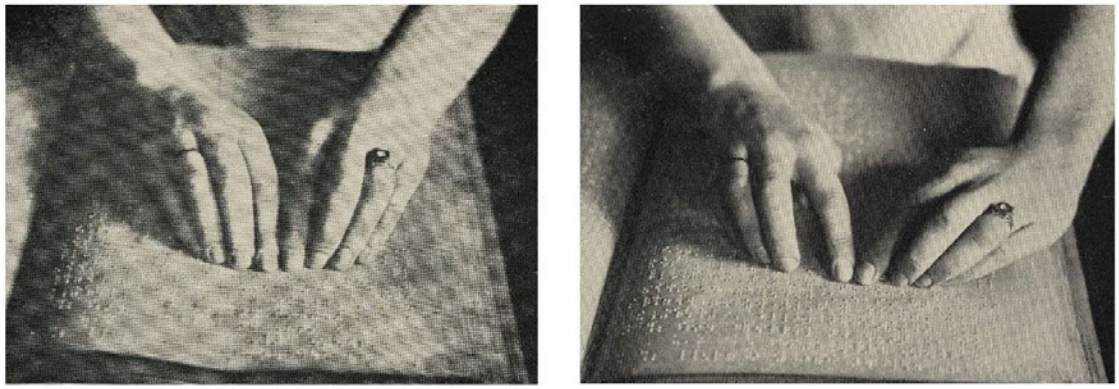

Figure 3-11 : Positions of hands by braille experienced readers (a), represents the classic 'butterfly technique' where the forefingers of both hands follow the same line until approximately 2/3 of the way where the left hand will then move to the start position of the next line while the right completes the previous line. (b) represents a possible variation of hand position while still following the 'butterfly technique'. [127]

Placing the camera at the tip of the finger would increase the distance between the finger and the reading medium, thus decreasing proprioceptive response of the user. Further, the focal distance must also be considered when selecting the camera. The focal distance refers to the distance required between the lens and the object to ensure the object is in focus. This was a particularly challenging requirement since most Raspberry Pi fixed focus camera modules had a focal distance of 1 m to infinity [128]. Autofocus camera modules such as the Arducam Autofocus Camera improved upon this limitation by reducing this to 4 cm to infinity [129]. However, the overall board size of the Arducam module (25 x 24 mm) did not lend itself to a compact, unobtrusive placement on the finger. This same obstacle was encountered with commercially available OCR scanning pens and highlighters which utilised a series of lenses to reflect light from a light-emitting diode (LED) onto a photosensitive element. The distance between the photosensitive element and lenses limited the degree of miniaturisation, particularly in the longitudinal direction [130]. Figure 3-12 presents a disassembled view of the Anoto pen, indicating the position and relative size of the optics subassembly of the device. A further limitation on utilising scanner pen optics in a finger-mounted application is the sensitivity to correct scan position. Scanner-pens perform optimal pattern detection when held perpendicular to the text [130] or at a specified angle such as 60° to the right for designs such as the Scanmarker [131]. In braille reading where finger position is dependent on reader preference, forcing the user into an unfamiliar finger posture will impact on the ergonomics and performance of the device.

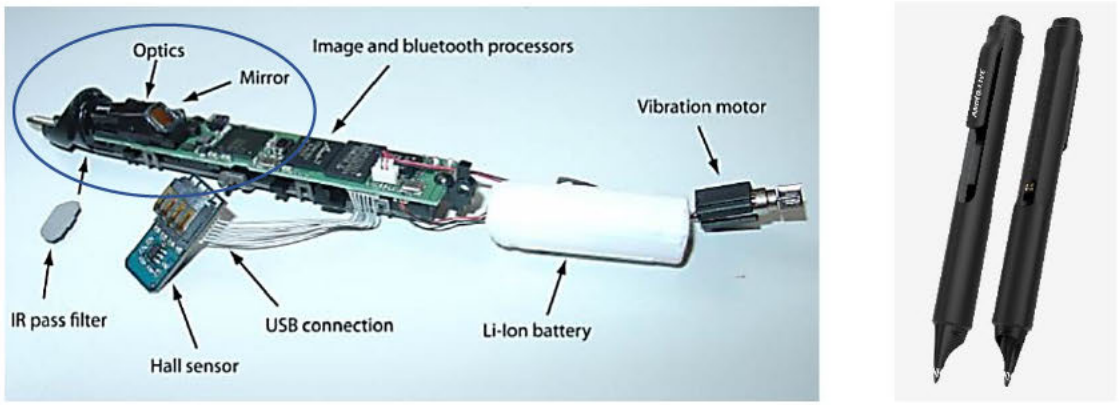

(a) (b)

Figure 3-12 Anoto Scanner Pen (a), Exploded view indicating the components of the pen [130] (b), fully assembled pen [132]

Upon consideration of the above-mentioned factors, it was concluded that a camera mounted on the dorsal side of the proximal or medial phalanx of the right index finger would avoid disrupting natural reading positions. Figure 3-13 illustrates the positions of the phalanges. Therefore, the camera will identify and scan the characters in the line of text above the position of the tip of the index finger. The tip of the finger will block the second line of text, providing a method to avoid scanning the incorrect line.

In order to determine the minimum allowable focal range of the camera, the dimensions of the average index finger were researched. Figure 3-13 and Table 3-5 provide a summary of the average size of the phalanges in the adult index finger. Since this device is also intended to be used as an educational tool, the average finger dimensions of children at reading age (6 years old) were also tabulated. Due to a lack of research material, a calculation was used to generate approximate index finger dimensions of children at age six. The average hand length of an adult and six-year-old child were compared, and it was determined that the child's hand was 70% the length of the adult hand [133] [134]. All adult index finger dimensions were then multiplied by 0,7 to determine equivalent six-year-old dimensions.

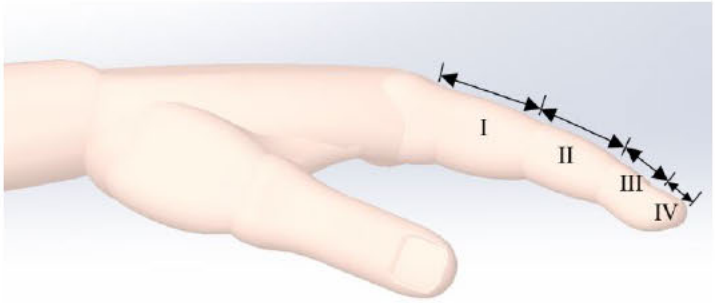

Figure 3-13 Representation of the sections of the human index finger where (I) is the proximal phalanx, (II) the medial phalanx, (III) the distal phalanx and (IV) indicates the average length of the soft tissues located at the tip of the finger.

Table 3-5 The average length of phalanges in the human hand.

Designation	Soft tissues at tip of distal phalanx (mm)	Distal Phalanx (mm)	Medial Phalanx (mm)	Proximal Phalanx (mm)	Reference
Adult	3.84±0.59	15.82±2.26	22.38±2.51	39.78±4.94	[135]
Child (6 Years)	2.67±0.41	11.06±1.58	15.67±1.75	27.85±3.46	[133]

According to Table 3-5, the average distance from the soft tissues at the tip of the index finger to the joint between the medial and proximal phalanx is 42.04 ± 5.36 mm for adults and 29.4 ± 3.75 mm for children age six. The average distance between the soft tissues at the tip of the index finger to the joint between the distal and medial phalanx is 19.66 ± 2.85 mm for adults and 13.73 ± 1.99 mm for children age six.

These values narrowed down the field of possible camera modules since the minimum focal range was required to correspond with the calculated values. Ideally having the camera module mounted on the medial phalanx would be preferrable to being mounted on the proximal phalanx. The medial phalanx would allow for greater control of the focal point of the camera and prevent the risk of the camera straying to the preceding line of text should the reader adjust the angle of finger position. Figure 3-14 and Figure 3-15 illustrate the expected focal points when the camera module is mounted on the medial and proximal phalanges respectively when the hand is in the correct reading position. Braille readers are taught to keep as many fingers on the line of braille as possible, therefore the index finger is restricted to an angle that allows the pad of the finger to line up with that of the longer middle finger. The hand in the Figure 3-14 and Figure 3-15 was simulated using the correct braille reading position.

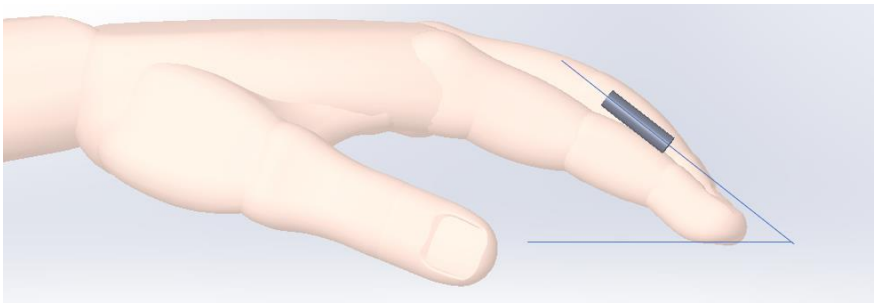

Figure 3-14 Projected focal point of camera when mounted on the medial phalanx, correct hand posture

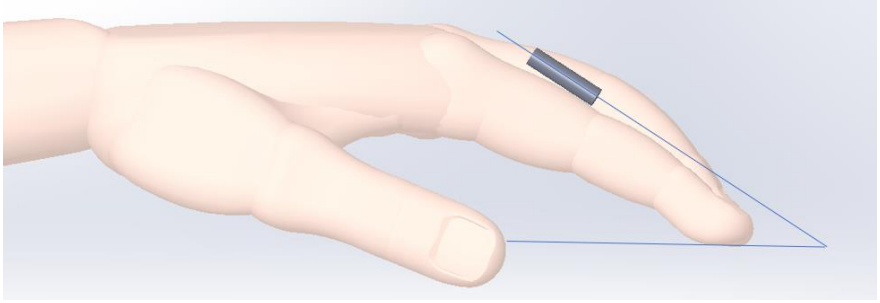

Figure 3-15 Projected focal point of camera when mounted on the proximal phalanx, correct hand posture

Figure 3-16 illustrates the change of focal position should the reader's hand stray from the correct reading posture when the camera is mounted on the proximal phalanx. The large angular offset will result in the device transcribing the text three lines above the current reading point and result in reader confusion. The limited degree of freedom of the medial phalanx relative to the proximal reduces the margin of error and is therefore the ideal position in which to mount the camera. However, it increases the complexity and cost of the camera required to meet the allowable focal range specifications.

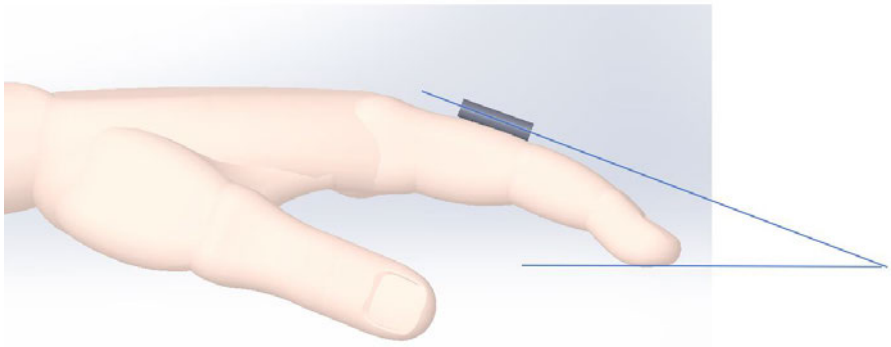

Figure 3-16 Projected focal point of camera when mounted on the proximal phalanx, incorrect hand posture

Upon consideration of the scale, focal range and robust design required of the camera module, a borescope/endoscope type module was selected. A borescope is a compact cylindrical camera module used to inspect small spaces. These modules are often equipped with LEDs to illuminate dark spaces and are enclosed in a waterproof casing, all of which are properties that would be useful in the application of a hand mounted braille scanner. The terminology of borescope and endoscope are used interchangeably in commercial distribution of these devices; however, endoscopes are typically more precise and achieve a greater level of miniaturisation than borescopes. Endoscopes are commonly used in the medical profession.

Borescopes or endoscopes were of particular interest due to their minimum focal distances relative to other camera modules while maintaining a clear image of the object. Majority of commercially available endoscopes specify a focal distance between 30 mm and 100 mm. Specialised medical use endoscopes further reduce this distance for focussed images, however, the cost of such inspection cameras prevented their application in this design. The borescope selected for the design was a 5.5 mm diameter camera module produced by T TAKMLY with a micro-USB cable which allowed for direct connection to the Raspberry Pi. The lens of the module is bordered by 6 adjustable LED lights for low light applications and had a resolution of 640 x 480. The length of the camera module in the waterproof casing is 30,25 mm. The cost of the camera was R 404.90 [136].

3.5.2 Finger mounting and configuration of tactile display

During the design of the mounting for the camera module and tactile display, the design of existing finger splint designs was considered. Existing finger splints prioritise the comfort of the wearer and a robust design capable of withstanding daily activities. Designs such as the Rolyan frog style splints and mallet finger splints, pictured in Figures 3-17 and 3-18, were considered.

Figure 3-17 Frog style aluminium finger splint [137]

Figure 3-18 Mallet finger splint [138]

The existing splint designs were used to develop the profile of the final finger mounting, particularly influencing the interior contours of the mounting since the device is intended to be worn for long periods of time. Figure 3-19 illustrates the final finger mounting design. The subassembly drawing SA3, exploded view SA2, and part drawing A4 in Appendix E provides further information on the configuration of the components. The mounting slides onto the right index finger and is secured by a Velcro strap around the medial phalanx. The camera module is secured along the slot indicated in Figure 3-19. The rear diameter of the slot and the keyway were designed to accommodate the additional rubber washer provided with the endoscope. The washer was designed to secure the accessories of the camera to its cylindrical body and therefore produces an interference fit when attached to the camera body. The small slot pictured to the left of the camera mounting in Figure 3-19 was also designed with an interference fit relative to the rubber washer, thus securing the camera and preventing motion during operation but allowing for easy removal should the device require disassembly during maintenance and storage. Circular cutouts

along the upper face provide airflow and prevent the user's finger from heating up inside the mounting.

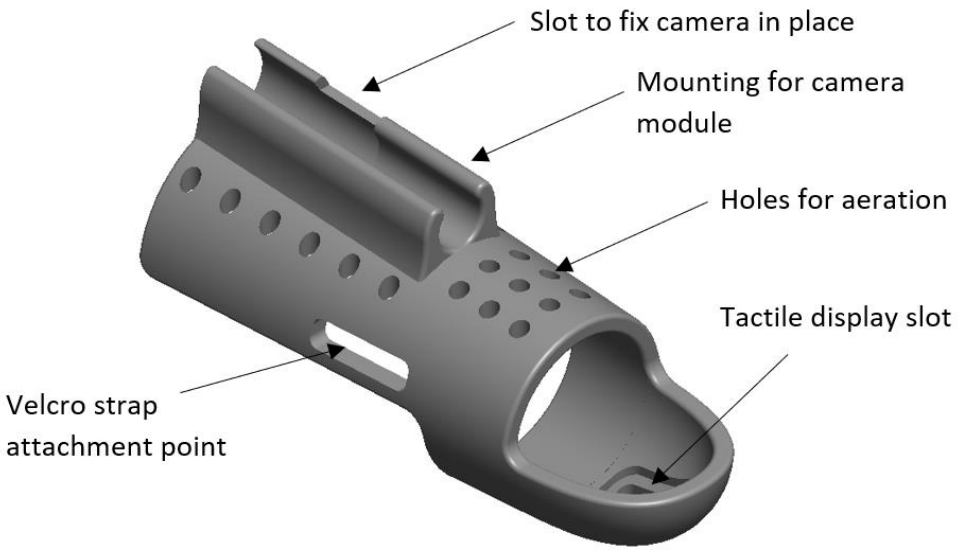

Figure 3-19 Final design of 3D printed finger mounting

The initial iteration of the design was to be 3D printed using Polylactic Acid (PLA). 3D printing allowed for the device to be easily manufactured during prototyping and to ensure that the measurements of the device corresponded with realistic hand sizes. Once prototyping is complete, later mass productions of the component can be completed using plastic injection moulding. Once a mould has been manufactured, the plastic injection moulding will be superior to the initial 3D printing production method both in terms of cost and time required for individual product fabrication.

As previously discussed in Section 3.5.1, the camera module mounted on the medial phalanx served as a more accurate text transcriber than when positioned on the proximal phalanx. However, with the camera requiring a minimum focal distance of 30 mm from the object, a position on the proximal phalanx would not suffice for children or adults with hands below the average size. This is where the mallet finger splint design provided a unique solution. The mallet splint locked the first finger joint in place, thus aligning the distal and medial phalanges while allowing the proximal phalanx free movement. The angle of the upper face of the finger mounting is thus equal to that of the distal and medial phalanges. Once the camera module is mounted on this face, it corresponds with the intended angle of the medial phalanx while providing the freedom to extend the position of the camera along this plane without creating interference with the joint between the medial and proximal phalanges. Thus, the locking of the first finger joint using a mallet design allowed the focal distance to be achieved while maintaining the correct view angle. It further allowed for customisation according to the finger size of the individual without impacting the camera position. Figure 3-20 illustrates the positions of the first and second joints

of the index finger of the average adult, labelled A and B respectively and the position of the camera module relative to these positions.

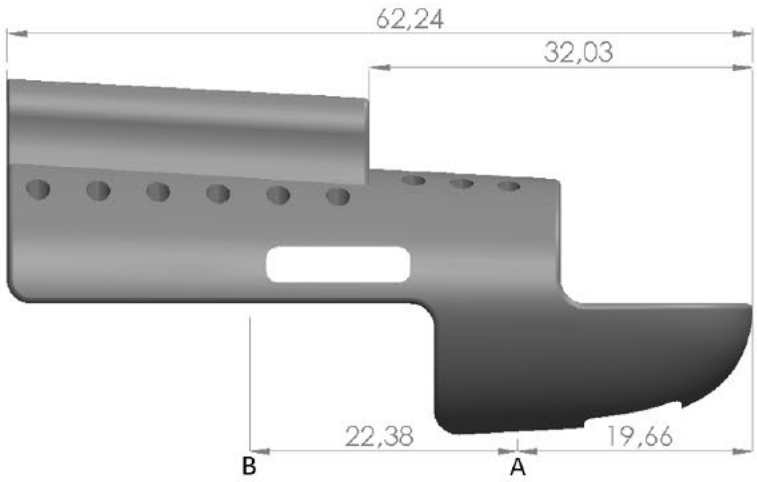

Figure 3-20 Finger mounting with dimensions indicating joint position

The 3D printed prototype in Figure 3-21 displays the design mounted on a reader's finger. The image indicates how the design was secured on the finger using the Velcro strap. Upon closer inspection, one can see how the first finger joint, labelled A in Figure 3-21, was successfully locked in place by the cavity wall and Velcro strap. This allowed the user free motion to adjust the second joint, point B, to achieve a comfortable reading position. The 3D printed prototype indicated that the design successfully achieved the anticipated finger position. The next design requirement was the provision of a simple method of inserting the DEA braille display onto the mounting.

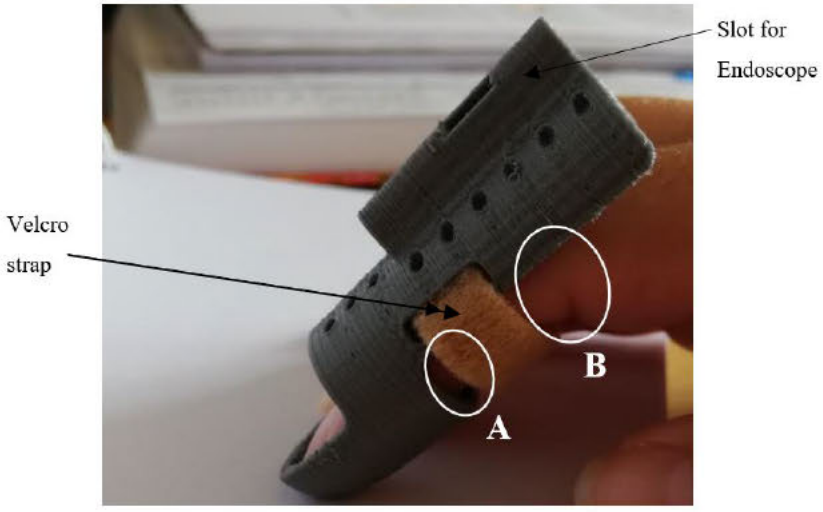

Figure 3-21 3D printed prototype of finger mounting

The design allowed the flexible DEA subassembly to be inserted through the back of the finger cavity and pressed into the rectangular slot indicated in Figure 3-21. This allowed the DEA tactile

display to be positioned directly below the pad of the index finger once the finger mounting was secured on the reader's finger.

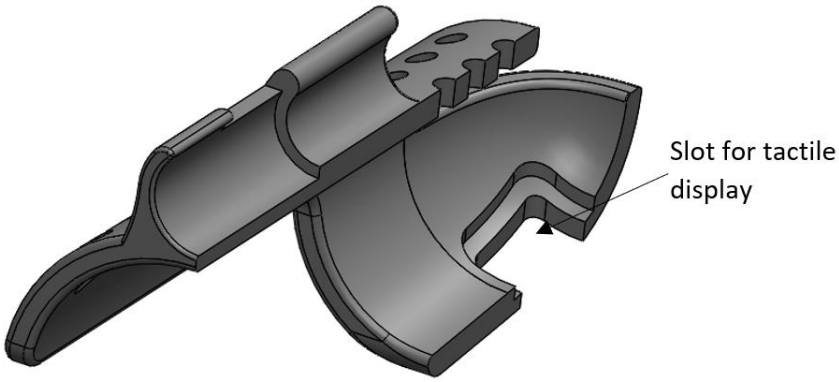

Figure 3-22 Sectional view of finger mounting

The DEA subassembly is comprised of seven layers, as illustrated in Figure 3-23. A detailed description of the DEA materials and method of synthesis of the DEA is presented in Chapters 5 and 6. The following paragraph provides a summary of the expected operation of the DEA tactile display.

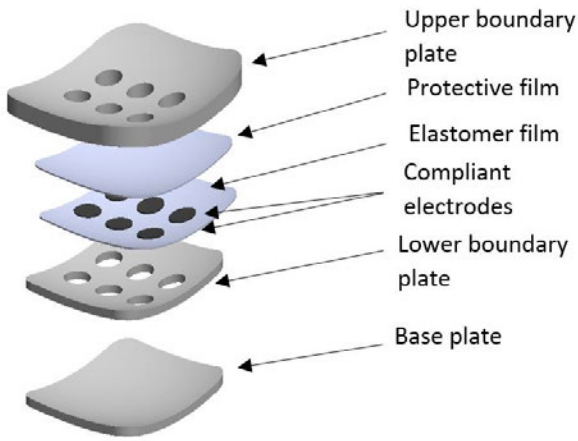

Figure 3-23 Exploded view of DEA subassembly

The thickness of the lower and base plates is 0.45mm and the material is a flexible Polypropylene electrical insulating film selected to conform to the shape of the finger mounting [139]. The thickness of the upper boundary plate is dependent on the initial radius of the DEA diaphragm before a voltage is applied, determined experimentally in Chapter 6. The initial radius when the DEA is at rest must be in line with the upper edge of the plate; therefore, the DEA will not make an indentation in the user's finger. Once a voltage is applied, the DEA braille dot radius will increase and stimulate the receptors in the fingertip. The sectional view presented in Figure 3-24 depicts the DEA braille dots at the initial height before the voltage is applied. The initial height of the DEA was determined in the experimentation recorded in Chapter 6. In order to determine

the approximate cost of materials, an upper base plate thickness of 2 mm was selected from the material was Polystone Polypropylene sheets [140]. This material was selected due to its thermoformable properties which allowed the DEA to conform to the shape of the finger mounting and finger.

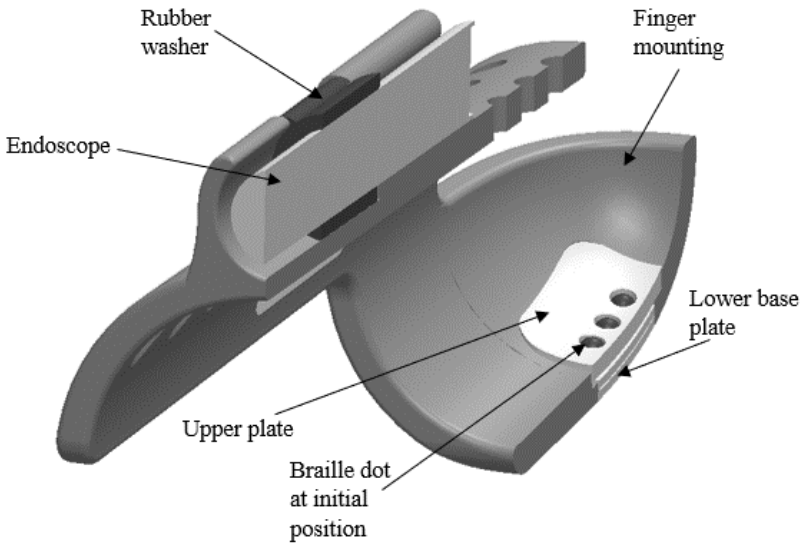

Figure 3-24 Sectional view illustrating position of inflated DEA on finger mounting

The material and synthesis procedure of the elastomer film and compliant electrodes was determined experimentally with results recorded in Chapter 5. The protective film will consist of the same material as that selected for the elastomer film. The lower boundary and base plates are secured using a silicone adhesive known as Sil-Poxy. The DEA is synthesised and assembled; thereafter a needle is inserted in the silicone layer between lower and base plates to inflate the diaphragm to initial heigh. The subassembly is then be secured inside the finger mounting and the DEAs are connected to the Pickering relays by wires mounted on the outer face of the mounting.

3.5.3 Electrical components in casing

The electrical components of the design required a casing to protect both the user and the circuitry. The only electrical component situated outside the casing are the Pickering relays which are already encapsulated in an insulating casing. The other electrical components were divided into three layers to make the design as compact as possible. The first layer consisted of the two LiPo batteries and the third layer included the Raspberry Pi Zero W. These two layers contained the components with the largest footprints and were therefore used to stipulate the base dimensions of the design (72 x 30 mm). The second layer consisted of the DC to HV DC converter, the MP2636 power booster and charger, the TP4056 battery charger and a printed circuit board (PCB) consisting of the ULN2003, Pololu S9V11F5 and five resistors.

Since the Pololu, TP4056 and MP2636 Power booster heat up during operation, it was necessary to include extruded cuts in the casing to allow for sufficient ventilation. To prevent water and dust ingress in the circuitry and components, a silicone insulating sealant is sprayed or brushed onto the surfaces of the components and PCB. It must be noted that active ports must be masked before the coating is applied. MG Chemical Silicone Conformal Coating was selected for this application [141].

The electrical components were arranged according to their prescribed dimensions and a base footprint of 72 x 30 mm. The total height of the combined components, including necessary gaps between electrical circuits was calculated as 34,2 mm. Upon consideration of the calculated dimensions and existing dimensions of the dorsal side of the human hand, it was concluded that the casing be split into two separate components. Therefore, a single casing could be mounted on the wrist to hold the batteries, and another casing could be mounted on the dorsal side of the hand containing the remaining components. Figure 3-25 illustrates the positions of the casings. Note, the glove and Velcro wrist strap are not represented in image. Part drawings A1, A2 and A3 in Appendix E illustrate the design of each structure.

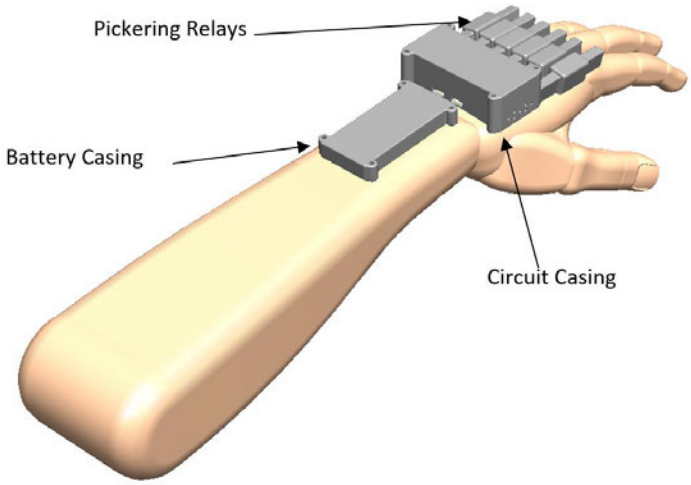

Figure 3-25 Casing position 1

Each of the casings and Pickering Relays includes snap fasteners adhered at the corners of the base which allow for a customisable fit on the glove. Each relay is separately attached to the glove using the fasteners in order to maintain mobility of the fingers. The glove is fingerless and therefore allows the reader to feel the reading medium with the thumb and three fingers. The electrical casing has two possible configurations based on the preference of the reader. The first configuration includes the casing attached to a Velcro strap on the wrist using the snap fasteners, and the second casing attached to the hand, see Figure 3-25. The second stacked configuration is possible since the casing containing the electrical components has been designed to be stacked on top of the battery casing using M3 or UTS No. 4 self-tapping screws of lengths between 18 mm

and 30 mm. This allows both cases to be attached to either the wrist or the hand depending on wearer comfort. In the case of children or small adults, the wrist mounting would be most applicable considering the limited dorsal area of the hand. The second configuration is illustrated in Figures 3-26 and 3-27. Note, the glove and Velcro wrist strap are not represented in images. Additional subassembly views and part drawings of the casing are available in Appendix E.

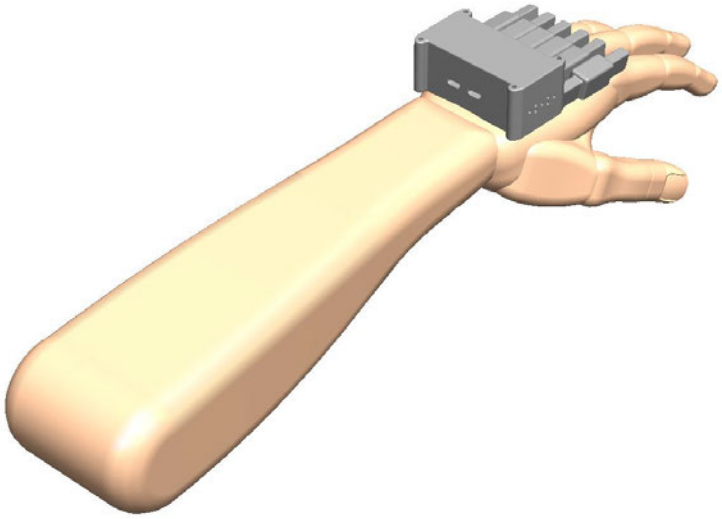

Figure 3-26 Casing position 2

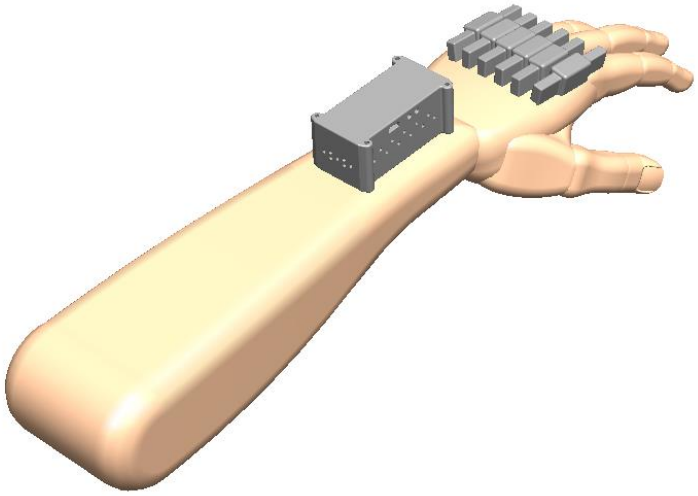

Figure 3-27 Casing position 3

3.5.4 Full assembly

The full assembly of the mechanical design is depicted in Figure 3-28 below. Note, the glove, Velcro wrist and finger straps, and wiring are not represented in the image. Approximate total weight of the mechanical and electrical design is 261 grams. Individual components weigh as follows: 160 g for electronics,17 g for electrical casing, 9 g for battery casing, 55g for endoscope,

12g for both casing lids and 8 g for finger mounting. The weights of the casings and finger mounting were calculated under the assumption that standard PLA filament would be used with 20% infill. Appendix B presents a budget overview of the mechanical and electrical subsystems.

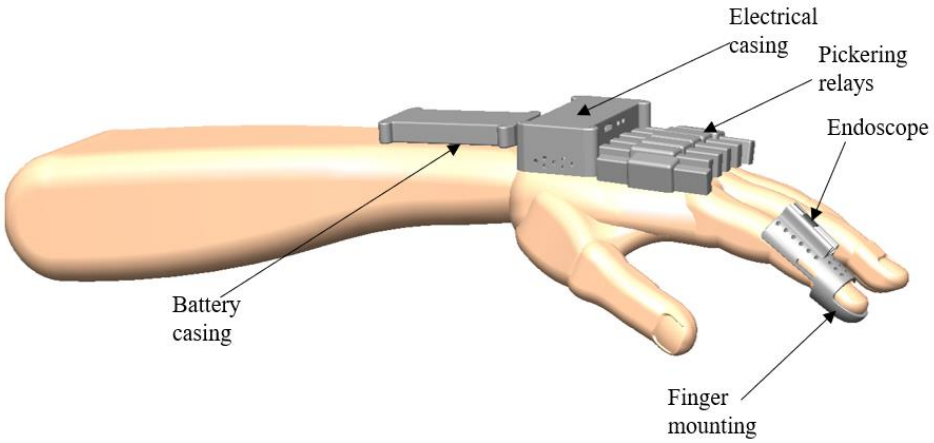

Figure 3-28 Full assembly of mechanical design

3.6 Assembly precedence diagram

Figure 3-29 represents the assembly precedence diagram of the tactile braille display device. The accompanying Table 3-6 details the bill of materials required in the precedence diagram. The exploded subassembly drawings in Appendix E (Drawings SA1, SA2 and SA3) provide illustrative depictions of the subassemblies described in the precedence diagram.

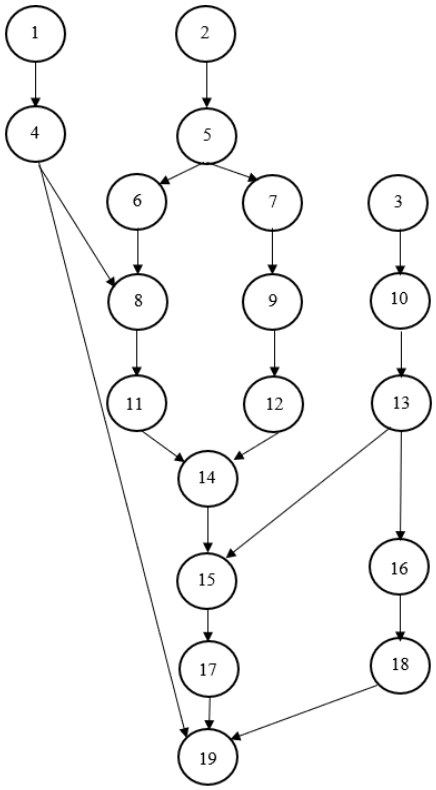

Figure 3-29 Assembly precedence diagram

Table 3-6 Bill of materials for assembly precedence diagram

Item	Description	Quantity
1	Camera Module	1
2	Battery Casing	1
3	DEA Rigid Boundaries	2
4	Rubber Washer	1
5	LiPo Battery	2
6	MP2636 Power Booster and Charger Module	1
7	TP4056 Charger	1
8	Raspberry Pi Zero W	1
9	Pololu S9V11F5 Buck/Boost Converter	1
10	VHB Elastomer	1
11	ULN 2003A Transistor Array	1
12	XP EMCO DC-HV DC Converter	1
13	Compliant Electrode	12
14	Circuit Casing	1
15	Pickering 67-1-A-5/2-D Reed Relay	6
16	Sealant Elastomer Layer	2
17	Glove	1
18	DEA Base Plate	1
19	Finger Mounting	1

3.7 Chapter Summary

Chapter 3 presented the specifications of the device, the conceptual designs and discussed the final subsystems. The electrical subsystem consisted of a Raspberry Pi Zero microcomputer which controlled six high voltage relays via the GPIO pins. The high voltage relays regulated the voltage supplied by the DC to HV DC XP-EMCO converter to the DEA output. The mechanical design subsections described the adjustable housing of the electrical circuit, which was to be mounted on the dorsal side of the hand and wrist. The circuit housing was designed to be arranged either completely on the hand or along the hand and wrist to cater for individuals of different ages and sizes. All components were to be 3D printed along with the finger mounting, which contained both the DEA and endoscope camera module.

The following chapter presents the configuration and testing of the OCR program. The code of the program utilises both OpenCV and Tesseract engines to complete the OCR functions required to transcribe the scanned input into six corresponding voltage outputs.

4. OCR USING TESSERACT AND OPENCV

4.1 Introduction

Chapter 4 analyses the viability of using a Tesseract-OpenCV engine to complete the optical character recognition required for the braille transcription system. The combination of a Tesseract OCR engine and OpenCV pre-processer was selected based on the research compiled in Chapter 2.8. The flow chart illustrated in Figure 4-1 describes the procedure utilized by Tesseract when extracting ASCII text from an image. The pre-processing and post-processing indicated in Figure 4-1 is completed by the OpenCV software package.

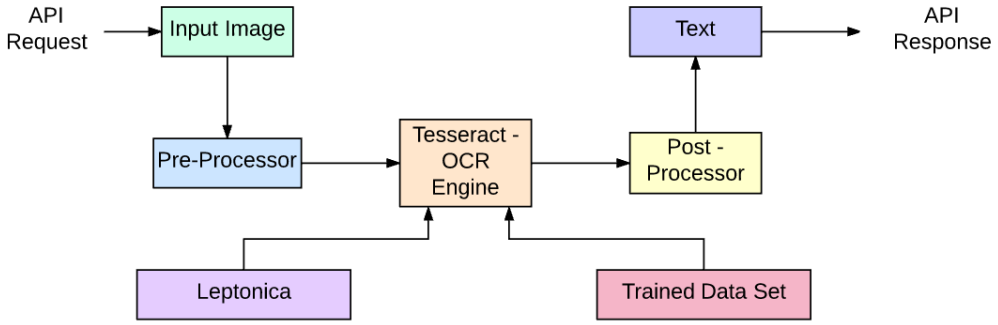

Figure 4-1 Tesseract OCR Process

The purpose of the analysis was to determine if the Tesseract-OpenCV OCR will meet the criteria of the device, particularly the processing time required to match the average reading speed of a braille reader. According to the specifications stipulated in Chapter 3.2 the average braille reading speed is 120 words/min. The proposed system transcribes each scanned text character to braille in real-time. Therefore, using the average reading speed stated above and the assumption of an average of 4,79 letters per word in the English language, a required reaction time of 0,418 seconds was calculated [142]. The investigation used this value to analyse the performance of the OCR and determine if any adjustments to the design were required.

The analysis consisted of configuring a Raspberry Pi Zero to run both the Tesseract and OpenCV software and process scanned images to produce a measurable output. The output consisted of the scanned characters displayed on a connected digital monitor and as a simulated braille output using a set of six LEDs. The LED output circuit was connected to the GPIO ports of the Raspberry Pi and was used to test the accuracy of the OCR code and the response time since the same code and ports will be used in the final dielectric elastomer design.

Chapter 4 details the apparatus and equipment used in the investigation, the installation and setup of the OCR engine, a description of the final command code, the results of the tests and a discussion on how the information will be utilized in the final design. The tests compared how

the OCR subsystem performed when inputting scanned images with different fonts, scan quality, image size, and the number of characters per scanned image.

4.2 Test apparatus and equipment

- Raspberry Pi Zero
- Digital Monitor
- Keyboard
- USB Computer Mouse
- HDMI cable
- Raspberry Pi Official Power Source
- Raspberry Pi Zero Official Case
- Breadboard
- 5mm Red LED x 6
- (300 Ω) Resistor x 6
- (750 Ω) Resistor x 6
- (330 Ω) Resistor x 6
- PN2222AL-BP Transistor x 6

4.3 LED Test circuit

The testing of the OCR subsystem and prototype DEA sub-system occurred within the same time frame. Therefore, in order to document accurate results pertaining to the specific response time of the OCR subsystem, an output response was simulated using six LEDs. These LEDs represented the voltage input experienced by the dielectric braille actuators. The decision to use LEDs was motivated by the need to monitor only the OCR subsystem time response visually without the discrepancies introduced by the prototype actuators. The sections of code in Section 4.6 that relate to the LED control was highlighted and included a commentary on how the same lines of commands can be used to control the relays that will be utilised in the final dielectric elastomer-based output.

The six LEDs were connected in parallel to the 5 Volt input pin and Ground pin of the Raspberry Pi. In order to prevent electrical damage to the GPIO pins, a PN2222A NPN transistor was placed between each LED and GPIO pin. Two resistors were required in the design, one resistor positioned between the 5V input and LED and the second positioned between the transistor and GPIO control pin. The resistor between input and LED had a selected resistance of 330 Ω and the minimum resistance calculated for the resistor between the transistor and GPIO was 1kΩ. Figure 4-2 illustrates the LED control schematic used in the OCR subsystem testing and Figure 4-3

depicts the final physical test circuit. Two resistors were placed between the GPIO control pin and transistor in order to achieve a total resistance of 1050 Ω.

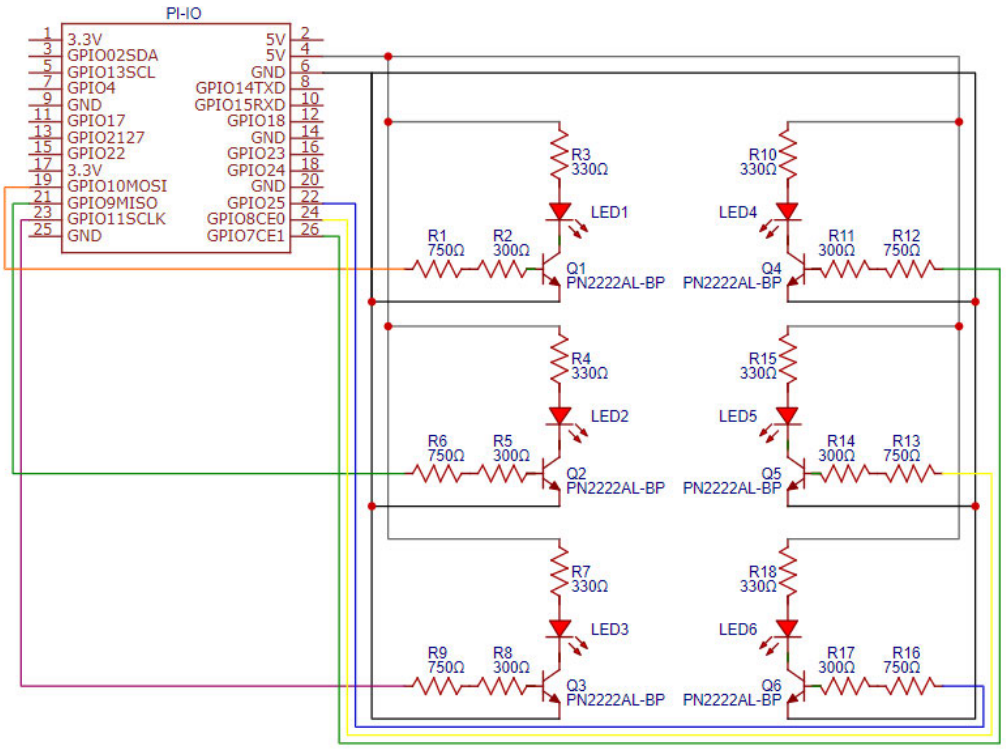

Figure 4-2 Circuit Schematic of LED test circuit

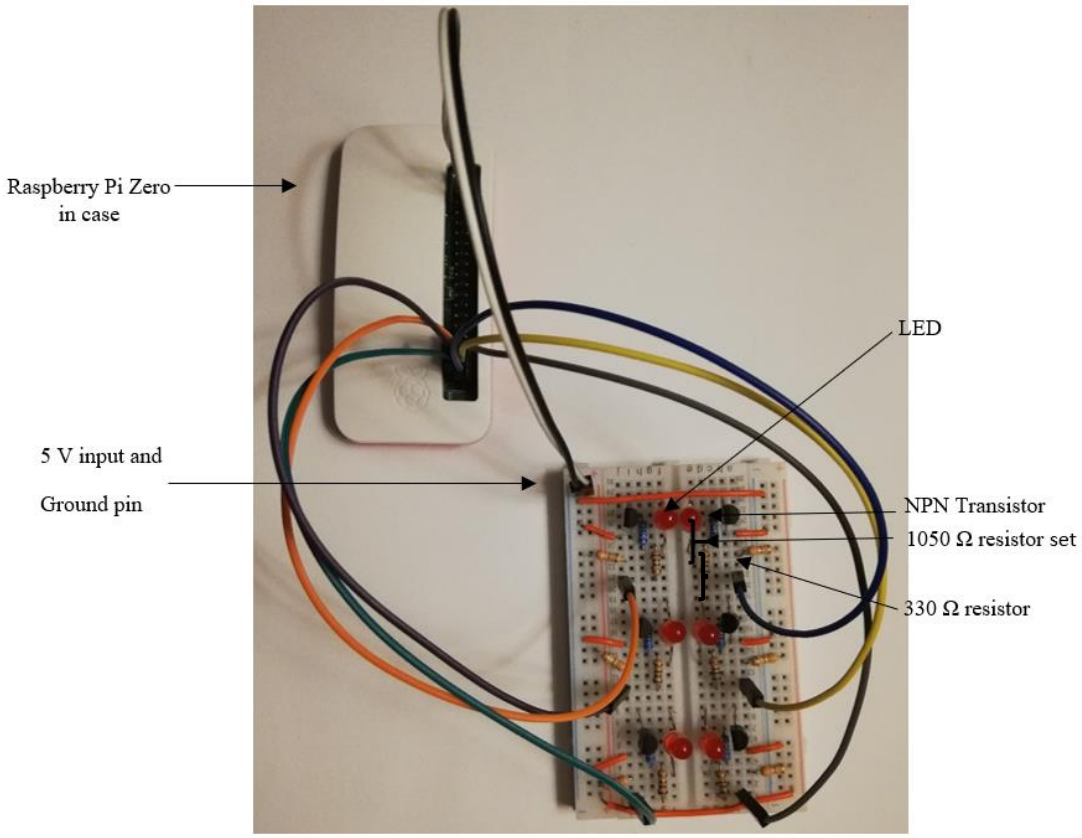

Figure 4-3 Physical test circuit

4.4 Raspberry Pi and OCR software setup

4.4.1 Preparing Raspberry Pi for OCR installation

In order to proceed with installing the required OCR programs, the Raspberry Pi had to first be prepared for installation by updating the operating system and downloading system pre-requisites.

All installation and setup commands were inputted using the Raspberry Pi Terminal.

The first stage was to ensure that the latest versions of all installed packages were available. To do this, the commands in Figure 4-4 were inputted in the terminal. Note the 1 and 2 seen in Figure 4-4 are only used as markers to link to comments and were not inputted on terminal.

```
1 sudo apt-get update
2 sudo apt-get upgrade
```

Figure 4-4 Terminal commands to update all installed packages

The OCR packages, particularly OpenCV, are notorious for requiring majority of the available disk space to run effectively. OpenCV itself requires approximately 5.5 Gigabytes [143]. In order to increase the total available memory on the system, unnecessary packages were removed by using the commands in lines 1 and 2 of Figure 4-5. Next, any unnecessary programs were removed using the command line 3 in Figure 4.5. Note, this specific line targeted the removal of the Wolfram application.

```
1 sudo apt-get clean
2 sudo apt-get autoremove
3 sudo apt-get purge wolfram-engine
```

Figure 4-5 Terminal commands to clean system

Both OpenCV and Tesseract were installed using Python's package manager known as pip. In order to commence with installation of the programs, pip was installed on the system using the code in Figure 4-6.

```
1 wget https://bootstrap.pypa.io/get-pip.py
2 sudo python3 get-pip.py
```

Figure 4-6 Terminal commands to install pip

4.4.2 OpenCV Installation

OpenCV required the installation of prerequisite packages to operate successfully. Figure 4-7 identifies the packages required and the commands that were used in installation.

```
1 sudo apt-get install libatlas-base-dev
2 sudo apt-get install libjasper-dev
3 sudo apt-get install libqtgui 4
4 sudo apt-get install libhdf5-dev
5 sudo apt-get install libilmbase-dev
6 sudo apt-get install libopenexr-dev
7 sudo apt-get install libqtwebkit4
```

Figure 4-7 Terminal commands to install prerequisite packages

Once the prerequisite packages were installed a virtual environment was created in which to install the OpenCV package. A virtual environment acts as an isolated, independent environment on the system. This allows the user to create multiple projects on the system with customized packages without interfering with existing projects and packages. In the case of the OCR sub-system, a virtual environment was used as a safety precaution in the event that the OpenCV package was incorrectly modified. This was necessary since this was the first time that the author was using the OpenCV and Tesseract packages. Prototype devices that follow will not require a virtual environment once a set installation and setup protocol has been established and the next step can therefore be omitted. Line 1 of Figure 4-8 indicates the command that was used to install the virtual environment python wrapper using pip.

```
1 pip install virtualenv virtualenvwrapper
```

Figure 4-8 Terminal commands to install virtual environment wrapper

Thereafter the profile known as ~/.bashrc required modification to allow access to the virtual environment, Figure 4-9. The first line indicates the command used to access the specific profile, lines 2 to 4 were then appended to the end of the ~/.bashrc scripts. Line 5 was used once the ~/.bashrc profile was saved and exited. The purpose of Line 5 was to source (or update) the changes in the terminal. Alternatively, the Raspberry Pi can be restarted to update changes.

```
1 nano ~/.bashrc
2 export WORKON_HOME=$HOME/.virtualenvs
3 export VIRTUALENVWRAPPER_PYTHON=/usr/bin/python3
4 source /usr/local/bin/virtualenvwrapper.sh
5 source ~/.bashrc
```

Figure 4-9 Terminal commands to access virtual environments

It was at this stage that the name of the specific virtual environment was specified. Note in the Line 1 of Figure 4-10, the addition of the characters ‘cv’, this was the name used to define the specific virtual environment that was during the OCR testing. Line 2 of Figure 4-10 indicates the command to access the ‘cv’ virtual environment and Line 3 is how the virtual environment can

be deactivated to return to the terminal once work on the environment is complete. It is possible to check if the correct virtual environment is activated by inspecting the command line prompt. In this case, the command line prompt will begin with ‘cv’ to indicate that the subdirectory is active, for example: ‘(cv) pi@raspberrypi:~ $’.

```
1 mkvirtualenv cv -p python3
2 workon cv
3 deactivate cv
```

Figure 4-10 Terminal commands when working with virtual environment

Working within the activated ‘cv’ virtual environment, the final command was inputted to install the full OpenCV package, Figure 4-11.

```
1 pip install opencv-python
```

Figure 4-11 Terminal command to install OpenCV package

4.4.3 Tesseract Installation

The tesseract installation was comprised of three steps as indicated in Figure 4-12; installing the Tesseract library (Line 1), installing command line tool (Line 2), and then installing the Tesseract Python wrapper (Line 3).

```
1 sudo apt install tesseract-ocr
2 sudo apt install libtesseract-dev
3 sudo pip install pytesseract
```

Figure 4-12 Terminal commands to install Tesseract

4.4.4 Verifying the Installations

The installations of the OpenCV and Tesseract packages were verified by inputting terminal requests to check the versions of the packages. If the packages were incorrectly installed or any prerequisite packages were not installed, then the versions would not be printed to the terminal.

The OpenCV installation was checked by inputting Lines 1, 2, 6 and 7 in Figure 4-13.

```
1 pi@raspberrypi:~ $ workon cv
2 (cv) pi@raspberrypi:~ $ python3
3 Python 3.7.3 (default, Jul 25 2020, 13:03:44)
4 [GCC 8.3.0] on linux
5 Type "help", "copyright", "credits" or "license" for more information.
6 >>> import cv2
7 >>> cv2.__version__
8 '4.4.0'
```

Figure 4-13 Terminal commands to verify OpenCV package

The Tesseract package was checked by inputting Line 1 of Figure 4-14 and receiving the output indicated in Lines 2-4. It must be noted that beyond confirming that the package is installed correctly by printing out the version number, the specific version also indicates the functionality of the installed package. In this case Tesseract 4 was installed which can perform neural network (LSTM) based OCR as well as access the older Legacy Tesseract Engine (Version 3 and older) [98]. The LSTM engine allows for the training of the system to improve accuracy of the OCR. It is possible to switch between the Legacy and LSTM engines if necessary, as discussed in section 4.5.

```
1 (cv) pi@raspberrypi:~ $ tesseract --version
2 tesseract 4.0.0
3 leptonica-1.76.0
4 libgif 5.1.4 : libjpeg 6b (libjpeg-turbo 1.5.2) : libpng 1.6.36 : libtiff
4.1.0 : zlib 1.2.11 : libwebp 0.6.1 : libopenjp2 2.3.0
```

Figure 4-14 Terminal commands to verify Tesseract

4.5 OCR Program Code

Once installation was complete, the final OCR program was written using Python's Integrated Development and Learning Environment (IDLE) and tested. The final program consisted of six primary functions:

- Import scanned image
- Pre-process image using OpenCV
- Perform OCR using Tesseract
- Print output characters to the screen
- Output braille equivalent of characters via GPIO pins
- Print total processing time to screen

The code represented in Figures 4-15 – 4-17 was used as the final OCR test program. The customizability of the code allowed for multiple tests to be run to analyse the performance of different components of the OpenCV and Tesseract programs. The discussion below details the specific functions of each section of the code in Figures 4-15 – 4-17.

Note: The Figures 4-15 – 4-17 present a condensed version of the final program code for ease of reference, refer to Appendix A.1 for full program code.

```
1 #processing time initialise

2 import time

3 start = time.process_time()

4 #import libraries

5 import re

6 import pytesseract

7 import cv2

8 from PIL import Image

9 import RPi.GPIO as GPIO

10 import os

12 #import image

13    img    =    cv2.imread('/home/pi/Pictures/Text    demo    images/single letters/Ariel/lower case/z.JPG',cv2.IMREAD_COLOR) #Open the image from which characters has to be recognized

14 #resize image

15 img = cv2.resize(img,(620,480))

16 #convert to gray to reduce details

17 gray = cv2.cvtColor(img, cv2.COLOR_BGR2GRAY)

18 #Blur to reduce noise

19 gray = cv2.bilateralFilter(gray, 11, 17, 17)

20 #use for multiple characters

21 #test = pytesseract.image_to_string(gray, config='')

22 #Specify psm and oem (psm 10 for single char identification)

23 custom_oem_psm_config = r"--oem 3 --psm 10"

24 test = pytesseract.image_to_string(gray, config=custom_oem_psm_config)

25 #Remove the line break symbol from output

26 pattern = re.compile('\W')

27 char = re.sub(pattern, '', test)
```

Figure 4-15 OCR Python Code

```
28 print (char)
29 #Get confidence level if required
30 #test = (pytesseract.image_to_data(gray, lang=None, config='', nice=0) )
31 #if you don't want line breaks removed
32 #print (test)
33 #check processing time of ocr only
34 print(time.process_time() - start)
35 #identify GPIO number (used 3 leds in this example)
36 GPIO.setmode(GPIO.BCM)
37 GPIO.setwarnings(False)
38 GPIO.setup(13,GPIO.OUT)
39 GPIO.setup(19,GPIO.OUT)
40 GPIO.setup(26,GPIO.OUT)
41 GPIO.setup(21,GPIO.OUT)
42 GPIO.setup(20,GPIO.OUT)
43 GPIO.setup(16,GPIO.OUT)
44 #represent using LEDs
45 read_sequence= (char)
46 seq_list = list(str(read_sequence))
47 for n in seq_list:
48 if n == 'A':
49        GPIO.output(13, GPIO.HIGH)
50        time.sleep(1)
51        GPIO.output(13, GPIO.LOW)
52       time.sleep(1)
53    if n == 'B':
54        GPIO.output(13, GPIO.HIGH)
55        GPIO.output(19, GPIO.HIGH)
```

Figure 4-16 OCR Python Code Continued

```
56        time.sleep(1)
57        GPIO.output(13, GPIO.LOW)
58        GPIO.output(19, GPIO.LOW)
59        time.sleep(1)
60    if n == 'C':
61        GPIO.output(13, GPIO.HIGH)
62        GPIO.output(21, GPIO.HIGH)
63        time.sleep(1)
64        GPIO.output(13, GPIO.LOW)
65        GPIO.output(21, GPIO.LOW)
66        time.sleep(1)
67 GPIO.cleanup()
68 #check processing time of entire operation
69 #print(time.process_time() - start)
```

Figure 4-17 OCR Python Code Continued

4.5.1 Processing time monitor

Line 2 of Figure 4-15 imported the time library to the OCR program. The following line established the start of the timer and was followed by the body of the OCR code. Two sections of code were included to stop the timer at two points of the program. Line 35 was included to measure the processing time of only the OCR functions of the program; therefore, it would measure from the moment the program was run to the point that the scanned characters were printed to the screen. The alternative option was provided in Line 69 to instead print the total processing time, including the time required to display the braille representation via LEDs. To display Line 69, the hash symbol at the start of the line was removed and a hash symbol was included at the start of Line 35 to disable the previous timer.

When testing the ASCII code to LED output as a standalone program it was noted that the processing time between program start and the first LED output was negligible with the LED outputs to follow being set at a specific time interval of 1 second. The specified time interval appeared in Line 50 of Figure 4-17 which utilized the time library and could be altered by adjusting the numerical value within the bracket to increase/decrease the interval. Therefore, it was concluded that the requirement for a displayed processing time of the full OCR process

including the LED display was not necessary since the LED display functioned according to a pre-set time interval specified by the user. Thus, the time display function in Line 35 was preferred during testing since this measured the unknown duration of scanned image to ASCII output and omitted the time duration of LED activation.

4.5.2 Import libraries

Lines 5 – 10 in Figure 4-15 indicate the libraries required to complete the OCR program. The time library was imported previously in Line 2, as discussed in section 4.6.1. The libraries include: Regular Expression module for string matching, the python Tesseract wrapper (pytesseract), OpenCV (cv2), the Imaging module from the Pillow library (PIL), the Raspberry Pi GPIO library and the miscellaneous operating system interfaces (os) was required to implement the GPIO sequencing.

4.6.3 Import image

Line 13 was used to import the test images. Once testing is complete, this line of code can be replaced by Figure 4.-18 which utilizes OpenCV to capture the camera image and prepare for preprocessing. Therefore, the camera input will automatically be fed into the program without having to manually import an image file.

```
1 import cv2
2 cam=cv2.VideoCapture(0)
3 img=cam.read()
4 cv2.namedwindow("camera", cv2.CV_WINDOW_AUTOSIZE)
5 cv2.imshow("camera",img)
6 cv2.waitKey(0)
7 cv2.destroywindow("camera")
```

Figure 4-18 Direct USB camera input to OCR program

4.5.3 Preprocessing of image

The preprocessing of the input image was completed in three stages; resize, greyscale and blur reduction. Line 13 of Figure 4-15 resized the image to 480 pixels by 620 pixels. Through converting the image to grey (Line 17), details were reduced and allowed for more accurate recognition. Blur reduction sharpened the characters of the image, Line 19.

4.6.5 Image processing using Tesseract

Lines 21 to 27 of Figure 4-15 consisted of the commands to process the image using the Tesseract OCR software. Line 21 was used when the recognition of images with multiple characters were required. As can be seen in the image, it is currently disabled in order to instead use the command

Lines 23 and 24. These commands were used when the Page Segmentation Modes (PSM) and OCR Engine Modes (OEM) required specification. The OEM specified whether the Legacy or Neural Network based OCR engines were required. The PSM indicated if the image contained a predicted set of characters and therefore controlled how Tesseract split the image into lines of text and words. The set of PSM modes are shown in Figure 4-19. The previously discussed command Line 21 of Figure 4-15 assumed a PSM of 1 for automatic page segmentation. If single characters are to be recognized, then a PSM of 10 is required for more accurate and faster results.

```
0    Orientation and script detection (OSD) only.
1    Automatic page segmentation with OSD.
2    Automatic page segmentation, but no OSD, or OCR.
3    Fully automatic page segmentation, but no OSD. (Default)
4    Assume a single column of text of variable sizes.
5    Assume a single uniform block of vertically aligned text.
6    Assume a single uniform block of text.
7    Treat the image as a single text line.
8    Treat the image as a single word.
9    Treat the image as a single word in a circle.
10   Treat the image as a single character.
11   Sparse text. Find as much text as possible in no particular order.
12   Sparse text with OSD.
13   Raw line. Treat the image as a single text line,
                  bypassing hacks that are Tesseract-specific.
```

Figure 4-19 PSM designations [144]

4.5.4 Print characters to screen

Lines 26 and 27 of Figure 4-15 removed any line breaks from the OCR output. The GPIO output commands were not programmed to indicate line breaks and could therefore be removed before the characters were printed.

Line 28 of Figure 4-16 printed the characters to the screen.

4.5.5 Represent braille combination of characters

The GPIO pins 13, 19, 26, 21 and 20 were configured for sequential response using the GPIO.setup command, as seen in Lines 38 – 43 in Figure 4-16. These pins corresponded with the pins connected to the LEDs in the circuit schematic, Figure 4-2. The general Raspberry Pi GPIO library and setup was used instead of the LED specific module illustrated in Figure 4-20. Therefore, the code need not be changed once the final relay controlled dielectric elastomer are connected to the OCR subsystem. The relays will respond to the same code as the LEDs that were used during testing.

```
1 from gpiozero import LED
```

Figure 4-20 Module reference for LED-specific control

Once the correct pins were configured, each number, lower case and upper-case letters were assigned a sequence of GPIO responses that corresponded with the braille representation of each character. Examples of this are Lines 48 through 66 of Figure 4-17. The time.sleep function that divides each character-sequence relationship is the time delay between each new character. This value can be customized according to reader preference. In the case of testing, the time interval between each character was set to 1 second.

Finally Line 67 resets the braille display after each character was represented and sets all outputs to zero or ‘off’.

This section established the purpose of each section of the program code. Chapter 4.6 will now describe the tests completed and results obtained using the referred OCR test program.

4.6 OCR Program Test Results

4.6.1 Structure of testing

A total of 5 experiments were run with the aim to test processing speed and accuracy of the OCR subsystem. In order to retain homogeneity within the tests, all test samples were arranged as the alphabet from A to Z. The variables that were changed were font, number of characters per sample, quality of scan image and lower case versus upper case.

Each image sample was uploaded to the OCR program using Line 13 of Figure 4-15. Thereafter, the code was run, and the processing time and output were recorded for analysis.

The alphabetic sequence of multiple character images was analysed under seven different conditions:

1. All pre-processing active with PSM automatically selected and remove line-break activated
2. Remove line-break deactivated
3. All pre-processing deactivated
4. PSM configured to 3, image resize deactivated
5. Blur deactivated
6. Greyscale deactivated.

Single character images were first processed by the system with all pre-processing activated. Then, should the output be inaccurate, each pre-processing command was toggled on or off to confirm if an accurate result can be achieved.

4.6.2 Results and analysis

The Table 4-1 below summarises the processing speed and percentage accuracy of the different Font and character sequence samples with all pre-processing functions activated. The accuracy was calculated as a percentage of characters correctly identified for each test sample. Full results of each test were tabulated in Appendix C.3.

Table 4-1 Results of OCR Testing

Test Sample Number	Multiple/Single Character Image	Font	Average Response Time (s)	Average Accuracy
1	Multiple	Ariel	7,016	100 %
2	Multiple	Serif	6,875	3.846 %
3	Multiple	Typewriter	9,162	88,46 %
4	Multiple	Times New Roman	6,953	100 %
All multiple character samples			**7,501**	**73 %**
5	Single	Ariel	5,696	84,62 %
6	Single	Serif	5,629	84,62 %
7	Single	Typewriter	5,781	34,62 %
8	Single	Times New Roman	5,663	80,77 %
All single character samples			**5,692**	**71,16 %**

Beyond the results indicated in Table 4-1, three lower case tests samples were also analysed to compare performance to the uppercase OCR results, Appendix C.3.1. Two of the samples contained multiple characters and were in fonts Ariel and Times New Roman, both produced an average accuracy of 100 % and response times of 6,599 s and 7,117 s respectively. The single character lower case test batch was in the Ariel font and produced an average accuracy of 38,46 % and an average response time of 5,638 s. Therefore, it can be concluded that the performance of the OCR when recognizing multiple characters in either upper or lower case remains consistent, however, the accuracy of recognizing single lowercase characters reduces by 45,24 %.

As indicated in Table 4-1 the average response time required to perform OCR of a single character was measured as 5,692 s. This far exceeded the required response time of maximum 0,418 seconds. In comparison, the multiple character samples (26 letters of the alphabet) produced an average response time of 7,501 s, therefore 0,288 s per character. Two possible solutions to the single character response time are discussed below.

The first option would be the implementation of a Raspberry Pi model possessing a processing speed greater than 1 GHz and a Random Access Memory (RAM) exceeding 512 MB. This will drastically improve performance; however, it will come at the cost of a larger design footprint that will impact the portability of the device. An alternative solution would be to scan sections of text at a time instead of single characters. This option would also ensure a higher OCR accuracy. Once the section of text is scanned, the user can still simulate the action of reading

traditional braille by moving their finger across the page, without the chance of inaccurate braille output. The implementation of such a system is further discussed in Chapter 7.

Table 4-2 compared the variance and standard deviation of multiple character and single character recognition tests. Table 4-2 was populated using the results of Table 4-1 to calculate the variance and standard deviation of all multiple character samples and all single character samples.

Table 4-2 Standard Deviation of Multiple versus Single Character Recognition Performance

Multiple/Single Character Samples	Average Response Time (s)	Time Response Variance (s)	Time Response Standard Deviation (s)	Average Accuracy	Accuracy Variance	Accuracy Standard Deviation
All multiple character samples	7,501	0,0005	0,0223	73 %	1619,684	40,245%
All single character samples	5,692	0,003	0,0565	71,16 %	447,467	21,153%

The variance and standard deviation results presented in Table 4-2 were calculated to assess the reliability of the OCR program under different conditions, with the variable in this case being font. The software response time standard deviation was calculated to be 0,0223 s for multiple character samples and 0,0565 s for a single character sample. Considering the average response time for multiple and single character samples were 7,501 s and 5,692 s, respectively, the magnitude of the standard deviation to the 10^{-2} power indicated a negligible variance between the results and the average performance. However, the standard deviation observed for the accuracy of the software displayed larger margins of error. A standard deviation of 40,245% was calculated for all multiple character samples. According to the data presented in Table 4-1, this was a result of the notably low accuracy of 3,846% when the Serif font multiple character sample was processed by the program. Similarly, the Typewriter font delivered a lower accuracy of 34,62% for the single character samples. In the case of the multiple character samples, the Serif font was chosen specifically for its structural divergence from the Arial and Cambria fonts which is known to perform best when sampled by the Tesseract OCR. Fortunately, Tesseract can be trained to recognise new fonts through the use of training data images. [98] According to Table C-39 in Appendix C, the primary reason for the poor recognition performance of the Typewriter font single characters is the image resize pre-processing function. Table C-39 indicated that the performance improved for 12 out of the 27 letters when image resize was deactivated. In conclusion, the increase in resolution and the Dots Per Inch (DPI) of the images was decreasing the accuracy of the image recognition. A possible solution is to include an auto-scale command in the code, which assesses the DPI of the existing image before rescaling to 620 by 480 pixels. Another possible reason for the poor performance of the image rescale command was the set pixel width and height dimensions which resulted in distortion of the original image. A possible solution would be to implement the following command in line 15 of the program code (Figure 4-15) instead of the existing rescale command. The line in Figure 4-21 will scale up the image

using a set fx and fy value instead of distorting the image to fit the exact 620x480 pixel resolution. [145]

```
15 img = cv2.resize(img, None, fx=2, fy=2, interpolation=cv2.INTER_CUBIC)
```

Figure 4-21 Updated Image Re-Scale Command

Further testing was completed on the impact of pre-processing, line-removal and PSM specification on the multiple character sample sets. Table 4-3 summarises the results of these experiments.

Table 4-3 Accuracy and response time of multiple character OCR testing under various pre-processing conditions

Font	**Ariel**		**Serif**		**Typewriter**		**Times New Roman**	
Description	Accuracy (%)	Response Time (s)	Accuracy (%)	Response Time (s)	Accuracy (%)	Response Time (s)	Accuracy (%)	Response Time (s)
All activated	100	7.0157	3,846	6.875	88,46	9,162	100	6.953
Line-removal deactivated	100	6.975	3,846	6.843	88,46	9.143	100	7.009
All pre-processing deactivated	100	4.734	3,846	4.438	76,92	4.772	100	4.724
PSM configured to 3	100	7.031	3,846	6.858	88,46	9.173	100	7.061
Blur deactivated	100	4.286	3,846	4.203	76,92	4.586	100	4.356
Gray deactivated	100	8.108	3,846	8.291	76,92	9.732	100	8.297
Image Resize deactivated	100	12.091	3,846	7.382	92,31	7.764	100	9.398
Average	100	7,177	3,846	6,413	84,064	7,762	100	6,828
Variance	0	5,633	0	1,978	39,869	4,109	0	1,829
Standard Deviation	0	2,373	0	1,406	6,314	2,027	0	1,352

The information presented in Table 4-3 indicated that the pre-processing is most useful in scenarios where the original character quality is reduced e.g., the typewriter text sample. Line removal had a marginal impact on processing time, however, the 10^{-1} ms effect did not sufficiently support the deactivation of the line-removal operation when compared to the advantages of remaining active. The deactivation of image resize increased the length of processing time of multiple character images, an interesting observation since the opposite was observed in single character recognition. Referring to Appendix C.3, it was noted that the deactivation of image resizing not only increased accuracy of most single character tests but also reduced the total processing time.

When considering the standard deviation of the results in table 4-3, the performance percentage deviation was considered marginal; however, notable variances were observed for the response time. The largest standard deviation recorded for response time was for the Ariel font samples. Since the results of the Ariel samples indicated that the accuracy would remain at 100% regardless of pre-processing functions, it could be concluded that pre-processing can be disabled for the sake of a faster response time. However, as indicated by the results of the Typewriter font, pre-processing is necessary to maintain the integrity of more structurally variant fonts. Since the device is intended for use on a wide range of printed mediums, the deviation in response time is a necessary sacrifice to maintain the accuracy of the OCR subsystem.

4.7 Chapter Summary

Chapter 4 discussed the implementation of the OCR subsystem and analysed the quality of the program output using a variety of samples including both single and multiple character images. The six-segment braille display was simulated using LEDs to ensure that the correct output was being represented.

The results indicated that the average time required to complete the OCR of a single character exceeded the maximum specified processing time by 5,272 s. This observation, along with the greater accuracy displayed by OCR of an image containing multiple characters suggest that scanning the printed page in segments and then delivering as sections of braille output would produce results that agreed with design specifications to a higher degree than single character recognition. Alternatively, a more expensive Raspberry Pi model such as the Pi 4 could be implemented to increase processing speed. However, replacing the existing microcomputer not only increases the cost of the design, but also presents a problem with maintaining a design footprint that can comfortably fit on the hand of the user. Therefore, it was concluded that a multiple line scanning approach would be more applicable to the proposed design.

5. EXPERIMENTAL MATERIAL SELECTION

5.1 Introduction

The variety of potential material choices to produce DEA technology introduces both advantages and disadvantages to the rate at which research in the field can progress. Advantages can be attributed to the ability to continuously find new materials that can target specific design requirements e.g., inexpensive designs, transparent sensors and actuators and highly customisable performance parameters. However, the disadvantage of having a variety of material options is the variety of new variables introduced alongside them. Thus, many of the initial equations used to predict the performance of DEA's are no longer valid. This is partially due to the assumption of ideal conditions but also due to the relationships predicted using particular elastomer and electrode materials. In order to establish updated numerical relationships and accurately predict the response of materials, it is necessary to conduct an experimental analysis of the specific materials to be implemented in the design.

The experimental analysis of the ideal elastomer and electrode materials to be used in the tactile display were divided into three sets of trials. The first trial compared two grades of graphite powder as potential electrodes, followed by the second trial which compared the VHB 4905 and VHB 4910 elastomer materials at various percentage pre-strain. The third trial acted as an iteration of the first by comparing the graphite powder with the best performance in the previous experiment to a carbon grease alternative.

Chapter 5 details the methodology and experimental results used to select the materials with which the final DEA's were synthesised.

5.2 Methodology

5.2.1 Materials

Two brands of carbon powder were selected to be used in the synthesis of the experimental samples of the first iteration of electrode testing. The first brand of graphite powder was Pressol lubricant graphite and sourced from a local supplier in South Africa [146]. This brand was selected due to its availability and low cost since it is commonly used in household and commercial lubrication of equipment. The second brand, Microfyne graphite powder lubricant, was ordered from an international supplier and consisted of 44-micron particles with a carbon content of 95% [147]. This brand was selected for its fine particle size and higher purity.

The two grades of acrylic elastomer materials used in the second set of tests were selected based on the research and conclusions recorded in Chapter 2.5. Both VHB 4905 and VHB 4910 were sourced in order to compare the properties of each under various percentages of pre-strain.

The second iteration of electrode testing consisted of the more successful graphite powder, Microfyne, and a common carbon grease known as MG Chemicals 846 carbon conductive grease, which was sourced from RS Components South Africa. This brand of carbon grease is marketed for use as a preventative measure against corrosion, mechanical wear and to improve electrical connections between loose, vibrating or irregularly shaped components [148].

Conductive copper tape was used as conductive connections between the electrodes and the experimental circuit. The copper tape was selected for to its low resistivity, which could therefore be neglected in the results of the experiments while providing an effective method to create a large surface area connection between the circuit and the electrode. A larger surface area was necessary to prevent a mechanical failure of the thin film by reducing the stress at the electrical contact. The contact surface area of the final design will be capable of reduction due to the mechanical stability provided by the protective elastomer layers, which sandwich the DEA and thus strengthen the inner film.

Each test consisted of two sample sets (A and B) to be compared. Eight sample sets were prepared in total, of which the composition is detailed in Table 5-1.

Table 5-1 Experimental Sample Composition

	Sample Set A	**Sample Set B**
	Trial 1: Electrode test first iteration	
1.	VHB 4905, Microfyne Powder, 300% pre-strain	VHB 4905, Pressol Powder, 300% pre-strain
	Trail 2: Elastomer and pre-strain test	
2.	VHB 4905, Microfyne Powder, 0% pre-strain	VHB 4910, Microfyne Powder, 0% pre-strain
3.	VHB 4905, Microfyne Powder, 200 % pre-strain	VHB 4910, Microfyne Powder, 200 % pre-strain
4.	VHB 4905, Microfyne Powder, 300 % pre-strain	VHB 4910, Microfyne Powder, 300 % pre-strain
	Trail 3: Electrode test second iteration	
5.	VHB 4910, Microfyne Powder, 300 % pre-strain	VHB 4910, Carbon Grease, 300% pre-strain

5.2.2 DEA experimental design

Three samples of each sample set were produced for testing. Each DEA was synthesized using the following method.

The VHB acrylic films were purchased in packs of pre-cut sections of 76 x 127 mm. One side of the film backing was peeled away, and a circle of predetermined diameter was marked in the centre of the section of tape. A stencil cut from sticker backing was used to mark off the circle.

The second layer of backing was peeled off and the film was stretched over a laser cut circular PVC frame. The markings on the film were used to determine the percentage of pre-strain by lining up the marked off points with the inner edge of the PVC frame. Therefore, the diameter of the circle marked on the film was calculated using the PVC frame diameter and the percentage of pre-strain required for each test. Once the marked circle was lined up with the inner edge of the frame, a second frame of equal diameter was secured on the opposite side of the film, allowing

the mechanism to be placed flat on a surface without risk of contaminating the adhesive film. A stencil cut from the film backing was then placed at the centre of the mechanism and the carbon powder was dusted onto the surface using a brush. The stencil allowed a section of powder to extend out from the circle as an arm to which the conductive copper tape was to be attached, seen in Figure 5-1. A piece of duct tape was then placed across the film and stencil, removing any excess carbon powder when peeled away. This ensured a more uniform electrode thickness and reduced the risk of smudging the edges of the electrode once the stencil was removed. Copper tape was then applied from the arm of the electrode to the edge of the frame where it would serve as the connection between the mechanism and the circuit.

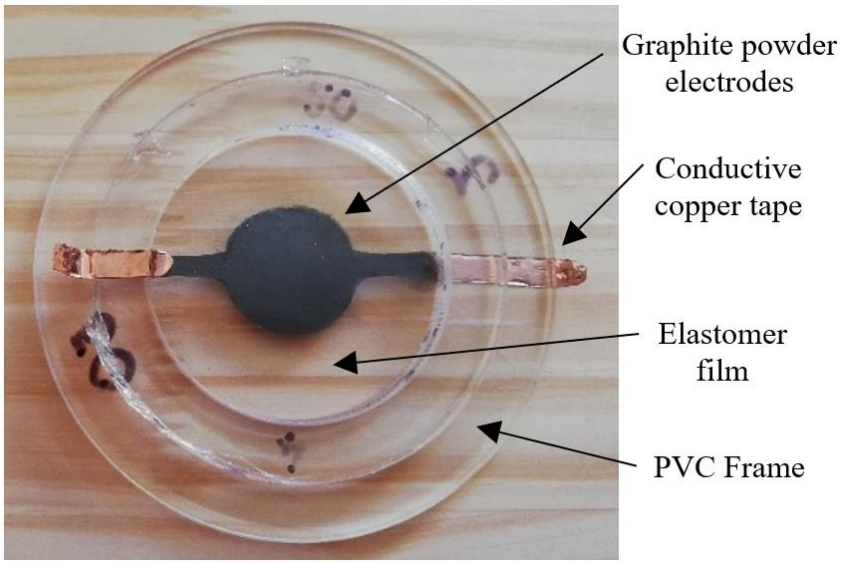

Figure 5-1 Completed graphite powder DEA sample

The application of the carbon grease electrodes followed a similar process as described above, however; the grease was applied using a cotton swab instead of a brush as used for the powder. The cotton swab allowed for a more controlled application procedure since the uniformity of the thickness of the electrode grease layer was affected by the pressure of the individual brush bristles. An image of a carbon grease sample connected to electrical circuit leads is illustrated in Figure 5-2. Additional images of the sample preparation are included in Appendix D.

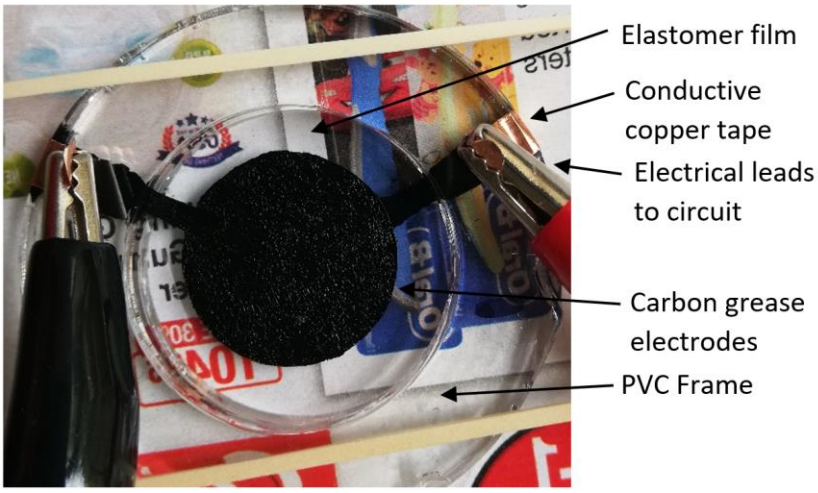

Figure 5-2 Completed carbon grease DEA sample

5.2.3 Electrical Design and Layout

The experimental circuit in the testing discussed in this chapter utilized a G series proportional DC to high voltage DC converter. This converter required a voltage input of 12V and provided a proportional output of maximum 5kV and a rated current output of 0.3mA at 1.5W. The G series DC to high voltage DC converter was purchased early in the design phase to be used during proof-of-concept testing. The final prototype will utilise the A series A50P-5 model which has a lower input voltage of 0-5 V and power rating of 1 W which will allow a more compact power source to be used. Figure 5-3 illustrates the final experimental circuit design.

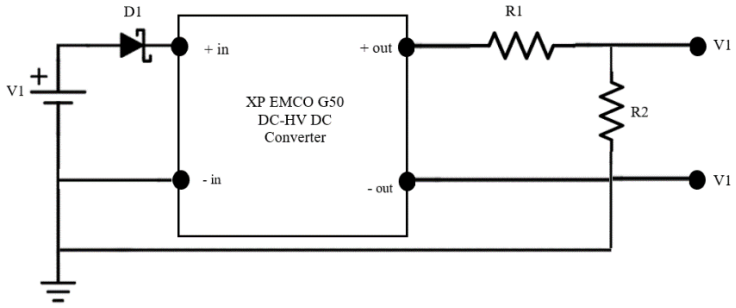

Figure 5-3 Experimental circuit design [75]

The converter divided the circuit into a low voltage (input) side and high voltage (output) side. The converter was equipped to isolate the input and output, however, due to the capacitive characteristics of the DE and the potential for arcing at high voltage, a further three components were implemented for circuit protection. A Schottky diode was included on the low voltage side of the circuit to act as reverse polarity protection should the converter be connected incorrectly, or the built-in input/output isolation fail. In order to protect the user from charge build up in the dielectric elastomer a resistor (R2) was connected in parallel to the output of the converter. This bleeder resistor served to discharge the high voltage capacitor (DE) after the circuit was turned

off. The application notes of the XP EMCO converter states that a bleeder current of less than 10% of the converter's rated output should be used to calculate the required resistance [62]. The subsequent calculation indicated that a 200MΩ resistor capable of withstanding 0.15W be selected as the bleeder resistor. The final component on the high voltage side consisted of a small resistor (R1) connected in series with the converter output. This limited peak current and protects the converter should high voltage arcing occur.

5.2.4 Experimental procedure

1. The sample was arranged on a flat surface and connected to the positive and negative terminals of the electrical test circuit. The variable power source remained switched off during set up.

2. A camera was set up a fixed vertical distance above the sample. Once the image was centered, the camera was secured to ensure it did not shift during testing.

3. The variable DC voltage source was set to 0 V and switched on. An image was taken of the sample.

4. The variable DC voltage source was then increased in intervals of 3 V from 0 V to 12 V with a photo taken by the overhead camera at each new voltage rating.

5. Once 12 V was reached, voltage was then decreased to 0 V in 3 V intervals. A photo was taken at each interval.

6. The above process was repeated three times for each sample.

7. The images were then uploaded to a laptop and arranged according to each test set.

8. Each image was then opened in the GIMP image manipulation software.

9. The image properties were set to grayscale and a filter was used to sharpen the image. This was done to reduce the effect of shadows and stray particulates on measured results.

10. The image was magnified to 400% and horizontal and vertical guides were placed tangential to the upper, lower, left and right points of the circular sample.

11. The number of pixels between each guide was measured and recorded on Microsoft Excel and the average was calculated.

12. Steps 8-11 was repeated for each image.

13. The virtual displacement was calculated by subtracting the pixel count at 0V from the pixel at each successive voltage input.

14. The displacement values were then used to the calculate the percentage strain of each sample at each voltage interval using the Equation 5-1 below where ε represents the strain, ΔL represents the change in length and L the original length.

$$\varepsilon = \frac{\Delta L}{L} \tag{5-1}$$

15. Graphs were produced using the resultant percentage strain values at 3V intervals between the input voltage of 0 V and 12 V.

Raw data and calculated displacement and strain values are recorded in Appendix A.1.

5.3 Experimental results

All results were recorded relative to the initial input voltage before being stepped up by the high voltage converter. Figure 5-4 illustrates the voltage output as a percentage of full output (5 kV) and can be used to identify projected output voltages [62]. Figure 5-5 illustrates an experimental analysis conducted of the input versus output voltages of the converter. Experimental output displayed a similar trend line; however, the experimental results were diverged from the theoretical values by approximately 6.6% at 2 V input and greater.

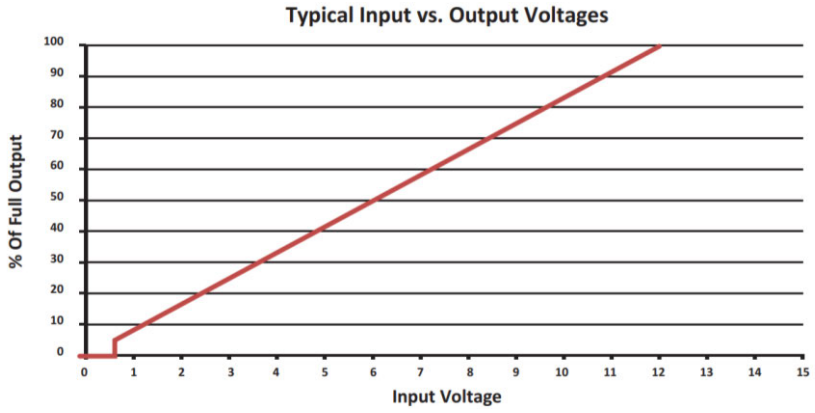

Figure 5-4 Typical Input vs. Output Voltages of an EMCO G50 DC-HV DC converter where full output is 5 kV [62]

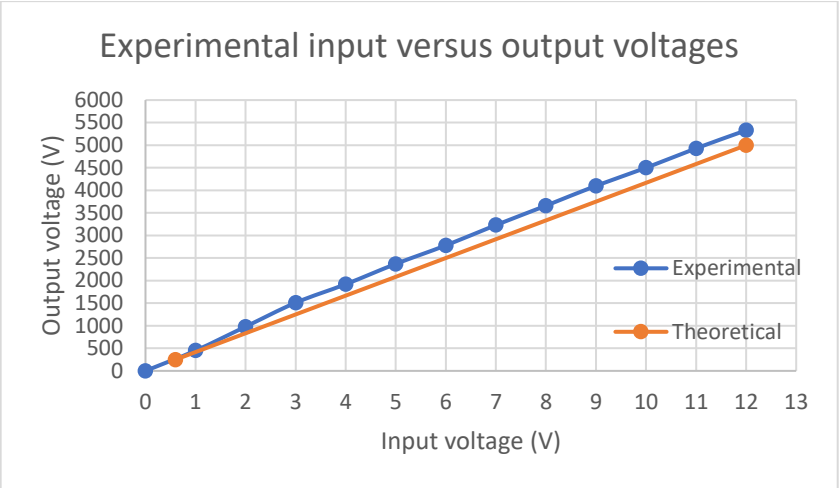

Figure 5-5 Experimental input versus output voltages

The graphical results were divided according to the division of trials stipulated in Table 5-1, where Trial 1 consisted of the first iteration of electrode material tests, Trial 2 consisted of elastomer and percentage pre-strain tests and Trial 3 consisted of the second iteration of electrode material tests. The graphical results of each trial are directly followed by an analysis and further comments on test results.

5.3.1 Graphical results of Trial 1

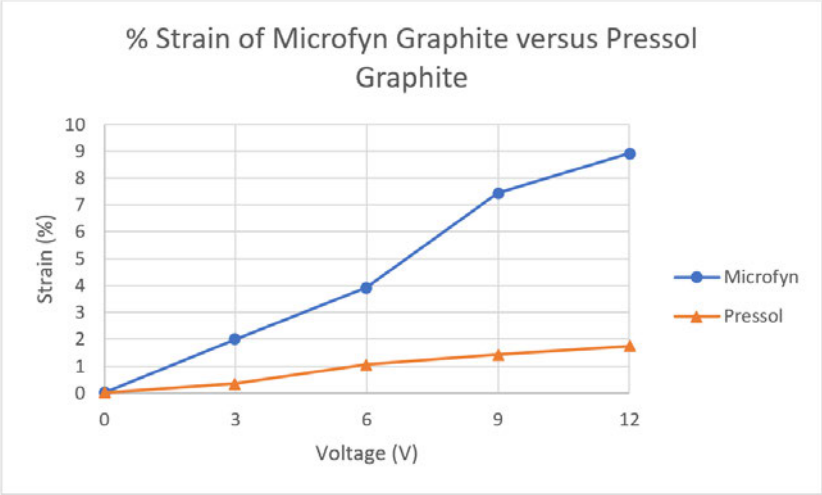

Figure 5-6 Graph comparing the percentage strain of the graphite powder brands Microfyne and Pressol

5.3.2 Analysis of Trial 1

Trial 1 consisted of comparing the Microfyne and Pressol graphite powders at various voltage inputs. As exhibited in Figure 5-6, it was determined that the Microfyne graphite samples exhibited a much larger average displacement than that of the Pressol samples. It could therefore be concluded that a finer grade carbon/graphite powder produced the best results. This agreed with the hypothesis that finer grade powders exhibit enhanced electrical conductivity properties. The Pressol samples also produced a non-uniform increase of electrode area. This could be

identified since individual particles were reflected by the light of the camera. Therefore, in the magnified images of a sample, the shift of individual particles around the centre of the electrodes was observed while the particles along the circumference, which was used to determine the percentage strain, produced little to no observable change in position for the same sample. In the aforementioned example, the patches of the electrode that exhibited larger area deformation were also observed to contain a higher population of particles, see Figure 5-7.

This observation motivated the decision to conduct the second iteration of electrode tests using carbon grease as an electrode for two reasons. The first reason being the presence of an adhesive (grease) medium in which the carbon particles are suspended. The medium allows for multiple layers of conductive carbon particles to be in contact with each other without the requirement for a large increase of overall sample thickness. Therefore, reducing the risk of electrode density thinning at the edges of the desired electrode shape.

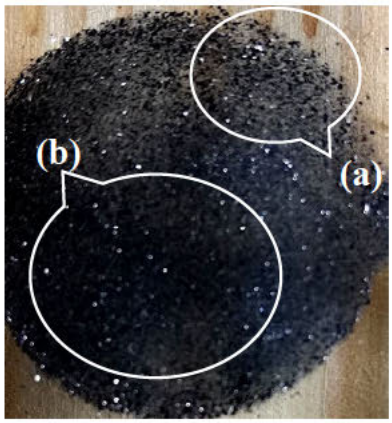

Figure 5-7 Pressol sample exhibiting non-uniform particle density; (a) Area of low density exhibiting negligeable strain response, (b) Area of high density exhibiting larger strain response

The second motivation for conducting carbon grease tests was to purposefully bias the strain reaction in a certain direction. The observation made in Figure 5-7 indicated that it is possible to generate a biased strain reaction to manipulate the direction and magnitude of strain produced in select areas of the DEA. Through controlling this arrangement of variable density sections, the achievement of larger strains may be possible, particularly in the out of plane direction required in the diaphragm type DEAs that were tested once acceptable electrode and elastomer materials were selected. Carbon grease is more conducive to testing this hypothesis since patterns could be drawn in the exposed electrode area without disrupting the conductivity of the lower layers of carbon, thus preventing an electrical short occurring along the thin film and causing mechanical rupture.

5.3.3 Graphical results of Trial 2

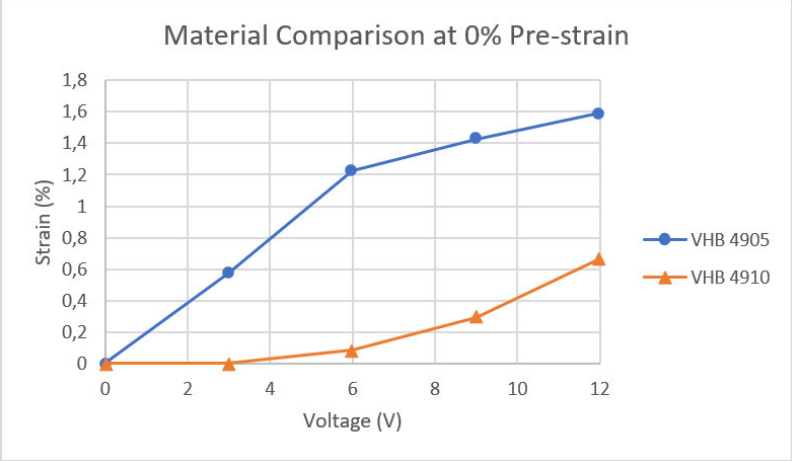

Figure 5-8 Graph representing the comparison of percentage strain of two elastomer materials (VHB 4910 and VHB 4905) at 0 % pre-strain

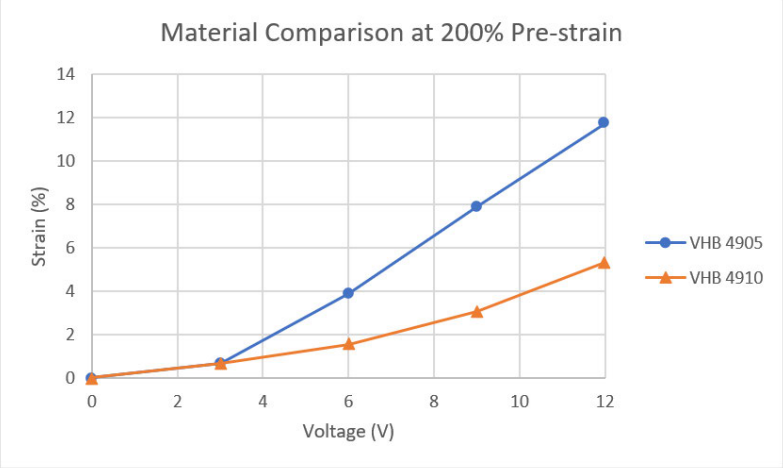

Figure 5-9 Graph representing the comparison of percentage strain of two elastomer materials (VHB 4910 and VHB 4905) at 200 % pre-strain

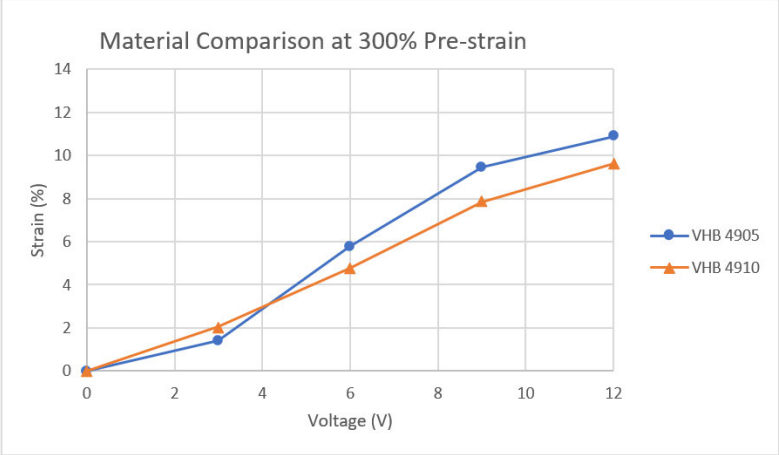

Figure 5-10 Graph representing the comparison of percentage strain of two elastomer materials (VHB 4910 and VHB 4905) at 300 % pre-strain

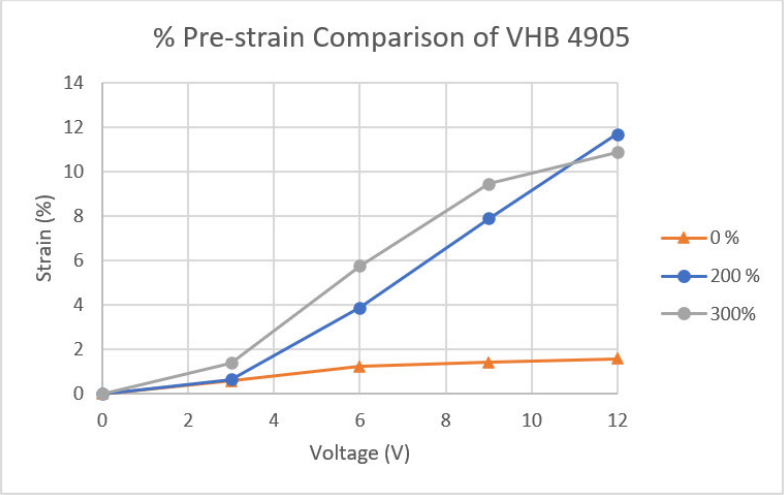

Figure 5-11 Graph representing the comparison of percentage strain of elastomer VHB 4905 at various pre-strain percentages

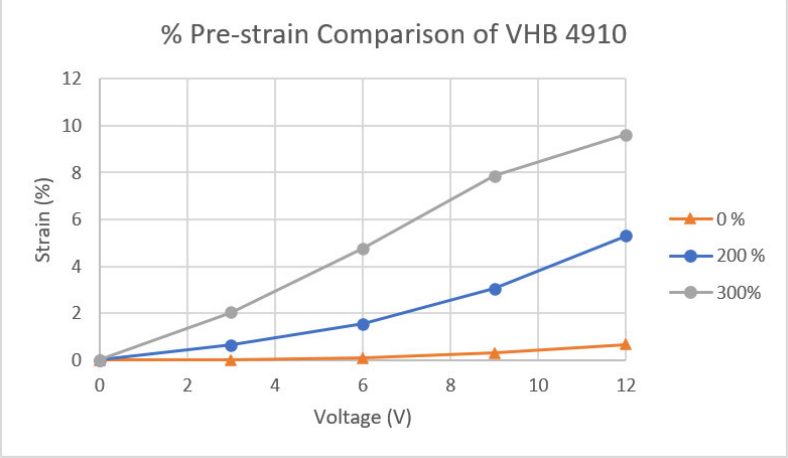

Figure 5-12 Graph representing the comparison of percentage strain of elastomer VHB 4910 at various pre-strain percentages

5.3.4 Analysis of Trial 2

Trial 2 investigated the performance of the two elastomer films at different percentages of pre-strain. Figure 5-8, Figure 5-9, and Figure 5-10 compared the behaviour of the two grades of elastomer films at 0%, 200% and 300% pre-strain. Figures 5-11 and 5-12 combined the graphical pre-strain results for each film type to determine the ideal pre-strain and to investigate the homogeneity of the film behaviour. The sample that produced the greatest displacement was the VHB 4905 with a Microfyne graphite electrode and a 200% pre-strain. However, throughout these experiments, the VHB 4910 film behaved most consistently and produced the most consistent relationship of curves at each increase of pre-strain. The characteristics of the VHB 4905 started to change drastically after the 200% pre-strain. The initial sample tested at 300% caused the VHB 4905 DEA to fail at 9V input, the second and third samples produced average displacements that

were smaller than the displacements achieved by the 200% pre-strain sample. This was most likely caused by the distortion of mechanical properties by the greater percentage of pre-strain. A high degree of pre-strain results in the elastomer no longer exhibiting constant volume properties and becoming susceptible to electromechanical instability, mechanical rupture and dielectric breakdown [52].

Therefore, taking the above behaviour into consideration, even though 200 % pre-strained VHB 4905 produced the largest average strain of 11,75 % at 5 kV input, it was prudent to select the 300 % pre-strained VHB 4910 with a maximum average strain of 9,61 % as the final elastomer choice. This decision was particularly influenced by the further pre-strain of an indeterminable percentage that the final sample will undergo during inflation to produce the diaphragm-type DEA. Thus, the stable 200 % pre-strain of the VHB 4905 will be altered and face a greater risk of failure under repeated load testing.

5.3.5 Graphical results of Trial 3

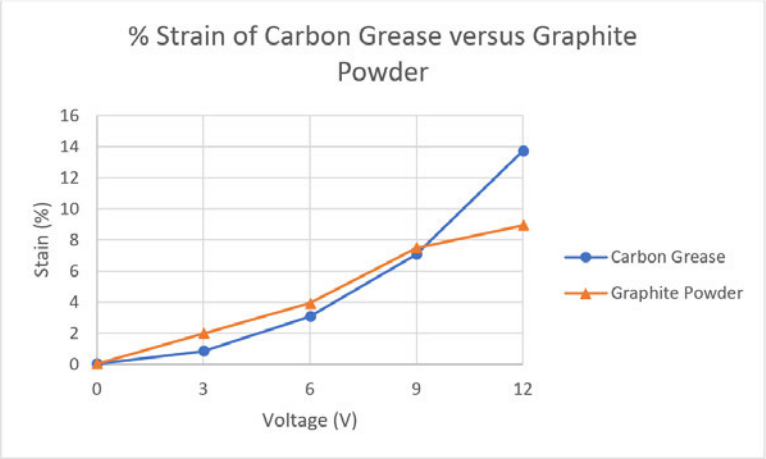

Figure 5-13 Graph comparing the percentage strain produced by electrode materials: MG Chemicals 846 carbon conductive grease and Microfyne graphite powder

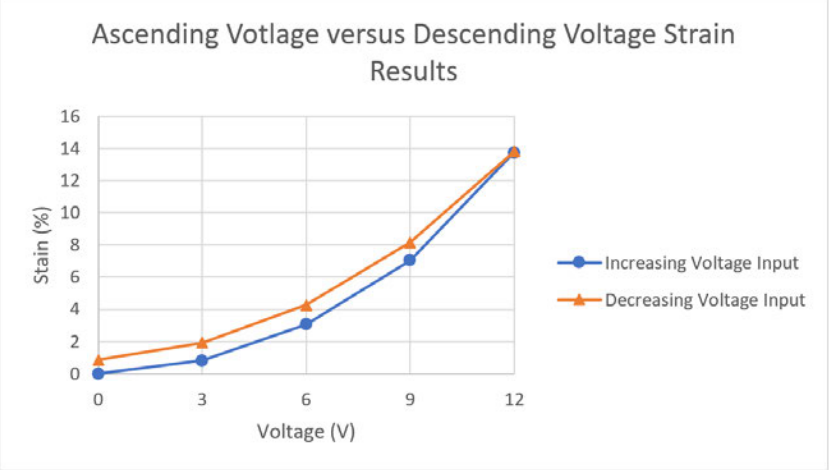

Figure 5-14 Graph comparing the strain results when measured in voltage intervals of 0 V to 12 V and 12 V to 0 V.

5.3.6 Analysis of Trial 3

Figure 5-13 depicts the graphical results of the carbon grease as compared to the Microfyne graphite powder. The comparison was made using VHB 4910 at 300 % pre-strain. The behaviour of the grease and powder electrodes were similar up to the 9 V input, at which the voltage was stepped up to approximately 3750V according to Figure 5-4. Thereafter, the grease samples demonstrated an exponential increase to produce an average strain of 13,73 % at 5000 kV as compared to the more linear curve of the graphite powder experiments which generated a maximum strain of 8,91 %.

Figure 5-14 illustrates an interesting mechanical phenomenon that was observed when comparing the displacement when increasing input from 0V to 12V to the corresponding displacement when decreasing voltage input from 12V to 0V. The percentage strain values when returning to 0 V were affected by the capacitive properties of the DEA and exhibited evidence of energy storage. This resulted in a final displacement of greater than 0 mm even when there was no voltage supply. This will cause problems in applications where extreme sensitivity to percentage strain during actuation is required and if samples undergo repeated loading within a short space of time. A possible solution to this would be to increase the resistance of the bleeder resistor that is positioned in parallel to the output. This will assist in draining the remaining charge from the DEA at an increased rate.

5.4 Chapter Summary

Various material selections for the elastomeric film and compliant electrodes were analysed experimentally, and the ideal combination was selected. The DEA material combination that exhibited the largest radial strain before the second iteration of testing was the VHB 4905 acrylic elastomer film with 200% pre-strain and Microfyne graphite as the electrode. This sample set produced a maximum strain of 11,75%. However, the unpredictable behaviour of the VHB 4905 at pre-strain greater than 200 % made this combination an unsuitable selection for an application where repeated loading and additional pre-strain will be experienced after DEA synthesis. Therefore the 300 % pre-strained VHB 4910 was selected as the final elastomer choice.

An observation made in the first iteration of electrode testing suggested that a second iteration of trials needed to be run using a carbon grease electrode. According to the analysis, the layers of conductive particulates within the grease matrix would improve the stability of electrode behaviour. On the same note, the malleability of the carbon grease could also be used advantageously in future experiments to produce biased strain results in sections of the electrode and favour larger displacements in the out-of-plane direction required during diaphragm-type DEA actuation. This was tested in the inflated test chapter.

When comparing the powder and grease electrodes, the grease samples produced a larger percentage strain of approximately 13,73 %. Therefore, indicating that the MG Chemicals 846 carbon grease electrode applied to a 300 % pre-strained VHB 4910 film would produce the greatest strain performance as compared to other materials in the series of tests.

Chapter 6 utilised the results of Chapter 5 to construct a scaled-up model of the DEA proof-of-concept. The performance of the model was analysed experimentally to determine if the proposed design was suitable for application as a refreshable braille display.

6. ANALYSIS OF ACTUATOR PERFORMANCE

6.1 Introduction

Chapter 6 details the experimental procedure followed, and results achieved during the testing of the proof-of-concept diaphragm DEA. The proof of concept consisted of a scaled version of a single braille dot to be implemented in the tactile braille display. The original refreshable braille dot size was enlarged 13,88 times in the 20 mm diameter proof of concept. The dimensions of the original refreshable braille dot included a base diameter of 1,44 mm and a nominal dot height of 0,48 mm. Therefore, the goal vertical displacement to be achieved in the following series of testing was 6,66 mm.

Two variables were adjusted and compared during testing. The first variable was the initial height of the inflated DEA before voltage was applied. The diaphragm DEA required a directional bias in order to control the direction of actuation, and this was achieved by injecting air into the cavity of the sample. The second variable to be tested was identified during the first series of strain experiments detailed in Chapter 5. It was observed that a non-uniform density of the compliant electrodes affected the strain of areas of the electrode. Upon assessment of this information, it was hypothesised that the magnitude of strain in selected directions could be manipulated by increasing or decreasing the thickness of areas of the electrode during synthesis to improve strain and displacement in the vertical or out-of-plane direction.

6.2 Methodology

Subsection 6.2 details the experimental design and procedure that was adhered to during testing. The experimental design included the synthesis of the proof of concept and the materials used.

6.2.1 Experimental design

The synthesis of the DEA film before assembly was visually recorded and included in Appendix D for further information. The procedure used to manufacture the DEA was similar to that used in the initial strain testing. The size of the electrode stencil differed from previous tests since the electrodes were now required to touch the inner diameter of the rigid frame to prevent outward strain in the radial direction. The following text and images describe the synthesis procedure of each sample used in actuator testing.

The VHB 4910 film was pre-stretched to 300% across a large Perspex frame. The 300% pre-stretch was achieved by marking off a circle on the film. The internal diameter of the Perspex frame was 300% the size of the marked circle. Therefore, when stretching the film across the frame, the marked points of the circle were lined up with the internal diameter of the Perspex frame. A non-adhesive mask was then applied to either side of the stretched elastomer surface.

The carbon conductive grease was applied on the unprotected areas of the film to produce 20 mm diameter electrodes. A cotton swab was used to apply the carbon conductive grease.

Three sample sets were synthesised using three methods of applying the carbon grease to the acrylic film. The first sample set was synthesised by stippling the carbon grease onto the film surface. The film was placed over a light source to ensure that the entire electrode area was covered. The second method of application involved smearing the carbon grease in a uniform direction across the exposed face. When applying this method to the opposite face of the film, care was taken to ensure that the direction of application corresponded with the initial face. The third method of application involved smearing the carbon grease from the radius toward the centre of the exposed face, thus creating a radial pattern within the grease electrode.

The mask was removed, and adhesive copper leads were attached to the elastomer. The rigid frames illustrated in Figure 6-1 were then applied to either side of the elastomer film. The device was removed from the pre-stretch frame by cutting away excess material. The rigid frames prevented the adhesive elastomer from contracting and returning to its unstretched shape. Once aligned, a pin or suitably sharp object was used to break through the areas of film located at the bolt holes of the frame. Care was taken during the placement of the rigid frames that the copper leads did not intersect the holes where the bolts were to be placed.

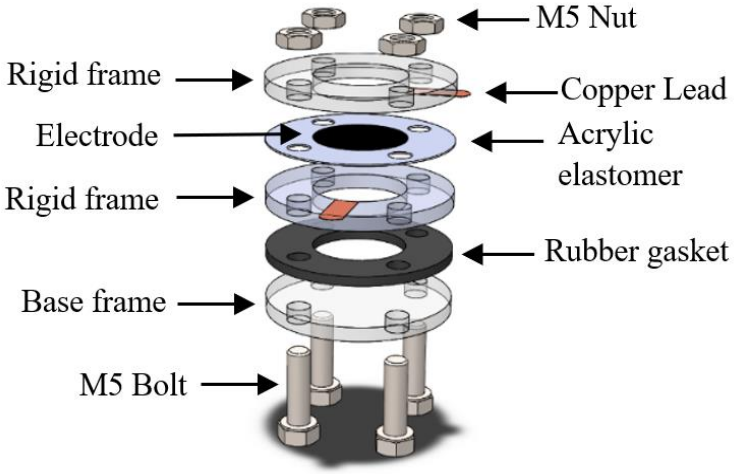

Figure 6-1 Exploded view of diaphragm DE [149]

The components were assembled to form the sealed cavity between the lower rigid frame and the base frame. A syringe was inserted between the base Perspex frame and rubber gasket to inflate the diaphragm, Figure 6-2. Once inflated to the correct initial height, the syringe was removed, the bolts tightened, and the sample attached to the electrical circuit via the copper leads and crocodile clips.

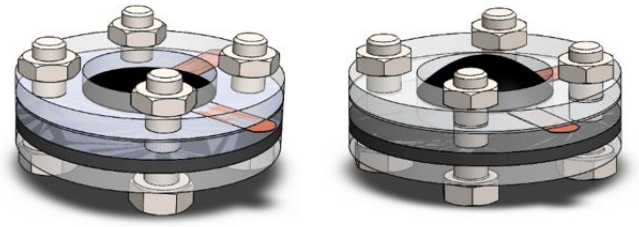

Figure 6-2 DEA assembly before and after inflation using syringe [149]

The final assembly of the diaphragm-shaped DEA is illustrated in Figure 6-3. This design represents the scaled proof of concept of a single braille cell. Additional images of the synthesis procedure are available in Appendix D.

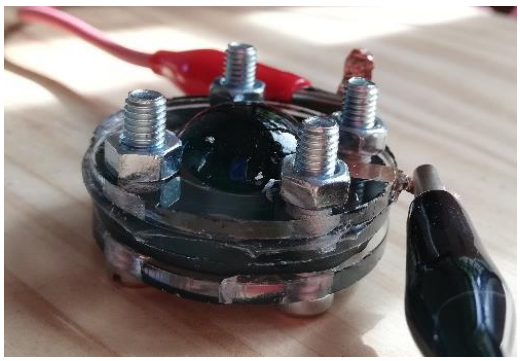

Figure 6-3 Diaphragm-shaped DEA prototype [149]

6.2.2 Experimental procedure

The experiments detailed in this chapter were conducted to investigate the effect of electrode application and initial diaphragm geometry on actuator performance. The variables of interest included the effect of initial diaphragm height and the method of non-homogenous electrode application.

The carbon grease electrodes were applied using three methods of application: stippled, smeared diagonally across the area and smeared from radius to centre of the area. The methods of application are discussed in Section 6.1.1. A fourth sample was investigated, which included a pre-strained VHB 4905 film as a protective layer on the convex side of the DEA.

Each sample was prepared, connected to the variable power source, and maximum displacement readings were recorded at 0V, 3V, 6V, 9V and 12V, respectively.

A camera was mounted alongside the specimen, and a photo was taken at each voltage interval. In order to ensure the camera was level, two pieces of ruled rigid card were attached at the foreground and back of the sample frame.

During the initial height tests, the sample would then be removed from the test rig, the bolts loosened to deflate the DEA and then the needle inserted between the layers to reinflate to the desired height.

6.3 Theoretical results

Using the Equation 2-12 derived in Chapter 2.4 a theoretical prediction of vertical displacement of the actuator could be calculated. Where a is the initial unactuated length or diameter, and δ_a is the induced strain in the lateral/radial direction.

$$h = \sqrt{\frac{(1-\delta_a)^3 a^2}{24\delta_a}} \left[1 - \cos\left(\frac{\sqrt{\frac{24\delta_a}{(1+\delta_a)}}}{2}\right)\right] \qquad 2\text{-}12$$

Variables were then substituted into the equation. A diameter of 20 mm was used, and the average displacement recorded at 5000 kV (12 V input) for carbon grease was taken from the previous set of test results. A final height of $1.474\ \mu m$ was generated using the equation. It must be noted that this calculation was only based on the geometric reaction of the DEA and does not consider variances in materials nor an initial height of greater than 0 mm.

$$h = \sqrt{\frac{(1-0{,}1373)^3 (20)^2}{24(0{,}1373)}} \left[1 - \cos\left(\frac{\sqrt{\frac{24(0{,}1373)}{(1+0{,}1373)}}}{2}\right)\right]$$

$$h = 13.36293\ (1.10322 \times 10^{-4})$$

$$h = 1.474 \times 10^{-3}\ mm$$

$$h = 1.474\ \mu m$$

6.4 Experimental results

The results of the experiments were recorded, and Figures 6-4 to 6-7 were graphed using the data. Raw data of the sample sets can be found in Appendix A.2. The voltage readings displayed on the figures were recorded from the variable power source interface. The output voltages at each can be extrapolated from the G50 model illustrated by Figure 5-4 in Chapter 5. The initial heights (Hi) indicated in the figures detail the maximum vertical displacement of the inflated diaphragm at 0V.

6.4.1 Graphical results

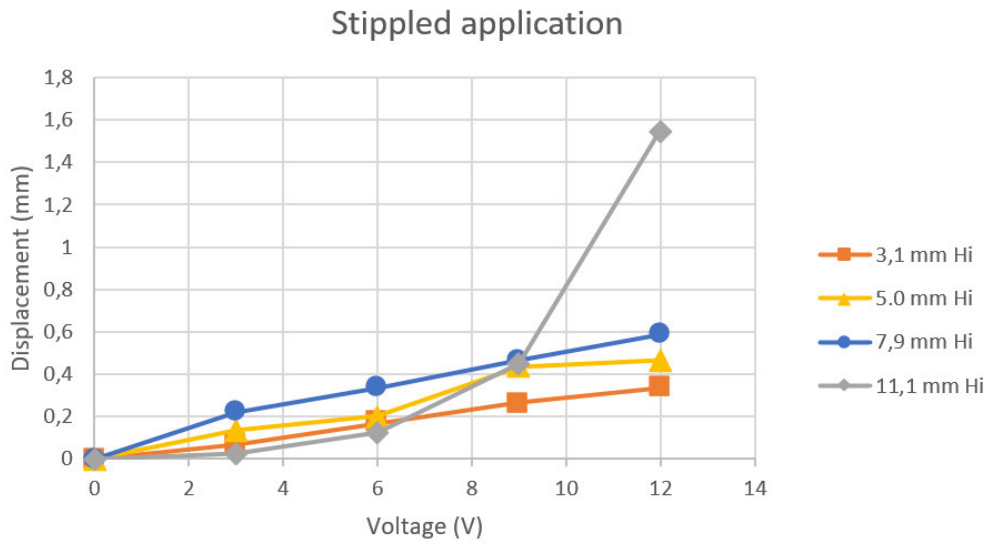

Figure 6-4 Maximum displacement of stippled DEA at various initial heights (Hi) versus input voltage [149]

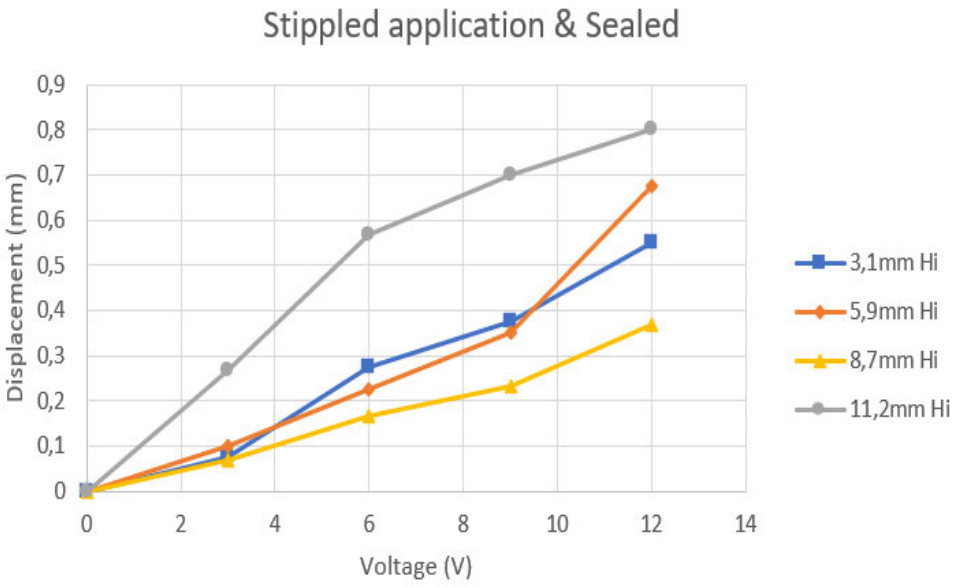

Figure 6-5 Maximum displacement of stippled and sealed DEA at various initial heights (Hi) versus input voltage [149]

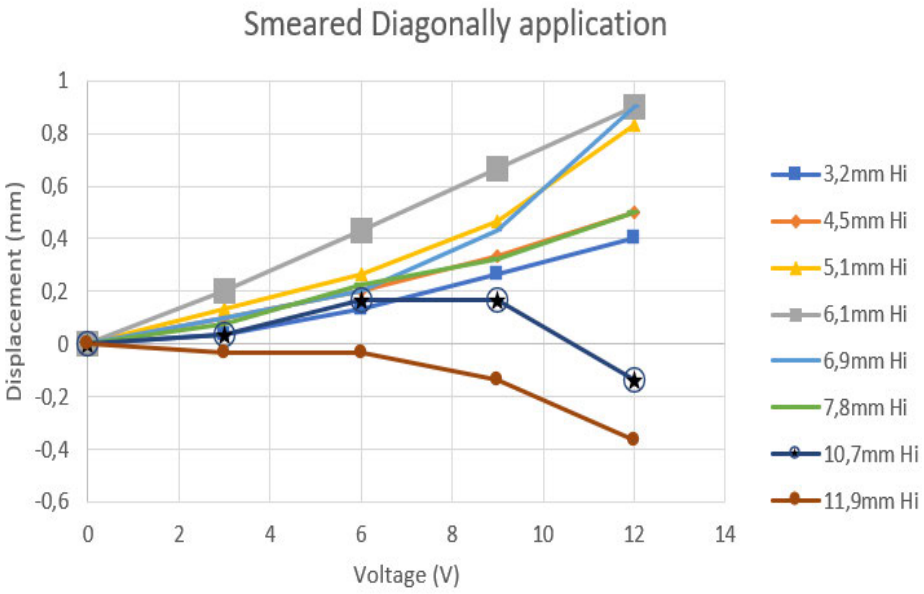

Figure 6-6 Maximum displacement of DEA with diagonally smeared electrode application at various initial heights (Hi) versus input voltage [149]

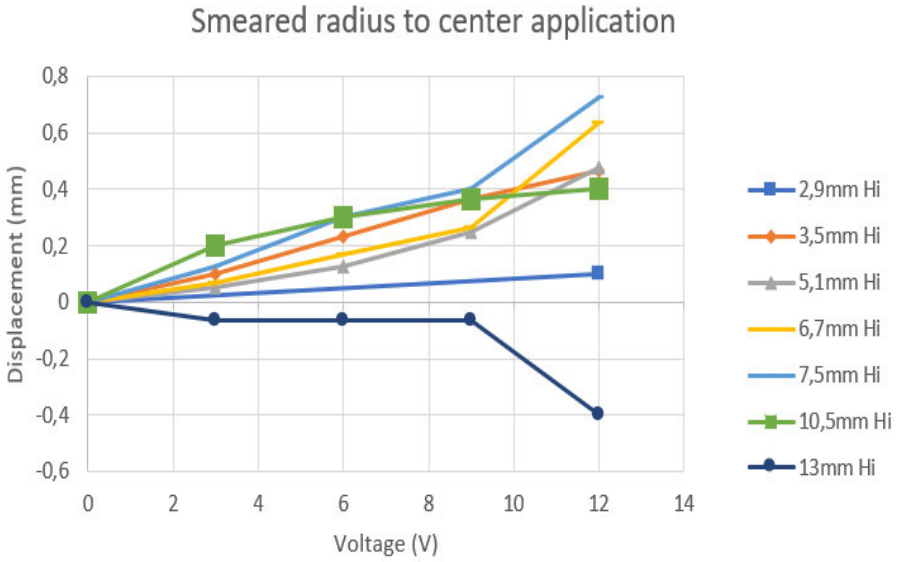

Figure 6-7 Maximum displacement of DEA with radially smeared electrode application at various initial heights (Hi) versus input voltage [149]

6.4.2 Analysis of results

All samples that were tested responded with an increase in strain when a voltage was applied to the compliant electrodes. Electrode application method and initial height had a marked effect on maximum displacement readings.

The stippled electrode application produced the largest displacement results at approximately 1,6 mm from initial diaphragm height. An increase in initial diaphragm height resulted in increased displacement values in the stippled sample. This observation was supported by the theoretical vertical displacement calculated at 12 V, which equalled to $1.474\ \mu m$ and was surpassed at all experimental initial heights that were greater than 0 mm. Therefore, an increase in initial height impacts positively on vertical displacement. The relationship between voltage increase and displacement was observed as linear at small initial height measurements. An exponential increase was observed at an initial height of 11.1mm.

A similar increase was noted in the stippled and sealed sample. However, the additional protective film stabilised the curve at the maximum initial height of 11.2mm. This stabilising force returned the behaviour to a linear relationship like those experienced at smaller initial heights. The more predictable behaviour due to the addition of the protective layer came at the cost of the maximum displacement being halved at 11.2mm initial height (0.8 mm).

The smeared samples produced similar maximum displacement readings of approximately 0,8mm. Contrary to the stippled sample, these maximum readings were not achieved at the maximum initial heights. Both the diagonally and radially smeared samples experienced non-uniform strain at larger initial heights. The samples continued to expand as a result of the increase of total electrode area; however, vertical displacement decreased. This indicated that these non-homogeneous application methods resulted in a displacement that was not in the radial direction of the diaphragm at larger voltage input values.

It can be observed that the maximum displacement curve of the stippled sample also favours a displacement direction that is not entirely dependent on the radial expansion of the diaphragm, thus creating the exponential curve. However, where the maximum curves of the smeared samples favour a latitudinal direction of expansion, the stippled sample favours a longitudinal direction of expansion.

Upon considering the application of the diaphragm and the requirement for larger vertical displacements, the behaviour of the stippled sample is preferred.

A further observation was made during testing, which involved the stability of the device and the conductive copper leads. Since the lead was adhered to the elastomer film and electrode after the electrode application, the carbon grease resulted in the delamination of the lead. As the lead

delaminated from the compliant electrode, an area of stress was created where the two conductive elements remained in contact. As this area decreased with each cycle of the DEA, the risk of voltage arcing increased. The voltage arc resulted in mechanical failure at the point of contact. Therefore, it is recommended in future tests that the copper lead be adhered to the elastomer film before the electrode is applied. The contact between the lead and film will prevent the delamination from occurring.

6.5 Chapter Summary

The experimental results agreed with the hypothesis that by altering the homogeneity of the electrode application, greater strain can be influenced in a specific direction of the DEA. It was further observed that an increase in initial diaphragm height resulted in the increased vertical displacement of the diaphragm. This observation was true for all application methods at small initial height values. The stippled sample demonstrated this behaviour at all initial height values while the smeared samples began favouring latitudinal displacement as the initial height increased beyond 10 mm. Therefore, the stippled carbon grease electrode application was selected to be implemented when producing miniature actuators that require displacements along the vertical axis. The presence of the protective elastomer layer on the convex face of the DEA reduced the maximum vertical displacement that could be achieved using the stipple application from 1,6 mm to 0,9 mm. However, the protective layer caused a stabilising effect on the DEA deflection curves and thus demonstrated that it not only protects the electrodes from environmental factors but also reduces the chance of elastomer matrix failure by controlling the exponential increase of vertical displacement as voltage input increases from 9 to 12 volts.

7. DISCUSSION

7.1 Introduction

The intention of this dissertation was to research and design a device that improved the accessibility of the blind and visually impaired in the workplace and education system. Chapter 7 provides an overview of the research and design work completed and discusses the validity of the proposed solution when compared to the objectives and research question. Further, proposed future work in the fields of diaphragm DEA development and portable text to braille transcription devices are discussed.

7.2 Overview of Research

7.2.1 Background and Literature Review

When considering the initial problem statement of how a mechatronic approach can improve the job accessibility crisis affecting the blind and visually impaired in South Africa, the first objective was to determine the principal reason behind the high unemployment statistics within the country for the research demographic. Research indicated that the lack of appropriate educational materials, techniques and equipment impacted the number of students capable of completing their schooling and achieving a matric certificate. Evidence of this was provided in the statement made by Khumalo et al. [11] that, of the 22 schools dedicated to the visually impaired in South Africa, 17 of those schools do not have access to the latest CAPS syllabus textbooks in braille. Therefore, the educational limitations placed on these students had a rollover effect on their probability of finding a job after completing their schooling. Evidence provided by affected individuals in successful careers indicated that access to funding and the availability of appropriate braille resources were significant contributors to their independence and job candidacy [12] [8] [11]. This information supported the conclusion that the ideal mechatronic approach to this situation was the provision of a low-cost portable device that allowed students to work with paper-based notes and textbooks provided by the department of education and public libraries. The economic situation of South Africa did not lend itself to working with digital sources since majority of specialised schools do not have access to sufficient number of computers and tablets for each student [11].

The next objective was the identification of an appropriate medium to which the printed or written text was to be transcribed. Commercially available devices were divided between audio output or braille output as possible options. The research conducted in Section 2.3 indicated that text-to-speech or audio output was the more common alternative. This was due to an interest in text-to-speech devices by both sighted and non-sighted individuals, thus expanding the target market and attracting commercial bodies to fund further development. There are numerous text-to-audio

scanning applications available for download on mobile devices free of charge [18], and most smartphones have voice-over technology specifically targeted to improve accessibility [19]. However, where audio output is more convenient, braille provides long-term advantages to the reader that transcends the immediate paragraph or line of text that requires transcription. Braille literacy provides the same cognitive development to readers as visual literacy to sighted individuals [24]. Braille literacy results in improved problem solving and socio-psychological behaviour and improves employment statistics by 40,35%, according to Ryles [28]. In light of the aim of this project targeting job accessibility and improved education quality, a braille output was selected as the transcription medium.

The third objective was to identify a haptic feedback system that would facilitate real-time text to braille transcription while meeting the requirements of the research question. Specifications of a refreshable braille cell were first collected before possible solutions were explored. Major specifications included the dimensions of the braille cell and a minimum touching force of 50 mN [45]. The primary challenge in selecting an appropriate actuation system was the degree of miniaturisation required to make the design portable while still meeting budget constraints. The majority of existing braille actuators consist of piezoelectrics; however, the drawbacks of these actuators include the high cost and the presence of auxiliary mechanics that limits further miniaturisation from the present configurations used in braille note-takers and readers. Pneumatic alternatives faced a similar limitation of miniaturisation due to the requirement for additional pressure control components. The requirement for such a large degree of miniaturisation introduced the flexile electroactive polymer known as dielectric elastomers. Dielectric elastomers produced competitive force and displacement results while allowing for a large degree of scalability due to the variety of possible material combinations and synthesis configurations. However, due to the variety of materials and corresponding properties, the mathematical approximations of strain results would not produce accurate results. Therefore, it was deemed necessary to conduct experimental analyses of the strain achieved when different elastomer and electrode materials were used. Beyond the discrepancy between true results and theoretical approximations another disadvantage presented by DEAs was the requirement for a high voltage input between 1000 V and 6000 V. Through further research this was deemed a simple challenge to overcome through the implementation of modern small-scale DC to high voltage DC converters along with the fact that a high current output was not necessary. The absence of a high current requirement resulted in an overall power rating that could be retained at 1 W, thus reducing battery demands and ensuring the user's safety. The DC to high voltage DC converter was sourced from XP EMCO [89].

The next objective was to identify the applicable software approach to complete the optical character recognition. Through further research, it was deemed that the OCR was achievable using

the open-source software known as Tesseract. Tesseract would be used in conjunction with Open-Source Computer Vision (Open CV) to perform the OCR and convert the digital characters into a voltage output corresponding to the six dots that make up the braille cell. The performance requirements, particularly the pre-processing of the image was reduced through the decision to use single character identification. Thus, reducing the computational load required of the pre-processor. The conversion from digital character to voltage output was achieved by assigning each ASCII character a corresponding 6-digit binary configuration.

7.2.2 Design of Mechanical Subsystem

The next research objective included the design of the mechanical, software and electrical subsystems to satisfy the summarised list of specifications of the design. This was completed by drawing up conceptual designs of potential DEA configurations and selecting the design best suited to the application. An inflated diaphragm type DEA was selected due to its low-cost synthesis techniques and scalability relative to other DEA designs. The resultant mechanical design consisted of a 3D printed mounting that slides onto the index finger, a series of six relays attached along the knuckles of a fingerless glove, a casing for the electrical components and a battery casing. The finger mounting contained the DEA tactile display embedded into the design beneath the tip of the finger and an endoscopic camera as the scanning hardware. An endoscopic camera was necessary to attain the shortest focal distance possible while maintaining a high-quality image. This was possible due to the small dimensions of the cylindrical camera module that allowed for an inobtrusive attachment and a minimum focal distance of 30 mm.

The design of the finger mounting was based on a simple mallet finger splint which allowed the camera module to be mounted along the crest of the medial phalanx and constrained the distal and medial phalanges along the same plane of rotation. This was necessary to provide the full range of movement of the proximal phalanx and corresponding joints as well as the freedom to adopt a natural braille reading position with the rest of the digits and hand posture. The conservation of the natural braille reading position of the hand was emphasised in order to ensure the comfort of the reader and maintain a high degree of proprioception present when reading traditional braille texts. Since natural reading techniques differ amongst individuals it was necessary to retain a large degree of freedom in all other joints of the hand and to design the mounting and camera module in as unobtrusive manner as possible to allow neighbouring fingers to rest in their natural reading position. The relays and electrical casings were designed with snap clips on the base of the components, the glove and the wrist strap; therefore, the position of components was modifiable depending on user preference and hand size. For example, should a child with a smaller dorsal palm area require use of the device, the electrical and battery casings can be stacked on top of each other and secured along the forearm directly behind the wrist. This

new position will relieve the load applied on the hand while maintaining flexibility in the wrist and between the metacarpals. The total cost of the synthesis and material of the mechanical design was calculated at R 1421.00 (Appendix B). However, this was the total cost of all materials that could be purchased in minimum quantities and resulted in a large amount of excess capable of producing multiple units. In order to calculate a more accurate cost approximation, the total number of samples cut from one pre-strained VHB 4910 tape section was used as a limiting factor. One unit of VHB 4910 tape was used to synthesise six 20mm DEA samples, and the pack contained a total of 25 VHB tape units. Therefore, the total mechanical component cost for one unit was approximately R 11,69 since 150 units could be manufactured from one pack of VHB 4910 tape.

7.2.3 Design of Electrical Subsystem

The electrical control posed a challenge to design since the system was limited to a single DC to high voltage DC converter to control all six braille dots. This limitation was placed upon the system since a single DC to high voltage DC converter cost approximately R4465,44. Therefore, it was necessary to control the high voltage side of the circuit using the Raspberry Pi. In order to achieve this, high voltage Pickering relays were used to allow the Raspberry Pi to control the high voltage output without destroying the sensitive circuitry of the single-board computer. The footprint of the Pickering relays negatively impacted the compactness of the design since it was not possible to mount the relays inside the electrical casing and required separate mountings. However, through using six relays instead of six separate DC to high voltage DC converters, the total cost of the device was reduced by R23 638,8. The total cost of the electrical subsystem equated to R 8953,04 (Appendix B). Therefore, the total cost of a single unit of the entire mechatronic design was calculated as R 8964,73.

7.2.4 Configuration and Testing of OCR Program

Thereafter, the Optical Character Recognition program was constructed and tested, as detailed in Chapter 4. The program required the installation and setup of two OCR engines; Tesseract and OpenCV. Once the software was installed and configured on the Raspberry Pi Zero, a test program was developed to analyse system performance. The variables under observation were the accuracy of the OCR and the response time of the subsystem. The system was tested using a simple six-segment LED circuit which served to simulate the braille interface response. The results disproved the hypothesis that single character OCR would require a shorter processing time than an image containing multiple characters. According to Table 4.1, the difference between the average response time of performing OCR on a single letter of the alphabet and all 26 letters at once was 1,809 s. This was negligible when considering the average response time of single character OCR measured at 5,692 s, which far exceeded a required maximum response time of 0,418 s. In

retrospect, the multiple character recognition tests produced superior results. This was proven by calculating the response time per character when all letters of the alphabet were scanned at once by dividing the total response time by 26. This produced a response time per character of 0,288 s, which fell within the required design specification. A response time standard deviation of 0,0223 s was observed in the multiple character sample sets when comparing different font types. This variance was considered negligible when compared to the average time of 5,692 s.

Of course, it was possible to increase single character OCR by selecting a microcomputer with a greater processing speed and RAM capabilities. However, this would come at the cost of decreased portability since the Raspberry Pi Zero W was specifically selected for its size. Therefore, it was preferable to retain the abovementioned microcomputer by adjusting the system to instead process multiple lines of text at once and then allow the reader to read the segment using the braille display before scanning the next section of the page.

Such a system design would be possible through the addition of a secondary finger mounting on the left index finger. This Secondary Mounting (SM) will be used to create a reference point around which the Primary Mounting (PM) on the right hand will operate. Through the application of a sensor system such as electromagnetic tracking, the position of the PM will be measured according to the transmitter attached to the SM. The purpose of tracking the PM is to ensure that the page of printed text is scanned in segments without repeating or missing lines of text. The electromagnetic tracking system will operate based on the range of the camera module and calculate the required number of segments and position of PM relative to SM to scan each section. This type of multiple character scanning system would also allow the user to scroll their right index finger along the text as they would when reading traditional braille printed books. However, now the reader would no longer have to cautious of moving between lines of printed text since the braille interface is delivering a pre-scanned section of text and not relying on the camera during the hand movement.

7.2.5 Analysis of Actuator Performance

The final objective required the haptic feedback subsystem to be tested and analysed to ensure it met the requirements of the design. Two sets of experiments were conducted. The first tested various materials and degrees of percentage pre-strain in order to determine the elastomer and electrode materials best suited to the design. The second set of testing analysed the performance of a scaled proof of concept of the diaphragm type DEA and compared the resultant vertical displacements under different synthesis conditions.

The first round of testing determined that the best performing electrode material relative to the test group was MG Chemicals 846 carbon grease which produced a total strain of 13,73%. However, this was 8,65 % smaller than the projected theoretical strain [53]. Observations made

during testing indicated that percentage strain results could be biased in a specific direction if the patterning of electrode application were adjusted; this was further explored in the second round of inflated tests. Pre-straining the VHB 4905 to 300 % resulted in mechanical failures at full load, specifically at the edges of the electrode. Further, the percentage strain results presented by VHB 4905 at 300 % pre-strain differed from the curves at lower pre-strain values. This agreed with the observations presented by Pei et al. [150], which recorded that the induced electric field had a non-linear effect on the VHB 4905 grade and was therefore not recommended as the DEA elastomer matrix. Therefore, it was concluded that the VHB 4910 elastomer at 300% pre-strain was the more reliable option, even though there was a small percentage of strain reduction of 2,14% as compared to the VHB 4905 results.

The second round of testing analysed the performance of a scaled proof of concept design of a single inflated braille dot or diaphragm DEA. The diameter of the scaled test sample was 20 mm and therefore 13,88 times larger than the diameter of the average braille cell. The analysis also compared the effect of the initial height of diaphragm inflation on the resultant vertical displacement as well as the impact of non-uniform electrode preparation. Biased displacement in the vertical direction could not be achieved, however, smeared samples were observed to favour latitudinal displacement at higher voltage inputs. The more uniform stippled application method produced the largest vertical displacements of average 1,6 mm from an initial inflated height of 11,1 mm. The experimental results confirmed that an increase in initial height positively impacted the vertical displacements and resulted in overall performance that exceeded the calculated 1.474 µm at 0 mm initial height. However, the largest recorded displacement, once scaled down by 13.88, did not achieve the required 0,48 mm displacement common in refreshable braille cells. Once the scale ratio was applied, the stippled results would produce a predicted maximum displacement of 0.115 mm. It can be argued that, even though nominal dot height is 0,48 mm, the maximum displacement required to stimulate the shallowest mechanoreceptor is 0,25 mm [45]. If this displacement is considered the benchmark, then the maximum experimental result of the proof of concept must only increase from 1,6 mm to 2,34 mm to attain the required vertical displacement once scaled down. According to literature, the required vertical displacement of the refreshable braille dot can be achieved using DEA technology, however, it will increase the cost of the design materials and synthesis procedures, thus impacting the low-cost design objective. On the contrary, it can be argued that, since the current design cost of R 8 964,73 is significantly lower than the nearest competitor at R 20 187,17 there is still a high chance that a more expensive synthesis procedure will fall within the required budget [38]. Alternative synthesis procedures to improve the design and achieve the intended vertical displacement are explored in Section 7.3.

7.3 Future work in diaphragm-type DEA synthesis

The major research area to be covered in future research is the increase of actuated diaphragm DEA height. A possible solution could be applied by stacking multiple DEA layers to increase the displacement at a decreased driving voltage [56]. The VHB films do not lend themselves to conformal stacking due to the risk of air bubbles and inconsistent adhesion. Therefore, it is more common to see silicone elastomers be used in stacked configurations. Silicone elastomers can be spin-coated from a liquid form onto previous layers to a predetermined thickness. In order to achieve this method of synthesis, a spin coating machine must be sourced and factored into production costs.

It must be noted that the electrode material used in the diaphragm DEA experiments was selected for its low cost, availability in South Africa and ease of manual synthesis to produce multiple samples. Carbon solutions using highly electro-conductive and more expensive electrode materials such as Ketjenblack will produce improved displacement results [65]. The resistivity of Ketjenblack decreases as the network of particles increases in density [151]. Therefore, a matrix is required within which to suspend the particles and improve conductivity, similar to the approach used in the MG Chemicals 846 carbon grease used in the experiments recorded in Chapter 5. However, where MG Chemicals 846 exhibited a resistivity of 114 Ω·cm, Ketjenblack suspended in a polydimethylsiloxane elastomer (PDMS) exhibited a resistivity of $\approx 10^{-2}$ Ω·cm, thus indicating the superior conductive properties of Ketjenblack [148] [151]. The approximate cost difference between 50g of Ketjenblack powder (without PDMS matrix) and an 80g tube of MG Chemicals Carbon Grease was R466,35 [152] [153]. Therefore, spin-coated PDMS elastomer layers and Ketjenblack based electrodes will be analysed in future work to determine if the increased DEA displacement performance justifies the additional costs.

7.4 Future work in the development of a portable text to braille transcription device

Once the required vertical displacement has been achieved, the diameter of the prototype sample will be reduced to 1,5mm which will simulate the true size of the actuators present in the braille cell. Testing will then be conducted in conjunction with scanning hardware and optical character recognition software to transcribe written text to braille using the actuated interface. These tests will allow the reaction time of a hand-mounted braille reading device to be analysed and determine if the DEA braille interface is a feasible solution to the lack of braille printed books and media.

Future prototypes can combine a line tracking system with the current feedback system and an additional finger mounting on the left hand. The alert feedback could include a vibration system above and below the braille interface to indicate the direction of path correction. Since high

voltage components will not be required in the secondary system, the cost of the additional finger mounting and supporting electronics will be a feasible design addition.

7.5 Chapter Summary

Chapter 7 detailed a concise discussion on the research dissertation and linked to the objectives set out in Chapter 1.5. The conclusions drawn from the literature review were analysed against the first four objectives. Thereafter, the mechanical, electrical and software subsystem designs were discussed. A possible solution to the delayed processing time of single character OCR was explored in Section 7.2.4. Notable results of the OCR testing, material selection experiments and the actuator performance analyses were discussed with reference to the design specifications stipulated in Chapter 3.1. Future work in the Mechatronic device and the field of dielectric elastomers were explored.

8. CONCLUSION

8.1 Introduction

This chapter serves to conclude the research dissertation and emphasise the research contribution, insights, limitations, and recommendations that were established over the course of the project. Future work on the device and within the field of dielectric elastomers is summarised.

The dissertation addressed how a mechatronic system could be implemented to improve the accessibility of the blind and visually impaired in the workplace and education system. The mechatronic solution included a printed text to braille transcription device that utilised OCR software and a DEA braille display. The device was required to be portable, lightweight, robust, and designed to address the economic limitations of the target market.

8.2 Research Contribution

The research targeted three previously ill-defined areas of research. The first research area included the identification of how information and printed media could be made available to visually impaired school-age students in a cost-effective manner. Previous devices and solutions were financially inaccessible to majority of the blind demographic of South Africa, thus resulting in 97% of the population being unemployed [1]. An absence of accessible learning material and infrastructure in schools resulted in majority of students leaving before completing Grade 12. The proposed solution was comprised of a low cost, portable text to braille transcription device.

The next research contribution included the development of miniature actuators that could pose as a competitor to the exceedingly expensive piezoelectric actuators that dominated the refreshable braille market. A novel dielectric elastomer-based actuator was proposed which could compete with the maximum force and strain performance of piezoelectric actuators while retaining a lower cost due to the robust structure and materials required. The total cost of a single DEA braille device was approximated at R 8 964,73, which was significantly lower than the closest priced commercially available refreshable braille device valued at R 20 187,17 [38].

The final research contribution included the experimental investigation of the ideal synthesis and structure of the DEA to achieve the required vertical strain while maintaining the dimensional requirements of a traditional braille cell. This was accomplished through a series of iterative experiments. The first set explored the synthesis of the DEA braille cell using various low-cost materials. Once appropriate materials were selected, the second set of experiments examined the performance of the final proof of concept.

8.3 Insights of novel DEA text to braille device

The research completed provided valuable insights into both DEAs as a subsystem and how it can be implemented in a single system to provide a tactile response. Notable insights gained from the research included how a high voltage control circuit could be designed to produce a 5 kV output while retaining portability and ensure the safety of the user. This was made possible by the small footprint XP-EMCO DC to high voltage DC converters and a high voltage relay control system. A further insight gained was the execution of text-based OCR using a 65 mm x 30 mm Raspberry Pi Zero W through the implementation of a customised Tesseract-OpenCV OCR engine to achieve accurate results.

Insights specific to DEA operation included the control of actuator deflection and direction using a rigid boundary and inflated cavity. A second insight was derived through experimental observation, which included the impact of carbon grease application methods on strain direction. It was observed that radial strain could be biased to favour a longitudinal or latitudinal direction of expansion by applying a non-homogenous coating of carbon grease during electrode synthesis.

8.4 Limitations of research

Limitations of research included having to conduct research under Covid-19 National Lockdown conditions. The Lockdown restricted access to equipment that was required to assist with the synthesis of DEAs. Particularly, spin coating machinery to synthesise thin elastomer films and laser ablation facilities that could present an alternative approach to graphite powder application. However, the Lockdown also presented the opportunity to investigate what degree of DEA performance could be achieved using samples prepared entirely by hand.

The sourcing and delivery of internationally supplied high voltage relays and the endoscope camera module were also impacted by the global travel regulations. In order to circumvent the effect this would have had on collecting experimental data, a “visual” braille display output was simulated using LEDs during OCR performance testing. This allowed the GPIO output to be monitored and ensured that the correct code was being implemented. The program code was constructed in such a manner that the LED test circuit could be interchanged with the final relay-DEA circuit without any adjustments to the existing code.

8.5 Recommendations

The aim of the research project was to investigate, design and analyse the validity of a portable, low-cost text to braille transcription device as a solution to the lack of accessible information available to the visually impaired.

All objectives specified at the outset to fulfil this aim were achieved; however, the diaphragm-type DEA failed to achieve the required vertical displacement required of a refreshable braille cell. Therefore, it was recommended that future research be conducted on alternative material and synthesis procedures of the DEA to meet specifications.

It was further recommended that electrode applications methods that achieved a greater degree of homogenous carbon dispersion across the elastomer film were investigated.

8.6 Future Work

Future work includes the following areas of research. The investigation of the structural changes to the diaphragm DEA synthesis in order to achieve an increased actuated height. This includes alternative elastomer materials with properties that allow for the stacking of multiple layers. Alternative electrode materials can also be explored; however, this should be limited to circumstances in which the aim of the project is not dependent on a low-cost design. Electrode materials such as Ketjenblack will provide improved performance but are significantly more expensive than the materials used in this research project.

Future work is also suggested in the to-scale prototyping of the proposed text to braille transcription device. The introduction of an additional finger mounting on the left hand would allow for more accurate line tracking and page segmentation by providing a point of reference to the right finger mounting. This would be particularly useful in the circumstance where multiple character recognition of sections of text is being performed to increase the OCR processing speed. This would improve the reaction time of the scanning subsystem and ensure that inaccuracies are not encountered by the reader accidentally skipping lines of text. Additionally, the accuracy of multiple line OCR can be improved by training the Tesseract software to recognize less common fonts, such as the Serif font used during the experimental analysis of the OCR subsystem.

8.7 Chapter Summary

Chapter 8 concluded the research dissertation and summarised key elements of the project. A portable, low-cost text to braille transcription device was researched and designed as a possible solution to the lack of accessible information available to the visually impaired. The performance of the subsystems was analysed through three stages of experimental procedures. The dissertation detailed how all objectives were met and the aim of the project achieved.

REFERENCES

[1] "Life Healthcare tackles biggest disability in the country," Life Healthcare, 07 August 2018. [Online]. Available: https://www.lifehealthcare.co.za/news-and-info-hub/latest-news/life-healthcare-tackles-biggest-disability-in-the-country/. [Accessed 27 June 2020].

[2] ISSUU, "Orbis 2018 Annual Report," 2018. [Online]. Available: https://issuu.com/orbisintl/docs/2018_annual_report_digital_copy. [Accessed 27 June 2020].

[3] A. Foster, C. Gilbert and G. Johnson, "Changing patterns in global blindness: 1988-2008," *Community Eye Health,* vol. 21, no. 67, pp. 37-39, 2008.

[4] Y. Tswanya, "Blindness affects millions in Africa," *Cape Argus,* 2017.

[5] "Diabetes and your eyesight," Glaucoma Research Foundation, 29 October 2017. [Online]. Available: https://www.glaucoma.org/glaucoma/diabetes-and-your-eyesight.php#:~:text=Diabetes%20and%20Glaucoma&text=People%20with%20diabetes%20are%20twice,person%20without%20the%20eye%20disease.. [Accessed 25 August 2020].

[6] American Printing House for the Blind, "Careers for Blind and Visually Impaired Individuals," CareerConnect, 2020. [Online]. Available: https://aphcareerconnect.org/explore-careers/careers-for-blind-and-visually-impaired-individuals/. [Accessed 25 August 2020].

[7] National Center for Blind Youth in Science, "Nathaneal Wales, Civil Engineer Interview," National Federation of the Blind, 2018. [Online]. Available: https://blindscience.org/wales-interview. [Accessed 26 August 2020].

[8] N. Wales, "On blindness and the study of civil engineerin," *National Federation of the BLind,* 1999.

[9] J. McElroy, "Sawdust Is My Glitter: The Story of Blind Craftsman John Furniss," Patagonia Workwear, 2020. [Online]. Available: https://www.patagonia.com/stories/sawdust-is-my-glitter/story-73575.html. [Accessed 26 August 2020].

[10] M. Robinson, “Chapter 1: Measuring and Marking,” in *Manual for Blind Woodworkers*, Woodworking for the Blind Inc., 2008.

[11] S. Khumalo and T. Fish-Hodgson, “Left in the dark: Failure to provide access to quality education to blind and partially sighted individuals in South Africa,” Section27, Johannesburg, 2016.

[12] M. Singh, R. Bajaj and A. Reddy, “IDAP Interview Series: Interview I with Justice Zak Mohammed Yacoob,” IDIA, 2016 July 22. [Online]. Available: https://www.idialaw.org/blog/idap-interview-series-interview-i-with-justice-zak-mohammed-yacoob/. [Accessed 26 August 2020].

[13] R. Umoh, “How this 26-year-old who has been blind since birth got a job writing code at Amazon,” CNBC, 24 April 2018. [Online]. Available: https://www.cnbc.com/2018/04/24/this-blind-26-year-old-got-a-job-writing-code-at-amazon.html. [Accessed 26 August 2020].

[14] M. Burke, “How I use technology as a blind person! - Molly Burke (CC),” Youtube, 18 December 2015. [Online]. Available: https://youtu.be/TiP7aantnvE?list=PL_Xm8PicNxr3cmrh0NRzXv56O7Y-0MXMx. [Accessed 26 August 2020].

[15] M. Burke, “How To Read & Write Braille + The History of Braille!,” Youtube, 17 March 2020. [Online]. Available: https://www.youtube.com/watch?v=a8AEkwtNEiM&list=PL_Xm8PicNxr3cmrh0NRzXv56O7Y-0MXMx&index=1. [Accessed 26 August 2020].

[16] K. E. Wolffe, “Career education for students with visual impairment,” in *The Routledge Handbook of Visual Impairment: Social and Cultural Research*, New York, Routledge Handbooks, 2019.

[17] National Federation of the Blind, “The Braille Literacy Crisis in America,” National Federation of the Blind, Jernigan Institute, 2009.

[18] “The History of KNFB Reader,” KNFB Reader, 2018. [Online]. Available: https://knfbreader.com/about-knfb-reader. [Accessed 24 January 2019].

[19] “Download and access NVDA,” NV Access, 2020. [Online]. Available: https://www.nvaccess.org/download/. [Accessed 13 July 2020].

[20] R. Aviv, “Listening to Braille,” *The New York Times Magazine,* 03 December 2009.

[21] J. Laurance, “The Big Question: Why is Braille under threat, and would it really matter if it died out?,” *Independent,* 6 January 2009.

[22] P. J. Molloy, The role of individual differences in working memory in reading and listening comprehension in intermediate grade students, Vancouver: University of British Columbia, 1997.

[23] B. A. o. N. America, “Music Braille Code,” 2015. [Online]. Available: http://www.brailleauthority.org/music/Music_Braille_Code_2015.pdf. [Accessed 24 January 2019].

[24] T. Pultarova, “How Learning to Read Rewrites the Brain,” *LiveScience,* 01 June 2017.

[25] M. Nivedita and H. Falk , “Word reading skill predicts anticipation of upcoming spoken language input: A study of children developing proficiency in reading,” *Journal of Experimental Child Psychology,* vol. 126, pp. 264-279, 2014.

[26] L. Knaflič, “Psychological aspects of literacy,” in *Libellarium,* Slovenia, 2014.

[27] A. M. Silverman, “The Association between Braille Reading History and Well-being for Blind Adults,” *Journal of Blindness Innovation and Research,* vol. 8, no. 1, 2018.

[28] R. Ryles, “The impact of braille reading skills on employment, income, education, and reading habits.,” *Journal of Visual Impairment & Blindness,* vol. 90, no. 3, pp. 219-226, 1996.

[29] E. C. Bell and N. M. Mino, “Blind and visually impaired adult rehabilitation and employment survey: Final results.,” *Journal of Blindness Innovation and Research,* vol. 3, no. 1, 2013.

[30] E. Foulke, “Increasing the Braille Reading Rate,” *Journal of Visual Impairment and Blindness,* vol. 73, no. 8, pp. 318-323, 1979.

[31] J. D. Burruss and L. Kaenzig, “Introversion: The often forgotten factor impacting the gifted,” *Virginia Association for the Gifted,* vol. 21, no. 1, 1999.

[32] “Braille Printers,” American Foundation for the Blind, 2020. [Online]. Available: https://www.afb.org/blindness-and-low-vision/using-technology/assistive-technology-products/braille-printers. [Accessed 27 August 2020].

[33] “The Braille Express 150, Writing Machine,” Woodlake Technologies. [Online]. Available: https://www.globalhand.org/system/assets/6938d62f70488c5251fadea3c21ad233e6c73f7c/original/Brailleinfo.leaflet.pdf?1350034584. [Accessed 27 August 2020].

[34] “Perkins Brailler,” Perkins: School for Blind Solutions, 2020. [Online]. Available: https://brailler.perkins.org/pages/perkins-brailler. [Accessed 27 August 2020].

[35] “4 Lines 28 Cells Braille Writing Slate and Stylus (Red),” Amazon, 2020. [Online]. Available: https://www.amazon.com/Lines-Cells-Braille-Writing-Stylus/dp/B06XNS5D1T/ref=rtpb_1/146-7609958-9157764?_encoding=UTF8&pd_rd_i=B06XNS5D1T&pd_rd_r=7792cdca-3525-4ea9-b9ce-6d034bea9a79&pd_rd_w=2C8vg&pd_rd_wg=zDSv4&pf_rd_p=e3464036-7ac0-415f-8736-4a31ff917eb7. [Accessed 27 August 2020].

[36] B. Cheadle, “A parent's guide to slate and stylus,” National Foundation of the Blind, 2007. [Online]. Available: https://www.nfb.org/images/nfb/publications/fr/fr25/fr07spr18.htm. [Accessed 27 August 2020].

[37] “FOCUS 80 BLUE - 5TH GENERATION,” Freedom Scienetific, 2020. [Online]. Available: https://store.freedomscientific.com/collections/all/products/focus-80-blue-5th-generation. [Accessed 07 November 2020].

[38] “FOCUS 14 BLUE - 5TH GENERATION,” Freedom Scinetific, 2020. [Online]. Available: https://store.freedomscientific.com/products/focus-14-blue-5th-generation. [Accessed 07 November 2020].

[39] “Focus 80 Blue Braille Display,” Canadialog, 2020. [Online]. Available: https://www.canadialog.com/produit/focus-80-blue. [Accessed 27 August 2020].

[40] HIMS Inc., “Actilino Brochure,” 2016. [Online]. Available: https://hims-inc.com/product/actilino/. [Accessed 27 August 2020].

[41] P. Smithmaitrie, “Analysis and Design of Piezoelectric Braille Display,” in *Rehabilitation Engineering*, IntechOpen, 2009.

[42] “BrailleNote Touch 32 Plus – Braille note taker/tablet,” Human Ware, 2020. [Online]. Available: https://store.humanware.com/hus/blindness-braillenote-touch-plus-32.html. [Accessed 23 September 2020].

[43] National Library Service for the Blind and Physically Handicapped, *Specification 800, Braille Books and Pamphlets,* Library of Congress, 2008.

[44] Oxford Dictionary of English, Oxford University Press, 2015.

[45] X. Wu, H. Zhu, S.-H. Kim and M. Allen, "A PORTABLE PNEUMATICALLY-ACTUATED REFRESHABLE BRAILLE CELL," in *The 14th International Conference on Solid-State Sensors, Actuators and Microsystems,* Lyon, 2007.

[46] A. Russomanno, S. O'Modhrain, B. Gillespie and M. Rodger, "Refreshing Refreshable Braille Displays," *IEEE TRANSACTIONS ON HAPTICS,* vol. 8, no. 3, 2015.

[47] E. Foulke and W. Schiff, Tactual Perception: A Sourcebook., Cambridge University Press, 1982.

[48] M. Heller, "Active and passive tactile braille recognition.," *Bulletin of the Psychonomic Society,* vol. 24, no. 3, pp. 201-202, 1986.

[49] M. A. Darden and C. J. Schwartz, "Skin tribology phenomena associated with reading braille print: The influence of cell patterns and skin behavior on coefficient of friction," *Wear 332,* pp. 734-741 DOI: 10.1016/j.wear.2014.12.053, 2015.

[50] H. Hern´andez, E. Preza and R. Vel´a, "Characterization of a Piezoelectric Ultrasonic Linear Motor for Braille Displays," in *Electronics, Robotics and Automotive Mechanics Conference,* Aguascalientes, 2009.

[51] N. H. Runyan and F. Carpi, "Seeking the 'holy Braille' display: might electromechanically active polymers be the solution?," *Expert Review of Medical Devices,* vol. 8, no. 5, pp. 529-532, 2011.

[52] P. Brochu and Q. Pei, "Advances in Dielectric Elastomers for Actuators and Artificial Muscles," *Macromolecular Rapid Communication,* vol. 31, pp. 10-36, 2010.

[53] R. Pelrine, R. Kornbluh, J. Joseph, R. Heydt, Q. Pei and S. Chiba, "High-field deformation of elastomeric dielectrics for actuators," *Materials Science and Engineering C,* vol. 11, pp. 89-100, 2000.

[54] A. Russomanno, R. B. Gillespie, S. O'Modhrain and M. Burns, "The Design of Pressure-controlled Valves for a Refreshable Tactile Display," in *IEEE World Haptics Conference (WHC),* Evanston, USA, 2015.

[55] R. Velázquez, E. E. Pissaloux, M. Hafez and J. Szewczyk, “Tactile Rendering With Shape-Memory-Alloy Pin-Matrix,” *IEEE TRANSACTIONS ON INSTRUMENTATION AND MEASUREMENT,* vol. 56, no. 5, 2008.

[56] K. Igmo, J. Kwangmok, K. Jachoon, N. Jea-do, L. Youngkwan and C. Hyouk , “Wearable Tactile Display Based on Soft Actuator,” in *IEEE International Conference on Robotics and Automation,* Florida, 2006.

[57] B. Banter, “Touch Screens and Touch Surfaces are Enriched by Haptic Force Feedback,” *Information Display,* 2010.

[58] R. Jussi, R. Roope, L. Jani, S. Veikko, R. Jukka, S. Katri, P. Toni and H. Arto, “Methods for Presenting Braille Characters on a Mobile Device with a Touchscreen and Tactile Feedback,” *and Tactile Feedback,* vol. 2, no. 1, pp. 28-39, 2009.

[59] Haptx, “VR Solutions,” haptx.com, [Online]. Available: https://haptx.com/solutions/. [Accessed 10 10 2019].

[60] Y. Bar-Cohen, “Electroactive, Polymer (EAP) Actuators as Artificial Muscle,” *SPIE Press,* vol. 2, 2004.

[61] Y. O. Muzaffer, S. Mark and M. Constantinos, “Haptic Interfaces Using Dielectric Electroactive Polymers,” *Sensors and Smart Structures Technologies for Civil, Mechanical, and Aerospace Systems SPIE,* vol. 7647, pp. 764737-2, 2010.

[62] EMCO High Voltage, *Design Considerations for Q Series: Application Note 1,* Sutter Creek, CA: EMCO High Voltage Corporation.

[63] L. Romasanta, M. Lopez-Manchado and R. Verdejo, “Increasing the performance of dielectric elastomer actuators: A review from the materials perspective,” *Progress in Polymer Science,* 2015.

[64] J. Kwangmok, C. K. Ja, N. Jae-do and K. L. Young, “Artificial annelid robot driven by soft actuators,” *Bioinspiration and Biomimetics,* vol. 2, p. S42–S49, 2007.

[65] N. Hosoya, “Hemispherical breathing mode speaker using a dielectric elastomer actuator,” *The Journal of the Acoustical Society of America,* vol. 138, no. 4, 2015.

[66] S. Seelecke, G. Rizzello, A. York and D. Naso, “Closed loop control of dielectric elastomer actuators based on self-sensing displacement feedback,” *Smart Materials and Structures,* vol. 23, no. 3, 2016.

[67] B. Hugh, F. Gabriele, P. Stefan, B. James and C. Federico, “A dielectric elastomer actuator-based tactile display for multiple fingertip interaction with soft bodies,” in *SPIE Smart Structures and Materials, Nondestructive Evaluation and Health Monitoring*, Portland, Oregon, 2017.

[68] G. Rizzello, D. Naso, A. York and S. Seelecke, “A Self-Sensing Approach for Dielectric Elastomer Actuators Based on Online Estimation Algorithms,” *IEEE/ASME Transactions on Mechatronics,* vol. 22, pp. 728-738, 2017.

[69] R. Pelrine, R. Kornbluh and J. Joseph, “Electrostriction of polymer dielectrics with compliant electrodes as a means of actuation,” *Sensors and Actuators A: Physical,* vol. 64, no. 1, p. 77–85, 1998.

[70] R. Pelrine, R. Kornbluh, J. Joseph, R. Heydt, P. Qibing and S. Chiba, “High-field deformation of elastomeric dielectrics for actuators,” *Materials Science and Engineering C,* vol. 11, pp. 89-100, 2000.

[71] B. M. O’Brien, E. P. Calius, T. Inamura, S. Q. Xie and I. A. Anderson , “Dielectric elastomer switches for smart artificial muscles,” *Applied Physics A volume,* vol. 100, pp. 385-389, 2010.

[72] C. T. Nguyen, H. Phung, T. D. Nguyen, C. Lee, U. Kim, D. Lee, H. Moon, J. Koo and H. R. Choi, “A small biomimetic quadruped robot driven by multistacked dielectric elastomer actuators,” *Smart Materials and Structures,* vol. 23, no. 6, 2014.

[73] H. R. Choi, “Soft Actuator Based on Dielectric Elastomer,” *計測と制御.* , vol. 54, pp. 21-26, 2015.

[74] H. Boys, G. Frediani, S. Poslad, J. Busfield and F. Carpi, “A dielectric elastomer actuator-based tactile display for multiple fingertip interaction with virtual soft bodies,” in *SPIE Smart Structures and Materials + Nondestructive Evaluation and Health Monitoring*, Portland, USA, 2017.

[75] I. Botha, G. Bright and J. Collins, “Evaluation of Dielectric Elastomers in Applications as Low Cost, Small-Scale Actuators,” in *SAUPEC/ROBMECH/PRASA 2020*, Cape Town, South Africa, 2019.

[76] S. Ha, W. Yuan, Q. Pei, R. Pelrine and S. Stanford, “Interpenetrating Polymer Networks for High-Performance Electroelastomer Artificial Muscles,” *Advanced Materials,* vol. 18, no. 7, pp. 887-891, 2006.

[77] S. Rosset and H. R. Shea, “Flexible and Stretchable Electrodes for Dielectric Elastomer Actuators,” *Applied Physics a Manuscript,* vol. 110, no. 2, 2012.

[78] W. Yuan, L. B. Hu , Z. B. Yu , T. Lam , J. Biggs J, S. M. Ha , D. J. Xi, B. Chen, M. K. Senesky, G. Grüner G and Q. Pei , “Fault-Tolerant Dielectric Elastomer Actuators using Single-Walled Carbon Nanotube Electrodes.,” *Advanced Materials,* vol. 20, pp. 621-625, 2008.

[79] F. Galantini, S. Bianchi, G. Gallone and V. Castelvetro, “Functionalized carbon nanotubes as a filler for dielectric elastomer composites with improved actuation performance,” *Smart Materials and Structures,* vol. 22, no. 5, 2013.

[80] G. Moretti, M. Fontana and R. Vertechy, “Parallelogram-shaped dielectric elastomer generators: Analytical model and experimental validation,” *Journal of Intelligent Material Systems and Structures,* vol. 26, no. 6, pp. 740-751, 2015.

[81] S. Rosset, M. Niklaus, P. Dubois and H. R. Shea, “Metal Ion Implantation for the Fabrication of Stretchable Electrodes on Elastomers,” *Advanced Functional Materials,* vol. 19, pp. 470-478, 2009.

[82] C. Christianson, N. Goldberg, C. Shengqiang and M. Tolley, “Fluid electrodes for submersible robotics based on dielectric elastomer actuators,” *Electroactive Polymer Actuators and Devices,* vol. 10163, 2017.

[83] F. Carpi, G. Gallone, F. Galantini and D. De Rossi, “Enhancement of the electromechanical transduction properties of a silicone elastomer by blending with a conjugated polymer,” *Electroactive Polymer Actuators and Devices,* vol. 6927, 2008.

[84] O. A. Araromi, S. Rosset and H. R. Shea, “High-resolution, large-area fabrication of compliant electrodes via laser ablation for robust, stretchable dielectric elastomer actuators and sensors,” *Applied Materials and Interfaces,* vol. 7, no. 32, 2015.

[85] “XP Power signs global distribution agreement with RS Components and Allied Electronics,” 10 November 2016. [Online]. Available: https://www.xppower.com/Media/Press-Releases/ArtMID/938/ArticleID/391/RS-Allied.

[86] J. Li, Y. Wang, L. Liu, S. Xu, Y. Liu, J. Leng and S. Cai, “A Biomimetic Soft Lens Controlled by Electrooculographic Signal,” *Advanced Funtional Materials,* vol. 29, no. 36, 2019.

[87] XP Power, “G Series DC- HVDC Converter,” 28 February 2020. [Online]. Available: https://www.xppower.com/portals/0/pdfs/SF_G_Series.pdf. [Accessed 08 September 2020].

[88] XP Power, “ Series DC-HVDC Converter,” 11 August 2020. [Online]. Available: https://www.xppower.com/portals/0/pdfs/SF_Q_Series.pdf. [Accessed 08 September 2020].

[89] XP Power, “A Series DC-HVDC Converter,” 24 March 2020. [Online]. Available: https://www.xppower.com/portals/0/pdfs/SF_A_Series.pdf. [Accessed 08 September 2020].

[90] XP Power, “ Series DC-HVDC Converter,” 12 August 2020. [Online]. Available: https://www.xppower.com/portals/0/pdfs/SF_C_Series.pdf. [Accessed 08 September 2020].

[91] XP Power, “ E Series DC-HVDC Converter,” 06 March 2020. [Online]. Available: http://www.eie-ic.com/Images/EMCO/EMCO/E_Series.pdf. [Accessed 08 September 2020].

[92] Illinois Library, “Introduction to OCR and Searchable PDFs: An Introduction to OCR,” 2019. [Online]. Available: https://guides.library.illinois.edu/OCR. [Accessed 02 June 2020].

[93] American Foundation for the Blind, “Optical Character Recognition Systems,” American Foundation for the Blind, [Online]. Available: https://www.afb.org/node/16207/optical-character-recognition-systems. [Accessed 07 July 2020].

[94] R. Smith, “An Overview of the Tesseract OCR Engine,” Google Inc., [Online]. Available: https://static.googleusercontent.com/media/research.google.com/en//pubs/archive/33418.pdf. [Accessed 09 July 2020].

[95] Google, “tesseract-ocr,” Github, 2020. [Online]. Available: https://github.com/tesseract-ocr/tesseract. [Accessed 08 November 2020].

[96] F. Karandish, “The Comprehensive Guide to Optical Character Recognition (OCR),” MOOVAI, 10 September 2019. [Online]. Available: https://moov.ai/en/blog/optical-character-recognition-ocr/. [Accessed 09 July 2020].

[97] A. D. V and S. B. S , “Embedded Optical Character Recognition On Tamil Text Image Using Raspberry Pi,” *International Journal of Computer Science Trends and Technology (IJCST),* vol. 2, no. 4, 2014.

[98] Tesseract-OCR, “Tesseract Documentation,” Github, 2020. [Online]. Available: https://tesseract-ocr.github.io/tessdoc/ImproveQuality. [Accessed 08 November 2020].

[99] E. Ehiorobo, “Basic OCR with Tesseract and OpenCV,” How-Tos, 10 October 2019. [Online]. Available: https://medium.com/building-a-simple-text-correction-tool/basic-ocr-with-tesseract-and-opencv-34fae6ab3400. [Accessed 08 November 2020].

[100] T. Tran, “[C++] Extracting Text From Image With OpenCV And Tesseract,” Machine Talk, 23 March 2020. [Online]. Available: https://machinetalk.org/2020/03/23/c-extracting-text-from-image-with-opencv-and-tesseract/. [Accessed 08 November 2020].

[101] V. S. Chandel, “Deep Learning based Text Recognition (OCR) using Tesseract and OpenCV,” LearnOpenCV, 16 June 2018. [Online]. Available: https://www.learnopencv.com/deep-learning-based-text-recognition-ocr-using-tesseract-and-opencv/. [Accessed 6 November 2020].

[102] C. Brizio, “ASCII-Braille Real-Time Translation via Arduino,” Arduino Project Hub, 3 July 2019. [Online]. Available: https://create.arduino.cc/projecthub/CesareBrizio/ascii-braille-real-time-translation-via-arduino-dd97a9. [Accessed 08 November 2020].

[103] NASA, “MSIS Volume 1: Standards, Section 3: Anthropometry and Biomechanics,” 2020. [Online]. Available: https://msis.jsc.nasa.gov/sections/section03.htm. [Accessed 11 September 2020].

[104] J. Nadankutty and N. M. Shaharuddin, “Digit ratio, 2D:4D (Index finger: Ring finger) in the right and left hand of males and females in Malaysia,” *Journal of Anthropology,* p. DOI: 10.7392/openaccess.45011806, 2014.

[105] Y. French, “Braille Displays and Notetakers,” National Library Serivce for the Blind and Print Disabled Library of Congress, 2017. [Online]. Available: https://www.loc.gov/nls/resources/blindness-and-vision-impairment/devices-aids/braille-displays-notetakers/. [Accessed 11 September 2020].

[106] “Printing Basics: Font Tips and Tricks,” Print Place, 2020. [Online]. Available: https://www.printplace.com/articles/printing-basics#:~:text=Long%20passages%20of%20text%20should,from%2018%20to%2028%20points.. [Accessed 11 September 2020].

[107] R. Zhang, P. Lochmatter, A. Kunz and G. Kovacs, “Spring roll dielectric elastomer actuators for a portable force feedback glove,” in *Smart Structures and Materials 2006: Electroactive Polymer Actuators and Devices (EAPAD)*, Zurich, 2006.

[108] A. Marette, C. de Saint-Aubin, S. Rosset, D. Briand and H. Shea, “FULL INTEGRATION OF A DIELECTRIC ELASTOMER ACTUATOR WITH A FLEXIBLE 1 kV THIN-FILM TRANSISTOR,” in *Transducers IEEE*, Kaohsiung. Taiwan, 2017.

[109] D. Molloy, “Beaglebone: Video Capture and Image Processing on Embedded Linux using OpenCV,” 2013. [Online]. Available: http://derekmolloy.ie/beaglebone/beaglebone-video-capture-and-image-processing-on-embedded-linux-using-opencv/. [Accessed 15 September 2020].

[110] E. Upton, “New product! Raspberry Pi Zero W joins the family,” Raspberry Pi, 28 February 2017. [Online]. Available: https://www.raspberrypi.org/blog/raspberry-pi-zero-w-joins-family/. [Accessed 15 September 2020].

[111] “TE Connectivity HB Series Radial Fixed Resistor 5MΩ ±1% 1W ±100ppm/°C,” Mantech South Africa, 2020. [Online]. Available: https://za.rs-online.com/web/p/through-hole-fixed-resistors/2960566/. [Accessed 16 September 2020].

[112] “TE Connectivity HB Series Radial Fixed Resistor 20MΩ ±1% 1W ±100ppm/°C,” RS Components South Africa, 2020. [Online]. Available: https://za.rs-online.com/web/p/through-hole-fixed-resistors/2960588/. [Accessed 16 September 2020].

[113] Behlke, “Fast High Voltage Transistor Switches,” 2011. [Online]. Available: https://www.behlke.com/pdf/160-01.pdf. [Accessed 16 September 2020].

[114] BRIGHT TOWARD INDUSTRIAL CO.,LTD., “LRL Series Hi-Voltage Relays,” 2017. [Online]. [Accessed 16 September 2020].

[115] Pickering, “High Voltage Dry Reed Relays Pickering Series 67.68,” 2020. [Online]. Available: https://www.pickeringrelay.com/pdfs/67-68-high-voltage-reed-relays.pdf. [Accessed 16 September 2020].

[116] Gigavac, “5kV SPDT HV Relay,” 2015. [Online]. Available: https://www.gigavac.com/sites/default/files/catalog/spec_sheet/g41c.pdf. [Accessed 16 September 2020].

[117] “K41A234,” TE Connectivity, 2020. [Online]. Available: https://www.te.com/usa-en/product-1-1618239-6.html. [Accessed 16 September 2020].

[118] “PIJUICE ZERO LIPO BATTERY 3.7V 1200MAH 1CELL,” DIY Electronics, 30 09 2020. [Online]. Available: https://www.diyelectronics.co.za/store/li-ion-li-po/2830-pijuice-zero-lipo-battery-37v-1200mah-1cell.html. [Accessed 30 09 2020].

[119] “General Purpose Input/Output pins on the Raspberry Pi,” Raspberry Pi, 2020. [Online]. Available: https://www.raspberrypi.org/documentation/hardware/raspberrypi/gpio/README.md. [Accessed 30 09 2020].

[120] “Power Supply,” Raspberry Pi, 2020. [Online]. Available: https://www.raspberrypi.org/documentation/hardware/raspberrypi/power/README.md. [Accessed 30 09 2020].

[121] L. George, “Interfacing Relay with PIC Microcontroller,” electroSome, 2 March 2020. [Online]. Available: https://electrosome.com/interfacing-relay-with-pic-microcontroller/. [Accessed 30 09 2020].

[122] “MP2636 Power Booster,” DIY Electronics, 2020. [Online]. Available: https://www.diyelectronics.co.za/store/dfrobot/2064-mp2636-power-booster-charger-module.html. [Accessed 6 December 2020].

[123] “Pololu 5V Step-Up / Step-Down Voltage Regulator S9V11F5,” Robotshop, 2020. [Online]. Available: https://www.robotshop.com/en/pololu-5v-step-up---step-down-voltage-regulator-s9v11f5.html. [Accessed 30 09 2020].

[124] “1A LITHIUM BATTERY CHARGING MODULE WITH PROTECTION,” DIY Electronics, 2020. [Online]. Available: https://www.diyelectronics.co.za/store/battery-charger/1195-1a-lithium-battery-charging-module-with-protection.html. [Accessed 30 9 2020].

[125] J. Yadernuk, “HONORING DIVERSITY GRADES 4-6,” BLIND AND VISUALLY IMPAIRED STUDENTS IN THE CLASSROOM, 2020. [Online]. Available: https://blindandvisuallyimpairedstudents.weebly.com/grades-4-6.html. [Accessed 28 September 2020].

[126] A. Thomas and E. Rufus, “Exploring the design of a tactile reader for braille and non-braille users,” *Technology and Disability,* vol. 31, no. 4, pp. 153-167, 2019.

[127] K. E. Maxfield, The blind child and his reading, a handbook for teachers of primary Braille reading, New York: American foundation for the blind, inc., 1928.

[128] “Camera Module,” Raspberry Pi, 2020. [Online]. Available: https://www.raspberrypi.org/documentation/hardware/camera/README.md. [Accessed 13 September 2020].

[129] L. Jackson, “Solving the Raspberry Pi Camera V2 Focus Issue with An Auto-Focus Camera Module,” ArduCam, 6 September 2018. [Online]. Available: https://www.arducam.com/programmable-motorized-focus-camera-raspberry-pi/. [Accessed 13 September 2020].

[130] R. Hofer and A. Kunz, “Digisketch: Taming Anoto Technology on LCDs,” in *2nd ACM SIGCHI Symposium on Engineering Interactive Computing System*, Berlin, 2010.

[131] ScanMarker, “Scanmarker Windows and Mac user guide,” 2020. [Online]. Available: https://sites.library.ualberta.ca/wp-content/uploads/2020/03/Scanmarker-Air-Win-Mac-User-Manual.pdf. [Accessed 28 September 2020].

[132] “Live Pen™ 2 - Documentation,” Anoto, 18 August 2020. [Online]. Available: https://support.anoto.com/article/362-live-pene284a2-2-documentation. [Accessed 28 September 2020].

[133] J. K. Shim, M. A. de Oliveira, J. Hsu and J. Huang, “Hand digit control in children: Age-related changes in hand digit force interactions during maximum flexion and extension force production tasks,” *Experimental Brain Research ,* vol. 176, no. 2, pp. 374-86, 2007.

[134] “Average Hand Size For Men, Women, And Children,” The Average Body.com, 12 November 2019. [Online]. Available: https://www.theaveragebody.com/average-hand-size/. [Accessed 28 September 2020].

[135] B. Alexander and V. Kotiuk, “Proportions of Hand Segments,” *International Journal of Morphology*, vol. 28, no. 3, pp. 755-758, 2010.

[136] “USB Endoscope for Otg Android Phone, Computer, 5.5 mm Borescope Inspection Snake Camera,” Amazon, 2020. [Online]. Available: https://www.amazon.com/Seesi-Endoscope-Waterproof-Inspection-Semi-Rigid/dp/B07PBF6DX5/ref=pd_rhf_dp_s_pd_crcd_0_3/146-7609958-9157764?_encoding=UTF8&pd_rd_i=B07PBF6DX5&pd_rd_r=992d8b44-f051-483f-af46-f83693eadf1b&pd_rd_w=Figl0&pd_rd_wg=CckyF&pf_rd_p=8019b. [Accessed 29 October 2020].

[137] “Rolyan Frog Style Aluminum Padded Finger Splint,” Health Products For You, 2020. [Online]. Available: https://www.healthproductsforyou.com/p-rolyan-frog-foam-lined-aluminum-finger-splint.html. [Accessed September 29 2020].

[138] “10 Pieces Finger Splint Mallet Finger Support,” Amazon.com, 2020. [Online]. Available: https://www.amazon.com/Protector-Adjustable-Immobilizer-Basketball-Protection/dp/B08422X1HC/ref=sr_1_6?dchild=1&keywords=mallet+finger+splint&qid=1604209961&sr=8-6. [Accessed 29 September 2020].

[139] “Polypropylene Electrical Insulating Film, 304mm x 200mm x 0.45mm,” RS Components, 2020. [Online]. Available: https://za.rs-online.com/web/p/plastic-film/7757797. [Accessed 29 September 2020].

[140] “POLYSTONE® P POLYPROPYLENE SHEET -NATURAL 2 MM,” Maizey Plastics, 2020. [Online]. Available: https://www.maizeyonline.co.za/engineering-plastics/pp-polypropylene/pp-sheets/polystone-p-polypropylene-sheet-natural-2-mm-ppsn0220001000i?returnurl=%2fsearch%3fq%3d2%2bmm%2b. [Accessed 29 September 2020].

[141] “MG Chemicals Clear 55 ml Bottle Conformal Coating,” RS Components, 2020. [Online]. Available: https://za.rs-online.com/web/p/conformal-coatings/1462878/. [Accessed 29 September 2020].

[142] P. Norvig, “English Letter Frequency Counts: Mayzner Revisited,” 2012. [Online]. Available: http://norvig.com/mayzner.html. [Accessed 05 November 2020].

[143] “Install OpenCV 4.1.2 on Raspberry Pi 4,” Q-Engineering, 2021. [Online]. Available: https://qengineering.eu/install-opencv-4.1-on-raspberry-pi-4.html. [Accessed 24 November 2020].

[144] Tesseract-ocr., “Tesseract Documentation,” Github, 2020. [Online]. Available: https://tesseract-ocr.github.io/tessdoc/ImproveQuality.html. [Accessed 03 December 2020].

[145] K. Kuguoglu, “How to use image preprocessing to improve the accuracy of Tesseract,” freeCodeCamp, 6 June 2018. [Online]. Available: https://medium.com/free-code-camp/getting-started-with-tesseract-part-ii-f7f9a0899b3f. [Accessed 24 June 2021].

[146] RS Pro, “Pressol Lubricant 50 g Graphite Bottle,” RS Components, [Online]. Available: https://za.rs-online.com/web/p/lubricants/7031086/. [Accessed 09 10 2019].

[147] Amazon, “Microfyne Graphite Powder Lubricant, 12oz can,” Asbury, [Online]. Available: https://www.amazon.com/Microfyne-Graphite-Powder-Lubricant-12oz/dp/B079X4LK36/ref=sr_1_1?crid=2D5JNRUD6XMA0&keywords=microfyne+graphite&qid=1570649391&sprefix=microfyn%2Caps%2C606&sr=8-1. [Accessed 09 10 2019].

[148] “846 - Carbon Conductive Grease,” MG Chemicals, 2020. [Online]. Available: https://www.mgchemicals.com/products/grease-for-electronics/electrically-conductive-grease/carbon-conductive-grease/. [Accessed 22 September 2020].

[149] I. R. Botha, J. E. Collins and G. Bright, “Impact of Electrode Application and Geometry on Performance of Diaphragm-Shaped Dielectric Elastomer Actuator,” in *IEEE MIBEC*, Kuala Lumpur, Malaysia, 2020.

[150] M. Mehnert, M. Hossain and P. Steinmann, “Experimental and numerical investigations of the electro-viscoelastic behavior of VHB 4905TM,” *European Journal of Mechanics - A/Solids,* vol. 77, 2019.

[151] FuelCellStore, “Ketjenblack EC-300J Specification Sheet,” 2020. [Online]. Available: https://www.fuelcellstore.com/spec-sheets/ketjenblack-ec-300j-fact-sheet.pdf. [Accessed 07 November 2020].

[152] “MG Chemicals Carbon Conductive Grease, 80g Tube,” Amazon, 2020. [Online]. Available:

https://www.amazon.com/gp/product/B005T8ROWA/ref=ppx_yo_dt_b_asin_title_o00_s00?ie=UTF8&psc=1. [Accessed 07 November 2020].

[153] “Carbon Black - Ketjenblack EC-300J,” Fuel Cell Store, 2020. [Online]. Available: https://www.fuelcellstore.com/ketjenblack-carbon-black-ec300j. [Accessed 07 November 2020].

[154] “File:ASCII-Table.svg,” Wikimedia Commons, 27 June 2008. [Online]. Available: https://commons.wikimedia.org/wiki/File:ASCII-Table.svg. [Accessed 08 November 2020].

APPENDICES

Appendix A – Project Code

The code below was used as the OCR control program on a Raspberry Pi Zero W.

```
#processing time initialise
import time
start = time.process_time()
#import libraries
import re
import pytesseract
import cv2
from PIL import Image
import RPi.GPIO as GPIO
import os
#import image
img = cv2.imread('/home/pi/Pictures/Text demo images/single letters/Ariel/lower case/z.JPG',cv2.IMREAD_COLOR) #Open the image from which characters has to be recognized
#resize image
img = cv2.resize(img,(620,480))
#convert to gray to reduce details
gray = cv2.cvtColor(img, cv2.COLOR_BGR2GRAY)
#Blur to reduce noise
gray = cv2.bilateralFilter(gray, 11, 17, 17)
#use for multiple characters
#test = pytesseract.image_to_string(gray, config='')
#Specify psm and oem (psm 10 for single char identification)
custom_oem_psm_config = r"--oem 3 --psm 10"
test = pytesseract.image_to_string(gray, config=custom_oem_psm_config)
#Remove the line break symbol from output
pattern = re.compile('\W')
char = re.sub(pattern, '', test)
print (char)
#Get confidence level if required
#test = (pytesseract.image_to_data(gray, lang=None, config='', nice=0) )
#if you don't want line breaks removed
#print (test)
#check processing time of ocr only
print(time.process_time() - start)
#identify GPIO number (used 3 leds in this example)
GPIO.setmode(GPIO.BCM)
GPIO.setwarnings(False)
GPIO.setup(13,GPIO.OUT)
GPIO.setup(19,GPIO.OUT)
GPIO.setup(26,GPIO.OUT)
GPIO.setup(21,GPIO.OUT)
GPIO.setup(20,GPIO.OUT)
GPIO.setup(16,GPIO.OUT)
#represent using LEDs
read_sequence= (char)
```

```
seq_list = list(str(read_sequence))
for n in seq_list:
if n == 'A':
       GPIO.output(13, GPIO.HIGH)
       time.sleep(1)
       GPIO.output(13, GPIO.LOW)
      time.sleep(1)
   if n == 'B':
       GPIO.output(13, GPIO.HIGH)
       GPIO.output(19, GPIO.HIGH)
       time.sleep(1)
       GPIO.output(13, GPIO.LOW)
       GPIO.output(19, GPIO.LOW)
       time.sleep(1)
   if n == 'C':
       GPIO.output(13, GPIO.HIGH)
       GPIO.output(21, GPIO.HIGH)
       time.sleep(1)
       GPIO.output(13, GPIO.LOW)
       GPIO.output(21, GPIO.LOW)
       time.sleep(1)
   if n == 'D':
       GPIO.output(13, GPIO.HIGH)
       GPIO.output(21, GPIO.HIGH)
       GPIO.output(20, GPIO.HIGH)
       time.sleep(1)
       GPIO.output(13, GPIO.LOW)
       GPIO.output(21, GPIO.LOW)
       GPIO.output(20, GPIO.LOW)
       time.sleep(1)
   if n == 'E':
       GPIO.output(13, GPIO.HIGH)
       GPIO.output(20, GPIO.HIGH)
       time.sleep(1)
       GPIO.output(13, GPIO.LOW)
       GPIO.output(20, GPIO.LOW)
       time.sleep(1)
   if n == 'F':
       GPIO.output(13, GPIO.HIGH)
       GPIO.output(19, GPIO.HIGH)
       GPIO.output(21, GPIO.HIGH)
       time.sleep(1)
       GPIO.output(13, GPIO.LOW)
       GPIO.output(19, GPIO.LOW)
       GPIO.output(21, GPIO.LOW)
       time.sleep(1)
   if n == 'G':
       GPIO.output(13, GPIO.HIGH)
       GPIO.output(19, GPIO.HIGH)
       GPIO.output(21, GPIO.HIGH)
       GPIO.output(20, GPIO.HIGH)
```

```
    time.sleep(1)
    GPIO.output(13, GPIO.LOW)
    GPIO.output(19, GPIO.LOW)
    GPIO.output(21, GPIO.LOW)
    GPIO.output(20, GPIO.LOW)
    time.sleep(1)
if n == 'H':
    GPIO.output(13, GPIO.HIGH)
    GPIO.output(19, GPIO.HIGH)
    GPIO.output(20, GPIO.HIGH)
    time.sleep(1)
    GPIO.output(13, GPIO.LOW)
    GPIO.output(19, GPIO.LOW)
    GPIO.output(20, GPIO.LOW)
    time.sleep(1)
if n == 'I':
    GPIO.output(19, GPIO.HIGH)
    GPIO.output(21, GPIO.HIGH)
    time.sleep(1)
  GPIO.output(19, GPIO.LOW)
    GPIO.output(21, GPIO.LOW)
    time.sleep(1)
if n == 'J':
    GPIO.output(19, GPIO.HIGH)
    GPIO.output(21, GPIO.HIGH)
    GPIO.output(20, GPIO.HIGH)
    time.sleep(1)
    GPIO.output(19, GPIO.LOW)
    GPIO.output(21, GPIO.LOW)
    GPIO.output(20, GPIO.LOW)
    time.sleep(1)
if n == 'K':
    GPIO.output(13, GPIO.HIGH)
    GPIO.output(26, GPIO.HIGH)
    time.sleep(1)
    GPIO.output(13, GPIO.LOW)
    GPIO.output(26, GPIO.LOW)
    time.sleep(1)
if n == 'L':
    GPIO.output(13, GPIO.HIGH)
    GPIO.output(19, GPIO.HIGH)
    GPIO.output(26, GPIO.HIGH)
    time.sleep(1)
    GPIO.output(13, GPIO.LOW)
    GPIO.output(19, GPIO.LOW)
    GPIO.output(26, GPIO.LOW)
    time.sleep(1)
if n == 'M':
    GPIO.output(13, GPIO.HIGH)
    GPIO.output(26, GPIO.HIGH)
    GPIO.output(21, GPIO.HIGH)
```

```
    time.sleep(1)
    GPIO.output(13, GPIO.LOW)
    GPIO.output(26, GPIO.LOW)
    GPIO.output(21, GPIO.LOW)
    time.sleep(1)
if n == 'N':
    GPIO.output(13, GPIO.HIGH)
    GPIO.output(26, GPIO.HIGH)
    GPIO.output(21, GPIO.HIGH)
    GPIO.output(20, GPIO.HIGH)
    time.sleep(1)
    GPIO.output(13, GPIO.LOW)
    GPIO.output(26, GPIO.LOW)
    GPIO.output(21, GPIO.LOW)
    GPIO.output(20, GPIO.LOW)
    time.sleep(1)
if n == 'O':
    GPIO.output(13, GPIO.HIGH)
    GPIO.output(26, GPIO.HIGH)
    GPIO.output(20, GPIO.HIGH)
    time.sleep(1)
    GPIO.output(13, GPIO.LOW)
    GPIO.output(26, GPIO.LOW)
    GPIO.output(20, GPIO.LOW)
    time.sleep(1)
if n == 'P':
    GPIO.output(13, GPIO.HIGH)
    GPIO.output(19, GPIO.HIGH)
    GPIO.output(26, GPIO.HIGH)
    GPIO.output(21, GPIO.HIGH)
    time.sleep(1)
    GPIO.output(13, GPIO.LOW)
    GPIO.output(19, GPIO.LOW)
    GPIO.output(26, GPIO.LOW)
    GPIO.output(21, GPIO.LOW)
    time.sleep(1)
if n == 'Q':
    GPIO.output(13, GPIO.HIGH)
    GPIO.output(19, GPIO.HIGH)
    GPIO.output(26, GPIO.HIGH)
    GPIO.output(21, GPIO.HIGH)
    GPIO.output(20, GPIO.HIGH)
    time.sleep(1)
    GPIO.output(13, GPIO.LOW)
    GPIO.output(19, GPIO.LOW)
    GPIO.output(26, GPIO.LOW)
    GPIO.output(21, GPIO.LOW)
    GPIO.output(20, GPIO.LOW)
    time.sleep(1)
if n == 'R':
    GPIO.output(13, GPIO.HIGH)
```

```
        GPIO.output(19, GPIO.HIGH)
        GPIO.output(26, GPIO.HIGH)
        GPIO.output(20, GPIO.HIGH)
        time.sleep(1)
        GPIO.output(13, GPIO.LOW)
        GPIO.output(19, GPIO.LOW)
        GPIO.output(26, GPIO.LOW)
        GPIO.output(20, GPIO.LOW)
        time.sleep(1)
    if n == 'S':
        GPIO.output(19, GPIO.HIGH)
        GPIO.output(26, GPIO.HIGH)
        GPIO.output(21, GPIO.HIGH)
        time.sleep(1)
        GPIO.output(19, GPIO.LOW)
        GPIO.output(26, GPIO.LOW)
        GPIO.output(21, GPIO.LOW)
        time.sleep(1)
    if n == 'T':
        GPIO.output(19, GPIO.HIGH)
        GPIO.output(26, GPIO.HIGH)
        GPIO.output(21, GPIO.HIGH)
        GPIO.output(20, GPIO.HIGH)
        time.sleep(1)
        GPIO.output(19, GPIO.LOW)
        GPIO.output(26, GPIO.LOW)
        GPIO.output(21, GPIO.LOW)
        GPIO.output(20, GPIO.LOW)
        time.sleep(1)
    if n == 'U':
        GPIO.output(13, GPIO.HIGH)
        GPIO.output(26, GPIO.HIGH)
        GPIO.output(16, GPIO.HIGH)
        time.sleep(1)
        GPIO.output(13, GPIO.LOW)
        GPIO.output(26, GPIO.LOW)
        GPIO.output(16, GPIO.LOW)
        time.sleep(1)
    if n == 'V':
        GPIO.output(13, GPIO.HIGH)
        GPIO.output(19, GPIO.HIGH)
        GPIO.output(26, GPIO.HIGH)
        GPIO.output(16, GPIO.HIGH)
        time.sleep(1)
        GPIO.output(13, GPIO.LOW)
        GPIO.output(19, GPIO.LOW)
        GPIO.output(26, GPIO.LOW)
        GPIO.output(16, GPIO.LOW)
        time.sleep(1)
    if n == 'W':
        GPIO.output(19, GPIO.HIGH)
```

```
        GPIO.output(21, GPIO.HIGH)
        GPIO.output(20, GPIO.HIGH)
        GPIO.output(16, GPIO.HIGH)
        time.sleep(1)
        GPIO.output(19, GPIO.LOW)
        GPIO.output(21, GPIO.LOW)
        GPIO.output(20, GPIO.LOW)
        GPIO.output(16, GPIO.LOW)
        time.sleep(1)
    if n == 'X':
        GPIO.output(13, GPIO.HIGH)
        GPIO.output(26, GPIO.HIGH)
        GPIO.output(21, GPIO.HIGH)
        GPIO.output(16, GPIO.HIGH)
        time.sleep(1)
        GPIO.output(13, GPIO.LOW)
        GPIO.output(26, GPIO.LOW)
        GPIO.output(21, GPIO.LOW)
        GPIO.output(16, GPIO.LOW)
        time.sleep(1)
    if n == 'Y':
        GPIO.output(13, GPIO.HIGH)
        GPIO.output(26, GPIO.HIGH)
        GPIO.output(21, GPIO.HIGH)
        GPIO.output(20, GPIO.HIGH)
        GPIO.output(16, GPIO.HIGH)
        time.sleep(1)
        GPIO.output(13, GPIO.LOW)
        GPIO.output(26, GPIO.LOW)
        GPIO.output(21, GPIO.LOW)
        GPIO.output(20, GPIO.LOW)
        GPIO.output(16, GPIO.LOW)
        time.sleep(1)
    if n == 'Z':
        GPIO.output(13, GPIO.HIGH)
        GPIO.output(26, GPIO.HIGH)
        GPIO.output(20, GPIO.HIGH)
        GPIO.output(16, GPIO.HIGH)
        time.sleep(1)
        GPIO.output(13, GPIO.LOW)
        GPIO.output(26, GPIO.LOW)
        GPIO.output(20, GPIO.LOW)
        GPIO.output(16, GPIO.LOW)
        time.sleep(1)
    if n == 'a':
        GPIO.output(13, GPIO.HIGH)
        time.sleep(1)
        GPIO.output(13, GPIO.LOW)
        time.sleep(1)
    if n == 'b':
        GPIO.output(13, GPIO.HIGH)
```

```
        GPIO.output(19, GPIO.HIGH)
        time.sleep(1)
        GPIO.output(13, GPIO.LOW)
        GPIO.output(19, GPIO.LOW)
        time.sleep(1)
    if n == 'c':
        GPIO.output(13, GPIO.HIGH)
        GPIO.output(21, GPIO.HIGH)
        time.sleep(1)
        GPIO.output(13, GPIO.LOW)
        GPIO.output(21, GPIO.LOW)
        time.sleep(1)
    if n == 'd':
        GPIO.output(13, GPIO.HIGH)
        GPIO.output(21, GPIO.HIGH)
        GPIO.output(20, GPIO.HIGH)
        time.sleep(1)
        GPIO.output(13, GPIO.LOW)
        GPIO.output(21, GPIO.LOW)
        GPIO.output(20, GPIO.LOW)
        time.sleep(1)
    if n == 'e':
        GPIO.output(13, GPIO.HIGH)
        GPIO.output(20, GPIO.HIGH)
        time.sleep(1)
        GPIO.output(13, GPIO.LOW)
        GPIO.output(20, GPIO.LOW)
        time.sleep(1)
    if n == 'f':
        GPIO.output(13, GPIO.HIGH)
        GPIO.output(19, GPIO.HIGH)
        GPIO.output(21, GPIO.HIGH)
        time.sleep(1)
        GPIO.output(13, GPIO.LOW)
        GPIO.output(19, GPIO.LOW)
        GPIO.output(21, GPIO.LOW)
        time.sleep(1)
    if n == 'g':
        GPIO.output(13, GPIO.HIGH)
        GPIO.output(19, GPIO.HIGH)
        GPIO.output(21, GPIO.HIGH)
        GPIO.output(20, GPIO.HIGH)
        time.sleep(1)
        GPIO.output(13, GPIO.LOW)
        GPIO.output(19, GPIO.LOW)
        GPIO.output(21, GPIO.LOW)
        GPIO.output(20, GPIO.LOW)
        time.sleep(1)
    if n == 'h':
        GPIO.output(13, GPIO.HIGH)
        GPIO.output(19, GPIO.HIGH)
```

```
        GPIO.output(20, GPIO.HIGH)
        time.sleep(1)
        GPIO.output(13, GPIO.LOW)
        GPIO.output(19, GPIO.LOW)
        GPIO.output(20, GPIO.LOW)
        time.sleep(1)
    if n == 'i':
        GPIO.output(19, GPIO.HIGH)
        GPIO.output(21, GPIO.HIGH)
        time.sleep(1)
        GPIO.output(19, GPIO.LOW)
        GPIO.output(21, GPIO.LOW)
        time.sleep(1)
    if n == 'j':
        GPIO.output(19, GPIO.HIGH)
        GPIO.output(21, GPIO.HIGH)
        GPIO.output(20, GPIO.HIGH)
        time.sleep(1)
        GPIO.output(19, GPIO.LOW)
        GPIO.output(21, GPIO.LOW)
        GPIO.output(20, GPIO.LOW)
        time.sleep(1)
    if n == 'k':
        GPIO.output(13, GPIO.HIGH)
        GPIO.output(26, GPIO.HIGH)
        time.sleep(1)
        GPIO.output(13, GPIO.LOW)
        GPIO.output(26, GPIO.LOW)
        time.sleep(1)
    if n == 'l':
        GPIO.output(13, GPIO.HIGH)
        GPIO.output(19, GPIO.HIGH)
        GPIO.output(26, GPIO.HIGH)
        time.sleep(1)
        GPIO.output(13, GPIO.LOW)
        GPIO.output(19, GPIO.LOW)
        GPIO.output(26, GPIO.LOW)
        time.sleep(1)
    if n == 'm':
        GPIO.output(13, GPIO.HIGH)
        GPIO.output(26, GPIO.HIGH)
        GPIO.output(21, GPIO.HIGH)
        time.sleep(1)
        GPIO.output(13, GPIO.LOW)
        GPIO.output(26, GPIO.LOW)
        GPIO.output(21, GPIO.LOW)
        time.sleep(1)
    if n == 'n':
        GPIO.output(13, GPIO.HIGH)
        GPIO.output(26, GPIO.HIGH)
        GPIO.output(21, GPIO.HIGH)
```

```
        GPIO.output(20, GPIO.HIGH)
        time.sleep(1)
        GPIO.output(13, GPIO.LOW)
        GPIO.output(26, GPIO.LOW)
        GPIO.output(21, GPIO.LOW)
        GPIO.output(20, GPIO.LOW)
        time.sleep(1)
    if n == 'o':
        GPIO.output(13, GPIO.HIGH)
        GPIO.output(26, GPIO.HIGH)
        GPIO.output(20, GPIO.HIGH)
        time.sleep(1)
        GPIO.output(13, GPIO.LOW)
        GPIO.output(26, GPIO.LOW)
        GPIO.output(20, GPIO.LOW)
        time.sleep(1)
    if n == 'p':
        GPIO.output(13, GPIO.HIGH)
        GPIO.output(19, GPIO.HIGH)
        GPIO.output(26, GPIO.HIGH)
        GPIO.output(21, GPIO.HIGH)
        time.sleep(1)
        GPIO.output(13, GPIO.LOW)
        GPIO.output(19, GPIO.LOW)
        GPIO.output(26, GPIO.LOW)
        GPIO.output(21, GPIO.LOW)
        time.sleep(1)
    if n == 'q':
        GPIO.output(13, GPIO.HIGH)
        GPIO.output(19, GPIO.HIGH)
        GPIO.output(26, GPIO.HIGH)
        GPIO.output(21, GPIO.HIGH)
        GPIO.output(20, GPIO.HIGH)
        time.sleep(1)
        GPIO.output(13, GPIO.LOW)
        GPIO.output(19, GPIO.LOW)
        GPIO.output(26, GPIO.LOW)
        GPIO.output(21, GPIO.LOW)
        GPIO.output(20, GPIO.LOW)
        time.sleep(1)
    if n == 'r':
        GPIO.output(13, GPIO.HIGH)
        GPIO.output(19, GPIO.HIGH)
        GPIO.output(26, GPIO.HIGH)
        GPIO.output(20, GPIO.HIGH)
        time.sleep(1)
        GPIO.output(13, GPIO.LOW)
        GPIO.output(19, GPIO.LOW)
        GPIO.output(26, GPIO.LOW)
        GPIO.output(20, GPIO.LOW)
        time.sleep(1)
```

```
if n == 's':
    GPIO.output(19, GPIO.HIGH)
    GPIO.output(26, GPIO.HIGH)
    GPIO.output(21, GPIO.HIGH)
    time.sleep(1)
    GPIO.output(19, GPIO.LOW)
    GPIO.output(26, GPIO.LOW)
    GPIO.output(21, GPIO.LOW)
    time.sleep(1)
if n == 't':
    GPIO.output(19, GPIO.HIGH)
    GPIO.output(26, GPIO.HIGH)
    GPIO.output(21, GPIO.HIGH)
    GPIO.output(20, GPIO.HIGH)
    time.sleep(1)
    GPIO.output(19, GPIO.LOW)
    GPIO.output(26, GPIO.LOW)
    GPIO.output(21, GPIO.LOW)
    GPIO.output(20, GPIO.LOW)
    time.sleep(1)
if n == 'u':
    GPIO.output(13, GPIO.HIGH)
    GPIO.output(26, GPIO.HIGH)
    GPIO.output(16, GPIO.HIGH)
    time.sleep(1)
    GPIO.output(13, GPIO.LOW)
    GPIO.output(26, GPIO.LOW)
    GPIO.output(16, GPIO.LOW)
    time.sleep(1)
if n == 'v':
    GPIO.output(13, GPIO.HIGH)
    GPIO.output(19, GPIO.HIGH)
    GPIO.output(26, GPIO.HIGH)
    GPIO.output(16, GPIO.HIGH)
    time.sleep(1)
    GPIO.output(13, GPIO.LOW)
    GPIO.output(19, GPIO.LOW)
    GPIO.output(26, GPIO.LOW)
    GPIO.output(16, GPIO.LOW)
    time.sleep(1)
if n == 'w':
    GPIO.output(19, GPIO.HIGH)
    GPIO.output(21, GPIO.HIGH)
    GPIO.output(20, GPIO.HIGH)
    GPIO.output(16, GPIO.HIGH)
    time.sleep(1)
    GPIO.output(19, GPIO.LOW)
    GPIO.output(21, GPIO.LOW)
    GPIO.output(20, GPIO.LOW)
    GPIO.output(16, GPIO.LOW)
    time.sleep(1)
```

```
if n == 'x':
    GPIO.output(13, GPIO.HIGH)
    GPIO.output(26, GPIO.HIGH)
    GPIO.output(21, GPIO.HIGH)
    GPIO.output(16, GPIO.HIGH)
    time.sleep(1)
    GPIO.output(13, GPIO.LOW)
    GPIO.output(26, GPIO.LOW)
    GPIO.output(21, GPIO.LOW)
    GPIO.output(16, GPIO.LOW)
    time.sleep(1)
if n == 'y':
    GPIO.output(13, GPIO.HIGH)
    GPIO.output(26, GPIO.HIGH)
    GPIO.output(21, GPIO.HIGH)
    GPIO.output(20, GPIO.HIGH)
    GPIO.output(16, GPIO.HIGH)
    time.sleep(1)
    GPIO.output(13, GPIO.LOW)
    GPIO.output(26, GPIO.LOW)
    GPIO.output(21, GPIO.LOW)
    GPIO.output(20, GPIO.LOW)
    GPIO.output(16, GPIO.LOW)
    time.sleep(1)
if n == 'z':
    GPIO.output(13, GPIO.HIGH)
    GPIO.output(26, GPIO.HIGH)
    GPIO.output(20, GPIO.HIGH)
    GPIO.output(16, GPIO.HIGH)
    time.sleep(1)
    GPIO.output(13, GPIO.LOW)
    GPIO.output(26, GPIO.LOW)
    GPIO.output(20, GPIO.LOW)
    GPIO.output(16, GPIO.LOW)
    time.sleep(1)
if n == '1':
    GPIO.output(13, GPIO.HIGH)
    time.sleep(1)
    GPIO.output(13, GPIO.LOW)
    time.sleep(1)
if n == '2':
    GPIO.output(13, GPIO.HIGH)
    GPIO.output(19, GPIO.HIGH)
    time.sleep(1)
    GPIO.output(13, GPIO.LOW)
    GPIO.output(19, GPIO.LOW)
    time.sleep(1)
if n == '3':
    GPIO.output(13, GPIO.HIGH)
    GPIO.output(21, GPIO.HIGH)
    time.sleep(1)
```

```
        GPIO.output(13, GPIO.LOW)
        GPIO.output(21, GPIO.LOW)
        time.sleep(1)
    if n == '4':
        GPIO.output(13, GPIO.HIGH)
        GPIO.output(21, GPIO.HIGH)
        GPIO.output(20, GPIO.HIGH)
        time.sleep(1)
        GPIO.output(13, GPIO.LOW)
        GPIO.output(21, GPIO.LOW)
        GPIO.output(20, GPIO.LOW)
        time.sleep(1)
    if n == '5':
        GPIO.output(13, GPIO.HIGH)
        GPIO.output(20, GPIO.HIGH)
        time.sleep(1)
        GPIO.output(13, GPIO.LOW)
        GPIO.output(20, GPIO.LOW)
        time.sleep(1)
    if n == '6':
        GPIO.output(13, GPIO.HIGH)
        GPIO.output(19, GPIO.HIGH)
        GPIO.output(21, GPIO.HIGH)
        time.sleep(1)
        GPIO.output(13, GPIO.LOW)
        GPIO.output(19, GPIO.LOW)
        GPIO.output(21, GPIO.LOW)
        time.sleep(1)
    if n == '7':
        GPIO.output(13, GPIO.HIGH)
        GPIO.output(19, GPIO.HIGH)
        GPIO.output(21, GPIO.HIGH)
        GPIO.output(20, GPIO.HIGH)
        time.sleep(1)
        GPIO.output(13, GPIO.LOW)
        GPIO.output(19, GPIO.LOW)
        GPIO.output(21, GPIO.LOW)
        GPIO.output(20, GPIO.LOW)
        time.sleep(1)
    if n == '8':
        GPIO.output(13, GPIO.HIGH)
        GPIO.output(19, GPIO.HIGH)
        GPIO.output(20, GPIO.HIGH)
        time.sleep(1)
        GPIO.output(13, GPIO.LOW)
        GPIO.output(19, GPIO.LOW)
        GPIO.output(20, GPIO.LOW)
        time.sleep(1)
    if n == '9':
        GPIO.output(19, GPIO.HIGH)
        GPIO.output(21, GPIO.HIGH)
```

```
        time.sleep(1)
        GPIO.output(19, GPIO.LOW)
        GPIO.output(21, GPIO.LOW)
        time.sleep(1)
    if n == '0':
        GPIO.output(19, GPIO.HIGH)
        GPIO.output(21, GPIO.HIGH)
        GPIO.output(20, GPIO.HIGH)
        time.sleep(1)
        GPIO.output(19, GPIO.LOW)
        GPIO.output(21, GPIO.LOW)
        GPIO.output(20, GPIO.LOW)
        time.sleep(1)
GPIO.cleanup()
#check processing time of entire operation
#print(time.process_time() - start)
```

Appendix B – Budget Overview

Table B-1 Project Cost Overview

Material/Component	Supplier	Units	Cost/unit	Cost Total
Mechanical				
MG Chemical Carbon Conductive Grease 846 80g tube	Amazon	1	R318.69	R318,69
3M VHB 4910 tape (12,7 x 10,16 cm) Pack of 25	Amazon	1	R129.82	R129,82
Sil Poxy Silicone Adhesive 13.6g	AMT Composites	1	R189.00	R189,00
Polypropylene Electrical Insulating Film, 304mm x 200mm x 0.45mm	RS Components	1	R254.37	R254,37
POLYSTONE® P POLYPROPYLENE SHEET - NATURAL 2 MM (1m x 1m)	Maizey Plastics	1	R333,48	R333,48
MG Chemicals Clear 55 ml Bottle Conformal Coating	RS Components	1	R270.12	R270,12
PLA 1 kg 3mm filament	DIY Electronics	1	R259	R259
Sub-total				R 1 754,48
Sub-total (Unit cost)*				
Electronics				
Raspberry Pi Zero W	DIY Electronics	1	R429,95	R429,95
PIJUICE ZERO LIPO BATTERY 3.7V 1200MAH 1CELL	DIY Electronics	2	R299,95	R599,90
XP Power DC-DC HV Converter A50	RS Components	1	R4465,44	R4465,44
Pickering Reed Relay	Pickering	6	R525,64	R 3153,84
MP2636 Power Booster+ Charger Module	DIY Electronics	1	R169,95	R169,95
MakerFocus 1A LITHIUM BATTERY CHARGING MODULE WITH PROTECTION (TP4056)	DIY Electronics	1	R24,95	R24,95
ULN2003 IC	Digi-Key Electronics	1	R 8,75	R 8,75
Pololu 5V Step-Up / Step-Down Voltage Regulator S9V11F5	Robotshop	1	R100,26	R100,26
Sub-total				R 8 953,04
Total				R 10 707,52
Total (Unit cost)				R 8964,73

*Unit cost calculated using the assumption that 150 units can be synthesised using a single order of VHB 4910. VHB 4910 was selected as the limiting factor since the specifications designated the maximum number of units capable of being manufactured from one order of mechanical components.

Appendix C – Test Results

C.1 Raw data of experimental material selection

The material selection stage of DEA synthesis was comprised of nine sets of tests. Each test evaluated a property of the DEA synthesis process, namely, grade of graphite powder used in electrodes, percentage pre-strain and elastomer thickness. The variable measured in each test included the percentage strain achieved at a range of voltage outputs from 0 V to 12 V.

Table C-1: Pressol Graphite Powder Strain Tests

Pixel Count			**Displacement (pixels)**				**Strain (%)**			
Sample Set 1										
Voltage	Horiz	Vert	Voltage	Horiz	Vert	Average	Voltage	Horiz	Vert	Average
0	1456	1470	0	0	0	0	0	0	0	0
3	1457	1482	3	1	12	6,5	3	0,068681	0,816327	0,442504
6	1468	1486	6	12	16	14	6	0,824176	1,088435	0,956306
9	1474	1490	9	18	20	19	9	1,236264	1,360544	1,298404
12	1480	1498	12	24	28	26	12	1,648352	1,904762	1,776557
12	1480	1499	12	24	29	26,5	12	1,648352	1,972789	1,81057
9	1470	1488	9	14	18	16	9	0,961538	1,22449	1,093014
6	1466	1484	6	10	14	12	6	0,686813	0,952381	0,819597
3	1460	1477	3	4	7	5,5	3	0,274725	0,47619	0,375458
0	1458	1470	0	2	0	1	0	0,137363	0	0,068681
Sample Set 2										
Voltage	Horiz	Vert	Voltage	Horiz	Vert	Average	Voltage	Horiz	Vert	Average
0	1493	1482	0	0	0	0	0	0	0	0
3	1493	1484	3	0	2	1	3	0	0,134953	0,067476
6	1517	1498	6	24	16	20	6	1,607502	1,079622	1,343562
9	1523	1507	9	30	25	27,5	9	2,009377	1,68691	1,848143
12	1523	1507	12	30	25	27,5	12	2,009377	1,68691	1,848143
12	1523	1507	12	30	25	27,5	12	2,009377	1,68691	1,848143
9	1512	1504	9	19	22	20,5	9	1,272605	1,48448	1,378543
6	1512	1504	6	19	22	20,5	6	1,272605	1,48448	1,378543
3	1505	1492	3	12	10	11	3	0,803751	0,674764	0,739257
0	1495	1484	0	2	2	2	0	0,133958	0,134953	0,134456
Sample Set 3										
Voltage	Horiz	Vert	Voltage	Horiz	Vert	Average	Voltage	Horiz	Vert	Average
0	1481	1484	0	0	0	0	0	0	0	0
3	1490	1490	3	9	6	7,5	3	0,607698	0,404313	0,506005
6	1498	1493	6	17	9	13	6	1,147873	0,606469	0,877171
9	1501	1499	9	20	15	17,5	9	1,350439	1,010782	1,18061
12	1507	1506	12	26	22	24	12	1,755571	1,48248	1,619025
12	1507	1506	12	26	22	24	12	1,755571	1,48248	1,619025
9	1501	1503	9	20	19	19,5	9	1,350439	1,280323	1,315381
6	1497	1485	6	16	1	8,5	6	1,080351	0,067385	0,573868
3	1483	1478	3	2	-6	-2	3	0,135044	-0,40431	-0,13463
0	1483	1478	0	2	-6	-2	0	0,135044	-0,40431	-0,13463

Table C-2: Microfyn Graphite Powder Strain Tests

Pixel Count			**Displacement (pixels)**				**Strain (%)**			
Sample Set 1										
Voltage	Horiz	Vert	Voltage	Horiz	Vert	Average	Voltage	Horiz	Vert	Average
0	1439	1485	0	0	0	0	0	0	0	0
3	1484	1526	3	45	41	43	3	3,127172	2,760943	2,944057
6	1514	1563	6	75	78	76,5	6	5,211953	5,252525	5,232239
9	1547	1592	9	108	107	107,5	9	7,505212	7,205387	7,3553
12	1564	1636	12	125	151	138	12	8,686588	10,16835	9,427469
12	1564	1636	12	125	151	138	12	8,686588	10,16835	9,427469
9	1550	1605	9	111	120	115,5	9	7,71369	8,080808	7,897249
6	1529	1583	6	90	98	94	6	6,254343	6,599327	6,426835
3	1498	1541	3	59	56	57,5	3	4,100069	3,771044	3,935557
0	1456	1493	0	17	8	12,5	0	1,181376	0,538721	0,860048
Sample Set 2										
Voltage	Horiz	Vert	Voltage	Horiz	Vert	Average	Voltage	Horiz	Vert	Average
0	1023	1021	0	0	0	0	0	0	0	0
3	1028	1024	3	5	3	4	3	0,488759	0,29383	0,391294
6	1043	1044	6	20	23	21,5	6	1,955034	2,252693	2,103864
9	1089	1091	9	66	70	68	9	6,451613	6,856024	6,653818
12	1098	1102	12	75	81	78	12	7,331378	7,933399	7,632388
12	1098	1102	12	75	81	78	12	7,331378	7,933399	7,632388
9	1063	1063	9	40	42	41	9	3,910068	4,113614	4,011841
6	1049	1051	6	26	30	28	6	2,541544	2,938296	2,73992
3	1038	1039	3	15	18	16,5	3	1,466276	1,762977	1,614627
0	1030	1029	0	7	8	7,5	0	0,684262	0,783546	0,733904
Sample Set 3										
Voltage	Horiz	Vert	Voltage	Horiz	Vert	Average	Voltage	Horiz	Vert	Average
0	1444	1494	0	0	0	0	0	0	0	0
3	1489	1526	3	45	32	38,5	3	3,116343	2,141901	2,629122
6	1510	1558	6	66	64	65	6	4,570637	4,283802	4,427219
9	1563	1620	9	119	126	122,5	9	8,240997	8,433735	8,337366
12	1582	1641	12	138	147	142,5	12	9,556787	9,839357	9,698072
12	1582	1641	12	138	147	142,5	12	9,556787	9,839357	9,698072
9	1568	1629	9	124	135	129,5	9	8,587258	9,036145	8,811701
6	1534	1596	6	90	102	96	6	6,232687	6,827309	6,529998
3	1504	1526	3	60	32	46	3	4,155125	2,141901	3,148513
0	1454	1499	0	10	5	7,5	0	0,692521	0,334672	0,513596

Table C-3: VHB 4905 at 0% Pre-strain Strain Tests

Pixel Count			Displacement (pixels)				Strain (%)			
Voltage	Horiz	Vert	Voltage	Horiz	Vert	Ave	Voltage	Horiz	Vert	Average
0	1228	1220	0	0	0	0	0	0	0	0
3	1235	1227	3	7	7	7	3	0,570033	0,57377	0,571902
6	1246	1232	6	18	12	15	6	1,465798	0,983607	1,224702
9	1251	1232	9	23	12	17,5	9	1,872964	0,983607	1,428285
12	1253	1234	12	25	14	19,5	12	2,035831	1,147541	1,591686

Table C-4: VHB 4910 at 0% Pre-strain Strain Tests

Pixel Count			Displacement (pixels)				Strain (%)			
Voltage	Horiz	Vert	Voltage	Horiz	Vert	Ave	Voltage	Horiz	Vert	Average
0	1192	1217	0,0	0,0	0,0	0,0	0	0	0	0
3	1192	1217	3,0	0,0	0,0	0,0	3	0	0	0
6	1194	1217	6,0	2,0	0,0	1,0	6	0,167785	0	0,083893
9	1195	1221	9,0	3,0	4,0	3,5	9	0,251678	0,328677	0,290177
12	1200	1225	12,0	8,0	8,0	8,0	12	0,671141	0,657354	0,664248

Table C-5: VHB 4905 at 200% Pre-strain Strain Tests

Pixel Count			Displacement (pixels)				Strain (%)			
Voltage	Horiz	Vert	Voltage	Horiz	Vert	Ave	Voltage	Horiz	Vert	Average
0	1256	1256	0	0	0	0	0	0	0	0
3	1265	1270	3	9	14	11,5	3	0,716561	1,11465	0,915605
6	1307	1307	6	51	51	51	6	4,06051	4,06051	4,06051
9	1350	1355	9	94	99	96,5	9	7,484076	7,882166	7,683121
12	1379	1386	12	123	130	126,5	12	9,792994	10,35032	10,07166
0	1237	1235	0	0	0	0	0	0	0	0
3	1251	1255	3	14	20	17	3	1,13177	1,619433	1,375602
6	1292	1298	6	55	63	59	6	4,446241	5,101215	4,773728
9	1353	1358	9	116	123	119,5	9	9,377526	9,959514	9,66852
12	1413	1423	12	176	188	182	12	14,22797	15,22267	14,72532
0	1271	1272	0	0	0	0	0	0	0	0
3	1265	1270	3	-6	-2	-4	3	-0,47207	-0,15723	-0,31465
6	1307	1307	6	36	35	35,5	6	2,832415	2,751572	2,791994
9	1350	1355	9	79	83	81	9	6,215578	6,525157	6,370368
12	1399	1407	12	128	135	131,5	12	10,07081	10,61321	10,34201

Table C-6: VHB 4910 at 200% Pre-strain Strain Tests

Pixel Count			Displacement (pixels)				Strain (%)			
Voltage	Horiz	Vert	Voltage	Horiz	Vert	Ave	Voltage	Horiz	Vert	Average
0	1248	1221	0	0	0	0	0	0	0	0
3	1254	1231	3	6	10	8	3	0,480769	0,819001	0,649885
6	1268	1239	6	20	18	19	6	1,602564	1,474201	1,538383
9	1287	1257	9	39	36	37,5	9	3,125	2,948403	3,036701
12	1316	1284	12	68	63	65,5	12	5,448718	5,159705	5,304212

Table C-7: VHB 4905 at 300% Pre-strain Strain Tests

Pixel Count			Displacement (pixels)				Strain (%)			
Voltage	Horiz	Vert	Voltage	Horiz	Vert	Ave	Voltage	Horiz	Vert	Average
0	1224	1237	0	0	0	0	0	0	0	0
3	1263	1283	3	39	46	42,5	3	3,186275	3,718674	3,452474
6	1335	1348	6	111	111	111	6	9,068627	8,973323	9,020975
9	1383	1392	9	159	155	157	9	12,9902	12,53032	12,76026
12			12				12			
0	1262	1238	0	0	0	0	0	0	0	0
3	1271	1247	3	9	9	9	3	0,713154	0,726979	0,720066
6	1327	1303	6	65	65	65	6	5,150555	5,250404	5,200479
9	1377	1344	9	115	106	110,5	9	9,11252	8,562197	8,837358
12	1416	1380	12	154	142	148	12	12,20285	11,47011	11,83648
0	1291	1265	0	0	0	0	0	0	0	0
3	1291	1265	3	0	0	0	3	0	0	0
6	1328	1307	6	37	42	39,5	6	2,865995	3,320158	3,093077
9	1383	1347	9	92	82	87	9	7,126259	6,482213	6,804236
12	1425	1385	12	134	120	127	12	10,37955	9,486166	9,932858

Table C-8: VHB 4910 at 300% Pre-strain Strain Tests

Pixel Count			Displacement (pixels)				Strain (%)			
Voltage	Horiz	Vert	Voltage	Horiz	Vert	Ave	Voltage	Horiz	Vert	Average
0	1242	1225	0	0	0	0	0	0	0	0
3	1255	1240	3	13	15	14	3	1,046699	1,22449	1,135594
6	1293	1280	6	51	55	53	6	4,10628	4,489796	4,298038
9	1339	1334	9	97	109	103	9	7,809984	8,897959	8,353972
12	1360	1349	12	118	124	121	12	9,500805	10,12245	9,811627
0	1439	1485	0	0	0	0	0	0	0	0
3	1484	1526	3	45	41	43	3	3,127172	2,760943	2,944057
6	1514	1563	6	75	78	76,5	6	5,211953	5,252525	5,232239
9	1547	1592	9	108	107	107,5	9	7,505212	7,205387	7,3553
12	1564	1636	12	125	151	138	12	8,686588	10,16835	9,427469

Table C-9: Carbon Grease Strain Tests

Pixel Count			**Displacement (pixels)**				**Strain (%)**			
Sample Set 1										
Voltage	Horiz	Vert	Voltage	Horiz	Vert	Ave	Voltage	Horiz	Vert	Average
0	994	988	0	0	0	0	0	0	0	0
3	998	996	3	4	8	6	3	0,402414	0,809717	0,606066
6	1016	1023	6	22	35	28,5	6	2,21328	3,54251	2,877895
9	1058	1062	9	64	74	69	9	6,438632	7,489879	6,964255
12	1135	1124	12	141	136	138,5	12	14,18511	13,76518	13,97515
12	1135	1124	12	141	136	138,5	12	14,18511	13,76518	13,97515
9	1059	1066	9	65	78	71,5	9	6,539235	7,894737	7,216986
6	1017	1023	6	23	35	29	6	2,313883	3,54251	2,928197
3	995	1000	3	1	12	6,5	3	0,100604	1,214575	0,657589
0	993	992	0	-1	4	1,5	0	-0,1006	0,404858	0,152127
Sample Set 2										
Voltage	Horiz	Vert	Voltage	Horiz	Vert	Ave	Voltage	Horiz	Vert	Average
0	975	977	0	0	0	0	0	0	0	0
3	986	989	3	11	12	11,5	3	1,128205	1,22825	1,178227
6	1007	1012	6	32	35	33,5	6	3,282051	3,582395	3,432223
9	1047	1052	9	72	75	73,5	9	7,384615	7,676561	7,530588
12	1109	1114	12	134	137	135,5	12	13,74359	14,02252	13,88305
12	1109	1114	12	134	137	135,5	12	13,74359	14,02252	13,88305
9	1067	1071	9	92	94	93	9	9,435897	9,62129	9,528594
6	1025	1035	6	50	58	54	6	5,128205	5,93654	5,532373
3	1003	1007	3	28	30	29	3	2,871795	3,070624	2,97121
0	987	992	0	12	15	13,5	0	1,230769	1,535312	1,383041
Sample Set 3										
Voltage	Horiz	Vert	Voltage	Horiz	Vert	Ave	Voltage	Horiz	Vert	Average
0	979	984	0	0	0	0	0	0	0	0
3	985	991	3	6	7	6,5	3	0,61287	0,711382	0,662126
6	1007	1012	6	28	28	28	6	2,860061	2,845528	2,852795
9	1043	1050	9	64	66	65	9	6,537283	6,707317	6,6223
12	1110	1115	12	131	131	131	12	13,381	13,31301	13,347
12	1112	1116	12	133	132	132,5	12	13,58529	13,41463	13,49996
9	1054	1061	9	75	77	76	9	7,660878	7,825203	7,743041
6	1021	1027	6	42	43	42,5	6	4,290092	4,369919	4,330005
3	1001	1004	3	22	20	21	3	2,247191	2,03252	2,139856
0	989	995	0	10	11	10,5	0	1,02145	1,117886	1,069668

C.2 Raw Data of Inflated Actuation Tests

The performance of the DEA proof-of-concept was investigated through a series of strain tests. The effect of initial diaphragm height and direction of electrode application on vertical diaphragm displacement was investigated. The test sets were divided according to application method; stippled samples, diagonally smeared samples, radially smeared samples and sealed stippled samples. Each sample set was split into initial height columns with the measurement at 0 V indicating initial height before actuation. Multiple observations were recorded at each initial height in order to ensure the repeatability of the results and experiment.

C.2.1 Stippled Sample Set

Table C-10: Stippled Sample Set: Initial Height 1.

Voltage (V)	H 1 (mm)	H 2 (mm)	H 3 (mm)	Average (mm)	Displacement (mm)
0	3,2	3,2	3,2	3,2	0
3	3,3	3,2	3,3	3,27	0,07
6	3,4	3,3	3,4	3,37	0,17
9	3,5	3,4	3,5	3,47	0,27
12	3,6	3,5	3,6	3,56	0,37

Table C-11: Stippled Sample Set: Initial Height 2.

Voltage (V)	H 1 (mm)	H 2 (mm)	H 3 (mm)	Average (mm)	Displacement (mm)
0	5,1	5,1	5,1	5,1	0
3	5,3	5,2	5,2	5,23	0,13
6	5,4	5,2	5,3	5,3	0,2
9	5,6	5,5	5,5	5,53	0,43
12	5,6	5,6	5,5	5,57	0,47

Table C-12: Stippled Sample Set: Initial Height 3.

Voltage (V)	H 1 (mm)	H 2 (mm)	H 3 (mm)	Average (mm)	Displacement (mm)
0	7,9	7,9	7,9	7,9	0
3	8,2	8,1	8,1	8,13	0,23
6	8,3	8,2	8,2	8,23	0,33
9	8,4	8,2	8,4	8,33	0,43
12	8,5	8,4	8,4	8,43	0,53

Table C-13: Stippled Sample Set: Initial Height 4.

Voltage (V)	H 1 (mm)	H 2 (mm)	H 3 (mm)	Average (mm)	Displacement (mm)
0	11,1	11,1	11,1	11,1	0
3	11,1	11,2	11,1	11,13	0,03
6	11,2	11,4	11,1	11,23333	0,13
9	11,4	11,8	11,6	11,6	0,50
12	12,7	12,5	12,5	12,566	1,46

C.2.2 Diagonally Smeared Sample Set

Table C-14: Diagonally Smeared Sample Set: Initial Height 1.

Voltage (V)	H 1 (mm)	H 2 (mm)	H 3 (mm)	Average (mm)	Displacement (mm)
0	3,4	3,2	3,1	3,23	0
3	3,4	3,2	3,2	3,27	0,03
6	3,5	3,3	3,3	3,37	0,13
9	3,7	3,4	3,4	3,50	0,27
12	3,8	3,6	3,5	3,63	0,40

Table C-15: Diagonally Smeared Sample Set: Initial Height 2.

Voltage (V)	H 1 (mm)	H 2 (mm)	H 3 (mm)	Average (mm)	Displacement (mm)
0	4,5	4,5	4,5	4,50	0
3	4,6	4,6	4,6	4,60	0,10
6	4,7	4,7	4,7	4,70	0,20
9	4,8	4,9	4,8	4,83	0,33
12	5	5	5	5.00	0,50

Table C-16: Diagonally Smeared Sample Set: Initial Height 3.

Voltage (V)	H 1 (mm)	H 2 (mm)	H 3 (mm)	Average (mm)	Displacement (mm)
0	5,1	5,1	5,1	5,10	0
3	5,2	5,3	5,2	5,23	0,13
6	5,3	5,5	5,3	5,37	0,27
9	5,6	5,6	5,5	5,57	0,47
12	6	5,9	5,9	5,93	0,83

Table C-17: Diagonally Smeared Sample Set: Initial Height 4.

Voltage (V)	H 1 (mm)	H 2 (mm)	H 3 (mm)	Average (mm)	Displacement (mm)
0	6,1	6,1	6	6,07	0
3	6,3	6,3	6,2	6,27	0,20
6	6,5	6,6	6,4	6,50	0,43
9	6,8	6,6	6,8	6,73	0,67
12	7	7	6,9	6,97	0,90

Table C-18: Diagonally Smeared Sample Set: Initial Height 5.

Voltage (V)	H 1 (mm)	H 2 (mm)	H 3 (mm)	Average (mm)	Displacement (mm)
0	6,9	6,9	6,9	6,90	0
3	7	7	7	7.00	0,10
6	7,1	7,1	7,1	7,10	0,20
9	7,3	7,4	7,3	7,33	0,43
12	7,8	7,8	7,8	7,80	0,90

Table C-19: Diagonally Smeared Sample Set: Initial Height 6.

Voltage (V)	H 1 (mm)	H 2 (mm)	H 3 (mm)	Average (mm)	Displacement (mm)	Voltage (V)
0	7,8	7,8	7,8	7,8	7,8	0
3	7,9	7,8	7,9	7,9	7,875	0,075
6	8	8	8,1	8	8,025	0,225
9	8,1	8,1	8,2	8,1	8,125	0,325
12	8,3	8,3	8,3	8,3	8,3	0,5

Table C-20: Diagonally Smeared Sample Set: Initial Height 7.

Voltage (V)	H 1 (mm)	H 2 (mm)	H 3 (mm)	Average (mm)	Displacement (mm)
0	10,8	10,7	10,6	10,70	0
3	10,8	10,7	10,7	10,73	0,03
6	10,9	10,9	10,8	10,87	0,17
9	10,9	10,9	10,8	10,87	0,17
12	10,6	10,6	10,5	10,57	-0,13

Table C-21: Diagonally Smeared Sample Set: Initial Height 8.

Voltage (V)	H 1 (mm)	H 2 (mm)	H 3 (mm)	Average (mm)	Displacement (mm)
0	11,9	11,9	11,9	11,90	0
3	11,9	11,9	11,8	11,87	-0,03
6	11,9	11,9	11,8	11,87	-0,03
9	11,8	11,8	11,7	11,77	-0,13
12	11,5	11,5	11,6	11,53	-0,37

C.2.3 Radially Smeared Sample Set

Table C-22: Radially Smeared Sample Set: Initial Height 1.

Voltage (V)	H 1 (mm)	H 2 (mm)	H 3 (mm)	Average (mm)	Displacement (mm)
0	3,4	3,5	3,5	3,47	0
3	3,5	3,6	3,6	3,57	0,10
6	3,6	3,7	3,8	3,70	0,23
9	3,8	3,8	3,9	3,83	0,37
12	3,9	3,9	4	3,93	0,47

Table C-23: Radially Smeared Sample Set: Initial Height 2.

Voltage (V)	H 1 (mm)	H 2 (mm)	H 3 (mm)	H 4 (mm)	H 5 (mm)	Displacement (mm)
0	5	5,1	5,1	5,1	5,08	0
3	5,1	5,2	5,1	5,1	5,13	0,05
6	5,2	5,2	5,2	5,2	5,20	0,13
9	5,3	5,3	5,3	5,4	5,33	0,25
12	5,5	5,5	5,6	5,6	5,55	0,48

Table C-24: Radially Smeared Sample Set: Initial Height 3.

Voltage (V)	H 1 (mm)	H 2 (mm)	H 3 (mm)	Average (mm)	Displacement (mm)
0	6,7	6,8	6,7	6,73	0
3	6,8	6,8	6,8	6,80	0,07
6	6,9	6,9	6,9	6,90	0,17
9	7	7	7	7,00	0,27
12	7,3	7,4	7,4	7,37	0,63

Table C-25: Radially Smeared Sample Set: Initial Height 4.

Voltage (V)	H 1 (mm)	H 2 (mm)	H 3 (mm)	H 4 (mm)	Average (mm)	Displacement (mm)
0	7,5	7,5	7,5	7,5	7,50	0
3	7,6	7,6	7,7	7,6	7,63	0,13
6	7,8	7,8	7,8	7,8	7,80	0,30
9	8	7,9	7,9	7,8	7,90	0,40
12	8,3	8,2	8,2	8,2	8,23	0,73

Table C-26: Radially Smeared Sample Set: Initial Height 5.

Voltage (V)	H 1 (mm)	H 2 (mm)	H 3 (mm)	Average (mm)	Displacement (mm)
0	10,6	10,5	10,5	10,53	0
3	10,8	10,7	10,7	10,73	0,20
6	10,9	10,8	10,8	10,83	0,30
9	10,9	10,9	10,9	10,90	0,37
12	10,9	11	10,9	10,93	0,40

Table C-27: Radially Smeared Sample Set: Initial Height 6.

Voltage (V)	H 1 (mm)	H 2 (mm)	H 3 (mm)	Average (mm)	Displacement (mm)
0	12,9	13	13	12,97	0
3	12,9	12,9	12,9	12,90	-0,07
6	12,9	12,9	12,9	12,90	-0,07
9	12,9	12,9	12,9	12,90	-0,07
12	12,5	12,6	12,6	12,57	-0,40

C.2.4 Stippled Sealed Sample Set

Table C-28: Stippled Sealed Sample Set: Initial Height 1.

Voltage (V)	H 1 (mm)	H 2 (mm)	H 3 (mm)	H 4 (mm)	Average (mm)	Displacement (mm)
0	3,1	3,1	3,1	3,1	3,10	0
3	3,1	3,2	3,2	3,2	3,16	0,08
6	3,2	3,3	3,5	3,5	3,38	0,28
9	3,3	3,4	3,6	3,6	3,48	0,38
12	3,5	3,7	3,7	3,7	3,65	0,55

Table C-29: Stippled Sealed Sample Set: Initial Height 2.

Voltage (V)	H 1 (mm)	H 2 (mm)	H 3 (mm)	H 4 (mm)	Average (mm)	Displacement (mm)
0	5,8	5,9	6	6	5,93	0
3	5,9	6	6,1	6,1	6,02	0,10
6	6	6,1	6,3	6,2	6,15	0,23
9	6,1	6,2	6,4	6,4	6,28	0,35
12	6,5	6,5	6,7	6,7	6,60	0,68

Table C-30: Stippled Sealed Sample Set: Initial Height 3.

Voltage (V)	H 1 (mm)	H 2 (mm)	H 3 (mm)	Average (mm)	Displacement (mm)
0	11,2	11,2	11,2	11,20	0
3	11,3	11,5	11,6	11,47	0,27
6	11,7	11,8	11,8	11,77	0,57
9	11,9	11,9	11,9	11,90	0,70
12	12	12	12	12,00	0,80

Table C-31: Stippled Sealed Sample Set: Initial Height 4.

Voltage (V)	H 1 (mm)	H 2 (mm)	H 3 (mm)	Average (mm)	Displacement (mm)
0	8,8	8,7	8,7	8,73	0
3	8,8	8,8	8,8	8,80	0,07
6	8,9	8,9	8,9	8,90	0,17
9	9	9	8,9	8,97	0,23
12	9,1	9,1	9,1	9,10	0,37

C.3 Raw data of Optical Character Recognition program analysis

The analysis conducted on the OCR program included tests to compare the program reaction time and accuracy under various conditions. The variables included four types of font, and number of characters per sample image. The settings of the program were also toggled on/off to analyse the effect on the results. The number of characters per sample were divided into two categories; the first identified as ‘multiple characters’ included the full alphabet of each font type, the ‘single character’ category included individual images of each letter in the alphabet of each font type.

C.3.1 Multiple Character Sample Sets

Table C-31: Ariel font multiple sample test

Test no.	Description	Output	Time (s)
1	Ariel full alphabet. Resize, convert to gray, blur preprocessing active. Remove line break active. Psm not configured. LED output active.	ABCDEFGHIJK LMNOPQRSTU VWXYZ (all single line)	7.0157
2	Ariel full alphabet. Resize, convert to gray, blur preprocessing active. Remove line break deactivated. Psm not configured. LED output active.	ABCDEFGHIJ KLMNOPQRS TUVWXYZ Music symbol	6.975
3	Ariel full alphabet. Resize, convert to gray, blur preprocessing deactivated. Remove line break active. Psm not configured. LED output active.	ABCDEFGHIJK LMNOPQRSTU VWXYZ (all single line)	4.734
4	Ariel full alphabet. Resize, convert to gray, blur preprocessing active. Remove line break active. Psm configured to 3. LED output active.	ABCDEFGHIJK LMNOPQRSTU VWXYZ (all single line)	7.031
5	Blur deactivated	ABCDEFGHIJK LMNOPQRSTU VWXYZ (all Single line)	4.286
6	Gray deactivated	ABCDEFGHIJK LMNOPQRSTU VWXYZ	8.108
7	Image resize deactivated	ABCDEFGHIJK LMNOPQRSTU VWXYZ	12.091

Table C-32: Serif font multiple sample test

Test no.	Description	Output	Time (s)
1	Font 2 full alphabet. Resize, convert to gray, blur preprocessing active. Remove line break active. Psm not configured. LED output active.	ATQeVOMOUBNHeZkrrddnsOp	6.875
2	Font 2 full alphabet. Resize, convert to gray, blur preprocessing active. Remove line break deactivated. Psm not configured. LED output active.	AT Qe VOMOUBN He Zkrr ddnsOp music symbol	6.843
3	Font 2 full alphabet. Resize, convert to gray, blur preprocessing deactivated. Remove line break active. Psm not configured. LED output active.	ATAAEXKOONODESENMaeAMPqesOp	4.438
4	Font 2 alphabet. Resize, convert to gray, blur preprocessing active. Remove line break active. Psm configured to 3. LED output active.	ATQeVOMOUBNHeZkrrddnsOp	6.858
5	Blur deactivated	AmaneMOOMOWBNHaeZ2hppdQSOD	4.203
6	Gray deactivated	AmAnHMOOMOWBNHaeZ2hppdQHS0p	8.291
7	Image resize deactivated	ATAAEXKOOMNODESENMaeA2Mppqesop	7.382

Table C-33: Typewriter font multiple sample test

Test no.	Description	Output	Time (s)
1	Font 3 full alphabet. Resize, convert to gray, blur preprocessing active. Remove line break active. Psm not configured. LED output active.	When small letters removed: ABCDEEGHIJKLMCPORSTUVXYZ	9.162
2	Font 3 full alphabet. Resize, convert to gray, blur preprocessing active. Remove line break deactivated. Psm not configured. LED output active.	ABCDEEGHIJKL MCPORSTUVWYZ	9.143
3	Font 3 full alphabet. Resize, convert to gray, blur preprocessing deactivated. Remove line break active. Psm not configured. LED output active.	ABCDEFGHIJKLMNCPGRSTUVXYZ	4.772
4	Font 3 alphabet. Resize, convert to gray, blur preprocessing active. Remove line break active. Psm configured to 3. LED output active.	ABCDEEGHIJKLMCPORSTUVXYZ	9.173
5	Blur deactivated	ABCDREGHIJKLNOPORSTUIXYZ	4.586
6	Gray deactivated	ABCDEEGHIJKLMPORSTUVXYZ	9.732
7	Image resize deactivated	ABCDEFGHIJKLMNCPGRSTUVXYZ	7.764

Table C-34: Times New Roman font multiple sample test

Test no.	Description	Output	Time (s)
1	Font 4 full alphabet. Resize, convert to gray, blur preprocessing active. Remove line break active. Psm not configured. LED output active.	ABCDEFGHIJKLMNOPQRSTUVWXYZ All single line	6.953
2	Font 4 full alphabet. Resize, convert to gray, blur preprocessing active. Remove line break deactivated. Psm not configured. LED output active.	ABCDEFGHIJ KLMNOPQRS TUVWXYZ Music symbol	7.009
3	Font 4 full alphabet. Resize, convert to gray, blur preprocessing deactivated. Remove line break active. Psm not configured. LED output active.	ABCDEFGHIJKLMNOPQRSTUVWXYZ All single line	4.724
4	Font 4 full alphabet. Resize, convert to gray, blur preprocessing active. Remove line break active. Psm configured to 3. LED output active.	ABCDEFGHIJKLMNOPQRSTUVWXYZ All single line	7.061
5	Blur deactivated	ABCDEFGHIJKLMNOPQRSTUVWXYZ All single line	4.356
6	Gray deactivated	ABCDEFGHIJKLMNOPQRSTUVWXYZ All single line	8.297
7	Image resize deactivated	ABCDEFGHIJKLMNOPQRSTUVWXYZ All single line	9.398

Table C-35: Lower case Ariel font multiple sample test

Test no.	Description	Output	Time (s)
1	Ariel lower case alphabet. Resize, convert to gray, blur preprocessing active. Remove line break active. Psm not configured. LED output active.	abcdefghijklmnopgqrstuvwXyZ (All single line)	6.599
2	Resize, convert to gray, blur preprocessing active. Remove line break deactivated. Psm not configured. LED output active.	Abcdefghijkl mnopgqrstuvw XyZ Music symbol	6.609
3	Resize, convert to gray, blur preprocessing deactivated. Remove line break active. Psm not configured. LED output active.	abcdefghijklmnopgqrstuvwXyZ (All single line)	4.660
4	Resize, convert to gray, blur preprocessing active. Remove line break active. Psm configured to 3. LED output active.	abcdefghijklmnopgqrstuvwXyZ (All single line)	6.607
5	Blur deactivated	abcdefghijklmnoparstuvwXyZ (All single line)	4.289
6	Gray deactivated	abcdefghijklmnopgqrstuvwXyZ (All single line)	8.017
7	Image resize deactivated	abcdefghijklmnopqrstuvwXyZ (All single line)	8.843

Table C-36: Lower case Times New Roman font multiple sample test

Test no.	Description	Output	Time (s)
1	Times New Roman lowercase alphabet. Resize, convert to gray, blur preprocessing active. Remove line break active. Psm not configured. LED output active.	abcdefghijklmnopqrstuvwXyZ (single line)	7.177
2	Resize, convert to gray, blur preprocessing active. Remove line break deactivated. Psm not configured. LED output active.	Abcdefghijkl mnopqrstuvw XyZ Music symbol	6.864
3	Resize, convert to gray, blur preprocessing deactivated. Remove line break active. Psm not configured. LED output active.	abcdefghijklmnopqrstuvwXyZ (single line)	4.675
4	Resize, convert to gray, blur preprocessing active. Remove line break active. Psm configured to 3. LED output active.	abcdefghijklmnopqrstuvwXyZ (single line)	6.827
5	Blur deactivated	abcdefghijklmnopqrstuvwXyZ (single line)	4.269
6	Gray deactivated	abcdefghijklmnopqrstuvwXyZ (single line)	8.130
7	Image resize deactivated	abcdefghijklmnopqrstuvwXYZ (single line)	8.675

C.3.2 Single Character Sample Sets

Table C-37: Ariel font single characters sample test

Test no.	Description	Output	Time
1	A. Ariel single character. Resize, convert to gray, blur preprocessing active. Remove line break active. Psm configured to 10. LED output active.	A	5.672
2	B Same as above	B	5.774
3	C	C	5.640
4	D	D	5.620
5	E	E	5.710
6	F	NO OUTPUT SHOWS F WHEN IMAGE RESIZE DEACTIVATED	5.651 4.299
7	G	G	5.759
8	H	H	5.671
9	I	NO OUTPUT ALL PREPROCESSES TOGGLED, NO CHANGE	5.706
10	J	J	5.645
11	K	K	5.637
12	L	L	5.692
13	M	M	5.696
14	N	N	5.736
15	O	O	5.692
16	P	NO OUTPUT, P WHEN IMAGE RESIZE DEACTIVATED	5.709 4.126
17	Q	Q	5.675
18	R	rR, R WHEN IMAGE RESIZE DEACTIVATED	5.688 4.289
19	S	S	5.751
20	T	T	5.619
21	U	U	5.713
22	V	V	5.673
23	W	W	5.882
24	X	X	5.727
25	Y	Y	5.690
26	Z	Z	5.666

Table C-38: Serif font single characters sample test

Test no.	Description	Output	Time
1	A. Font 2 single character. Resize, convert to gray, blur preprocessing active. Remove line break active. Psm configured to 10. LED output active.	A	5.644
2	B	NO OUTPUT, B WHEN IMAGE RESIZE DEACTIVATED	5.641 4.077
3	C	C	5.641
4	D	D	5.639
5	E	Kk, E WHEN IMAGE RESIZE DEACTIVATED	5.675 4.104
6	F	F	5.596
7	G	G	5.669
8	H	H	5.575

9	I	I	5.616
10	J	J	5.589
11	K	K	5.619
12	L	L	5.609
13	M	M	5.623
14	N	N	5.644
15	O	O	5.682
16	P	Pp, Pp WHEN IMAGE RESIZE DEACTIVATED, Pp WHEN ALL PREPROCESSES DEACTIVATED	5.641 4.073 3.927
17	Q	Q	5.609
18	R	R	5.664
19	S	S	5.634
20	T	T	5.619
21	U	U	5.566
22	V	V	5.652
23	W	W	5.612
24	X	Xx,X WHEN IMAGE RESIZE DEACTIVATED	5.604 4.142
25	Y	Y	5.609
26	Z	Z	5.678

Table C-39: Typewriter font single characters sample test

Test no.	Description	Output	Time
1	A. Font 3 single character. Resize, convert to gray, blur preprocessing active. Remove line break active. Psm configured to 10. LED output active.	A	5.782
2	B	NO OUTPUT, B WHEN IMAGE RESIZE DEACTIVATED	5.788 4.109
3	C	C	5.824
4	D	D	4.074
5	E	Fe, E WHEN IMAGE RESIZE DEACTIVATED	5.807 4.089
6	F	LOWER CASE I, EF WHEN IMAGE RESIZE DEACTIVATED	5.782 4.099
7	G	NO OUTPUT, G WHEN IMAGE RESIZE DEACTIVATED	5.852 4.094
8	H	Hi, H WHEN IMAGE RESIZE DEACTIVATED	5.902 4.110
9	I	L, L WHEN IMAGE RESIZE DEACTIVATED	5.687 4.075
10	J	eS, LOWER CASE a WHEN IMAGE RESIZE DEACTIVATED, uo WHEN ALL PREPROCESSES DEACTIVATED	5.738 4.109 3.952
11	K	K	5.779
12	L	LL, L WHEN IMAGE RESIZE DEACTIVATED	5.761 4.047
13	M	Vi, Ni WHEN IMAGE RESIZE DEACTIVATED, Ni WHEN ALL PREPROCESSES DEACTIVATED	5.842 4.117 3.987
14	N	IN, N WHEN IMAGE RESIZE DEACTIVATED	5.893 4.096

15	O	C, CO WHEN IMAGE RESIZE DEACTIVATED, CO WHEN ALL PREPROCESSING DEACTIVATED	5.804 4.108 3.989
16	P	br, P WHEN IMAGE RESIZE DEACTIVATED	5.802 4.135
17	Q	heat, GQ WHEN IMAGE RESIZE DEACTIVATED,G WHEN ALL PREPROCESSES DEACTIVATED	5.844 4.137 3.994
18	R	R	5.894
19	S	S	5.933
20	T	L, BI WHEN IMAGE RESIZE DEACTIVATED, YT WHEN ALL PREPROCESSES DEACTIVATED	3.579 4.121 3.975
21	U	U	5.764
22	V	V	5.835
24	X	X	5.836
25	Y	Yy, Y WHEN IMAGE RESIZE DEACTIVATED	5.786 4.089
26	Z	3, ZA WHEN IMAGE RESIZE DEACTIVATED,Z WHEN ALL PREPROCESSING DEACTIVATED	5.803 3.963

Table C-40: Times New Roman font single characters sample test

Test no.	Description	Output	Time
1	A. Font 4 single character. Resize, convert to gray, blur preprocessing active. Remove line break active. Psm configured to 10. LED output active.	A	5.679
2	B	B	5.626
3	C	C	5.646
4	D	D	5.647
5	E	K, E WHEN IMAGE RESIZE DEACTIVATED	5.659 4.139
6	F	F	5.690
7	G	G	5.688
8	H	H	5.706
9	I	I	5.602
10	J	J	5.608
11	K	K	5.716
12	L	L	5.625
13	M	Mi, M WHEN IMAGE RESIZE DEACTIVATED	5.722 4.176
14	N	N	5.658
15	O	O	5.654
16	P	P	5.716
17	Q	Q	5.664
18	R	R	5.703
19	S	S	5.588
20	T	I, T WHEN IMAGE RESIZE DEACTIVATED	5.563 4.112
21	U	U	5.627
22	V	V	5.654
24	X	NO OUTPUT, xX WHEN IMAGE RESIZE DEACTIVATED, xX WHEN ALL PREPROCESSES DEACTIVATED	5.750 4.202 3.998
25	Y	Y	5.695
26	Z	LL, L WHEN IMAGE RESIZE DEACTIVATED, L WHEN ALL PREPROCESSES DEACTIVATED	5.696 4.137 3.936

Table C-41: Lowercase Ariel font single characters sample test

Test	Description	Output	Time
1	a. Font 1 single character. Resize, convert to gray, blur preprocessing active. Remove line break active. Psm configured to 10. LED output active.	a	5.647
2	b	D, b WHEN IMAGE RESIZE DEACTIVATED	5.630 4.171
3	c	C, Cc WHEN IMAGE RESIZE DEACTIVATED	5.616 4.106
4	d	re, d WHEN IMAGE RESIZE DEACTIVATED	5.651 4.123
5	e	NO OUTPUT, e WHEN IMAGE RESIZE DEACTIVATED	5.674 4.072
6	f	Ff, f WHEN IMAGE RESIZE DEACTIVATED	5.650 4.071
7	g	Gg, g WHEN IMAGE RESIZE IS DEACTIVATED	5.643 4.203
8	h	Nn, h WHEN IMAGE RESIZE IS DEACTIVATED	5.694 4.164
9	i	ll, NO OUTPUT WHEN IMAGE RESIZE DEACTIVATED, i WHEN ALL PREPROCESSING DEACITVATED	5.547 4.048 3.943
10	j	J, j WHEN IMAGE RESIZE DEACTIVATED	5.632 4.075
11	k	k	5.652
12	l	NO OUTPUT, I WHEN IMAGE RESIZE DEACTIVATED, I WHEN ALL PREPROCESSES DEACTIVATED	5.610 4.126 3.975
13	m	mM, m WHEN IMAGE RESIZE DEACTIVATED	5.640 4.142
14	n	Mm, Nn WHEN IMAGE RESIZE DEACTIVATED, Nn WHEN ALL PREPROCESSES DEACTIVATED	5.659 4.104 3.977
15	o	O, O WHEN IMAGE RESIZE DEACTIVATED	5.666 4.132
16	p	p	5.711
17	q	q	5.615
18	r	r	5.616
19	s	S	5.679
20	t	t	5.614
21	u	U, U WHEN IMAGE RESIZE DEACTIVATED	5.587 4.041
22	v	V, V WHEN IMAGE RESIZE DEACTIVATED	5.601 4.115
24	x	X, X WHEN IMAGE RESIZE DEACTIVATED	5.649 4.155
25	y	y	5.625
26	z	z	5.621

Appendix D – Sample Preparation

Chapters 5 and 6 discussed the results of experiments conducted on the proof-of-concept DEAs. The DEAs were constructed using an elastomer matrix, specifically VHB 4905 and VHB 4910, and two compliant electrodes. The electrodes were synthesised using a variety of materials to select the option most applicable to the performance of the design. The electrode materials that were tested included two grades of graphite powder, Pressol and Microfyn, and a carbon conductive grease manufactured by MG Chemicals. Additional materials required for synthesis included laser cut Perspex frames, non-adhesive stencils, copper tape, M6 nuts and bolts, silicone adhesive, rubber gasket, cotton swab and paintbrush. The images and description below were utilised during the testing discussed in both Chapters 5 and 6. Additional steps were required for Chapter 6, as indicated in the descriptions below.

The first step in preparing the DEA samples for testing included removing the white backing paper from the VHB double sided adhesive tape, as seen in Figure D-1. Thereafter a marker and non-adhesive stencil was used to mark off a circle of 35mm diameter. The marked off section of tape is illustrated in Figure D-2. The red backing layer was then removed from the opposite side of the VHB film. Care was taken at this point to ensure that the film did not warp and stick to itself or any particles on the work surface.

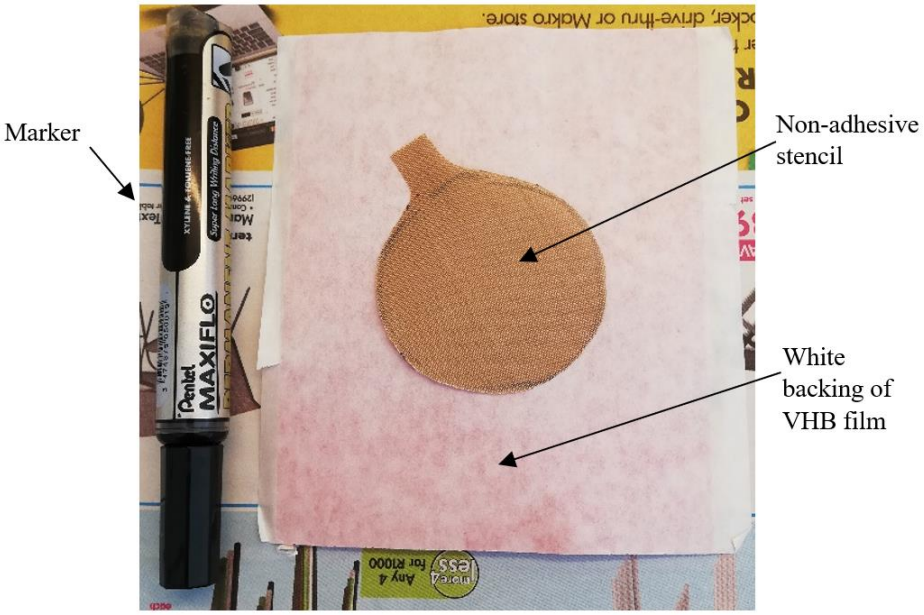

Figure D-1: VHB 4910 film before removal of backing and stencil used to mark circle for pre-strain

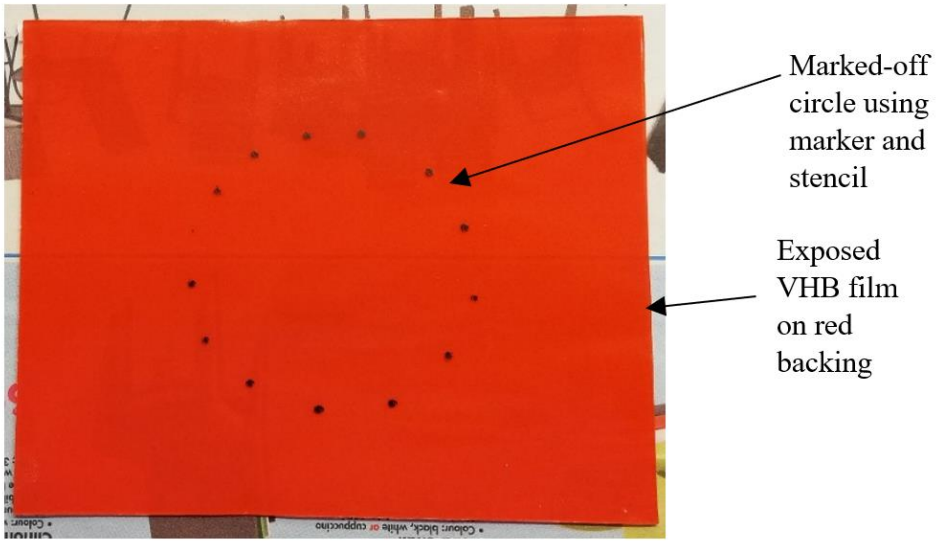

Figure D-2: VHB 4910 film with marked of 35mm diameter circle

The film was then stretched across a Perspex frame such as the example presented in Figure D-3. The diameter of the Perspex frames corresponded with the required percentage of pre-strain required of the sample. The sample was stretched across the frame until the marked off points on the film lined up with the inner face of the frame. A second frame was then lined up and pressed against the first to sandwich the film between them and allow for greater manoeuvrability during electrode synthesis.

Figure D-3: Elastomer film stretched across Perspex frame

Once stretched and secured using the frame, the pre-strained VHB film could now be placed on the work surface and the electrodes applied. Two methods were used to apply the electrode

materials. Both required a small non-adhesive circular stencil to be placed on the film to ensure a clean edge when applying the materials to the adhesive surface, labelled in Figure D-4. The stencils were laser cut from non-adhesive backing material to ensure precise dimensions. The graphite powder electrodes were applied using a fine paint brush. The paint brush was dipped in the powder, tapped lightly against the side of the container to remove excess and then brushed onto the exposed surface of the VHB film, see Figure D-5. Alternatively, the carbon conductive grease samples were applied using a cotton swab such as in Figure D-4 (a). The stencils were then removed to leave an electrode such as the sample seen in Figure D-4 (b). Multiple samples could be synthesised from a single pre-strained film. Thereafter the film was flipped over, and the electrode materials were applied on the opposite face.

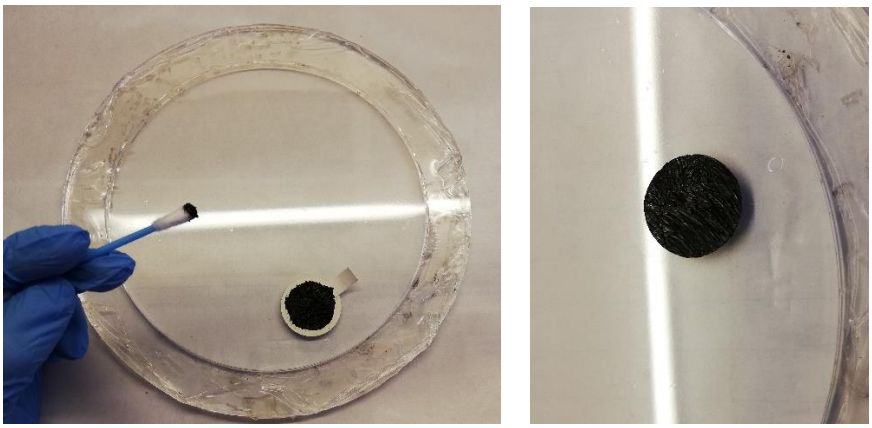

(a) (b)

Figure D-4: Application of carbon grease electrode on pre-strained film. (a) Patterning electrode using cotton swab and non-adhesive stencil, (b) Completed electrode with stencil removed

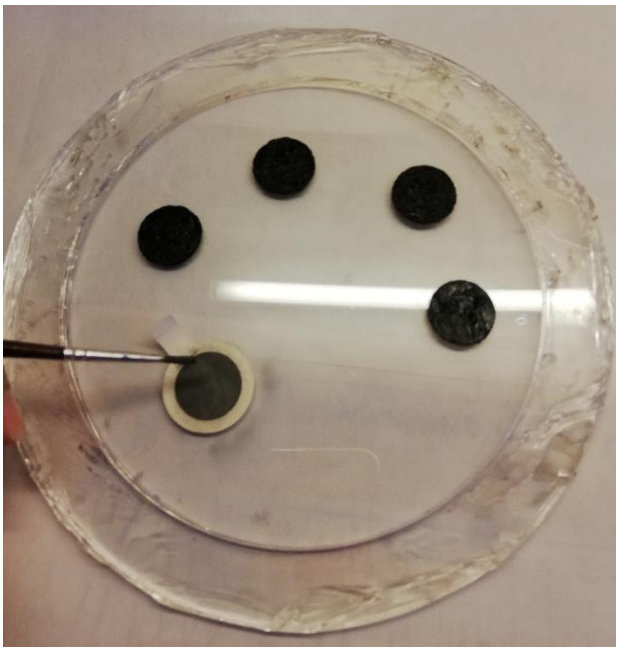

Figure D-5: Patterning of graphite electrode on pre-strained film

Once both sides of the electrodes were applied, conductive leads were constructed using the electrode material and copper tape, Figures D-6 and D-7. Once the leads were secured, smaller Perspex frames were attached to either side of the film. Once all samples on one pre-strained section were secured using the smaller frames, a craft knife was used to remove each sample form the larger Perspex frame. Note: the sample in Figure D-6 was used to investigate radial strain of the DEA, therefore the Perspex frame had to be larger than the electrode diameter to allow for radial expansion. The sample represented in Figure D-7 was instead used to analyse the properties of the inflated diaphragm-type DEA, therefore the edges of the electrode were required to be constrained by the frame.

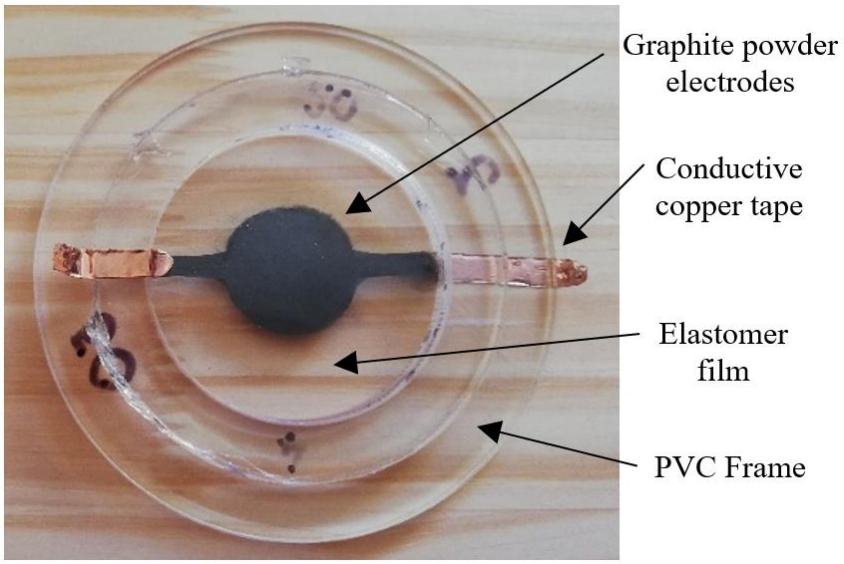

Figure D-6: Sample prepared for radial strain testing

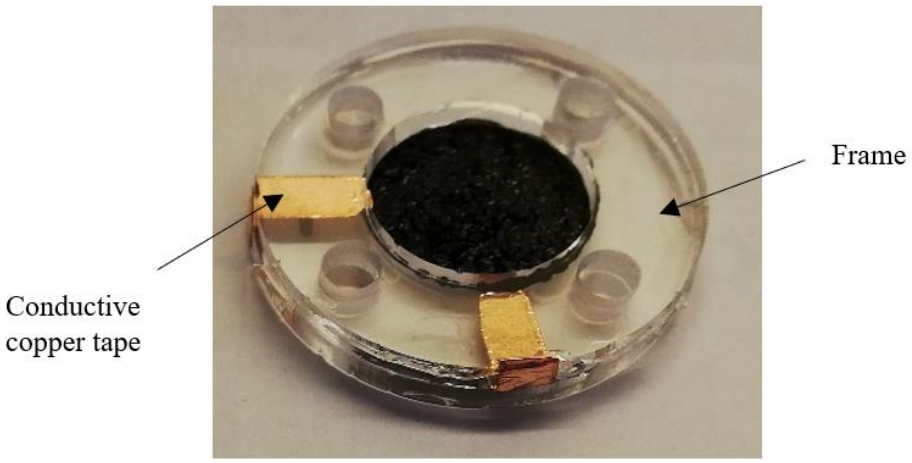

Figure D-7: Sample prepared for diaphragm DEA performance analysis

The following step was only required for the performance analysis of the diaphragm-type DEAs discussed in Chapter 6. Note in Figure D-7 the Perspex frame had four holes drilled along the

edge. Similarly, a rubber gasket of equal diameter also had four holes drilled along the edge. This was used to secure the third Perspex plate to the bottom of the assembly and create a sealed cavity, see Figure D-8. A needle and syringe were then used to inflate the cavity by inserting the needle along the edge of the gasket. Thereafter, the bolts were tightened, and the sample was ready for testing. Figure D-9 illustrates the finished sample attached to the test circuit.

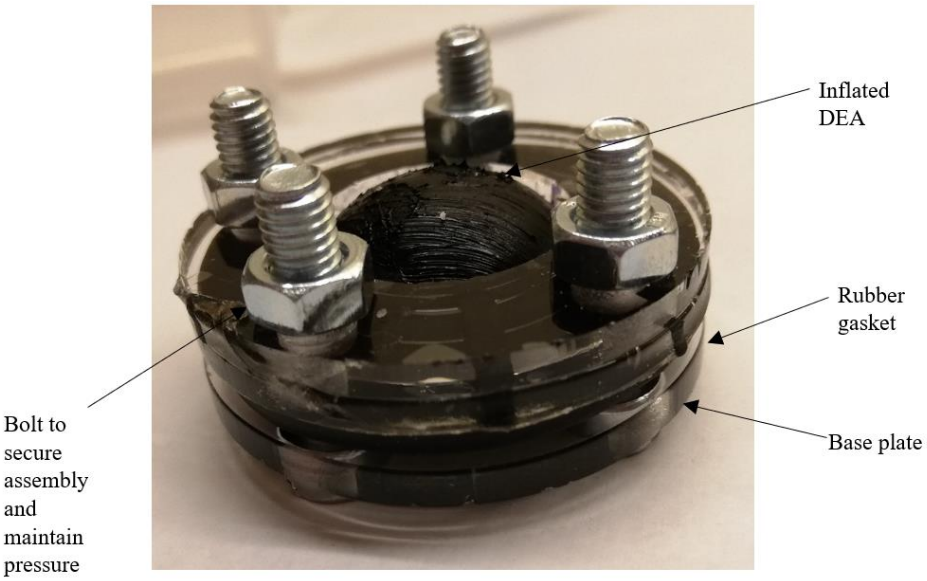

Figure D-8: Completed diaphragm-type DEA with inflated cavity

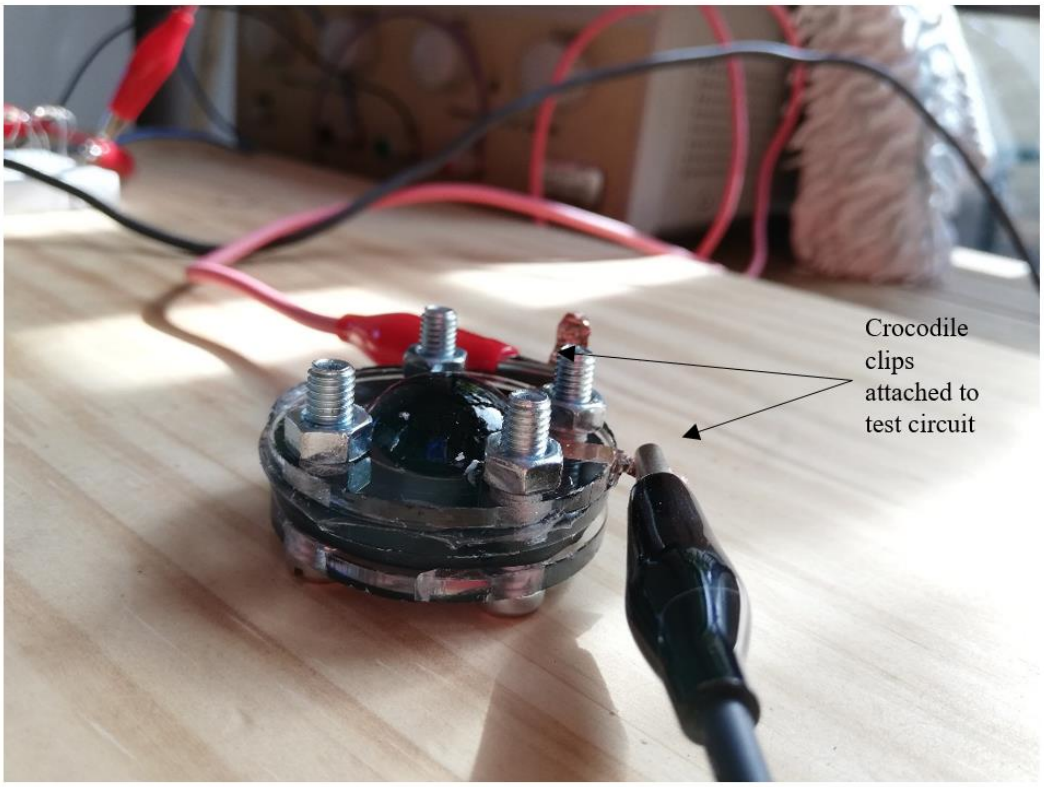

Figure D-9: DEA attached to test circui

Appendix E – Engineering Drawings

Table E-1: Schedule of drawings

No.	Drawing Description	Drawing Number
1	Circuit Casing Cover	A1
2	Battery Casing	A2
3	Circuit Casing	A3
4	Circuit Casing Subassembly Type 1	SA1
5	Circuit Casing Subassembly Type 2	SA2
6	Finger Mounting	A4
7	Exploded View of Actuator Assembly	SA3
8	Actuator Assembly	SA4

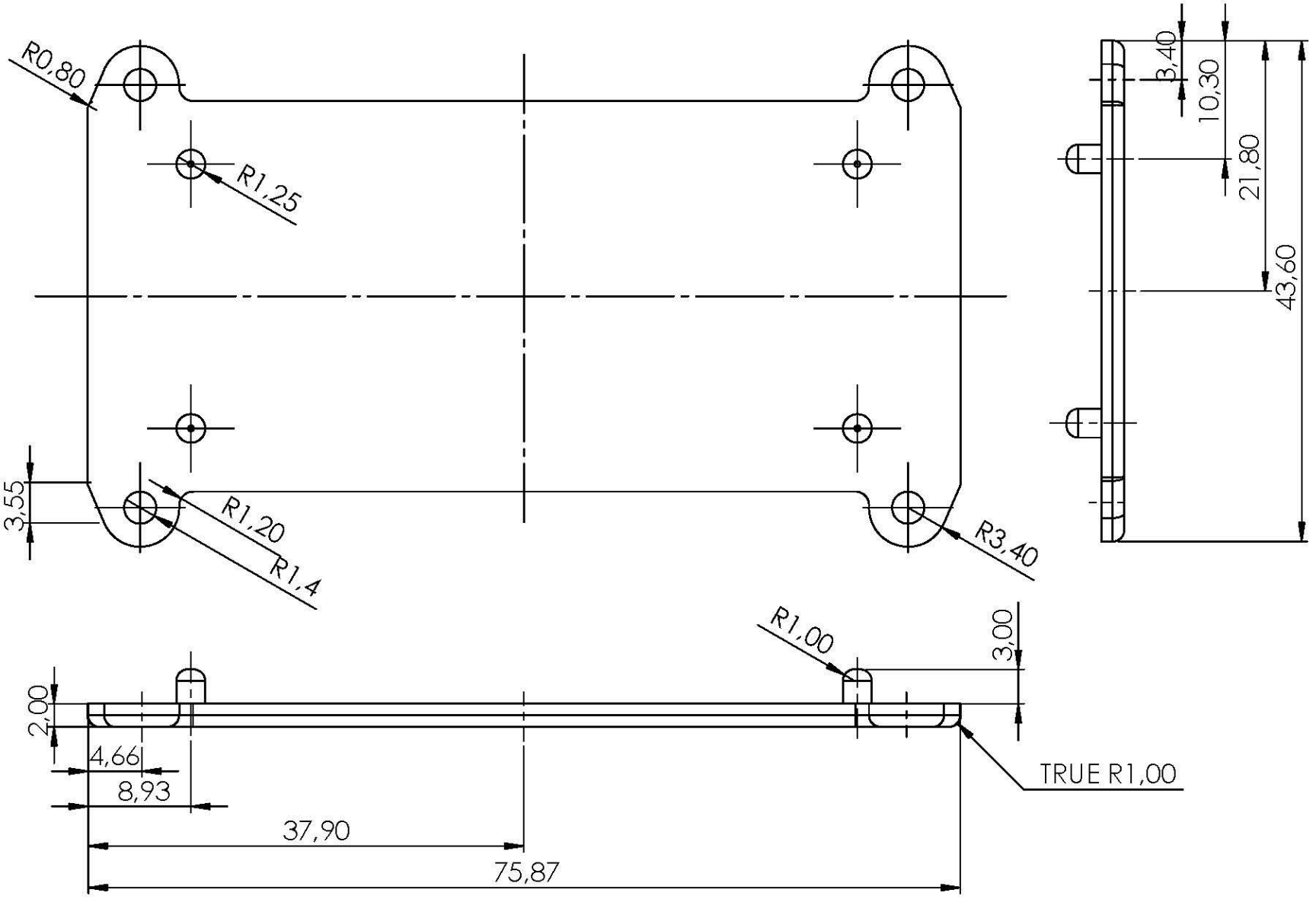

UNLESS OTHERWISE STATED GENERAL
TOLERANCES : 0,05 mm
ANGLES : 1

UNIVERSITY OF KWAZULU-NATAL	MAT.: PLA	No. REQ.: 1	SCALE: 2:1	UNITS: mm	PROJECT: TACTILE BRAILLE READER
	DATE	CHECKED	STUDENT NAME: INGRID BOTHA		No.: A1
SCHOOL OF ENGINEERING	PROJECT SUPERVISOR		STUDENT No.: 215024569		
MECHANICAL ENGINEERING	WORKSHOP TECHNICIAN		E-MAIL: 215024569@STU.UKZN		TITLE: CIRCUIT CASING COVER
	TECHNICAL OFFICER		TEL. No.: AC7A		

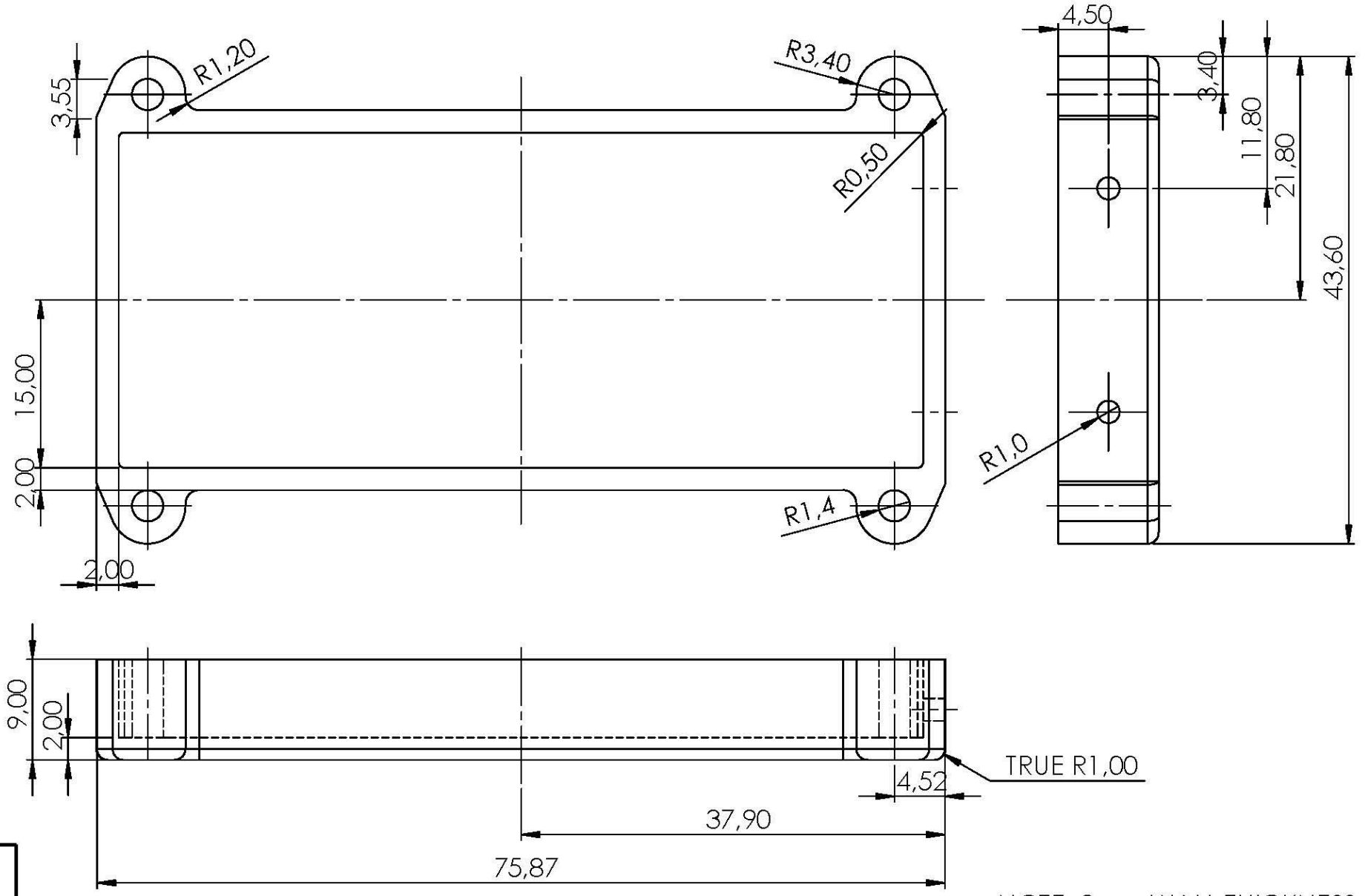

UNLESS OTHERWISE STATED GENERAL TOLERANCES : 0,01 mm
ANGLES : 1

NOTE: 2mm WALL THICKNESS

UNIVERSITY OF KWAZULU-NATAL	MAT.: PLA	No. REQ.: 1	SCALE: 2:1	UNITS: mm	PROJECT: TACTILE BRAILLE READER
SCHOOL OF ENGINEERING	DATE	CHECKED	STUDENT NAME: INGRID BOTHA		No.: A2
MECHANICAL ENGINEERING	PROJECT SUPERVISOR		STUDENT No.: 215024569		TITLE: BATTERY CASING
	WORKSHOP TECHNICIAN		E-MAIL: 215024569@STU.UKZN.AC.ZA		
	TECHNICAL OFFICER		TEL. No.:		

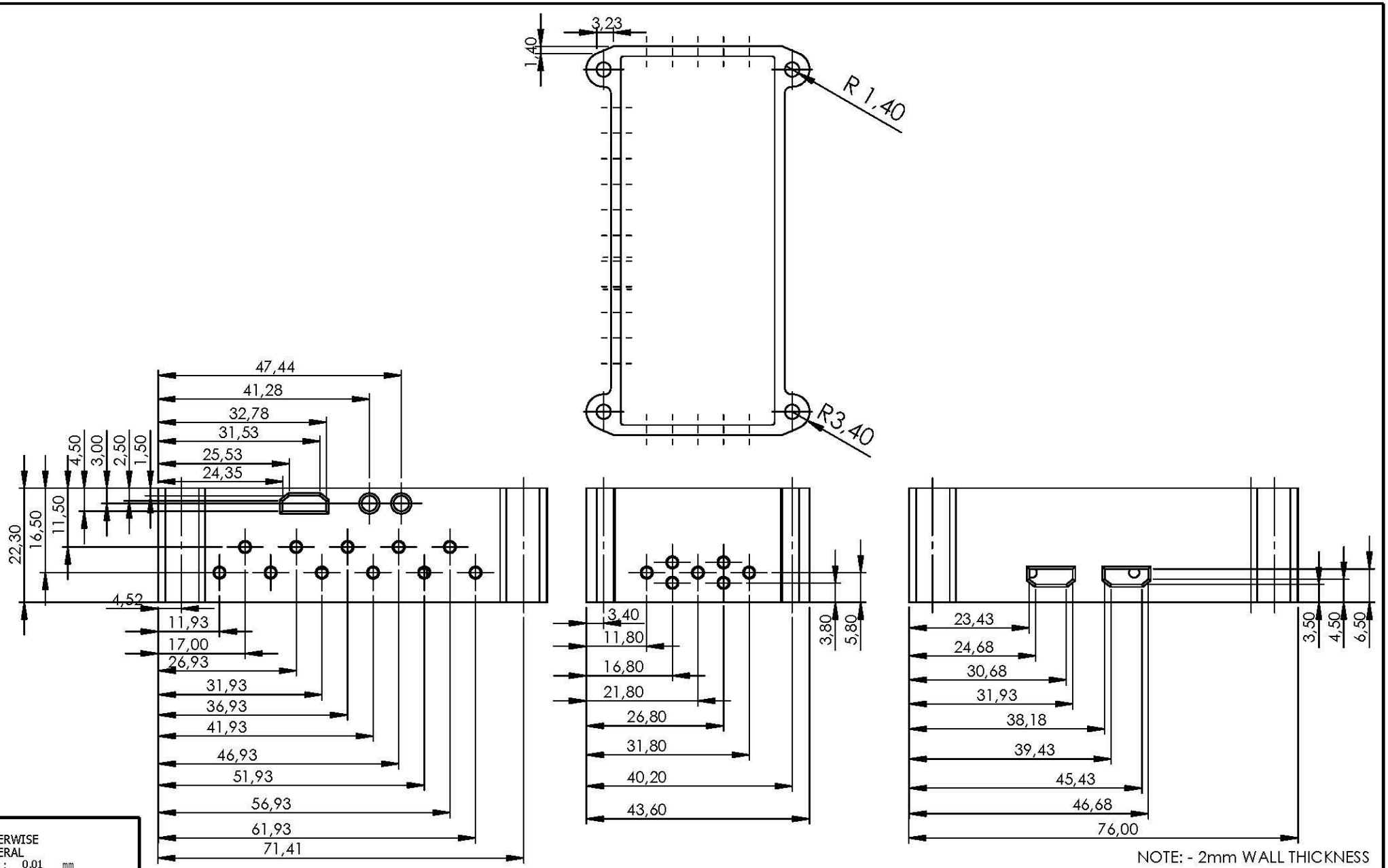

UNLESS OTHERWISE STATED GENERAL TOLERANCES : 0,01 mm
ANGLES : 1

NOTE: - 2mm WALL THICKNESS
- ALL FILLETS = R 1,00

UNIVERSITY OF KWAZULU-NATAL	MAT.: PLA	No. REQ.: 1	SCALE: 1:1	UNITS: mm	PROJECT: TACTILE BRAILLE READER
SCHOOL OF ENGINEERING	DATE	CHECKED	STUDENT NAME: INGRID BOTHA		No.: A3
MECHANICAL ENGINEERING	PROJECT SUPERVISOR		STUDENT No.: 215024569		TITLE: CIRCUIT CASING
	WORKSHOP TECHNICIAN		E-MAIL: 215024569@STU.UKZN.AC.ZA		
	TECHNICAL OFFICER		TEL. No.:		

ITEM NO.	PART NUMBER	DRAWING NO.	QTY.
1	BATTERY CASING	A2	1
2	CIRCUIT CASING	A3	1
3	CIRCUIT CASING COVER	A1	1
4	RaspberryPiZeroW	NA	1
5	ISO 4027 - M3 x 30-N	NA	4

NOTE: LIPO BATTERIES AND ADDITIONAL CIRCUIT COMPONENTS NOT SHOWN IN DRAWING.

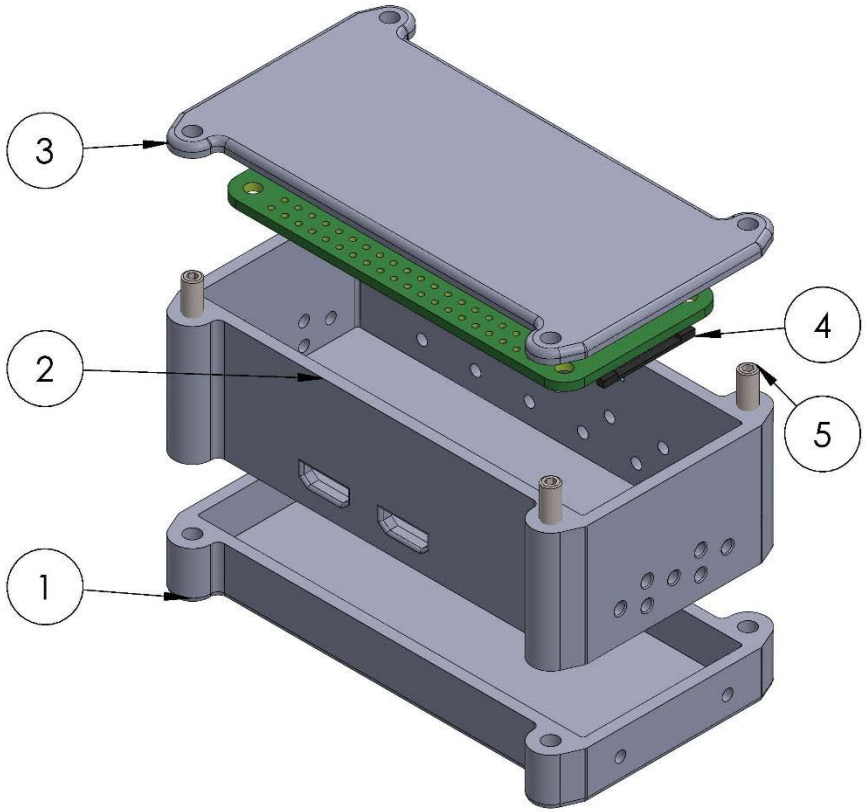

EXPLODED VIEW

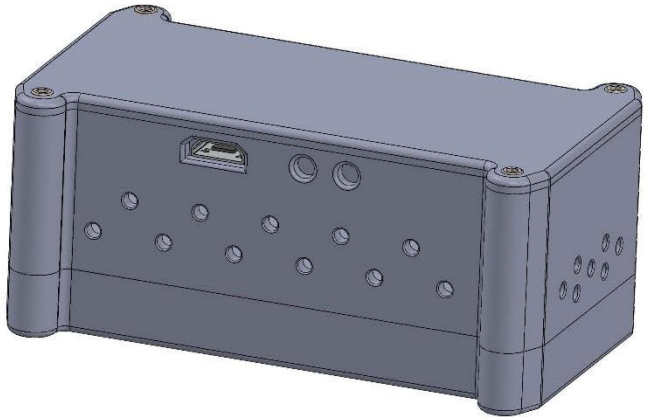

UNLESS OTHERWISE STATED GENERAL
TOLERANCES : 0,01 mm
ANGLES : 1

UNIVERSITY OF KWAZULU-NATAL	MAT.: NA		No. REQ.: 1	SCALE: 1:1	UNITS: mm
		DATE	CHECKED	STUDENT NAME: INGRID BOTHA	
SCHOOL OF ENGINEERING	PROJECT SUPERVISOR			STUDENT No.: 215024569	
	WORKSHOP TECHNICIAN			E-MAIL: 215024569@STU.UKZN.AC.ZA	
MECHANICAL ENGINEERING	TECHNICAL OFFICER			TEL. No.:	

PROJECT: TACTILE BRAILLE DISPLAY	No.: SA1
TITLE: CIRCUIT CASING SUBASSEMBLY TYPE 1	

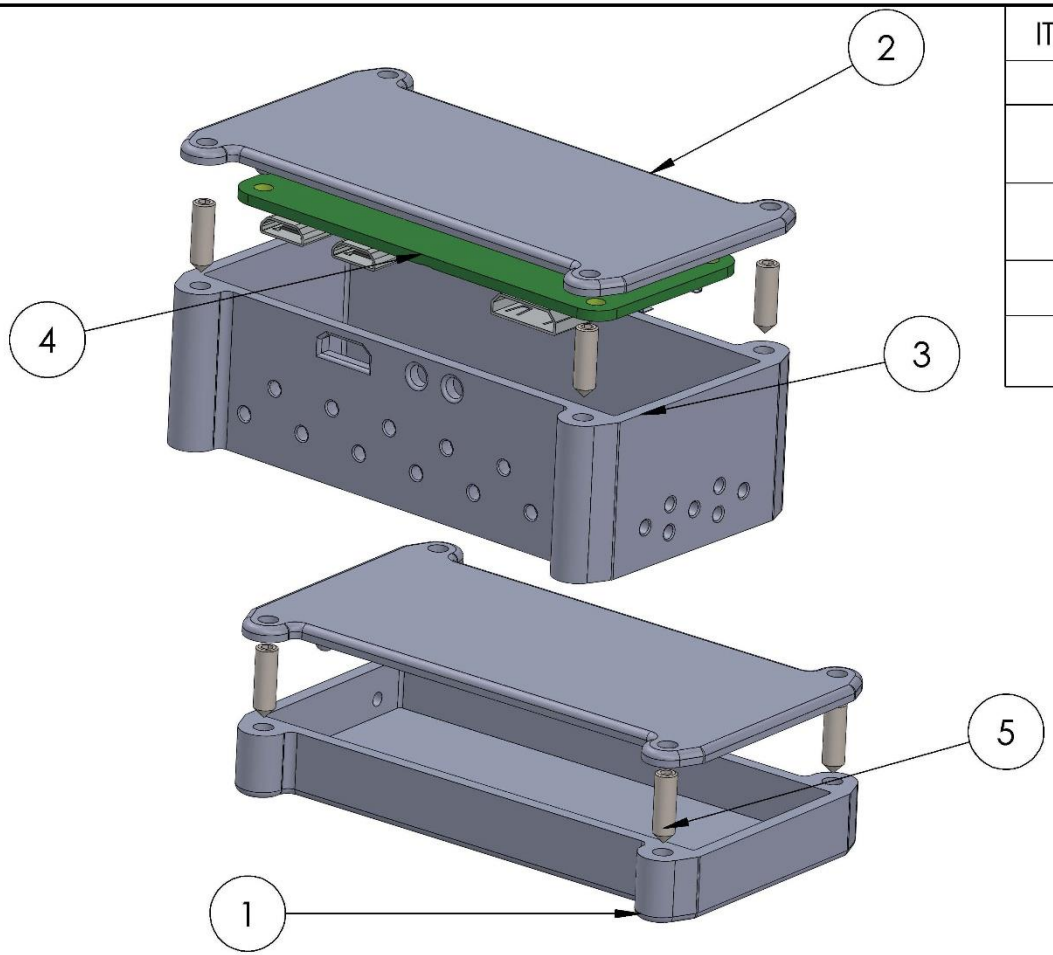

ITEM NO.	PART NAME	DRAWING NO.	QTY.
1	BATTERY CASING	A2	1
2	CIRCUIT CASING COVER	A1	2
3	CIRCUIT CASING	A3	1
4	RaspberryPiZeroW	NA	1
5	ISO 4027 - M3 x 10-N	NA	8

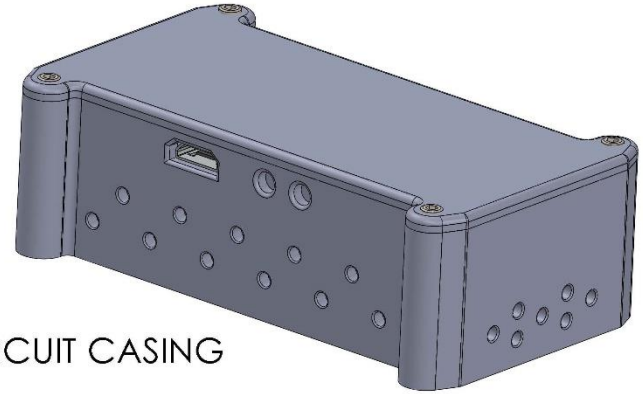

CIRCUIT CASING

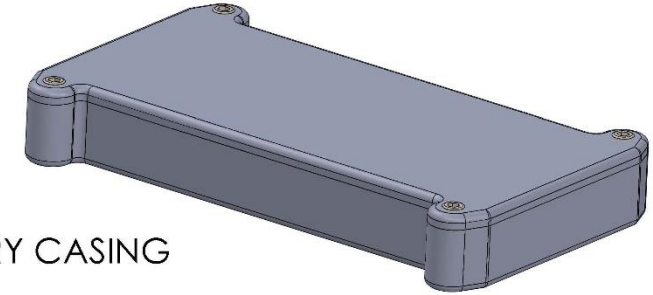

BATTERY CASING

NOTE: LIPO BATTERIES AND ADDITIONAL CIRCUIT COMPONENTS NOT SHOWN IN DRAWING.

UNLESS OTHERWISE STATED GENERAL
TOLERANCES : 0,01 mm
ANGLES : 1

UNIVERSITY OF KWAZULU-NATAL	MAT.: NA	No. REQ.: 1	SCALE: 1:1	UNITS: mm	PROJECT: TACTILE BRAILLE READER
SCHOOL OF ENGINEERING	DATE	CHECKED	STUDENT NAME: INGRID BOTHA		No.: SA2
MECHANICAL ENGINEERING	PROJECT SUPERVISOR		STUDENT No.: 215024569		TITLE: CIRCUIT CASING SUBASSEMBLY TYPE 2
	WORKSHOP TECHNICIAN		E-MAIL: 215024569@STU.UKZN.AC.ZA		
	TECHNICAL OFFICER		TEL. No.:		

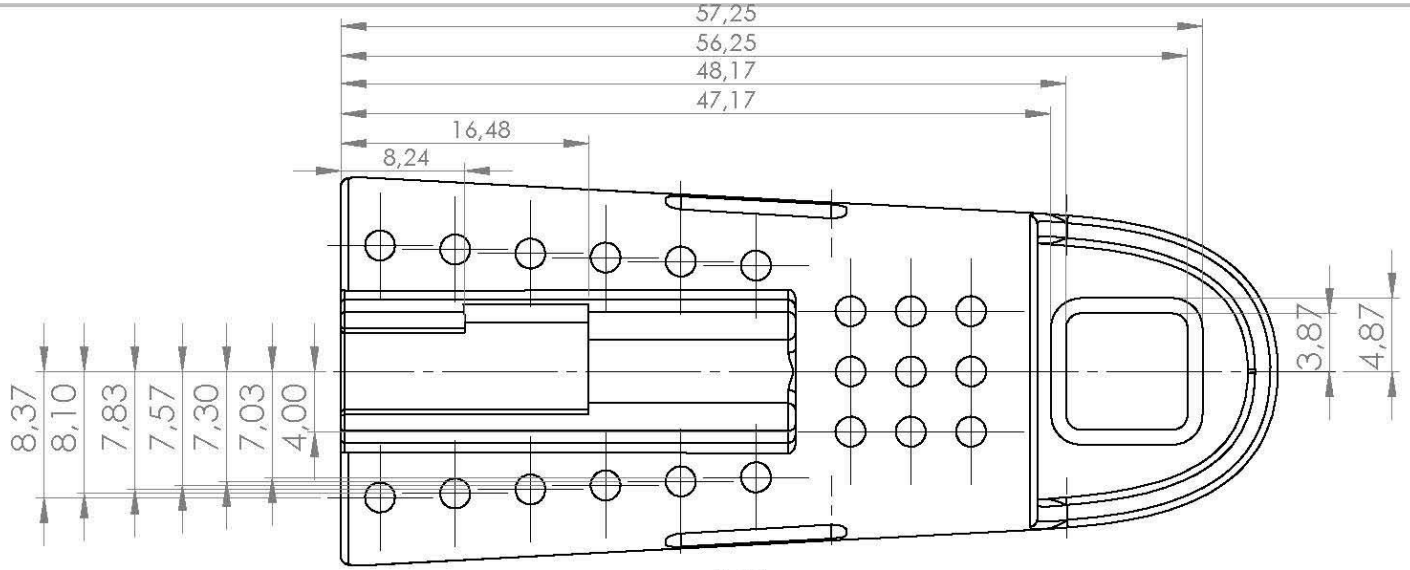

NOTE: WALL THICKNESS 2mm
ALL FILLETS = 0,5 mm

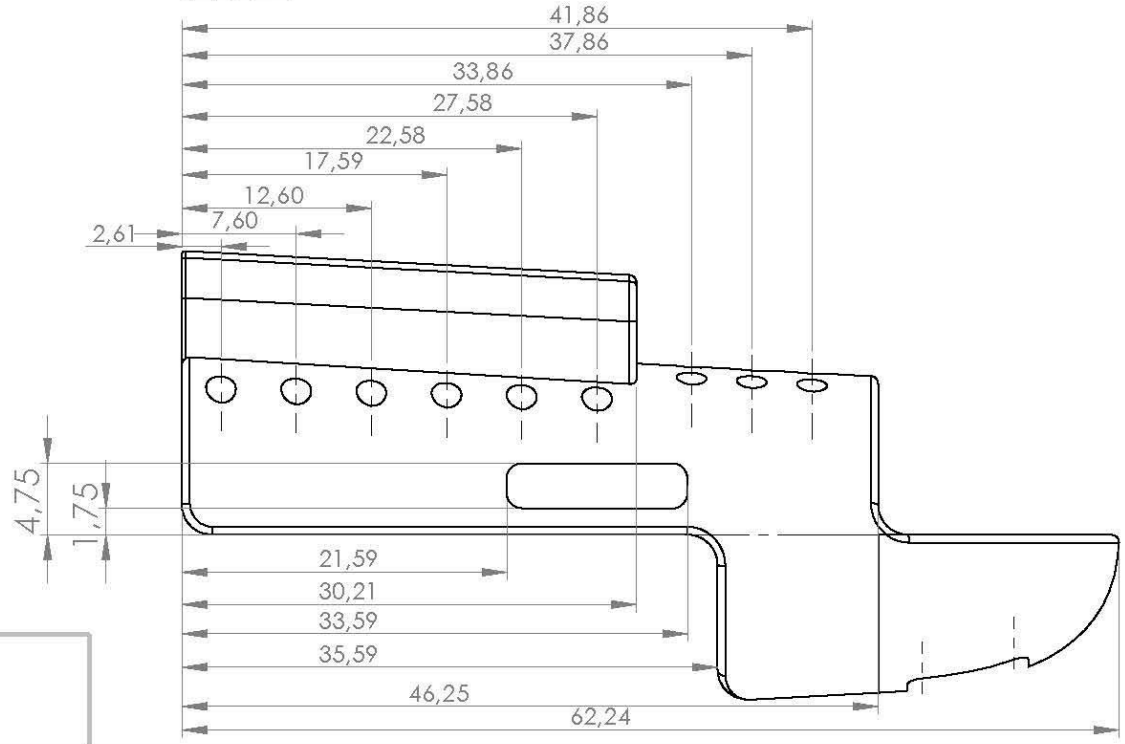

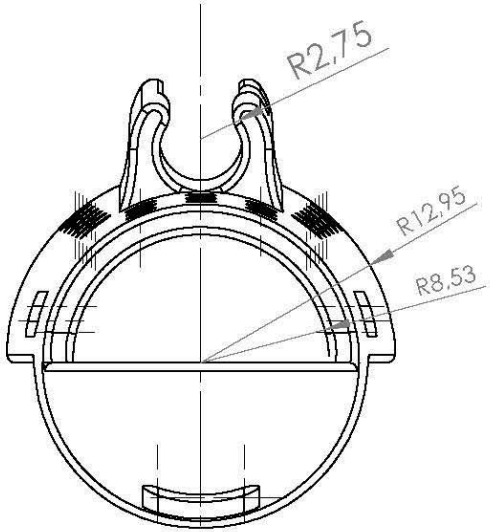

UNLESS OTHERWISE
STATED GENERAL
TOLERANCES : 0,01 mm
ANGLES : 1

UNIVERSITY OF KWAZULU-NATAL	MAT.: PLA		No. REQ.: 1	SCALE: 2:1	UNITS: mm
		DATE	CHECKED	STUDENT NAME: INGRID BOTHA	
SCHOOL OF ENGINEERING	PROJECT SUPERVISOR			STUDENT No.: 215024569	
MECHANICAL ENGINEERING	WORKSHOP TECHNICIAN			E-MAIL: 215024569@STU.UKZN.AC.ZA	
	TECHNICAL OFFICER			TEL. No.:	

PROJECT: TACTILE BRAILLE READER	No.: A4
TITLE: FINGER MOUNTING	

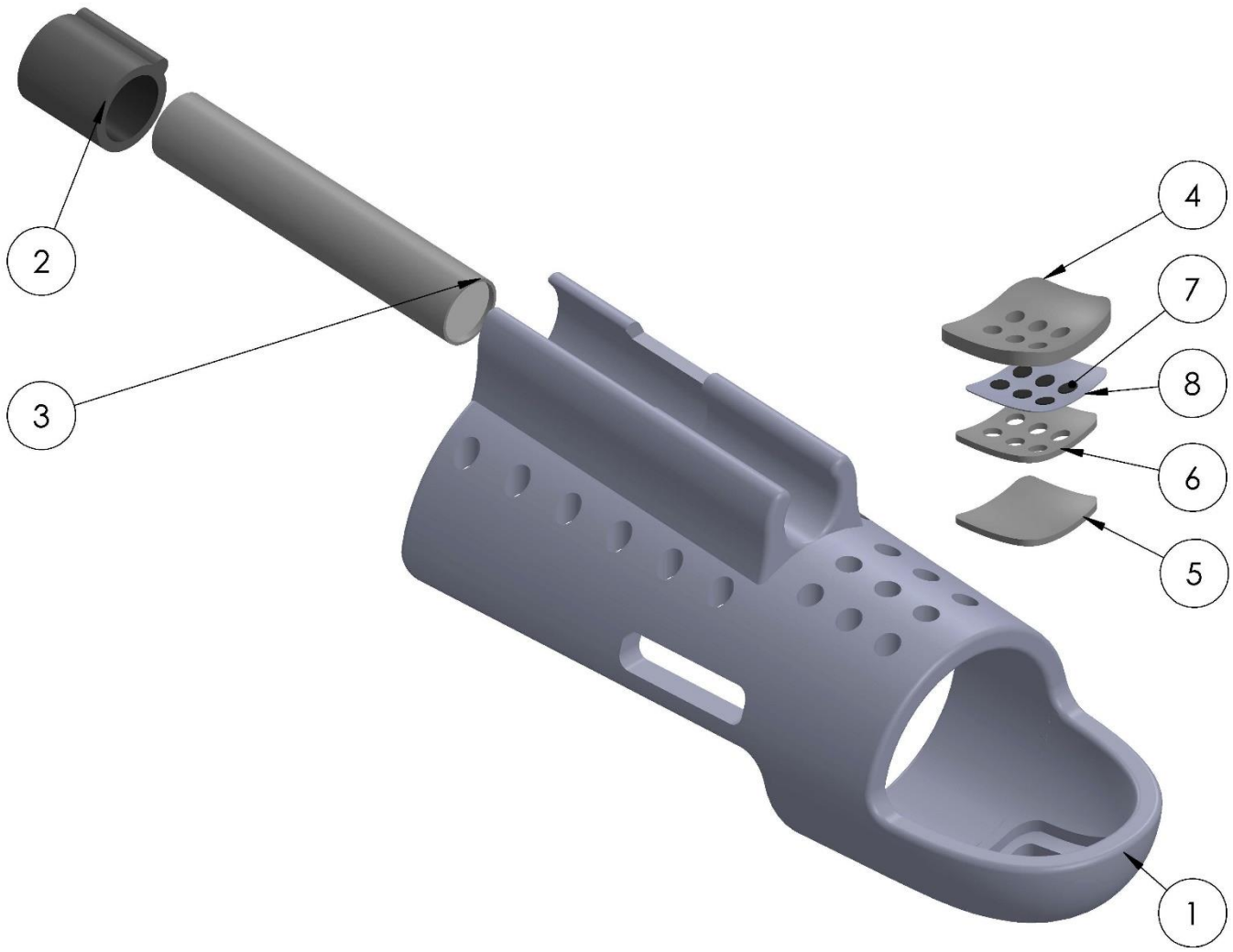

ITEM NO.	PART NAME	QTY.
1	FINGER MOUNTING	1
2	WASHER	1
3	ENDOSCOPE CAMERA MODULE	1
4	UPPER RIGID BOUNDARY	1
5	BASE PLATE	1
6	LOWER RIGID BOUNDARY	1
7	COMPLIANT ELECTRODE LAYER	2
8	ELASTOMER	1

UNLESS OTHERWISE STATED GENERAL
TOLERANCES : 0.05 mm
ANGLES : 1

UNIVERSITY OF KWAZULU-NATAL
SCHOOL OF ENGINEERING
MECHANICAL ENGINEERING

MAT.: NA	No. REQ.: 1	SCALE: 2:1	UNITS: mm
DATE	CHECKED	STUDENT NAME: INGRID BOTHA	
PROJECT SUPERVISOR		STUDENT No.: 215024569	
WORKSHOP TECHNICIAN		E-MAIL: 215024569@stu.ukzn.ac.za	
TECHNICAL OFFICER		TEL. No.:	

PROJECT: TACTILE BRAILLE READER

No.: SA3

TITLE: EXPLODED VIEW OF ACTUATOR ASSEMBLY

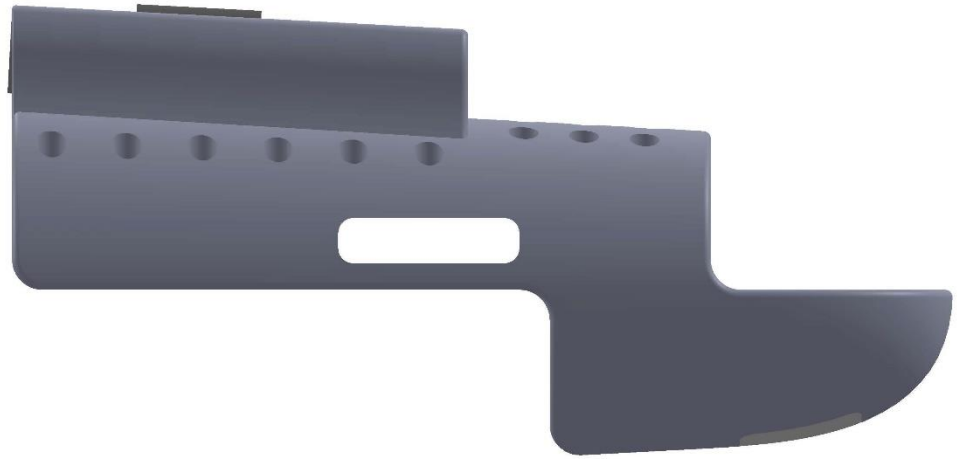

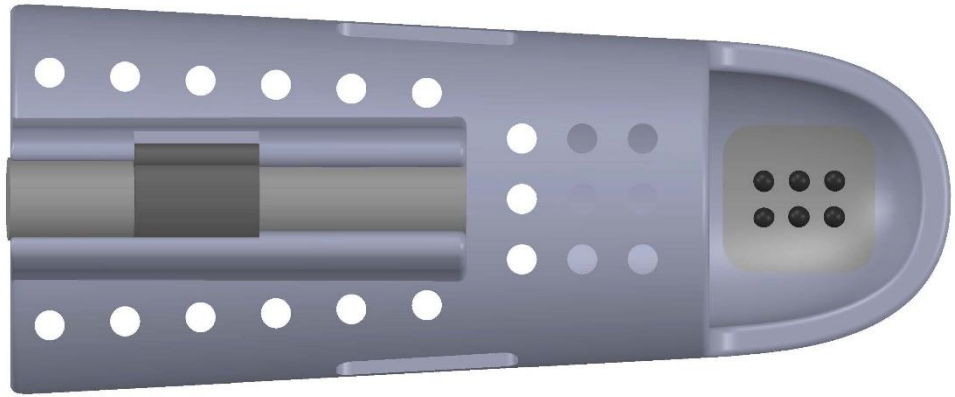

UNLESS OTHERWISE
STATED GENERAL
TOLERANCES : 0.05 mm
ANGLES : 1

UNIVERSITY OF KWAZULU-NATAL SCHOOL OF ENGINEERING MECHANICAL ENGINEERING	MAT.: NA	No. REQ.: 1	SCALE: 2:1	UNITS: mm	PROJECT: TACTILE BRAILLE READER
	DATE	CHECKED	STUDENT NAME: INGRID BOTHA		No.: SA4
	PROJECT SUPERVISOR		STUDENT No.: 215024569		TITLE: ACTUATOR ASSEMBLY
	WORKSHOP TECHNICIAN		E-MAIL: 215024569@stu.ukzn.ac.za		
	TECHNICAL OFFICER		TEL. No.:		